REPORT DOCUMENTATION PAGE		Form Approved OMB No. 0704-0188

The public reporting burden for this collection of information is estimated to average 1 hour per response, including the time for reviewing instructions, searching existing data sources, gathering and maintaining the data needed, and completing and reviewing the collection of information. Send comments regarding this burden estimate or any other aspect of this collection of information, including suggestions for reducing the burden, to Department of Defense, Washington Headquarters Services, Directorate for Information Operations and Reports (0704-0188), 1215 Jefferson Davis Highway, Suite 1204, Arlington, VA 22202-4302. Respondents should be aware that notwithstanding any other provision of law, no person shall be subject to any penalty for failing to comply with a collection of information if it does not display a currently valid OMB control number.
PLEASE DO NOT RETURN YOUR FORM TO THE ABOVE ADDRESS.

1. REPORT DATE (DD-MM-YYYY)	2. REPORT TYPE	3. DATES COVERED (From - To)
27-02-2015	Final Report	01-04-2012 to 28-02-2015

4. TITLE AND SUBTITLE	5a. CONTRACT NUMBER
Polarization-Based Radar Detection in Sea Clutter	
	5b. GRANT NUMBER
	N00014-12-1-0539
	5c. PROGRAM ELEMENT NUMBER
	ONR 312

6. AUTHOR(S)	5d. PROJECT NUMBER
Thomas G. Pratt and Robert D. Kossler	12PR07045-00
	5e. TASK NUMBER
	5f. WORK UNIT NUMBER

7. PERFORMING ORGANIZATION NAME(S) AND ADDRESS(ES)	8. PERFORMING ORGANIZATION REPORT NUMBER
University of Notre Dame Du Lac Research and Sponsored Programs 940 Grace Hall Notre Dame, IN 46556-5602	

9. SPONSORING/MONITORING AGENCY NAME(S) AND ADDRESS(ES)	10. SPONSOR/MONITOR'S ACRONYM(S)
Office of Naval Research 875 North Randolph Street Arlington, VA 22203-1995	
	11. SPONSOR/MONITOR'S REPORT NUMBER(S)

12. DISTRIBUTION/AVAILABILITY STATEMENT
Approved for Public Release; distribution is Unlimited.

13. SUPPLEMENTARY NOTES

14. ABSTRACT
The goal of the proposed research is to characterize and model polarization-related behaviors of sea clutter and to use these models to develop and evaluate methods for radar detection/characterization of a target on the surface of the sea. The specific propagation phenomenology that is to be exploited in this new form of detection is termed polarization mode dispersion (PMD), which is characterized by a spread in the received signal polarization state versus the signal frequency components in the radar returns. PMD is traditionally not analyzed in radar returns, but the hypothesis is that knowledge of the PMD in the returns (which is embedded via distributed clutter and target reflections) contains new forms of information.

15. SUBJECT TERMS

polarization mode dispersion; radar; sea surface; electromagnetic modeling; target identification; target detection

16. SECURITY CLASSIFICATION OF:			17. LIMITATION OF ABSTRACT	18. NUMBER OF PAGES	19a. NAME OF RESPONSIBLE PERSON
a. REPORT	b. ABSTRACT	c. THIS PAGE			Thomas Gregory Pratt
					19b. TELEPHONE NUMBER (Include area code)
					574 631-0973

Final Report:

Polarization-Based Radar Detection in Sea Clutter

Prepared by:
T. G. Pratt and R. Kossler
University of Notre Dame
Notre Dame, IN 46556

Submitted to:
Dr. Michael Pollock
Code 312
Office of Naval Research
Arlington, VA

TABLE OF CONTENTS

TABLE OF ACRONYMS

CP-MIMO	co-polarization multiple-input multiple-output
CSIT	channel state information at the transmitter
DARPA	Defense Advanced Research Projects Agency
DP-MIMO	dual-polarized multiple-input multiple-output
EA	electronic attack
EM	electro-magnetic
EP	electronic protection
ESM	electronic support measures
H	horizontal polarization
HH	horizontal transmit to horizontal receive
HV	horizontal transmit to vertical receive
ID	identification
MIMO	multiple-input multiple-output
OFDM	orthogonal frequency division multiplexing
PDL	polarization dependent loss
PMD	polarization mode dispersion
RF	radio frequency
SAR	synthetic aperture radar
SP-MIMO	space-polarization multiple-input multiple-output
V	vertical polarization
VH	vertical transmit to horizontal receive
VV	vertical transmit to vertical receive

I. INTRODUCTION

A. *Research Objective*

The objective of this research is to investigate radar detection methods that exploit a propagation phenomenology called polarization mode dispersion (PMD) for enhanced radar detection performance and for long range target identification, especially for targets in sea clutter. Performance is of particular interest for monostatic topologies involving either low incidence or near-normal incidence geometries and for bistatic topologies involving low-incidence geometries.

An important component of the research is to model polarization-related behaviors of sea clutter that, as yet, have not been considered in literature, and that can be used to develop and evaluate new methods for radar detection and characterization of targets on the surface of the sea. The specific propagation phenomenology that is to be exploited, PMD, occurs in propagation environments exhibiting both delay spread and depolarization. PMD is manifested as a spread in the received signal polarization state versus the signal frequency components in the radar returns. The phenomenology is described in Section VI.B.

A rather large body of literature exists addressing characterizations of sea clutter (see for example [1][2][3][4][5][41][45][46][47] and references contained therein). None that we have found appears to address or exploit PMD behaviors of sea clutter, suggesting that a potential avenue for enhancing radar performance through PMD-based detection modes remains to be pursued. We anticipate that PMD contains new forms of intelligence that can be elicited from the radar returns and also may enhance target detection. The goals of this work are to develop an understanding of the polarization dispersion behaviors associated with radar sea clutter, to formulate analysis models, and then to develop and evaluate preliminary PMD-based detection algorithms and approaches that have potential to enhance detection and characterization of targets on or near the surface of the sea.   The work is also expected to result in the identification of new techniques and methods that can be explored more rigorously in future research and experimental efforts.

This report documents the work completed towards an investigation of the exploitation of PMD in both forward scatter (e.g., bistatic) and backscatter (e.g., monostatic) radar modes. Topics that are considered in this report include the following:

- Background research describing channel modeling that led to observations of PMD in RF propagation channels and that serves as a springboard for characterizing PMD responses in radar applications.

- Sea surface modeling.

1

- Polarization-sensitive electromagnetic (EM) characterization of the scattering from the sea surface.

- Prevailing polarization-based detection methods based on a modest literature survey.

- PMD response models that extend EM reflection characterizations. Theoretical formulations for PMD are derived that augment the Sinclair matrix representation for sea and target scattering to enable PMD-based analyses. These formulations are used in conjunction with sea surface models and electromagnetic wave scattering theory to estimate PMD-based scattering responses from the collection of reflecting facets in a dynamic sea.

- Use of the developed models to analyze reciprocity for bistatic configurations.

- Field experimentation over water to illustrate PMD characterizations from changing surface water conditions. The trends from these latter characterizations help substantiate the underpinnings of the forward- and backscatter clutter response models of PMD used to evaluate PMD-based target detection and target feature characterization at different signal-to-clutter power ratio regimes.

- Forward scatter and backscatter characterizations as a function of radar system parameters. Radar system parameters, such as antenna directivity and waveform time and frequency-domain properties are incorporated to assess the impact of these parameters on target detection and identification.

- Target response characterizations and associated models for PMD-based analysis.

- Development of detection algorithms and analysis of these detection methods in sea clutter. The research involves theoretical/numerical modeling and analysis. Signal processing approaches that leverage PMD responses to achieve enhanced target detection (relative to conventional single-polarization detection approaches) in a background of sea clutter are developed and investigated. System performance is estimated through numerical simulations that incorporate modeling of the sea state, electromagnetic scattering, statistical modeling of the target and sea responses, radar system modeling, characterization of the resulting PMD responses, and target detection algorithms. These latter algorithms utilize PMD to help isolate the target response from the clutter response using a combination of space, time, polarization, and/or frequency dimensions.

- Development of target identification approaches, including attitude rate detection, and analysis of these techniques when applied to simulated targets in sea clutter.

- Qualitative consideration of adaptive transmission techniques and PMD-based wideband clutter suppression and their potential to aid target detection.

Ultimately, this report documents the foundational work that we anticipate will aid future analyses and experimentation associated with dispersion-based radar techniques.

B. *Motivation for Polarization-Based Systems*

Prior research in communications-based channel modeling and experimentation has led to an improved understanding of the polarimetric behavior of radio frequency (RF) propagation channels. In particular, the polarization behavior in space-polarization MIMO multipath channels has been characterized in new ways, eliciting input-to-output characterizations describing PMD, leading to improved understanding of antenna/channel correlations in space, time, frequency, and polarization.

These advancements were based primarily on experimentation and modeling performed on the Army's Collaborative Technology Alliance program between 2003 and 2008, where a wide range of MIMO channel sounding experiments were performed using different antenna architectures (arrays, dual-polarized antennas, and space-polarization architectures) and in different propagation environments (indoor, ground-to-ground; rooftop to ground; vehicle-to-vehicle on city surface streets and on metropolitan interstate highways). The analysis of these measurements led to insights on how to characterize the input-to-output polarization behavior in multipath channels through the mechanisms of PMD and polarization dependent loss (PDL).

More recently, the modeling of frequency-selective space-polarization channels has been considered with the objective of characterizing MIMO channels to support the analyses of MIMO systems communications energy efficiencies. This work led to several publications [78][86][87][88][89] that propose a model form for space polarization channels, propose a channel sounding method, demonstrate the ability to estimate model parameters associated with signals obtained from channel sounding, and finally show that the system performance from the estimated model closely matches the capacity statistics associated with the actual channel.

As a consequence of these advancements, the exploitation of polarization behaviors based on PMD is being considered for a number of RF applications. For example, these channel properties have been leveraged in wideband interference suppression [9][10], adaptive transmission approaches [49], and remote sensing applications [50][53]. Based on the many ways that PMD can be leveraged, we anticipate that polarization can provide new forms of intelligence to support target detection and identification. In this research, we investigate how these concepts can potentially be exploited to address target detection and ID in sea clutter.

Channel Statistics

One of the key reasons for considering polarimetric architectures is that the joint channel response of a dual-polarized receiver will generally be different than the response from single polarized systems, such as a copolarized array. As a consequence, new forms of detection may be possible that cannot be achieved with more conventional single-polarized architectures (including arrays) simply due to channel and target response behavior. A review of past literature, described in a later section, reveals that polarization is often leveraged through diversity approaches, i.e., the transmit and receive polarizations are varied with the intention of achieving good detection performance for at least one of the polarization pairs, e.g., see [1]. However, more effective polarization detection methods are possible that leverage the coherence between the signals received on the dual-polarized receive ports. A compendium of several polarimetric target descriptors formed with coherent processing and used in remote sensing is provided in [6] and [7]. These target descriptors attempt to extract information from the received signal's polarization behavior and can be used to help classify targets as described in [6]. The models employ *single-frequency* Sinclair matrices, and thus do not directly suggest approaches for frequency-selective target characterizations that are needed to accommodate PMD representations. A body of existing work does consider polarization characterizations at multiple widely spaced carrier frequencies. For example, [8] cites a number of references that have considered multi-frequency SAR to improve discrimination capability. These systems employ widely spaced frequencies (e.g., P-band, L-band, C-band, etc.), but ignore the frequency dependent polarization properties (e.g., polarization mode dispersion) embedded within the received pulses at any one of the carrier frequencies. *As yet, there does not appear to be any work that analyzes PMD-based frequency-dependencies in radar, which highly motivates the work being undertaken in this research program.*

Advanced Capabilities

Integration of a dual-polarized architecture also opens the door for advanced signal processing capabilities. Although detailed explorations of these methods are beyond the scope of the current effort, they are mentioned to delineate additional

gains that may accrue through the adoption of polarization-based architectures. This current effort considers 2x2 dual-pol systems. Future efforts will expand this to 2x4 and perhaps to even 4x4 space-polarization systems.. The first potential benefit of the MIMO architectures, is provision for wideband interference suppression using polarization-frequency filtering. The effectiveness of this approach has been demonstrated in Notre Dame's polarimetric testbed on a DARPA program to enable suppression of wideband interference based on the PMD response of the interference source. The methods are described in [9] and [10]. The ability to suppress interference based on the polarization response would suggest the possibility of mitigating main beam clutter responses for improved target detection. A further benefit of MIMO architectures is the potential for unique forms of electronic support measures (ESM), electronic attack (EA), and electronic protection (EP), where specific details of these methods could be discussed in an alternative forum.

An additional benefit is its ability to engage in adaptive transmission techniques. Adaptive techniques have been described for interference avoidance in communications systems [11], and similar approaches are anticipated to have benefit for radar systems to minimize the impact of sea clutter for one or more range cells. For example, adaptive transmission techniques coupled with PMD-based interference suppression can potentially be integrated to limit the impact of sea clutter, including clutter returns that bleed through time-domain and frequency-domain side lobes and those that occur within each range resolution cell. Conceptually, such approaches require channel knowledge at the transmitter, referred to as channel state information at the transmitter (CSIT), which can be measured during a dwell. A subsequent transmission with precoding can potentially be generated that provides improved resilience to sea clutter. The coherence time of the channel will dictate the latency that can be tolerated between channel state measurement and adaptive transmission for a given level of performance.

Researchers in the past have considered relatively simplistic forms of adaptive polarization architectures for communications [12][13]. These systems have adjusted the relative power between transmitter polarization states to increase the overall system performance, but they did not consider capability for arbitrary polarization control or control as a function of the frequency components of the transmitted waveform. Recently, more general adaptive transmission techniques with full-polarization control versus frequency have been considered for communications systems in the presence of channel impairments [11]. "Fully-adaptive" refers to the ability of the system to achieve arbitrary polarization (instead of merely being switched between a few states or adjusting only the relative powers between transmit modes), where the polarization states are controlled as a function of the frequency components of the signal. Adaptive

transmissions were used to either maximize the power transferred through the channel on a subcarrier-by-subcarrier basis, or to control the PMD response at the receiver, e.g., for interference avoidance. The former approach is synonymous with those proposed for conventional MIMO systems with link channel knowledge [14], although in the case of dual-polarized architectures, polarization-frequency rather than space-frequency characterizations are applied. The latter approach provides unique methods enabling mitigation of signal via polarization nulling [15]. Both adaptive approaches may have merit in radar applications to facilitate sea-clutter mitigation and target detection.

Simultaneous Characterizations

A critical benefit of 2x2 MIMO polarization architectures is the potential to obtain the full frequency-dependent channel matrix simultaneously at the receiver using an appropriately designed transmit waveform. For example, assuming transmissions with multiple orthogonal subcarriers (similar to OFDM), *odd* subcarriers could be transmitted using V polarization, and *even* subcarriers could be transmitted using H polarization. Channel estimates across all subcarriers can then be achieved through interpolation. Acquisition of the full-polarization characterization opens the door for efficient use of transmission resources to collect different forms of PMD, for example using the HH and VV components (which is typically not available to communications systems), and also HV and VH, which could be compared in monostatic topologies to determine if a nonreciprocity (from a target) exists in the returns.

This transmission approach has a secondary benefit that we believe is perhaps even more important. The technique provides a means to "tune" the transmit polarization via signal processing at the receiver, so that the receiver can generate the received signal particular to any specified transmit polarization state. Moreover, this can be accomplished on a cell-by-cell basis without the need for CSIT. The receiver would also retain its capability to utilize its MIMO degrees of freedom for frequency-selective interference suppression. These processing concepts extend to 2x4 and 4x4 MIMO architectures that will be considered in future research.

Space Constraints

A final motivation for employing polarization is the ability to achieve additional receiver ports in space-constrained platforms, i.e., there may be limits on the number of antennas (rather than receiver chains) that can be deployed due to available space. One strategy for increasing system capability in this case is to employ a dual-polarized antenna at each co-polarized antenna location, a strategy

that has been considered in communications systems [17][18][19][20], giving additional capability without substantially increasing the antenna footprint.

C.   Technical Approach

The specific technical objectives of the research articulated above are reflected in the various milestones pursued in the research. The first major milestone was the development of a time-varying sea surface model. Sea surface models of various complexity were identified in literature, and from these we chose to employ models based on the Weierstrass-Mandelbrot function to represent random surface characterizations where the height variations are derived from a statistical sum of multiple weighted waves with wave periods spaced by integer exponents of an irrational factor. However, we use an alternative distribution to characterize wave directions, one that is based on the von Mises distribution so that the mean wave directions and their concentrations (ranging from highly concentrated directions about the mean to isotropically distributed directions) are easily configured to synthesize a surface roughness function.

Presently, the sea surface is divided into facets based on a uniform grid in the mean plane (i.e., the projection of the wave onto the x-y plane, where the z direction corresponds to the wave height). Literature suggests that quarter-wavelength gridding represents a reasonable balance between accuracy and computational demands [54], and we employ comparable gridding strategies. Some of the primary sea surface descriptors associated with the sea surface synthesis model include wind direction, the mean wave direction, the distribution of the wave directions, the number of waves (each with a different wavenumber), and the amplitudes of the waves.

The next major milestone was to model the electromagnetic response reflected by the sea surface in the propagation path between the transmitter and the receiver. Initially, to accommodate polarization, the electric field was decomposed into components that are parallel and perpendicular to the plane of incidence [40]. Using this approach, we employed theory based on Snell's laws and assumptions about continuity at the boundary layer to arrive at electric field values for the orthogonally-polarized received signal components for both vertically and horizontally-polarized transmit signals. Realizing that arbitrary transmission polarization states can be represented as a complex weighting of these components, the model can accommodate any transmit polarization state.

The model was then extended using Kirchhoff theory in conjunction with far-field assumptions to arrive at the Stratton-Chu equation defining the far-field response from surface integrals over each facet, and we followed developments primarily from [38], [39], and [40]. The approach first involved reviewing perturbation

theory for rough-surface scattering, then scalar Kirchhoff theory, and then finally vector Kirchhoff theory. Vector Kirchhoff theory is the final form currently employed in our research, where the facets are assumed to provide a response that is uniform across each facet. With this assumption, the key difference between the initial Snell's law formulation and the vector Kirchoff theory appears to be a $cos\,\theta_{inc}$ term in the denominator that accounts for a scaling of the facet area as a function of incidence angle, θ_{inc} [39]. Technically, this factor could be integrated into the former model to arrive at similar results under the assumption of facet responses that are uniform across the individual facets. Generally, the Kirchhoff vector model is easier to work with and offers greater flexibility if modeling details need to be enhanced, and hence this is the chosen approach.

The current model supports monostatic and bistatic configurations. Responses for low grazing angles and for normal incidence, however, need to be treated with care. For example, assumptions associated with Kirchoff theory break down at low grazing angles. We intend to rely on modifications that reflect empirical trends reported in literature. For example, at low grazing angles, the amplitude response from the clutter becomes quite bursty with high peak values that decorrelate over a period of seconds. Thus care is required to represent these types of behaviors and correlations (in time, space, Doppler, etc.) to encapsulate many of the trends that are reported in literature from experiments. We also conducted a number of our own experiments, first using a wave tunnel, and then across the lakes on the Notre Dame campus.

Another milestone is the development of PMD responses from the EM reflections impinging upon the receiver. In general, these responses are time-varying, not only because of the spectral content of the radar signal, but especially due to the time variations in the sea surface and their associated impact on the properties of the reflected signals. PMD responses based on the EM responses have been integrated into the numerical models along with a time-varying sea surface to produce time-dependent PMD responses.

Another important milestone was to model the impact of the radar system parameters, such as antenna directivity, radar waveforms, the transmit polarization, and the carrier frequency. Given the sea clutter response models, a backscatter response was formulated to integrate the impact of radar beam and waveforms on the resulting PMD response in a radar resolution cell. We discuss the potential to modulate the polarization/frequency behavior at the transmitter to elicit a full-polarization characterization of the propagation channel. The forward scatter response problem was also considered. This part of the research involved consideration of a bistatic geometry involving spatially separated transmitter/receiver locations.

A key milestone was the consideration of basic target detection and target identification algorithms leveraging PMD. Candidate algorithms were drawn from detection approaches being employed in other PMD applications, such as vibrometry and spectrum sensing. Other novel algorithms were hypothesized and identified for further consideration that are based on the clutter response behavior trends observed in model simulations.

For target detection, we developed PMD-based detection algorithms and evaluated their performance in both backscatter and forward scatter topologies. One example of a detection algorithm involves the utilization of joint statistics in a background of clutter versus a background of clutter plus a target. This approach is quite similar to the approach taken in [37] for spectrum sensing applications. Goals of the target detection study were to determine if PMD detection methods provide improved performance relative to conventional pulse-Doppler radar detection. Another approach that was identified by not evaluated involves the detection of nonreciprocities in range cells, since some target features (e.g., those made from ferrites) will introduce nonreciprocal behavior. We anticipate evaluating the performance of this approach when experimental data are available to prove out the methods.

For target identification, we examined the potential for sensing target features based on time-variations in the PMD response. We considered possibilities of interpreting PMD signatures for target characterizations, for example to detect target attitude rates.

A final milestone was to qualitatively assess the feasibility of PMD-based clutter suppression and to determine if this technology warrants additional study in future efforts. Prior research funded by DARPA demonstrated the feasibility of wideband signal suppression using frequency-selective polarization filters. The extent to which such suppression is feasible for main beam sea clutter to improve signal-to-clutter ratios was addressed on a qualitative level. Additionally, a qualitative evaluation of adaptive transmission concepts was also considered. The purpose of this latter task was to determine if adaptive technologies warrant additional consideration in future research efforts. Given the ease with which monostatic radars can measure the channel state, we fully anticipate that adaptive transmission techniques could be particularly suited for these configurations especially for tracking modes. A more general approach, however has been postulated based on the use of simultaneous, separable orthogonally-polarized transmissions.

D.   Organization of the Report

The report is organized as follows. In Section II, background technologies are reviewed that form an important foundation for the research. These include some

work associated with space-polarization channel modeling for wireless communications systems, wideband polarization-based interference suppression, and adaptive transmission. In Section III, sea state models are discussed and a multiple-scale model is used to generate a time-varying sea state that incorporates both large-scale and small-scale component waves. Section III also presents a review of statistical characterization of clutter from rough surfaces drawn from literature. Such surfaces may be characterized by a height distribution function and a surface correlation function. The power spectra for several common surface correlation functions are presented.

Electromagnetic surface scattering models are described in Section IV. The development begins with a discussion of monochromatic wave scattering for the scalar case using Kirchhoff theory, and is then extended to the vector case to represent signal polarization and polarization-sensitive scattering responses. Section IV also provides a review of statistics and trends specific to electromagnetic signal reflections from sea clutter. Sea clutter behaviors as a function of sea state, radar resolution, and grazing angle are discussed and an empirical model incorporating many of these factors is presented. Based upon a literature review of numerous experimental investigations, trends in polarization-specific behaviors are noted. Statistical models and trends from both Section III and Section IV will fold into the PMD-based clutter model to improve the statistical behavior of the clutter model.

Section V describes additional system modeling topics such as radar system modeling and target modeling. Radar system modeling includes both monostatic and bistatic topologies, control of resolution cell size using pulse and beam parameters, and additional parametric control using RF center frequency and tone spacing. Target modeling consists of a multi-dipole model with random dipole orientations and reflection coefficients.

In Section VI, the Sinclair matrix is introduced for representing the polarimetric scattering response. Different polarization-based sensing methods employing the Sinclair matrix are then discussed, where examples were drawn from a modest survey of polarimetric sensing approaches described in literature. In this section, a theory is advanced to capture the principle EM scattering effects that are critical to PMD-based modeling. These are used to generate modified Sinclair representations for both the target and sea clutter responses that accommodate time-dispersive responses. The resulting formulation provides the needed mechanism to represent PMD responses. Using this formulation along with the sea-surface model and electromagnetic scattering response model, PMD responses can be numerically computed.

Section VII provides results from experimental measurements intended to characterize the polarimetric response of sea clutter. Wave tunnel measurements

were conducted with multiple antenna orientations and multiple wave types. Measurements at St Joseph Lake on the campus of Notre Dame included both monostatic and bistatic antenna orientations and multiple frequencies. Representative PMD curves from these experiments are presented. Periodicities in the PMD responses are identified by computing the FFT of the PMD centroid.

Section VIII presents an analysis of the correlations between the HV and VH scattering components for bistatic geometries. Recall that for the monostatic case (and assuming a reciprocal channel), HV=VH. However, for the bistatic case, this relationship does not hold in general, and the correlation between HV and VH will depend upon many parameters. The analysis shows that if narrowband processing (e.g., using subcarrier processing) is employed, HV and VH may be highly correlated over several degrees in a bistatic configuration. This section also discusses a method for target identification based on the periodic vibration rates characteristic of real-world targets. Experimental results (tuning fork experiment) as well as simulation results (using the distributed target model discussed in Section V) for estimating these attitude vibration rates are presented.

Section IX presents simulation results for a distributed target in a background of sea clutter using the models presented in Sections III, IV, and V. In each of the simulation runs, nine radar resolution cells are considered with the eight perimeter cells containing clutter only and the center cell containing both clutter and target. Multiple samples accumulated over both time and frequency subband are combined to estimate the cumulative distribution function (CDF) for a given cell. The results indicate that it is often possible to distinguish the distribution of the target cell from the distributions of the remaining clutter-only cells. Additionally, the results of a polarimetric detector are compared to a traditional detector in the form of receiver operating characteristic (ROC) curves. Finally, a promising detection approach is presented that computes the distance between the CDF estimate of a given cell and the "reference" CDF estimated from the average of all cells.

The polarization architecture can be exploited in different ways, and in Section X, we provide qualitative assessments of two special techniques: polarization-based interference suppression and adaptive polarization transmission techniques. We propose general techniques that would appear to give substantial benefit to polarization-based radar systems.

Due to the newness of the PMD radar concept, many topics still remain to help develop and evaluate PMD radar systems. In Section XI, we provide recommendations for future research that would build upon the work that has been completed to date. Finally, section XI contains a summary of the report.

11

II. BACKGROUND TECHNOLOGIES

Since 2002, efforts to experimentally measure and characterize polarization-sensitive MIMO communications channels have been undertaken by the author, leading to multiple papers [25][26][27][28][29][30][31] and patent submissions [48][49]. A particularly important outcome of some of this work was the observation that polarization mode dispersion occurs in wireless channels and provides a convenient mechanism for characterizing the input-to-output polarization behavior of the signal. Since the emergence of that work, various applications have been pursued in other fields that have potential relevance to the current study.

The first application involves the modeling of space-polarization MIMO communications channels to enable quantification of the relative energy efficiency of space-polarization (SP) architectures in comparison to conventional MIMO arrays. SP-MIMO architectures are of particular interest for the very reasons that have already been articulated defining potential benefits of polarization, and also because they provide benefits from the space dimension associated with the array configurations. Prior SP-MIMO research involved theoretical channel modeling, numerical analyses, and evaluations using an RF space-polarization testbed that incorporates channel emulation. The channel modeling work involved the use of theoretical models for the narrowband case and also statistical geometrical scattering models for the wideband case. These, as well as models instantiated into channel emulators were used to represent time-varying space-polarization MIMO channels and their attendant correlations in space, time, polarization, and frequency. Correlations in these same domains are anticipated to play an important role in the radar detection problem under consideration. The communications work has demonstrated that space-polarization architectures enable increased capacity (in space-constrained applications), as well as improved energy efficiency, especially at high SNR. The specific gains depend upon the encountered channel realization.

We first discuss DP-MIMO channels. These are of interest because they exploit polarization-based propagation behaviors using a dual-polarized received antenna. In the case of a dual-polarized 2x2 MIMO channel, a narrowband system model is given by

$$y = \begin{bmatrix} y_v \\ y_h \end{bmatrix} = \sqrt{g} \begin{bmatrix} h_{vv} & h_{vh} \\ h_{hv} & h_{hh} \end{bmatrix} \begin{bmatrix} s_v \\ s_h \end{bmatrix} + \begin{bmatrix} n_v \\ n_h \end{bmatrix}$$
$$= \sqrt{g}\mathbf{H}s + n \tag{1}$$

where the vector s represents the transmitted V and H signal components, $\mathbf{H}$ represents the channel matrix describing the complex gain from each transmit polarization to each receive polarization, g represents a complex propagation factor, and n represents a vector of additive white Gaussian receiver noise. The channel matrix may in general be decomposed into a fixed component ($\mathbf{H_c}$) and a variable component ($\mathbf{H_f}$) as follows

$$\mathbf{H} = \underbrace{\mathbf{E[H]}}_{\bar{\mathbf{H}}_c} + \underbrace{(\mathbf{H - E[H]})}_{\tilde{\mathbf{H}}_f} = \bar{\mathbf{H}}_c + \tilde{\mathbf{H}}_f \tag{2}$$

$$\bar{\mathbf{H}}_c = \mathbf{X} \odot \mathbf{K}_1 \odot \mathbf{\Phi}_c$$
$$\tilde{\mathbf{H}}_f = \mathbf{X} \odot \mathbf{K}_2 \odot \mathbf{C}_{Rx}^{1/2} \mathbf{G}\left(\mathbf{C}_{Tx}^{1/2}\right)^T \tag{3}$$

where the Rician K factors associated with the channel components are defined by the matrix

$$\mathbf{K} = \begin{bmatrix} k_{vv} & k_{vh} \\ k_{hv} & k_{hh} \end{bmatrix} \tag{4}$$

and where the K factors each consist of a constant component coefficient (K_1) and a variable component coefficient (K_2):

$$[\mathbf{K_1}]_{ij} = \sqrt{\frac{[\mathbf{K}]_{ij}}{1 + [\mathbf{K}]_{ij}}}, [\mathbf{K_2}]_{ij} = \sqrt{\frac{1}{1 + [\mathbf{K}]_{ij}}} \tag{5}$$

The model above reflects the tendency that the K factors associated with the various polarimetric channels are different.

DP-MIMO channels are also characterized by power asymmetries. In other words, the matrix X has the general form:

$$\mathbf{X} = \begin{bmatrix} 1 & \sqrt{\mu\chi_h} \\ \sqrt{\chi_v} & \sqrt{\mu} \end{bmatrix} \tag{6}$$

where the power ratios may be represented by the co-polarized power ratio (CPR) and the co- to cross-polarization power ratio (XPD):

$$\mathrm{CPR} = \frac{1}{\mu} = \frac{\mathrm{E}[\|h_{vv}\|^2]}{\mathrm{E}[\|h_{hh}\|^2]} \tag{7}$$

13

$$XPD_v = \frac{1}{\chi_v} = \frac{E[\|h_{vv}\|^2]}{E[\|h_{hv}\|^2]} \quad \text{(8)}$$

$$XPD_h = \frac{1}{\chi_h} = \frac{E[\|h_{hh}\|^2]}{E[\|h_{vh}\|^2]} \quad \text{(9)}$$

These formulations have been used to characterize narrowband 2x2 DP-MIMO channels. Corresponding representations that include space correlations and joint space-polarization correlations have also been developed to enable implementation of 4x4 SP-MIMO architectures in channel emulators.

As shown in Figure 1, SP-MIMO involves 16 different channels, corresponding to all of the transmit antenna/receive antenna pairings.
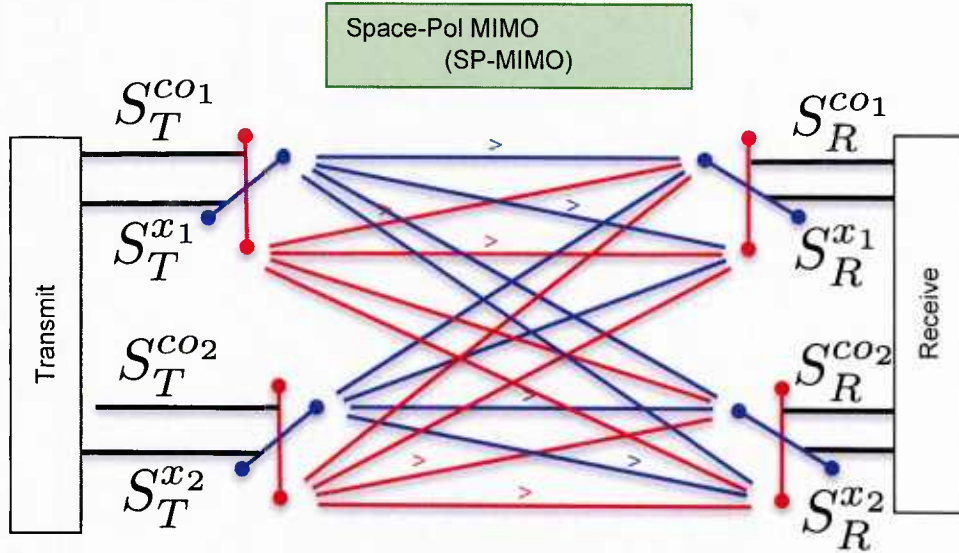

Figure 1. MIMO illustration 1 (4x4 SP-MIMO)

The channel response of SP-MIMO can be represented using a 4x4 time varying channel matrix with 16 time-varying channel impulse responses:

$$\mathbf{h}_{SP}(t,\tau) = \begin{bmatrix} h_{co_1co_1}(t,\tau) & h_{x_1co_1}(t,\tau) & h_{co_2co_1}(t,\tau) & h_{x_2co_1}(t,\tau) \\ h_{co_1x_1}(t,\tau) & h_{x_1x_1}(t,\tau) & h_{co_2x_1}(t,\tau) & h_{x_2x_1}(t,\tau) \\ h_{co_1co_2}(t,\tau) & h_{x_1co_2}(t,\tau) & h_{co_2co_2}(t,\tau) & h_{x_2co_2}(t,\tau) \\ h_{co_1x_2}(t,\tau) & h_{x_1x_2}(t,\tau) & h_{co_2x_2}(t,\tau) & h_{x_2x_2}(t,\tau) \end{bmatrix} \quad (10)$$

The channel is further characterized by the pairwise channel correlations (256 in all) derived from the 16 CIRS. These represent the combinations of space and polarization correlations at the transmitter and at the receiver.

An alternative approach for representing DP-MIMO and SP-MIMO channels has also been explored using statistical geometric modeling. Geometric modeling is an approach applied in various wireless communications standards bodies such as ETSI, LTE, and others. The particular approach that we advanced involved the use of concentric spheres at the transmitter and the receiver to facilitate modeling of the scattering environment as shown in Figure 2. The model is used to represent SISO channels, 2x2 co-polarization MIMO (CP-MIMO) channels, 2x2 DP-MIMO channels, and 4x4 SP-MIMO channels. Due to the ray-based approach, important correlations in space, polarization, time, and frequency, and in joint domains (e.g., polarization-frequency) are inherently represented. Application of the model yields time varying space-polarization channel impulse responses that are used to analyze communications system performance. Details of the model are presented in [44]. We anticipate that in the case of a radar that employs at least a 2x2 DP-architecture, time, polarization, and frequency correlations can be leveraged for both detection and identification.

	The center frequency
f_c	The center frequency
λ_c	The wavelength of center frequency
f_{tmax}, f_{rmax}	The maximum Doppler frequencies at the Tx and Rx respectively
γ	The path loss exponent
K	The Rician K factor
σ_h	

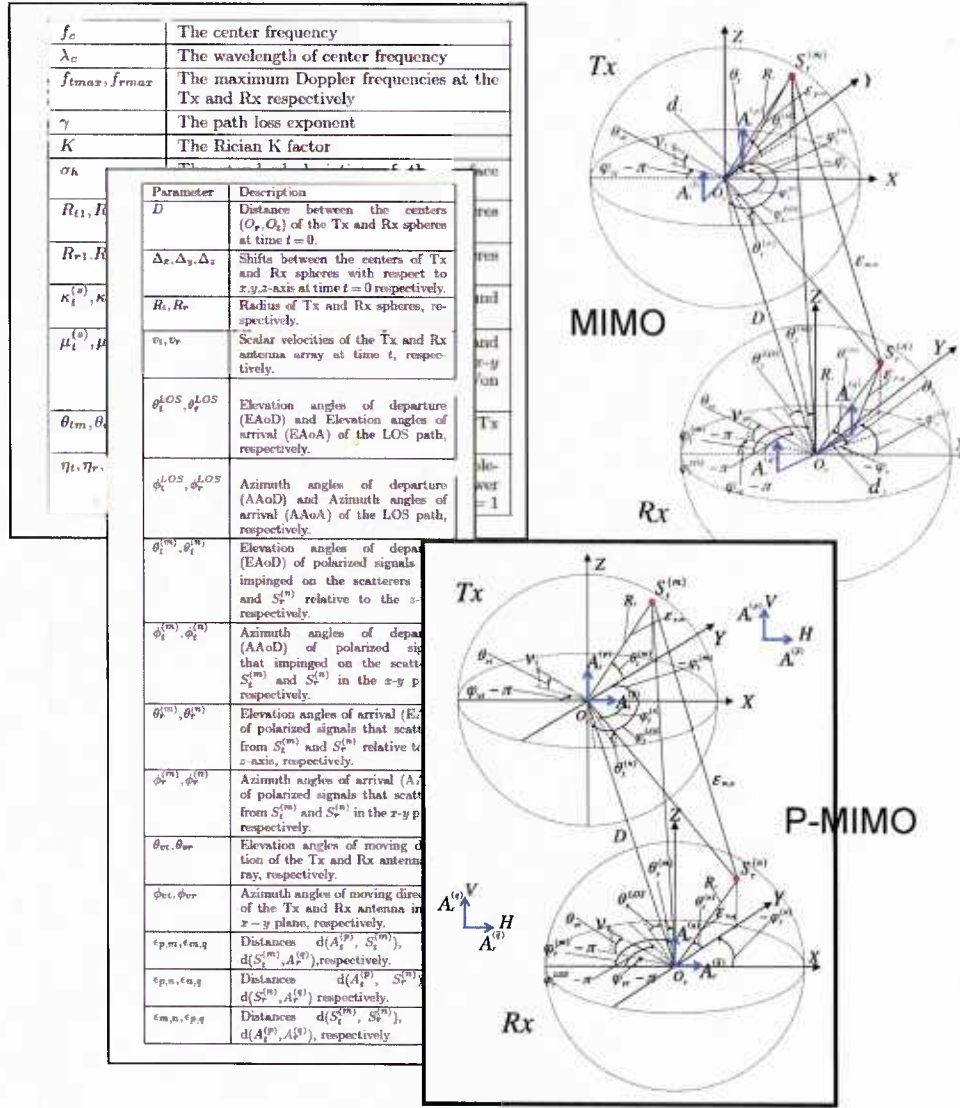| Parameter	Description
D	Distance between the centers (O_t, O_r) of the Tx and Rx spheres at time $t = 0$.
$\Delta_x, \Delta_y, \Delta_z$	Shifts between the centers of Tx and Rx spheres with respect to x, y, z-axis at time $t = 0$ respectively.
R_t, R_r	Radius of Tx and Rx spheres, respectively.
v_t, v_r	Scalar velocities of the Tx and Rx antenna array at time t, respectively.
$\theta_t^{LOS}, \theta_r^{LOS}$	Elevation angles of departure (EAoD) and Elevation angles of arrival (EAoA) of the LOS path, respectively.
$\phi_t^{LOS}, \phi_r^{LOS}$	Azimuth angles of departure (AAoD) and Azimuth angles of arrival (AAoA) of the LOS path, respectively.
$\theta_t^{(m)}, \theta_t^{(n)}$	Elevation angles of departure (EAoD) of polarized signals impinged on the scatterers and $S_r^{(n)}$ relative to the z-axis respectively.
$\phi_t^{(m)}, \phi_t^{(n)}$	Azimuth angles of departure (AAoD) of polarized signals that impinged on the scatterers $S_t^{(m)}$ and $S_r^{(n)}$ in the x-y plane respectively.
$\theta_r^{(m)}, \theta_r^{(n)}$	Elevation angles of arrival (EAoA) of polarized signals that scatter from $S_t^{(m)}$ and $S_r^{(n)}$ relative to z-axis, respectively.
$\phi_r^{(m)}, \phi_r^{(n)}$	Azimuth angles of arrival (AAoA) of polarized signals that scatter from $S_t^{(m)}$ and $S_r^{(n)}$ in the x-y plane respectively.
θ_{vt}, θ_{vr}	Elevation angles of moving direction of the Tx and Rx antenna array, respectively.
ϕ_{vt}, ϕ_{vr}	Azimuth angles of moving direction of the Tx and Rx antenna in x-y plane, respectively.
$\epsilon_{p,m}, \epsilon_{m,q}$	Distances $d(A_t^{(p)}, S_t^{(m)})$, $d(S_t^{(m)}, A_r^{(q)})$, respectively.
$\epsilon_{p,n}, \epsilon_{n,q}$	Distances $d(A_t^{(p)}, S_r^{(n)})$, $d(S_r^{(n)}, A_r^{(q)})$ respectively.
$\epsilon_{m,n}, \epsilon_{p,q}$	Distances $d(S_t^{(m)}, S_r^{(n)})$, $d(A_t^{(p)}, A_r^{(q)})$, respectively.

Figure 2. MIMO Illustration 2

In communications systems, the channel state is often estimated at the receiver. This information, termed channel state information (CSI) can be obtained when the receiver has knowledge of a preamble or of pilots used in the transmitted waveform. With CSI at the receiver only, the transmitter typically utilizes resources in an isotropic fashion, since it does not have information to exploit the channel. However, if the transmitter does have information about the channel state, referred to as channel state information at the transmitter (CSIT), then the transmitter can identify the eigenmodes of the system and utilize this knowledge to synthesize weighted transmissions among the transmit ports for efficient channel utilization. An illustration of CSIT for a 4x4 SP-MIMO system is shown in Figure 3. The figure

illustrates the potential of the MIMO system to transmit independent data streams through one, two, or all of the channel eigenmodes. We note that in the case of a monostatic radar system, since the receiver will have full knowledge of the transmitted signals, CSIT may be readily acquired. In the bistatic radar, CSIT can be obtained if the receiver has knowledge of the radar waveforms and relays the channel state information to the transmitter.
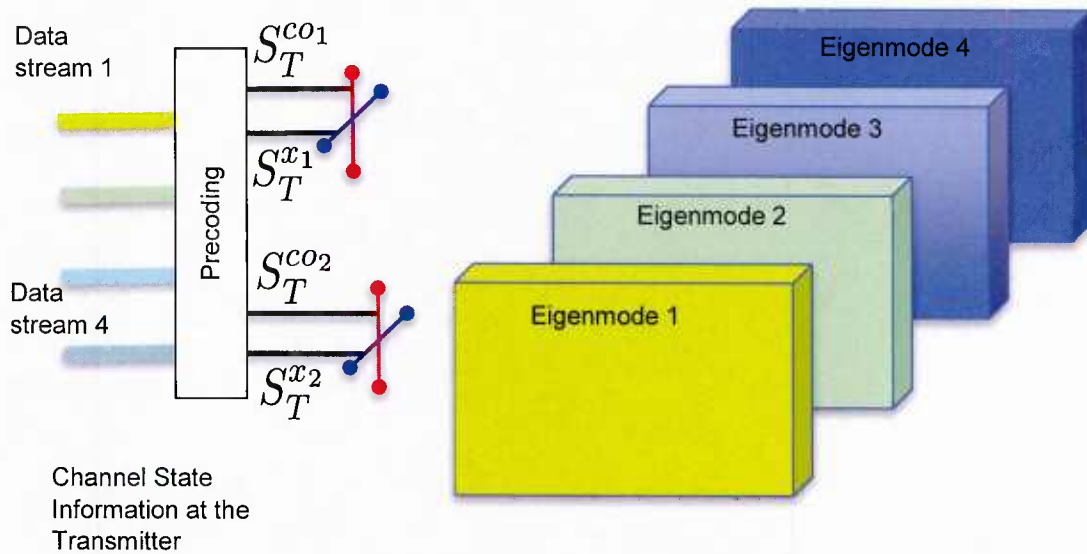
Data stream 1

$S_T^{co_1}$

$S_T^{x_1}$

Precoding

$S_T^{co_2}$

Data stream 4

$S_T^{x_2}$

Channel State Information at the Transmitter

Eigenmode 4

Eigenmode 3

Eigenmode 2

Eigenmode 1

Figure 3. Adaptive Transmission with Channel State Information at the Transmitter

Numerical analyses have been performed with and without CSIT for communications systems, and results illustrating the benefits of the approach are shown below in Figure 4. We anticipate that CSIT will provide corresponding benefits in radar applications. The availability of CSIT is particularly relevant in monostatic radar, which has the advantage that it can measure the response and adapt its waveforms without need for a feedback link since the transmitter and receiver are co-located. Hence adaptive transmission techniques may readily be applied in cognitive radar.
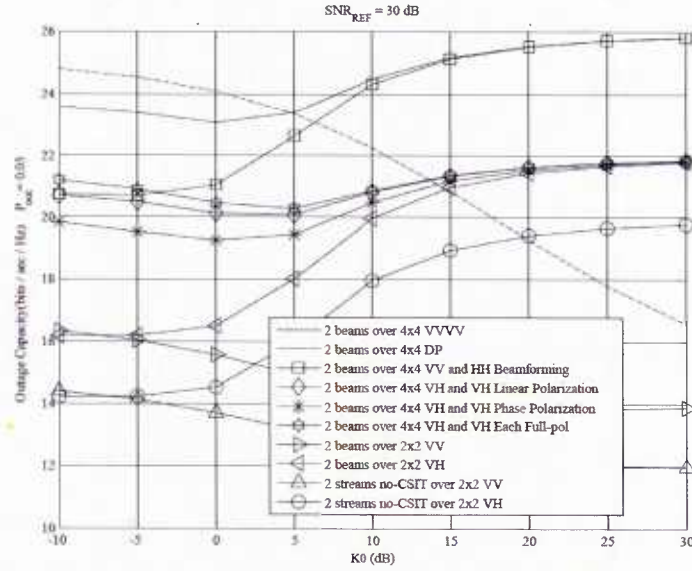
Figure 4. Performance of Various Adaptive Transmission Schemes for 2x2 and 4x4 MIMO Systems

Prior work has also examined the application of PMD-based processing to wideband polarization-based interference suppression. Conventional polarization-based interference techniques described in literature, such as those advanced by Compton [57] and others [32][33][34], provide effective polarization-based suppression in narrowband channels. However, the existence of PMD hampers their performance because the polarization state of the interference changes with frequency and a single polarization filter just cannot effectively suppress all of the signal energy.

To effectively deal with the effects of PMD, it has been proposed (and verified in the Notre Dame space-polarization testbed) that suppression can be applied in the polarization domain as a function of frequency, taking advantage of PMD measurements to mitigate unwanted signals. Results from this type of processing are shown below in Figure 5, which illustrates polarization-based suppression of a co-channel wideband signal to enable demodulation of a desired wideband signal (either signal may be suppressed in order to recover the other signal). The PMD responses for each signal are shown in the top left panel of the figure. The ability to separate the interference and desired signals using the polarization domain is characterized by the power coupling function (PCF) [9][10]. The PCF indicates the level to which a polarization filter suppressing an interference signal will also suppress the desired signal. As the PCF decreases towards negative infinity, the ability to separate the signals using polarization becomes impossible. As shown in the lower panel on the left side of the figure, there are several frequency components (the notches in the figure) where suppression of the interference will also lead to substantial suppression of the desired signal. The first and third panels on the right side show the spectra of the V and H signal components for the

18

interference and desired signals. The frequency selectivity associated with the multipath channels is evident. The second and fourth panels shows the signal power spectra at the output of the filter and show that the interference is suppressed substantially through the PMD-based filtering approach.
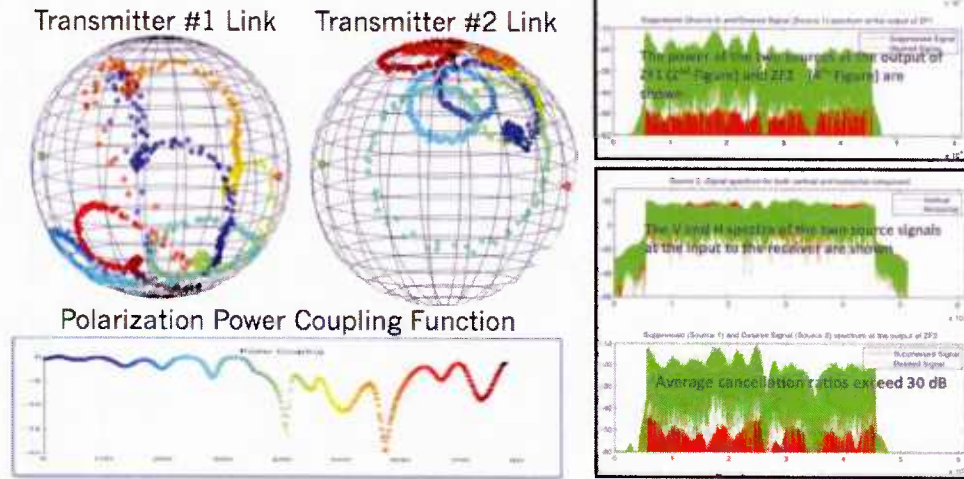

Figure 5. Polarization-based suppression of a co-channel wideband signal (from [9])

A similar suppression approach may also be useful in radar to mitigate the clutter response as a function of frequency so that responses induced by a target are more readily sensed. This approach is possible particularly if the radar employs orthogonally-polarized antennas.

The background research and technologies mentioned above all play a potential role in the development and modeling of polarization-based radar processing techniques to be considered in our research. In the next section, we begin our discussion of the models used in the investigation.

III.   SEA SURFACE MODEL

Sea waves generate significant clutter in maritime radar, where clutter responses depend upon reflections from the sea surface. In this section, we consider a first-order dynamic sea surface model to represent sea waves using an appropriate number of scales. The model is later integrated with electromagnetic scattering models for numerical analyses of PMD-based detection performance in clutter. Closed-form sea surface models that have been proposed in literature are initially discussed and then the particular model that has been adopted and modified for use in this study is described.

A.   *Wave Features*

Sea waves consist of a number of components that contribute to their overall structure. Gravity waves make up the larger surface structures associated with waves and capillary waves make up the small-scale surface structures. Typically, under the conditions of a sustained wind, the sea will develop into a "fully developed" sea in which larger waves will tend to move in the direction of the wind, while smaller waves will be more isotropic [56]. Other wave structures that can be present include wedges, cusps, foam, turbulence, spray, and breaking events [56]. All of these contribute to the overall wave structure and ultimately to the EM response from the sea. However, in the "first order" sea surface model that we adopt, these latter structures are not considered. The next sections describe results from a survey of sea surface models and the specific model that we adopt and utilize with EM scattering theory to develop clutter responses from the sea for different sea states and different incidence angles.

B.   *Sea Surface Modeling Background*

A partial survey of sea surface models was conducted to identify suitable models for characterizing sea surface structure and associated dynamics. Typical models employ an ensemble of time-varying waves with different wavenumbers. The surface height at a particular location is determined by adding the contribution of all of the component waves at that location. Several examples from literature are presented. We ultimately select a model based on the Weierstrass-Mandelbrot function. In later sections, this model is incorporated with EM scattering models to arrive at a time-varying PMD-based clutter response that depends upon the sea surface among other factors.

One sea surface model that has been proposed in literature incorporates a two-wave structure with a large-scale wave and a small-scale wave and dielectric facets[58][59][54]. The form of the surface function, h, using this model is

20

$$h(x,y,t)$$
$$= h_l \cos\left(|k_l|\sqrt{x^2+y^2}\cos\theta_l - \sqrt{g|k_l|}t\right) \quad (11)$$
$$+ h_s \cos\left(|k_s|\sqrt{x^2+y^2}\cos\theta_s - \sqrt{g|k_s|}t\right)$$

where $k_l = 2\pi/\lambda_l$, and $k_s = 2\pi/\lambda_s$, are the wavenumber vectors for the large-scale and small-scale waves, respectively, h_l and h_s are the corresponding amplitudes of these waves as shown in Figure 6, g is the acceleration due to gravity, and θ_l and θ_s are the corresponding wave directions. The small-scale wavelength is related to the carrier frequency by the relation

$$\lambda_s = \frac{\lambda}{2\sin\phi} \quad (12)$$

where ϕ is the incidence angle.
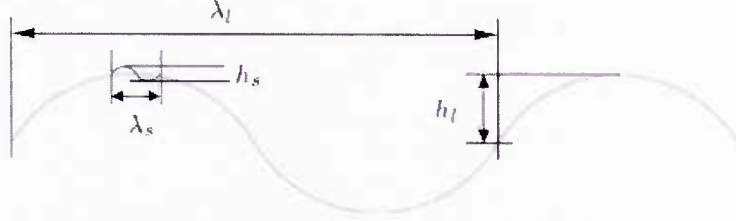
Figure 6. Two-scale sea surface model (from [54])

A related approach employs the Weierstrass-Mandelbrot function to model the sea surface. This model employs a sum of waves with periods that are spaced apart by an integer exponent of an irrational factor v:

$$f(x,y) = B\sum_{n=0}^{M-1} C_n v^{-Hn}\sin(k_0 v^n(x\cos\psi_n + y\sin\psi_n) + \phi_n) \quad (13)$$

where B is a scaling factor, H is the Hurst coefficient, k_0 is the fundamental wave number, C_n is the wave amplitude, ϕ_n is the wave phase, and ψ_n is the wave direction. With this model, C_n, ϕ_n, and ψ_n are all random variables. The number of sinusoids M is dictated by the highest and lowest scales contributing to the scattering and is approximately given by

$$M = \frac{\ln\left(\frac{\chi - L}{\lambda}\right)}{\ln(v)} \quad (14)$$

21

where L is the illuminated profile length and χ is a margin factor [54].

C. Time-varying sea surface model

An augmented version of this approach has been described in [64] [60]. This form represents the particular model that we have adopted. The time-varying sea surface function is given by:

$$h(x, y, t) =$$

$$\sigma\eta \sum_{m=1}^{M-1} a^{-(d-\xi)m} \sin\left(K_0 a^m \left[(x + V_x t) \cos \beta_{1m} + (y + V_y t) \sin \beta_{1m}\right] - \Omega_{1m} t + \alpha_{1m}\right)$$

$$+\sigma\eta \sum_{n=0}^{N-1} b^{(d-3)n} \sin\left(K_0 b^n \left[(x + V_x t) \cos \beta_{2n} + (y + V_y t) \sin \beta_{2n}\right] - \Omega_{2n} t + \alpha_{2n}\right)$$

(15)

where σ is the standard deviation of the wave heights, η is a normalization constant, d is the fractal dimension (between 2 and 3), ξ is a positive power ratio, K_0 is the fundamental spatial wavenumber, a and b are wavenumber scale factors ($a < 1$ and produces spatial wavenumbers less than K_o; $b > 1$ and produces spatial wavenumbers greater than K_o), V_x and V_y are the velocity components associated with radar motion, Ω_{1m} and Ω_{2n} are angular frequencies, α_{1m} and α_{2n} are random wave phases, and β_{1m} and β_{2n} are the angular directions of wave propagation.

This equation models the 2D sea surface dynamics over short durations of time for which the random variables β and α are considered constant.

1. Summary of parameter values

Table 1 lists the parameters from Equation (15) along with the constant values or equations used to calculate these parameters in our model. Some of these parameters are discussed further in subsequent sections.

Table 1. Summary of sea height model parameters

Param	Description	Value	Comment
b	Wavenumber spacing factor $(K > K_o)$	1.105	Note 1
a	Wavenumber spacing factor $(K < K_o)$	$1/b$	Note 1
d	Fractal dimension $(K < K_o)$	2.1	Note 1
ξ	Adjusts fractal dimension $(K < K_o)$	3.9	Note 1
N	Number of waves $(K > K_o)$	40	
M	Number of waves $(K < K_o)$	20	
K_o	Fundamental wavenumber	g/U^2	Note2
σ	Standard deviation of wave height	$0.0062U^2$	Note 3
η	Normalization constant	$\sqrt{\dfrac{2}{\sqrt{\left(\dfrac{1-a^{2(\xi-d)N}}{1-a^{2(\xi-d)}}\right)+\left(\dfrac{1-b^{2(d-3)N}}{1-b^{2(d-3)}}\right)}}}$	Note 4
Ω	Temporal Frequency	$\sqrt{gK + K^3\dfrac{\tau}{\rho}}$	Note 5
α	Phase	Random (uniform)	
β	Wave direction	Random (von Mises)	
V_x, V_y	Platform velocity	0	
g	Gravitational constant (m/s^2)	9.8	
U	Wind speed (m/s)	Varies	
τ	Sea surface tension (N/m)	0.074	
ρ	Sea water density (kg/m^2)	1025	

Notes:

1. Parameter values published in [63].

2. For a fully developed sea, the fundamental wavenumber is inversely proportional to the squared wind speed [41]

3. The constant 0.0062 was empirically determined based on significant wave height data as a function of wind speed (see Table 15.1 from [41] as well as subsequent section *Model height statistics versus wind speed*).

4. The normalization constant η was derived based on a similar formula in [62]. This constant normalizes Equation **(15)** such that σ represents the wave height standard deviation.

5. The temporal frequency Ω uses the formula from [62] which considers the effects of both gravity waves and capillary waves.

2.   Wave amplitude as a function of wavenumber

Equation (15) includes two summations of sinusoids with wavenumbers (spatial frequencies) spread about a fundamental wavenumber K_o dictated by the wind speed. The first summation consists of sinusoids with wavenumbers $(K_o a^m)$ less than the fundamental wavenumber K_o $(a < 1)$. The second summation consists of sinusoids with wavenumbers $(K_o b^n)$ greater than or equal to K_o $(b > 1)$. The factors d and ξ are constrained to produce wave amplitudes $a^{(-d-\xi)m}$ and $b^{(d-3)n}$ with negative exponents such that the wave amplitudes are less than or equal to one.

Figure 7 shows an example of the relative amplitudes (neglecting the overall $\sigma\eta$ factor) for the individual waves that constitute Equation (15). The blue dots represent the waves from the first summation while the green dots represent the waves from the second summation. Note the logarithmic versus logarithmic decrease in wave magnitude as the wavenumber deviates from the fundamental wavenumber, $K_o = 0.1$. This chart illustrates that the largest amplitude waves have wavenumbers near the fundamental wavenumber.
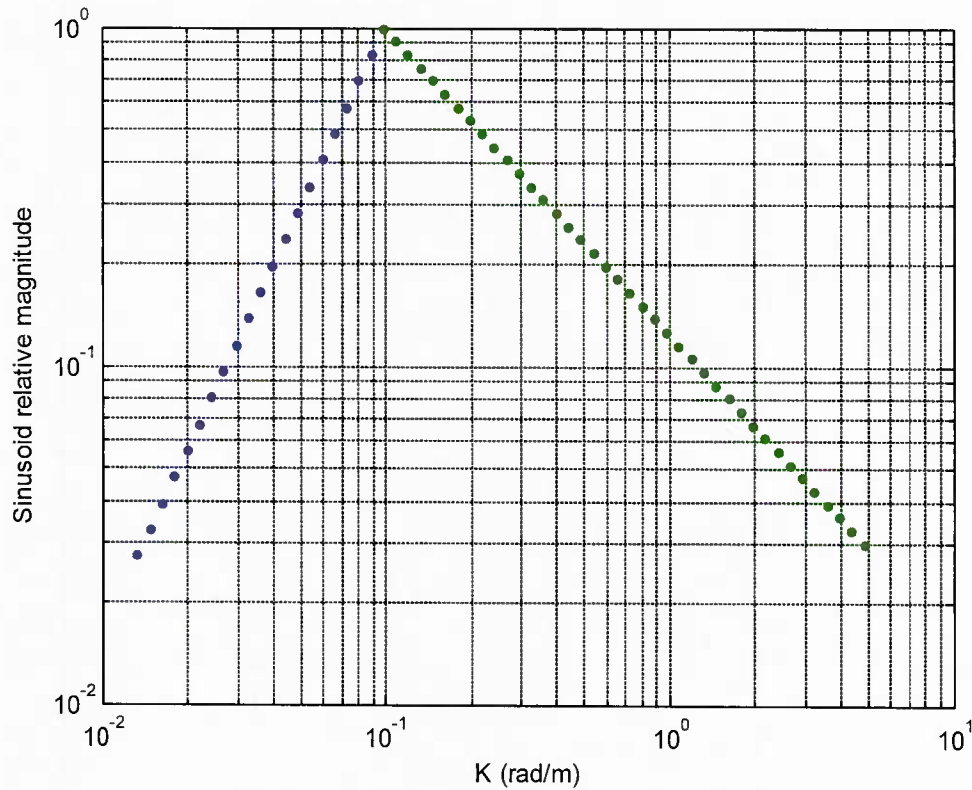
Figure 7. Relative wave magnitude as a function of wavenumber

3. Wave direction

The direction of waves is denoted by the random variable β. We employ a von Mises distribution for β

$$f(\beta \mid \mu, \kappa) = \frac{e^{\kappa \cos(\beta - \mu)}}{2\pi I_0(\kappa)} \qquad (16)$$

where I_0 is a modified Bessel function of order 0, μ is the mean of the distribution, and κ is the concentration of the distribution. Increasing κ leads to increased concentration about the mean. The configuration $\kappa = 0$ corresponds to uniformly distributed directions. Distributions for different values of κ are shown in Figure 8.
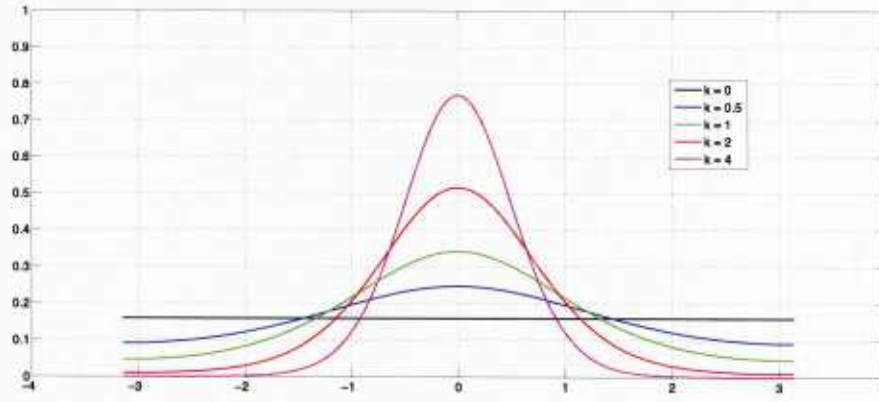
Figure 8. von Mises distributions for various values of k

An example of a sea surface generated using the model is shown in Figure 9 for the case when $\kappa = 10$ and $\mu = 45$ degrees.
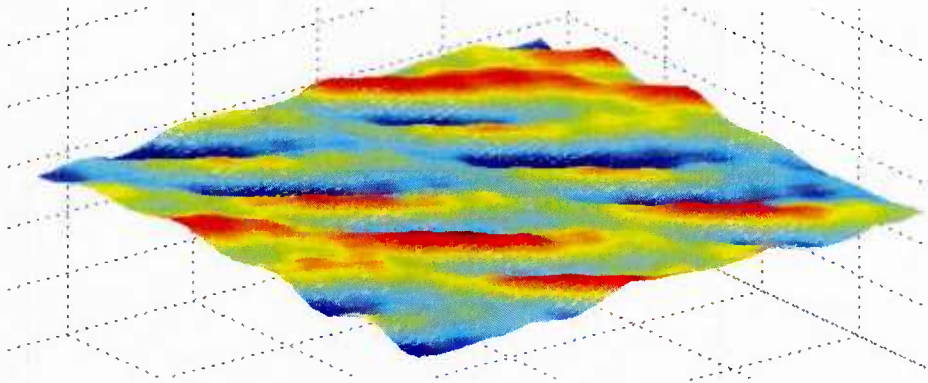
Figure 9. Sea surface rendering

25

4. Wind effects

Wind speed affects two parameters in the surface height model: the fundamental wavenumber K_o and the surface height standard deviation σ. The following equations show their dependence on the wind speed U.

$$K_o = \frac{g}{U^2}$$

where g is the gravitational constant $9.8\,\frac{m}{s^2}$

$$\sigma = c\, U^2$$

where c is an empirical constant.

Significant wave height is often expressed in two different but roughly equivalent ways:

- Significant wave height, H_{sig}, is defined as the mean value of the peak-to-trough height of the highest one third of the waves.

- Significant wave height, H_{m0}, is defined as four times the square root of the zeroth-order moment of the wave spectrum or, equivalently, four times the standard deviation of the surface elevation.

$$H_{m0} = 4\sigma = 4cU^2$$

The two definitions are approximately equal. That is,

$$H_{sig} \approx H_{m0}$$

For our model, the empirical constant c was determined based on tabular data from [41] (see Table 15.1) showing significant wave height as a function of wind speed for a fully developed sea. This data is shown below in Table 2.

Table 2. Significant wave height versus wind speed (data from [41], Table 15.1))

Wind speed (kn)	Significant Waveheight (ft)
7	1
12	3
16	5
19	8
23	12
30	20
45	40

Figure 10 shows a plot of H_{sig} for various values of c along with the tabular data from Table 2 (tabular data represented by the blue trace). The value $c = 0.0062$ is a very good match for the tabular data and is the value used in our model.
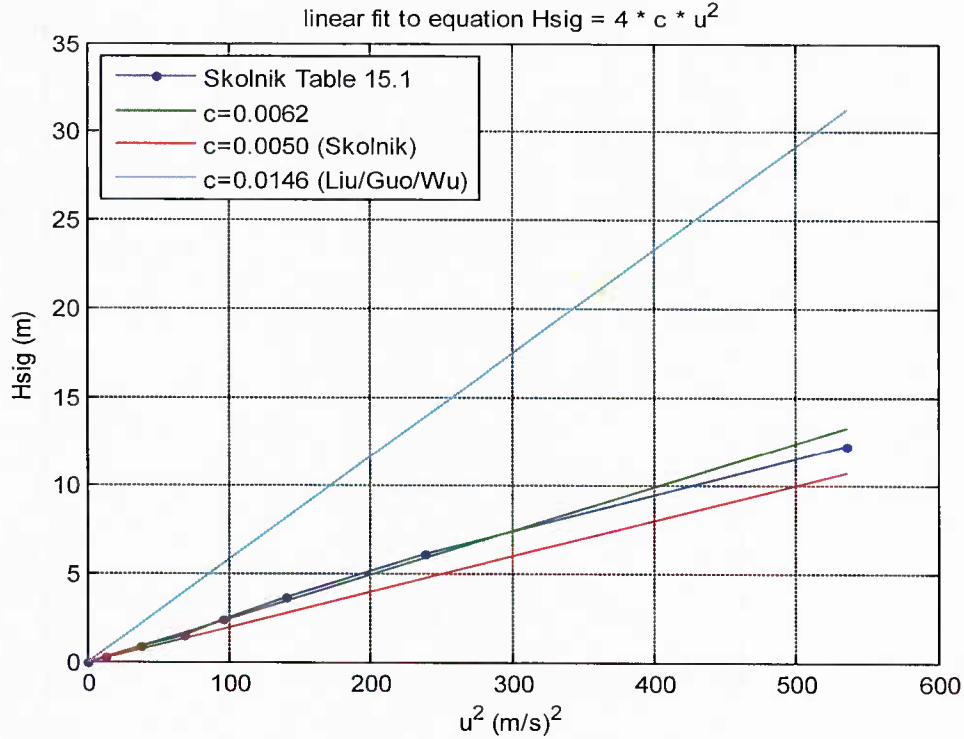
Figure 10. Significant wave height as a function of wind speed for various constants

5.   Model height statistics versus wind speed

Numerical simulations using the sea height model described by Equation **(15)** were performed to produce sea height data as a function of time for a single spatial point $(x = 0, y = 0)$ for various wind speeds U. This data was then processed to calculate the significant wave height using both formulations presented above, H_{sig} and H_{m0}. The objective was to verify that the model sea height statistics were consistent with those reported in literature (see Table 2).

In order to calculate significant wave height H_{sig} according to the definition above (*the mean value of the peak-to-trough height of the highest one third of the waves*), it is necessary to process the time domain data into individual waves determined by zero-crossings. Figure 11 shows an example of this processing where the green circles identify the zero-crossings and thus the individual wave boundaries. The height of each individual wave is then calculated as the max-to-min distance between the zero-crossings. Finally, the heights for all individual waves were sorted by value and the highest one third were averaged to produce the significant wave height.

27
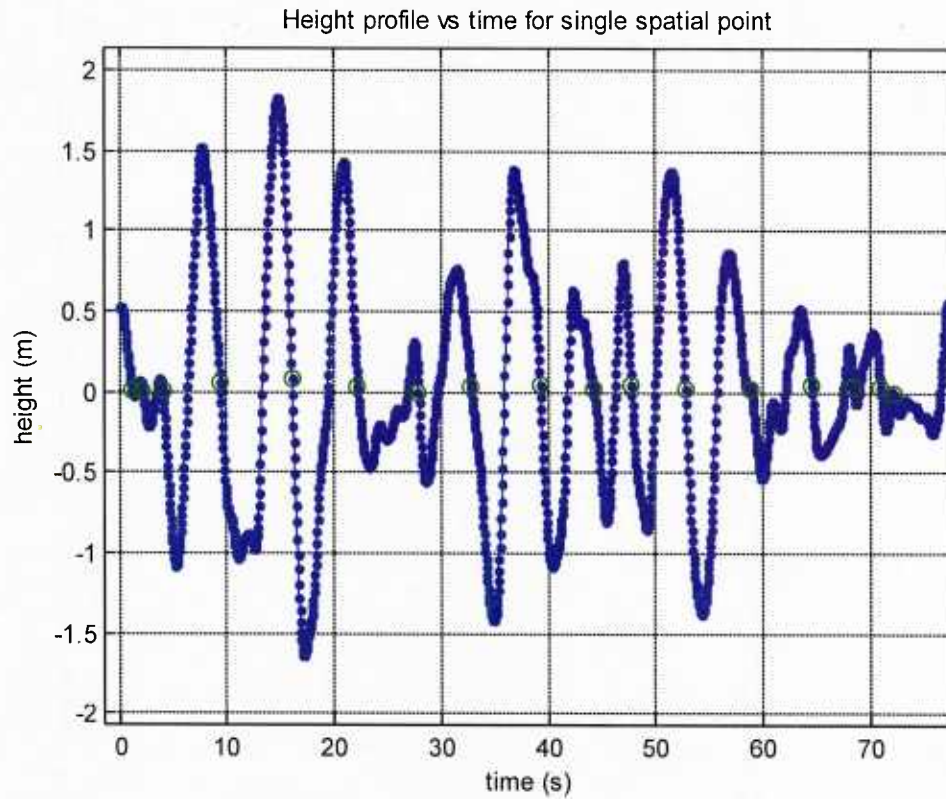
Figure 11. Wave height versus time with zero-crossings noted

In order to calculate significant wave height H_{m0} according to the definition above (*four times the standard deviation of the surface elevation*), it is simply necessary to calculate the standard deviation of the data and multiply by four.

Figure 12 shows the calculations for both definitions of significant wave height as a function of wind speed using the model generated height data. These data are compared to the values listed in Table 2. Note that the two calculations for significant wave height, H_{sig} and H_{m0}, are approximately equal and that both calculations match the tabular data very well.
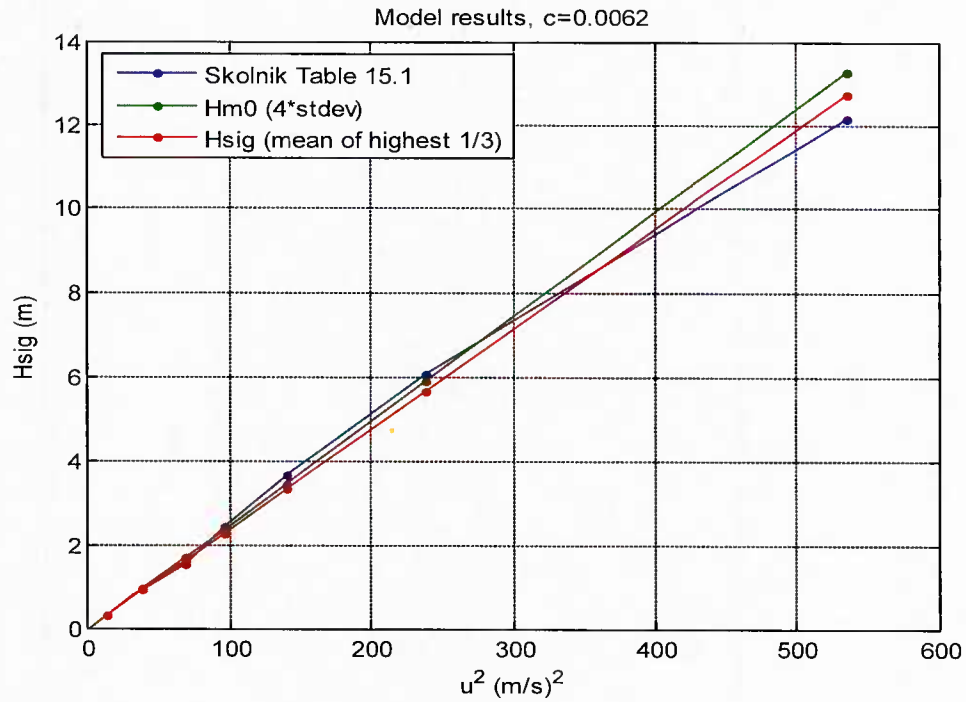
Figure 12. Validation of model results relating to significant wave height

6.   Example surface

Figure 13 shows an example surface (80m by 80m) generated by the model using the parameters from Table 1 at a single instant in time. In the left plot (pseudo-color), note the scale for the color bar which shows wave height varying from about -1.5 to 2 meters. The figure on the right shows a 2-D plot using the same data as the figure on the left, but only for center cuts such that 'x=0' for one trace and 'y=0' for the other.
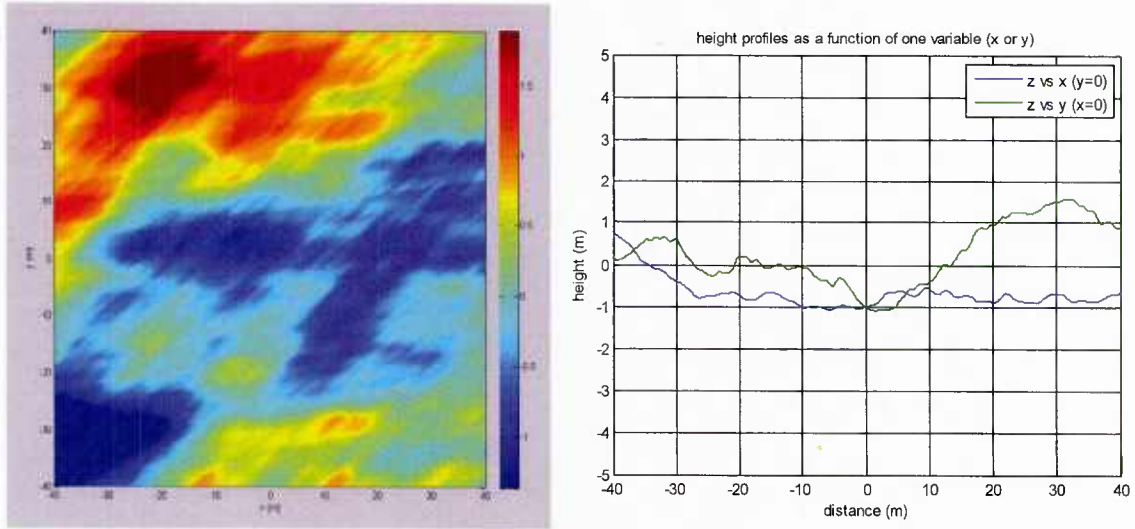
Figure 13. Example sea surface

D.   Rough Surface Statistics

The quality of the technique evaluations for target detection and target identification depends on the quality of the sea clutter representations. We have presented a model for the sea surface height. An important consideration, however, is the statistical response elicited from the model.

In this section we review general rough surface statistics that are commonly used to characterize rough surfaces and then we review other pertinent sea clutter statistical behaviors that have been reported in literature. Our reason for considering these behaviors is to help in the characterization of the model realizations and to "calibrate" the responses from the current mathematical models. Statistical behaviors will be used as guides in determining how the mathematical models are to be utilized to generate sea clutter responses that are consistent in some manner with trends observed in literature.

In particular, we review statistics characterizing the height distribution of rough surfaces. The theoretical characterizations associated with rough surfaces are drawn primarily from [38], and will be used to help characterize sea state model realizations in future analyses.

1.   Rough Surface Description

For a plane monochromatic wave incident at some angle θ_1 onto a rough surface that scatters in the azimuthal plane at some angle θ_2, the phase difference between two rays scattered from separate points on the surface is given by

$$\Delta\phi = k[(h_1 - h_2)(\cos\theta_1 + \cos\theta_2) + (x_1 - x_2)(\sin\theta_1 - \sin\theta_2)] \quad (17)$$

For specular scattering ($\theta_1 = \theta_2$), the phase difference becomes

$$\Delta\phi = 2k\Delta h\cos\theta_1 \qquad (18)$$

The Rayleigh criterion characterizes a surface as rough if $\Delta\phi > \pi/2$. By averaging over the surface, Δh may be replaced by an RMS deviation, σ, and the criterion can be rewritten as

$$R_a < \frac{\pi}{4} \qquad (19)$$

where $R_a = k\sigma\cos\theta_1$. For a smooth surface ($h_1 = h_2$) the phase difference becomes

$$\Delta\phi = k[(x_1 - x_2)(sin\theta_1 - sin\theta_2)] \qquad (20)$$

In the specular direction ($\theta_1 = \theta_2$), it is seen that $\Delta\phi = 0$, yielding a coherent gain from the rays. Away from this direction, the phase difference is nonzero and destructive interference can occur. When the surface is not smooth ($h_1 \neq h_2$), the amplitude of the specular field will be reduced. The loss may be approximated by $e^{-g/2}$ where

$$g = 4k^2\sigma^2\cos^2\theta_1 = 4R_a^2 \tag{21}$$

Surfaces may be characterized by a height distribution function (relative to a reference surface) and a surface correlation function. Normally the reference is chosen so that the height distribution has zero mean. Assuming this to be the case, the RMS height of the surface is given by

$$\sigma = \sqrt{\langle h^2 \rangle_s} \tag{22}$$

where $\langle x \rangle$ denotes the expected value of x.

Height distributions are usually assumed to be Gaussian:

$$p(h) = \frac{1}{\sigma\sqrt{2\pi}} exp\left(-\frac{h^2}{2\sigma^2}\right) \tag{23}$$

which is valid for surfaces with a profile that is everywhere the result of a large number of local events.

2.   *Surface Correlations*
Surface correlations are characterized by the correlation function

$$C(\boldsymbol{R}) = \frac{\langle h(\boldsymbol{r})h(\boldsymbol{r} + \boldsymbol{R}) \rangle_s}{\sigma^2} \tag{24}$$

Theory of wave scattering from rough surfaces often assumes that the surface correlations are Gaussian and that the surface is isotropic such that the vector $\boldsymbol{R}$ can be replaced by the scalar R

$$C(R) = exp\left(-\frac{R^2}{\lambda_o^2}\right)$$ (25)

where λ_o is the correlation length, which is the distance over which the correlation decreases by $1/e$. In place of Gaussian correlations, the exponential is often considered to give a better fit to measured surface data [38].

$$C_{exp}(R) = exp\left(-\frac{|R|}{\lambda_o}\right)$$ (26)

However, this exhibits a discontinuity at the origin. Weighted correlations that are Gaussian near the origin and exponential otherwise have been proposed, where selection of weighting parameters dictates the distance at which this transition occurs.

Numerical studies have shown that unless the discretization interval is less than 10% of the correlation length, the full exponential nature of the surface will not be measured. Also, surface correlations are likely inaccurate for distances greater than about 10% of the surface length. Below this distance, peaks in the correlation function at separations that are not integral multiples of the shortest correlation length is indicative of more than one correlation length. For example, the sea surface may be composed of wind-driven waves and smaller amplitude capillary waves of shorter correlation length [38].

3.   Power Spectrum

The power spectrum is the Fourier transform of the correlation function and is given by:

$$P(k) = \frac{\sigma^2}{(2\pi)^2} \int_{-\infty}^{\infty} C(R)e^{ik\cdot R} dR$$ (27)

It describes the spread of heights about the mean plane and the height variation along the surface. If the surface is anisotropic with a Gaussian correlation function, the power spectrum is given by

$$P(k_1, k_2) = \frac{\sigma^2 \lambda_1 \lambda_2}{4\pi} exp\left(\frac{-k_1^2 \lambda_1^2}{4}\right) exp\left(\frac{-k_2^2 \lambda_2^2}{4}\right)$$

(28)

The RMS gradient for isotropic surfaces with Gaussian correlation functions is given by

$$\sigma_g = \sqrt{\left\langle\left(\frac{\partial h}{\partial x}\right)^2\right\rangle} = \sqrt{\left\langle\left(\frac{\partial h}{\partial y}\right)^2\right\rangle} = \frac{\sigma\sqrt{2}}{\lambda_o}$$

(29)

Surfaces with an exponential correlation function have higher frequency components than the Gaussian surface. The associated correlation function is given by:

$$P(k_1, k_2) = \frac{\sigma^2}{\lambda_1 \lambda_2 \pi^2} \frac{1}{\left(\frac{1}{\lambda_1^2} + k_1^2\right)} \frac{1}{\left(\frac{1}{\lambda_2^2} + k_2^2\right)}$$

(30)

For sea surfaces, the Neumann-Pierson power spectrum is often preferred:

$$P(k_1, k_2) \propto \frac{1}{k^{9/2}} exp\left[-\left(\frac{a_g}{v^2 k}\right)\right] \cos^2\left[\tan^{-1}\left(\frac{k_2}{k_1}\right)\right]$$

(31)

4.   *Stationarity and Ergodicity*

Surface statistics exhibit translational invariance, or stationarity, which means that they don't depend upon the absolute coordinates. Statistical properties from different parts of a surface will be similar provided the lengths of these samples are

all the same. Typically, a sample must exceed 50 correlation lengths for the true statistical nature of the surface to be represented [38].

Ergodicity associated with a rough surface implies that any statistical average taken over many different parts of one surface realization is the same as an average over many realizations of a single part of the surface (spatial averaging = ensemble averaging).

5.   Example Statistics

Based on the discussion in the previous section, Rough Surface Statistics, the sea surface model was exercised in order to estimate the various surface statistics produced by the model. For these results, a wind speed of 10 m/s was used.

Figure 14 shows two histograms of sea surface height. The left histogram was generated at a single instant in time (t=0) for a large surface area. The right histogram was generated at a single spatial point (x=0, y=0) over an extended period of time. The two histograms are nearly identical with a Gaussian shape centered about zero, as expected.

The standard deviation for both cases was approximately 0.62 m. Recall that significant wave height is roughly four times the standard deviation, which in this case is approximately 2.5 m. This matches the curves from Figure 12 (wind speed squared is 100 m^2).
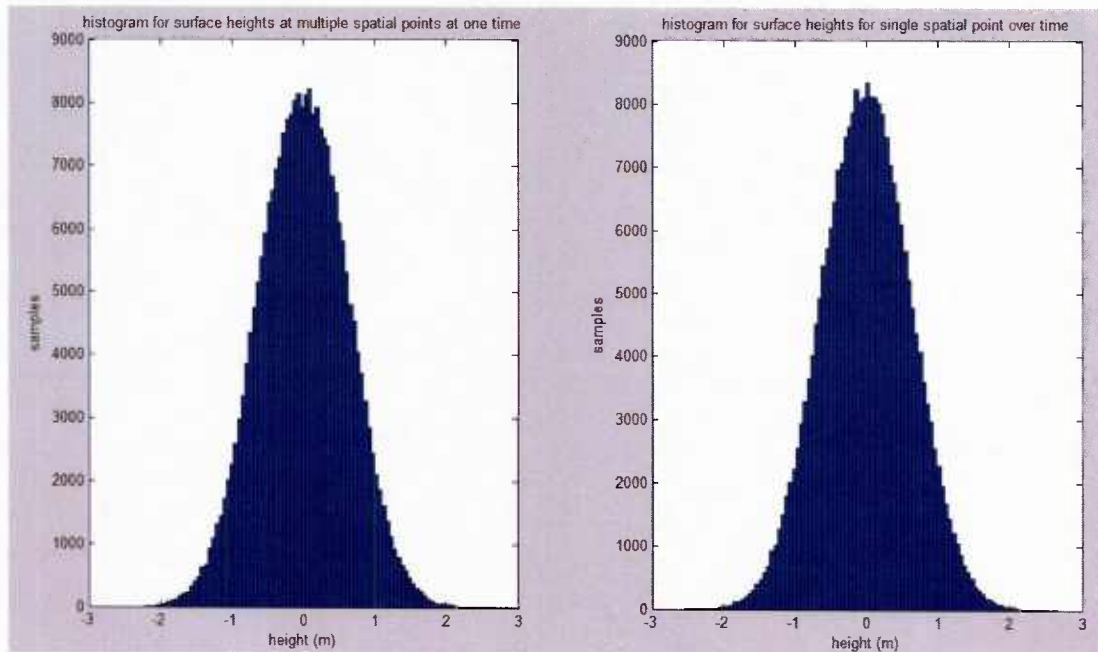
Figure 14. Histograms of surface height versus space and time

Figure 15 shows the correlation as a function of distance, R, where the distance is constrained to one dimension (along x axis for y=0). The bottom subplot is simply a zoomed-in section from the top subplot. Note that the correlation value at approximately 60 meters is reduced by a factor of four from the peak value at zero meters, but that the correlation function oscillates with increasing distance. This lack of decay at large correlation distances is related to the periodic nature of the sea height function and the finite number of sinusoids in the summation.
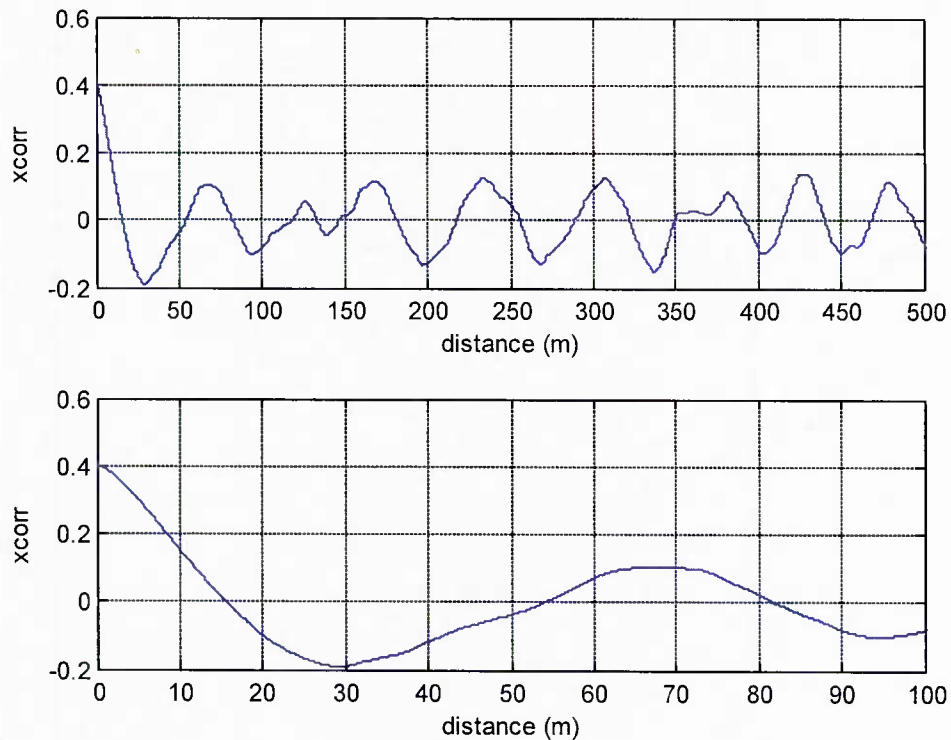
Figure 15. Correlation function over distance (x dimension)

Figure 16 shows the power spectrum obtained by taking the FFT of the correlation function. Note the peak in the power spectrum at about 0.1 rad/m, which matches the fundamental wavenumber for this wind speed of 10 m/s (see Figure 7).
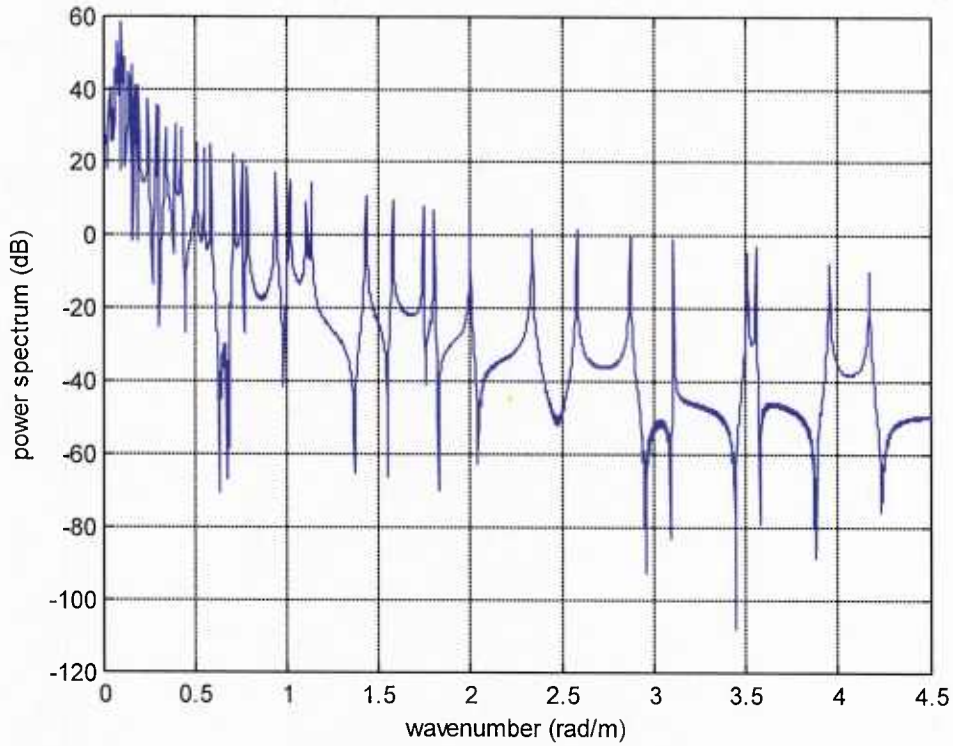
Figure 16. Power spectrum

E. Concluding remarks

In this section, a time-varying sea surface model was presented based on the work of [63], but with the introduction of a von Mises distribution to represent wave direction. Some of the main parameters that can be adjusted are wind speed, wave direction (mean & spread), number of waves, and frequency spacing. Model results showing significant wave heights as a function of wind speed demonstrate very good agreement with published sea state data (Table 15.1 from [41]).

Histograms of the model generated surface height show Gaussian shaped distributions with the expected standard deviation and mean of zero. The power spectrum estimate of the correlation data shows peak power occurring at the fundamental wavenumber.

In the next section, electromagnetic scattering models are presented that describe the polarization component reflection coefficients associated with reflections at a dielectric boundary layer. These models will be integrated with the sea surface model to estimate the aggregate response at the receiver.

IV.   ELECTROMAGNETIC SURFACE SCATTERING MODEL

In this section, we develop electromagnetic scattering models to represent the polarimetric response due to scattered energy from a boundary between two different dielectric media. We first consider electromagnetic reflections from a dielectric boundary at oblique incidence using Snell's law with appropriate boundary conditions. This model is particularly useful to represent reflections from discrete facets. An alternative approach, called Kirchhoff Theory, is then considered. The scalar case without polarization coupling is considered first, followed by the vector case where polarization coupling is included. The discussion leads to the adoption of the Stratton-Chu equation to estimate electromagnetic reflections from the sea surface model. The theoretical developments are drawn from several sources, including [40][38].

A.   *Reflection from a Dielectric Boundary at Oblique Incidence*

Signal reflections for both co- and cross-polarized signal components from a dielectric boundary are derived using Snell's law and Fresnel Equations. The results provide theory leading to expressions for the polarization response as a function of the dielectric materials, the angle of incidence, as well as the plane of incidence.

1.   *Complex Dielectric Permittivity*

If the electric conductivity σ of a medium is nonzero, the propagation constant γ of the medium is complex [66] and will satisfy:

$$\gamma^2 = \omega^2 \varepsilon \mu - j\omega\mu\sigma \tag{32}$$

where $\omega = 2\pi f$ is the angular frequency of electromagnetic field and f is the frequency of the electromagnetic field, ε is the dielectric permittivity of the medium, μ is the magnetic permeability of the medium, and $j = \sqrt{-1}$. For nonmagnetic media, μ is equal to the free space permeability, μ_o. The equation above can be recast using a complex dielectric permittivity:

$$\gamma^2 = \omega^2 \mu \varepsilon^* \tag{33}$$

where

$$\varepsilon^* = \varepsilon - j\frac{\sigma}{\omega} \tag{34}$$

The imaginary part of the dielectric permittivity is important for many media, including sea water, since it will affect the dielectric losses and electrical conduction and influence the ability to conduct electrical current[67][68].

2. *Reflection and Refraction of Electromagnetic Waves*

As shown in Figure 17, reflected waves and refracted waves are generated when a plane wave is incident on the boundary separating two different media. Here, θ_i is the incident angle, θ_r is the reflected angle, and θ_t is the refracted angle. The plane of incidence contains the propagation direction of the incident wave and the normal to the boundary surface. In this plane of incidence, according to the law of reflection:

$$\theta_r = \theta_i \tag{35}$$

and according to Snell's law [40]:

$$n_2 \sin \theta_t = n_1 \sin \theta_i \tag{36}$$

where n_1 and n_2 represent the refraction index of the respective media. The relation between refraction index and the complex permittivity is:

$$n = \sqrt{\varepsilon_r^*} \tag{37}$$

where the complex relative permittivity ε_r^* is defined as

$$\varepsilon_r^* = \frac{\varepsilon^*}{\varepsilon_o} \tag{38}$$

with ε_o representing the free space permittivity.
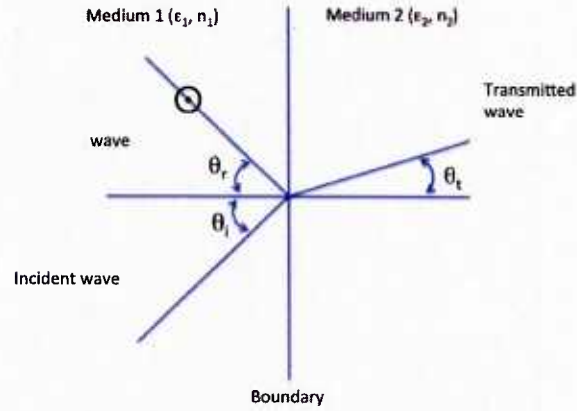
Figure 17. Plane wave incident obliquely on a plane dielectric boundary for the perpendicular polarization
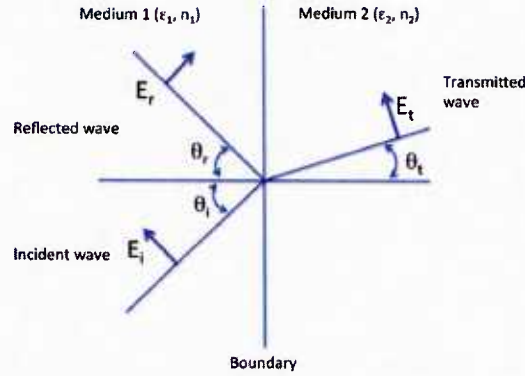
Figure 18. Plane wave incident obliquely on a plane dielectric boundary for the parallel polarization

An incident plane wave with arbitrary polarization can be decomposed into orthogonal components that are parallel and perpendicular to the plane of incidence. The two components have different reflection and refraction coefficients as predicted by Fresnel Equations [40].

1) *When the electric field is perpendicular to plane of incidence* (Figure 17): Let $\Gamma_{R\perp}$ be the reflection coefficient and $\Gamma_{T\perp}$ the transmission coefficient when the electric field is perpendicular to plane of incidence. Then,

$$\Gamma_{R\perp} = \frac{n_1 \cos\theta_i - n_2 \cos\theta_t}{n_1 \cos\theta_i + n_2 \cos\theta_t} \qquad (39)$$

40

And

$$\Gamma_{T_\perp} = \frac{2n_1 \cos \theta_i}{n_1 \cos \theta_i + n_2 \cos \theta_t} \tag{40}$$

where

$$\cos \theta_t = \sqrt{1 - \left(\frac{n_1}{n_2}\right)^2 \sin^2 \theta_i} \tag{41}$$

When n_2 is complex, $\cos \theta_t$ will also be complex. The choice of a plus or minus sign in the square root must be made such that the imaginary part of $\cos \theta_t$ corresponds to the direction of propagation.

2) *When the electric field is parallel to plane of incidence (*Figure 18*):* Let $\Gamma_{R_\parallel}$ be the reflection coefficient and $\Gamma_{T_\parallel}$ the refraction coefficient when the electric field is parallel to plane of incidence. Then,

$$\Gamma_{R_\parallel} = \frac{n_1 \cos \theta_t - n_2 \cos \theta_i}{n_1 \cos \theta_t + n_2 \cos \theta_i} \tag{42}$$

And

$$\Gamma_{T_\parallel} = \frac{2n_1 \cos \theta_i}{n_1 \cos \theta_t + n_2 \cos \theta_i} \tag{43}$$

3. *Scattering Model for Bistatic Reflection*

A model quantifying the orthogonally-polarized scattering response components from an arbitrary plane of incidence is described in this section, which is taken from [65]. Expressions for the cross polarization response and the co-polarized response for both horizontal and vertical polarization transmissions are presented.
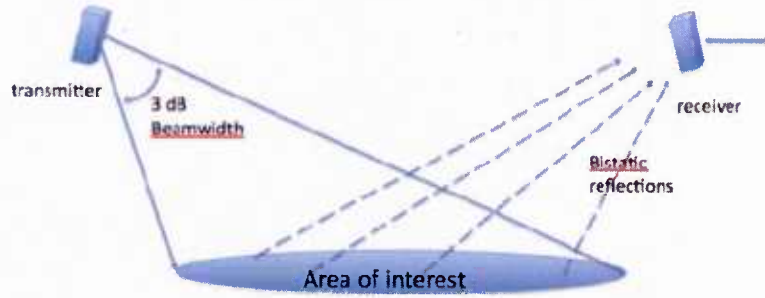
Figure 19. Sensor deployment geometry

The geometry considered includes an RF transmitter and a receiver deployed in a bistatic configuration so that the ground to be sensed lies between the transmitter and the receiver as shown in Figure 19, where the antenna heights, separations, and antenna characteristics are chosen depending upon the scale of the particular application [53]. The electromagnetic wave from the transmitting antenna is approximated as a plane wave in the far field and the scatterer is modeled as a planar boundary [70] so that the Fresnel Equations can be invoked.

The model for scattering is shown in Figure 20, where T and R correspond to the transmitter and receiver, respectively, and where G is the point of reflection. TG is the incident wave, GR is the scattered wave, and points A, B, T, R, O, P, and G are all in the plane of incidence. BA, which is perpendicular to GP, is the line defining the intersection of the ground plane and the plane of incidence, and OG is the angle bisector of $\angle TGR$. The upper panel of Figure 20 illustrates the case when the plane of incidence is normal to the ground and OG is perpendicular to BA, which implies that the ground is the reflecting surface and GO is normal to the ground plane.

For the case of rough surfaces, the position of G may deviate from the point of specular reflection on the mean surface, as shown in the lower panel of Figure 20. In this case, the angle between the ground plane and the plane of incidence is not necessarily $90°$, and is instead represented by the parameter α, which indicates the angle between the planes. Even though OG is in the normal plane of incidence, OG may not be perpendicular to BA. We define the parameter β to represent the angle $\angle PGO$, which indicates the angular deviation of the surface normal at G relative to GP.
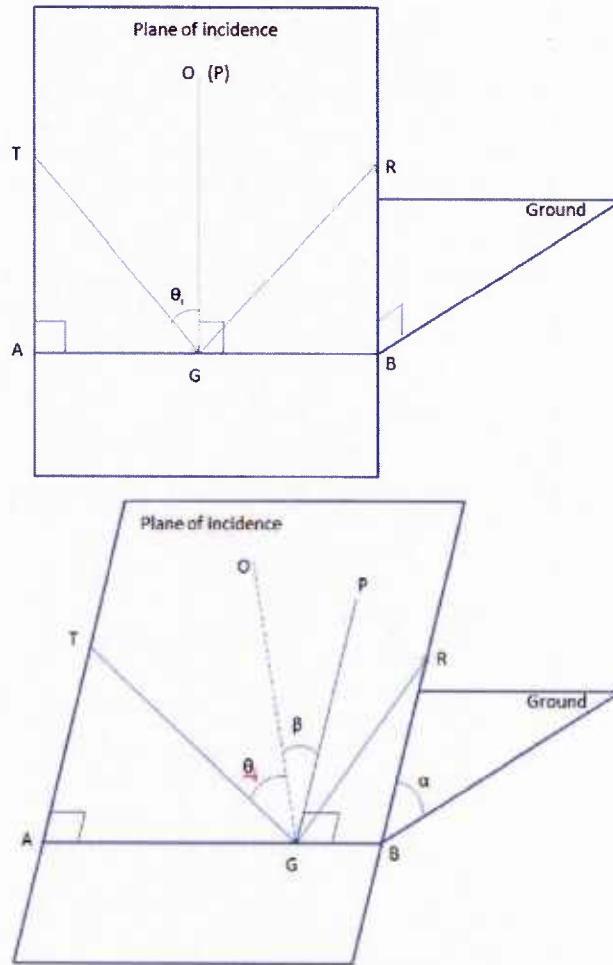
Figure 20. Model for ideal reflection and scattering

The vertical (V) and horizontal (H) polarization components of the fields at the transmitter and at the receiver are shown in Figure 21. The plane TCG that contains vector V and TG is normal to ground, and vector H is normal to plane TCG. Similarly, the plane RDG that contains vector V' and GR is normal to ground, and vector H' is normal to plane RDG. V, H, V', and H' refer to vertically and horizontally-polarized electric field directions, respectively for each pair.

The scattering response can be characterized through the corresponding reflection coefficients, $\Gamma_{VV}, \Gamma_{VH}, \Gamma_{HV}, \Gamma_{HH}$. The first subscript corresponds the transmit polarization and the second subscript to the receive polarization. These coefficients depend upon the Fresnel reflection coefficients and geometry as described below.
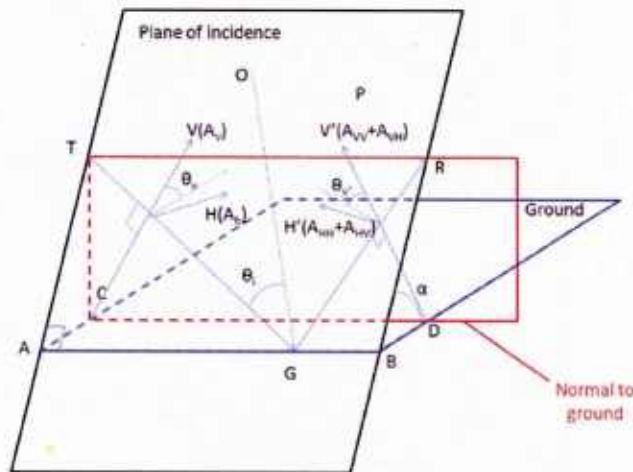
Figure 21. Model for ideal reflection and scattering (part 2)

In Figure 21, θ_v is the angle from V to the plane of incidence, $\theta_{v'}$ is the angle from V' to the plane of incidence. The value of θ_v and $\theta_{v'}$ can be expressed by parameters α, β in Figure 20 and the angle of incidence, θ_i:

$$\theta_v = \arccos \frac{\tan(\theta_i + \beta) \sin \alpha}{\sqrt{\cos^2 \alpha + \tan^2(\theta_i + \beta)}} \qquad (44)$$

$$\theta_{v'} = \arccos \frac{\tan(\theta_i - \beta) \sin \alpha}{\sqrt{\cos^2 \alpha + \tan^2(\theta_i - \beta)}} \qquad (45)$$

Proof:

To see this, NF and NE are perpendicular to TG because we assume a transverse wave, and thus EF is perpendicular to TG. Since V is in the transverse plane, CF is perpendicular to TG and it follows that CF is the height of triangle ΔTCG. TG is perpendicular to the plane EFC. AB is perpendicular to both AC and AT, hence AB is perpendicular to plane ATC and AB is perpendicular to line CE, thus CE is perpendicular to the plane ATG, and CE is perpendicular to line AT.

44

$$\sin\alpha\sqrt{\cos^2\alpha+\tan^2(\theta_i+\beta)}\cos(\theta_i+\beta)$$

Figure 22. Transmit signal geometry for oblique angle of incidence

CE is perpendicular to plane AGT (the plane of incidence), thus CE is perpendicular to EF. Since θ_v is the angle from V to the plane of incidence, it follows that $\angle EFC = \theta_v$. Since AT = 1, if the length of CE and CF is known, θ_v can be computed. CE is the height of a right triangle and is equal to $\sin\alpha\cos\alpha$. To find CF, we first note that since PG is parallel to line AT, then $\angle ATG = \angle TGO + \angle OGP = \theta_i + \beta$, so AG's length is $\tan(\theta_i+\beta)$, and CG is a hypotenuse of length $\sqrt{\cos^2\alpha+\tan^2(\theta_i+\beta)}$. In right triangle $\triangle TCG$, the hypotenuse TG is $\sqrt{1+\tan^2(\theta_i+\beta)}=\sec(\theta_i+\beta)$, and so the height of CF is equal to $\sin\alpha\sqrt{\cos^2\alpha+\tan^2(\theta_i+\beta)}\,\cos(\theta_i+\beta)$. Finally, based on the geometry shown in Figure 23, it follows that

$$\sin\theta_v = \frac{EC}{FC} = \frac{\cos\alpha}{\sqrt{\cos^2\alpha+\tan^2(\theta_i+\beta)}\cos(\theta_i+\beta)} \tag{46}$$

And

$$\cos\theta_v = \sqrt{1-\sin^2\theta_v} = \frac{\tan(\theta_i+\beta)\sin\alpha}{\sqrt{\cos^2\alpha+\tan^2(\theta_i+\beta)}} \tag{47}$$

Similarly, for $\theta_{v\prime}$, it can be shown that

45

$$\theta_{v'} = \arccos \frac{tan(\theta_i - \beta)\sin\alpha}{\sqrt{\cos^2\alpha + \tan^2(\theta_i - \beta)}} \qquad (48)$$
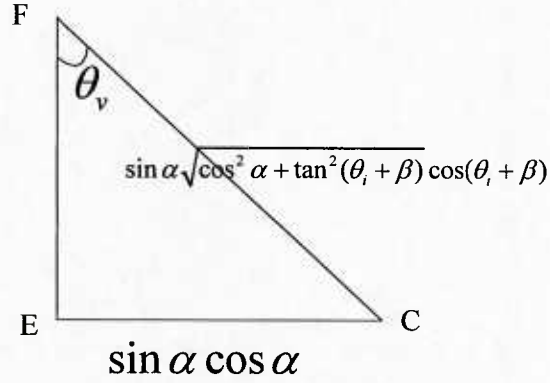
Figure 23. Geometry associated with Δ FEC

END OF PROOF

Using these angles and the component geometry for the incident and reflected signals shown in Figure 24 and Figure 25, respectively, the polarimetric reflection coefficient components $\Gamma_{VV}, \Gamma_{VH}, \Gamma_{HV}, \Gamma_{HH}$ can be derived.
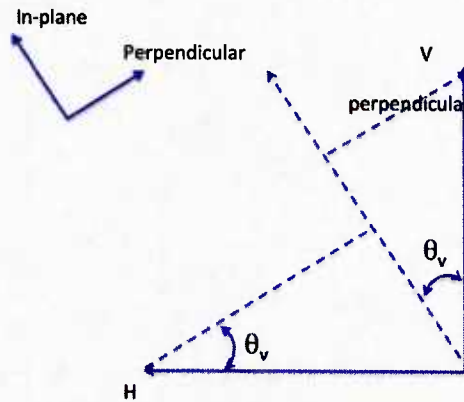
Figure 24. Incident wave geometry (wave propagating into page)
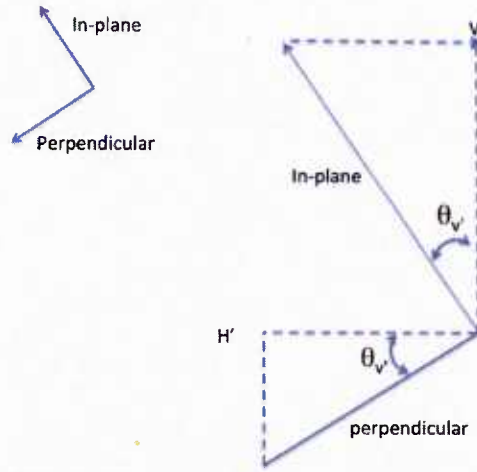
Figure 25. Reflected wave geometry (wave propagating into page)

1) *Vertically-Polarized Transmission:*

Vertical transmission is considered first. Let A_v be the complex amplitude of the vertically-polarized transmission A_{VV} be the complex amplitude of vertically-polarized component of the received signal, and A_{VH} the complex amplitude of the horizontally-polarized received component. Using the above equations and geometrical relationships, one obtains

$$\text{A}_{VV} = A_v\left(\Gamma_{R_\parallel} \cos\theta_v \cos\theta_{v'} - \Gamma_{R_\perp} \sin\theta_v \sin\theta_{v'}\right) \tag{49}$$

$$\text{A}_{HV} = A_v\left(\Gamma_{R_\parallel} \cos\theta_v \sin\theta_{v'} + \Gamma_{R_\perp} \sin\theta_v \cos\theta_{v'}\right) \tag{50}$$

2) *Horizontally-Polarized Transmission:*

Assuming the transmission of a horizontally-polarized signal, let A_h be the complex amplitude of transmitted signal, A_{VH} be the complex amplitude of vertically-polarized component of the received signal, and A_{HH} the complex amplitude of the received horizontally-polarized component. Then, it can be shown that

47

$$A_{HH} = A_h \left(\Gamma_{R_\parallel} \sin \theta_v \sin \theta_{v'} - \Gamma_{R_\perp} \cos \theta_v \cos \theta_{v'} \right) \qquad (51)$$

$$A_{VH} = A_h \left(\Gamma_{R_\parallel} \sin \theta_v \cos \theta_{v'} + \Gamma_{R_\perp} \cos \theta_v \sin \theta_{v'} \right) \qquad (52)$$

Based on **(49)-(52)**, the reflection coefficients are given by:

$$\Gamma_{VV} = \frac{A_{VV}}{A_V} = \Gamma_{R_\parallel} \cos \theta_v \cos \theta_{v'} - \Gamma_{R_\perp} \sin \theta_v \sin \theta_{v'} \qquad (53)$$

$$\Gamma_{HV} = \frac{A_{HV}}{A_V} = \Gamma_{R_\parallel} \cos \theta_v \sin \theta_{v'} + \Gamma_{R_\perp} \sin \theta_v \cos \theta_{v'} \qquad (54)$$

$$\Gamma_{HH} = \frac{A_{HH}}{A_h} = \Gamma_{R_\parallel} \sin \theta_v \sin \theta_{v'} - \Gamma_{R_\perp} \cos \theta_v \cos \theta_{v'} \qquad (55)$$

$$\Gamma_{VH} = \frac{A_{VH}}{A_h} = \Gamma_{R_\parallel} \sin \theta_v \cos \theta_{v'} + \Gamma_{R_\perp} \cos \theta_v \sin \theta_{v'} \qquad (56)$$

To summarize the modeling approach in [65], the scattering computation for a given ground reflector may be obtained as follows:

Given: The Tx and Rx locations and scattering surface locations

1) For a given scatterer location G, find TR, GT, and GR.
2) From these, find GP and RD
3) From GP and RD find α

48

4) From TGR find $2\theta_i$
5) From TGP and θ_i, find β
6) From α, β, and θ_i, find θ_v and $\theta_{v'}$
7) Calculate the in-plane and perpendicular reflection coefficients for V transmission and H transmission
8) Compute the full-polarization reflection coefficients matrix

4.   Numerical Results

This section presents analytical results for reflection coefficients based on equations (53)-(56). Figure 26 presents coefficient magnitudes for a vertically-polarized transmission as a function of the angle of incidence for $\varepsilon_r = 3$ and for different values of α and β.   Figure 27 presents corresponding results for a horizontally-polarized transmission.
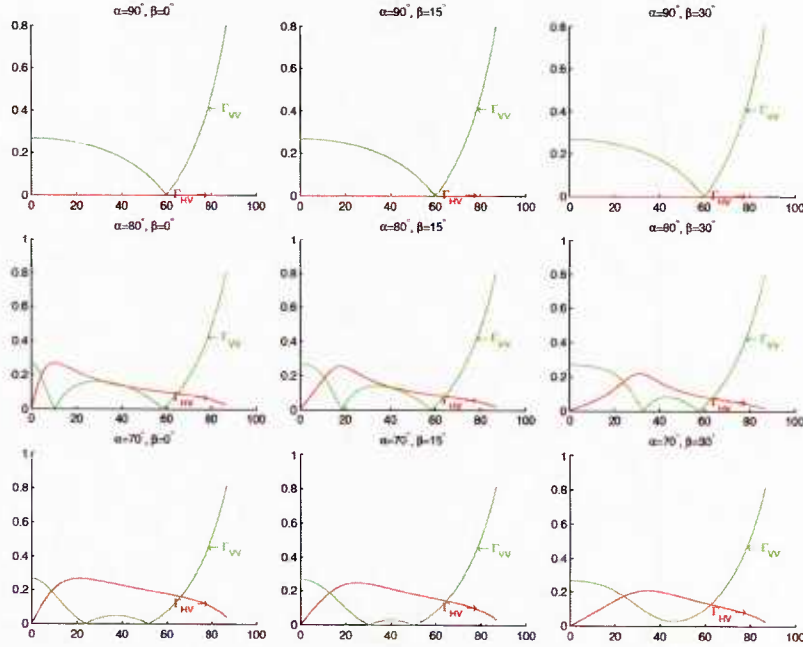
Figure 26. Analytical results for vertical transmission
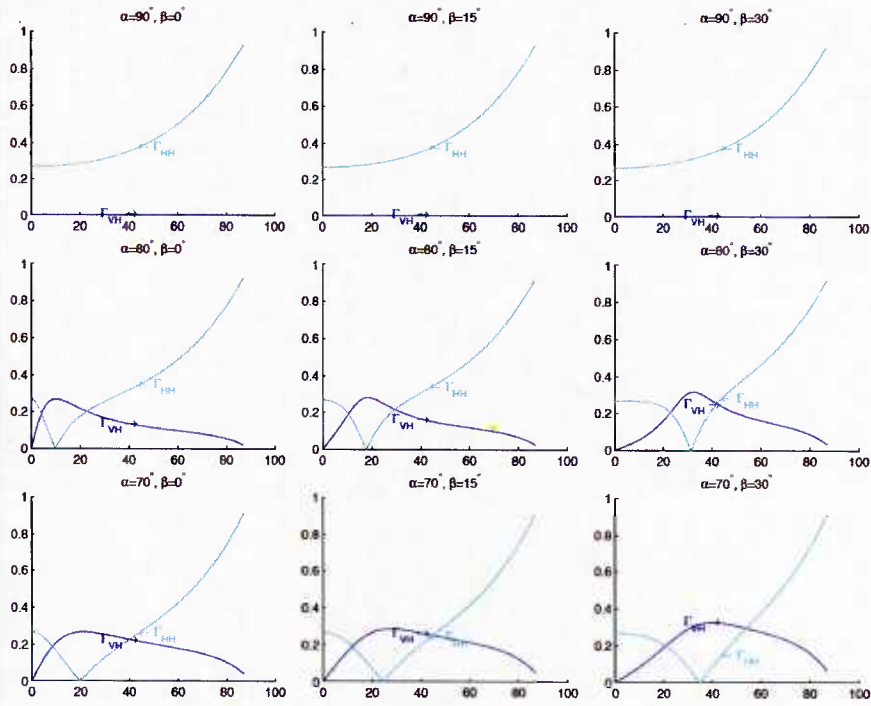
Figure 27. Analytical results for horizontal transmission

The results for α=90, β=0 are consistent with those reported in [68], which are shown in Figure 28 (with the x-axis reversed and scaled).
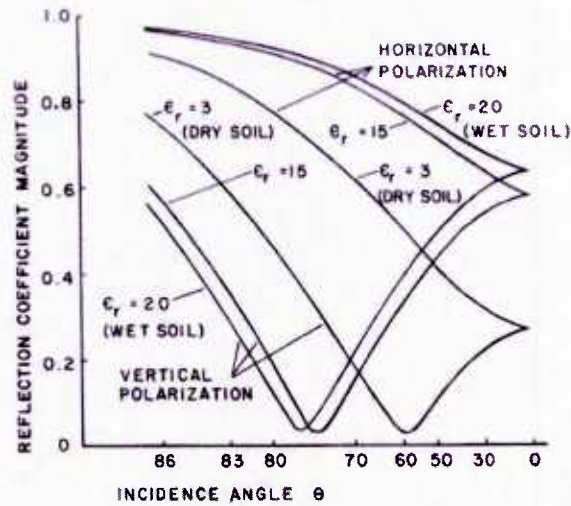
Figure 28. Reflection coefficients for VV and HH scattering

B.   *Kirchhoff Theory*

An alternative analysis approach involves the use Kirchhoff theory, which provides an approximation to the field on the surface of the scatterer. Any point on the scatterer is treated as though it were part of an infinite plane parallel to the local surface tangent. The surface is modeled as a continuum of such points, which serve as secondary radiators. An integral formula is then used to give the scattered field at a point r in the far field relative to the surface. The general approach involves determining the surface fields using the tangent plane approximation and using the integral formula to determine the scattered field. The theory is approximate for scatterers that are finite sized, non-planar or rough [38].

1.   *Scalar formulation:*

The scalar formulation applies to EM waves when there is no coupling between different wave polarizations. The total field at a point r is the sum of the co-polarized incident and scattered waves, i.e.,

$$\psi(r) = \psi^{inc}(r) + \psi^{sc}(r) \tag{57}$$

When the surface of the scatterer is closed, the total field at $\mathbf{r}$ is given by the Helmholtz interior or exterior scattering formula [38]:

$$
\begin{aligned}
\psi(r) \\
= \psi^{inc}(r) + \int_{S_o} \left[\psi^{sc}(r_o) \frac{\partial G(r, r_o)}{\partial n_o} - G(r, r_o) \frac{\partial \psi^{sc}(r_o)}{\partial n_o} \right] dS_o
\end{aligned}
\tag{58}
$$

In the case of the interior formulation, r is inside a closed volume that doesn't include the sources of $\psi^{inc}(r)$ or $\psi^{sc}(r)$. For the exterior formulation, r is outside a closed volume that contains all of the field sources. $G(r, r_o)$ is the Green's function representing the effect at r_o of a point force at r. For scattering from surfaces of finite dimensions, the following form of the Green's function is usually used [38]:

$$G(r, r_o) = \frac{\exp(ik|r - r_o|)}{4\pi|r - r_o|} \tag{59}$$

The surface can always be considered closed for mathematical purposes [38]. If only the scattered field is used in the integral (rather than the total field), then the rough surface can be closed with a surface joining the rough surface to a surface at infinity, so that all fields are within the interior and the reflection coefficients are assumed to be zero on this closing surface except at the rough surface. If the total field is used in the integral instead, then the surface can be closed without any interior sources by using a surface that is infinitesimally close to the rough surface and that is situated behind it so that it is shadowed from the incident field. The Kirchhoff solution for the fields scattered from the rough surface is independent of the approach, but yields results at the edges that depend upon the approach. We neglect the edge effects in our analysis.

The scattered field may be represented by

$$\psi^{sc}(r) = \psi(r) - \psi^{inc}(r)$$
$$= \int_{S_o} \left[\psi(r_o) \frac{\partial G(r, r_o)}{\partial n_o} - G(r, r_o) \frac{\partial \psi(r_o)}{\partial n_o} \right] dS_o \qquad (60)$$

The only quantities that are not known in the above equation are the field and its derivative on the surface. The total field on the surface is given by

$$\psi(r_o) = [1 + R_o(r_o)] \psi^{inc}(r_o) \qquad (61)$$

where R_o is the reflection coefficient for plane waves incident on a plane surface. In general, the reflection coefficient depends upon the surface location, as well as the angles of incidence and scattering. Assuming that the incident field is a monochromatic wave, i.e.,

$$\psi^{inc}(r) = e^{ik_{inc} \cdot r} \qquad (62)$$

then the normal derivative of the incident field on the surface is

$$\frac{\partial \psi^{inc}(r_o)}{\partial n_o} = i(k_{inc} \cdot n_o)\psi^{inc}(r_o) \qquad (63)$$

and combining the above equations, the derivative of the total field is

$$\frac{\partial \psi(r_o)}{\partial n_o} = i[1 - R_o(r_o)](k_{inc} \cdot n_o)\psi^{inc}(r_o) \qquad (64)$$

Using the far field approximation for the Green's function, the argument of the Green's function may be approximated as:

$$k|r - r_o| \sim kr - k\hat{r} \cdot r_o \qquad (65)$$

and the surface derivative becomes

$$\frac{\partial G(r, r_o)}{\partial n_o} \sim \frac{-ie^{ikr}}{4\pi r}(k_{sc} \cdot n_o)e^{-ik_{sc} \cdot r_o} \qquad (66)$$

The scattered field can then be rewritten as:

$$\psi^{sc}(r) =$$
$$\frac{ie^{ikr}}{4\pi r}\int_{S_0}\left[(R_0(k_{inc} - k_{sc}) - (k_{inc} + k_{sc})) \cdot n_o\right]e^{i(k_{inc} - k_{sc}) \cdot r_o}dS_o \qquad (67)$$

Integration can be performed over the rough surface S_o or can be translated to a mean plane integration by noting that

$$n_o dS_o \sim \left(-\hat{i}\frac{\partial h}{\partial x_o} - \hat{j}\frac{\partial h}{\partial y_o} + \hat{k}\right)dS_M \qquad (68)$$

where

$$n_o = \frac{-\hat{i}\frac{\partial h}{\partial x_o} - \hat{j}\frac{\partial h}{\partial y_o} + \hat{k}}{\left[1 + \left(\frac{\partial h}{\partial x_o}\right)^2 + \left(\frac{\partial h}{\partial y_o}\right)^2\right]^{1/2}} \qquad (69)$$

The mean plane integration strategy is exact only when the rough surface area elements are planar. The approximate result may be written as [38]

53

$$\psi^{sc}(r) \cong$$

$$\frac{ike^{ikr}}{4\pi r} \int_{S_M} \left(a \frac{\partial h}{\partial x_o} + b \frac{\partial h}{\partial y_o} - c \right) \tag{70}$$

$$\times \exp\{ik[Ax_o + By_o + Ch(x_o, y_o)]\} dx_o dy_o$$

where

$$
\begin{aligned}
A &= \sin\theta_1 - \sin\theta_2 \cos\theta_3 \\
B &= -\sin\theta_2 \sin\theta_3 \\
C &= -(\cos\theta_1 + \cos\theta_2)
\end{aligned}
\tag{71}
$$

and

$$
\begin{aligned}
a &= \sin\theta_1 (1 - R_o) + \sin\theta_2 \cos\theta_3 (1 + R_o) \\
b &= \sin\theta_2 \sin\theta_3 (1 + R_o) \\
c &= \cos\theta_2 (1 + R_o) - \cos\theta_1 (1 - R_o)
\end{aligned}
\tag{72}
$$

These coefficients are constant when the reflection coefficient is independent of position along the surface, which is a condition we assume in our analysis for each facet comprising the sea surface.

The integrated response is equivalent to summing the response from spherically spreading secondary sources from all points on the surface, where the amplitude response is determined by the local surface gradient and the phase response by the surface height (i.e., the path length). The general result for the field scattered from a rough surface, including the edge terms, may be written as [38]

$$\psi^{sc}(r) = \frac{-ike^{ikr}}{4\pi r} 2F(\theta_1, \theta_2, \theta_3) \int_{S_M} e^{ik\phi(x_o, y_o)} dx_o dy_o + \psi_e \tag{73}$$

$$F(\theta_1, \theta_2, \theta_3) = \frac{1}{2} \left(\frac{Aa}{C} + \frac{Bb}{C} + c \right) \tag{74}$$

$$\phi(x_o, y_o) = Ax_o + By_o + Ch(x_o, y_o) \tag{75}$$

54

and edge effects given by:

$$\psi_e =$$

$$\frac{-ike^{ikr}}{4\pi r}\left[\frac{ia}{kC}\int\left(e^{ik\phi(X,y_o)}-e^{ik\phi(-X,y_o)}\right)dy_o\right.$$

$$\left.+\frac{ib}{kC}\int\left(e^{ik\phi(x_o,Y)}-e^{ik\phi(x_o,-Y)}\right)dx_o\right] \tag{76}$$

This is the form that is widely used in literature where the edge terms are usually neglected. Since the edge terms are negligible only close to the specular direction, the edge terms should be included for other directions [38]. Nevertheless, edge effect terms will be neglected in our analysis to reduce the complexity of the numerical analysis. Generally, Kirchhoff Theory is recognized to be tractable when the following are satisfied [38]:

1) Scattering is in the far field

2) The incident wave is planar and monochromatic

3) The reflection coefficient is constant or slowly varying over the scattering surface

4) The dimensions of the scattering surface are much greater than the surface correlation length

2. Kirchhoff Theory: Vector Wave Scattering

When polarization coupling occurs, vector wave theory applies, and under far-field assumptions, the scattered field may be written in vector notation as:

$$E^{sc}(r) =$$

$$\frac{ie^{ikr}}{4\pi r}\int_S e^{-ik_{sc}\cdot r_o}$$

$$\times\left[(n_o\cdot E)k_{sc}+(n_o\wedge E)\wedge k_{sc}-k\eta(n_o\wedge H)\right]dS(r_o) \tag{77}$$

where $\eta=(\mu/\epsilon)^{1/2}$. The term $n_o\wedge H$ may be written as:

$$n_o\wedge H=\widehat{k}_{sc}\wedge\left[(n_o\wedge H)\wedge\widehat{k}_{sc}\right]+\left[\widehat{k}_{sc}\cdot(n_o\wedge H)\right]\widehat{k}_{sc} \tag{78}$$

and components parallel to the wave direction can be neglected.

The resulting expression for the scattered field in the vector case is given by the Stratton-Chu equation, which is the form employed in our analysis model:

$$E^{sc}(r) = -ik\frac{e^{ikr}}{4\pi r}\widehat{k}_{sc} \wedge \int_S \left(n_o \wedge E - \eta\widehat{k}_{sc} \wedge n_o \wedge H\right)e^{-ik_{sc}\cdot r_o}dS \quad (79)$$

Here,

$$
\begin{aligned}
n_o \wedge E = E^{inc}[&(1-R_V)(n_o \cdot \widehat{k}_{inc})(\widehat{k}_{inc} \wedge e) \\
&+(1-R_V)(n_o \cdot \widehat{k}_{inc})(e \cdot t)(t \wedge \widehat{k}_{inc}) \\
&+(1+R_H)(e \cdot t)(n_o \wedge t)]
\end{aligned}
\quad (80)
$$

and

$$
\begin{aligned}
\eta n_o \wedge H = E^{inc}[&(1+R_V)(n_o \cdot e)\widehat{k}_{inc} \\
&-(1+R_V)(n_o \cdot \widehat{k}_{inc})e \\
&+(R_V+R_H)(t \cdot e)(n_o \cdot \widehat{k}_{inc})t]
\end{aligned}
\quad (81)
$$

Table 3 describes the parameters from the equations above.

Table 3. Scattering model parameter description

Param	Description
$E^{SC}(r)$	Scattered electric field vector at far field location r
k_{inc}	Incident wave vector (transmitter to origin)
k_{sc}	Scattered wave vector (origin to receiver)
r	Distance to receiver
k	Wavenumber $k = \frac{2\pi}{\lambda}$
e	Incident electric field unit vector
E^{inc}	Incident electric field magnitude
r_o	Local surface location
n_o	Local surface normal (unit vector)
t	Local tangential electric field unit vector
R_H	Local reflection coefficient (H)
R_V	Local reflection coefficient (V)
θ_l	Local incident angle

t is in the direction tangent to the surface and perpendicular to the plane of incidence:

$$t = \frac{\hat{\imath} + \hat{k}\partial h/\partial x_o}{[1 + (\partial h/\partial x_o)^2]^{1/2}} \tag{82}$$

e is in the direction of the E-field in the transverse plane, n_o is the outer surface normal:

$$n_o = \frac{-\hat{\imath}\partial h/\partial x_o + \hat{k}}{[1 + (\partial h/\partial x_o)^2]^{1/2}} \tag{83}$$

and

$$R_V = \frac{\epsilon_r \cos\theta_\ell - \sqrt{\epsilon_r\mu_r - \sin^2\theta_\ell}}{\epsilon_r \cos\theta_\ell + \sqrt{\epsilon_r\mu_r - \sin^2\theta_\ell}} \tag{84}$$

$$R_H = \frac{\epsilon_r \cos\theta_\ell - \sqrt{\epsilon_r\mu_r - \sin^2\theta_\ell}}{\epsilon_r \cos\theta_\ell + \sqrt{\epsilon_r\mu_r - \sin^2\theta_\ell}} \tag{85}$$

with

$$\cos\theta_\ell = -n_o \cdot \hat{k}_{inc} \tag{86}$$

$$\sin\theta_\ell = t \cdot \hat{k}_{inc} \tag{87}$$

To extract the scattered horizontal and vertical polarization components, dot products are formed between the scattered waves and the unit vectors p_H and p_V:

$$E_V^{SC}(r) = E^{SC}(r) \cdot p_V \qquad (88)$$

$$E_H^{SC}(r) = E^{SC}(r) \cdot p_H \qquad (89)$$

where

$$p_H = -\hat{\imath} \sin\theta_3 + \hat{\jmath} \cos\theta_3 \qquad (90)$$

$$p_V = \hat{\imath} \cos\theta_2 \cos\theta_3 + \hat{\jmath} \cos\theta_2 \sin\theta_3 - \hat{k} \sin\theta_2 \qquad (91)$$

3.   Numerical Modeling

In our implementation, the surface integral from Equation (79) is numerically evaluated using a summation over a surface composed of a grid of facets. Each facet can be considered as an individual radiator with the composite signal at any far field location as the sum of the contributions from each facet.

For each facet,

- The local surface normal, n_o, is computed based on the gradient of the surface height model

- The local tangential electric field unit vector, t, is computed as the normalized cross product of n_o and k_{inc} (that is, t is perpendicular to both n_o and k_{inc})

- The local reflection coefficients, R_H and R_V, are calculated from these vectors as well as the relative permittivity and permeability of sea water

Thus, for a given incident electric field $E^{inc} = E^{inc}e$, the scattered electric field E_{sc} at a location r can be computed as the summation of the re-radiated fields from the individual facets.

For low grazing angles and moderate to rough seas, it is possible for the local incident angle, θ_l, for some facets to be greater than 90 deg. This implies that the incident wave vector is incident on the back side of the facet. Such facets are removed from the summation, but no other type of shadowing function is presently implemented.

4. Kirchhoff theory limitations

Kirchhoff theory is exact for surfaces that are infinite, smooth and planar. However, for finite surfaces, neglect of surface edges introduces inaccuracies caused by edge diffraction. Accuracy decreases with increasing angle of incidence where diffraction effects become more dominant.

For rough or non-planar surfaces, the local 'planar' assumption becomes increasingly less accurate with *decreasing* frequency and with increasing incident or scattered angles. Global effects such as multiple scattering and self-shadowing often become more dominant with *increasing* frequency thus reducing accuracy. Such effects are most severe at large incident angles. Additionally, accuracy decreases as the ratios $\frac{\lambda_o}{\lambda}$ and $\frac{\lambda_o}{\sigma}$ decrease, where λ_o is the surface correlation length, λ is the RF frequency, and σ is the surface standard deviation.

To summarize,

- Accuracy decreases at high incident angles (low grazing angles) where edge diffraction becomes significant, the local 'planar' assumption is least accurate, and global effects of multiple scattering and shadowing are most severe.

- Accuracy decreases with increasing surface roughness because the local planar assumption becomes less accurate and global effects of multiple scattering and shadowing become more dominant.

- Effects of increasing RF frequency are to increase accuracy of local 'planar' assumption, but to decrease accuracy due to neglect of global effects such as multiple scattering and shadowing.

C. Clutter Statistics

Radar echoes of sea clutter are recognized to depend on many factors, including (among other factors) the sea state, wind velocities, currents, the grazing angle, the radar frequency, radar beamwidth and range resolution, and the polarization state of the transmitter. In this section, various clutter response models and statistics drawn from literature are presented.

1. Clutter Power and Trends

The average clutter power is traditionally given by:

$$C = \frac{P_t G_t G_r \lambda^2 \sigma_c}{(4\pi)^3 R_c^4 L_s L_c} \tag{92}$$

where P_t is the transmit power, G_t is the transmit antenna gain, G_r is the receive antenna gain, λ is the carrier wavelength, R_c is the range to the clutter cell, L_s and L_c are both losses, and σ_c is the clutter radar cross section (clutter backscatter). The clutter backscatter, σ_c, is the product of the clutter reflectivity, σ_o (m²/m²), and the illuminated area. One empirical model for the reflectivity that is polarization-dependent (HH and VV components) has been proposed in [74] for low grazing angles:

$$\sigma_{H,V} = c_1 + c_2 \log_{10}(\sin \alpha) + \frac{(c_3 + c_4 \alpha)\log_{10} f}{1 + c_5 \alpha + c_6 SS} + c_7 (1 + SS)^{\frac{1}{2 + c_8 \alpha + c_9 SS}} \quad (dB) \tag{93}$$

here

$$SS = sea\ state$$
$$\alpha = grazing\ angle$$
$$f = frequency$$

The constants associated with the model are listed in Table 4.

Table 4. Constants used in empirical sea clutter model

Constants	Polarization	
	H	V
c1	-72.76	-48.56
c2	21.11	26.30
c3	24.78	29.05
c4	4.917	-0.5183
c5	0.6216	1.057
c6	-0.02949	0.04839
c7	26.19	21.37
c8	0.09345	0.07466
c9	0.05031	0.04623

In other literature, three distinct regions describing the behavior of sea clutter versus grazing angles exist, as shown in Figure 29 [21]. In the quasi-specular region near vertical incidence, the echo tends to be large (e.g., between 0 dB and 10 dB for medium seas). Below some grazing angle there will be little significant specular return from the facets constituting the surface of the sea [21]. The plateau region applies to grazing angles below those producing quasi specular reflection from facets. At very low grazing angles (several degrees or less), sea clutter RCS decreases rapidly with decreasing angle. Below the critical angle, the RCS varies as the fourth power of the grazing angle.
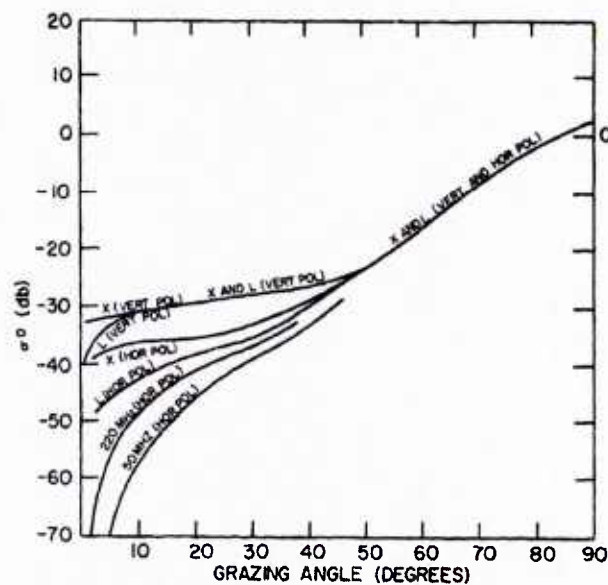
Figure 29. Sea clutter response as a function of grazing angle and for different transmit polarizations (from [21])

Employing the reflectivity model above for the sea state corresponding to SS= 4, we find the predicted reflectivity as a function of grazing angles for different frequencies. We find that the predicted values correlate well with the above figure for lower grazing angles, which was expected since this was the regime where the equations were designed to hold.

61
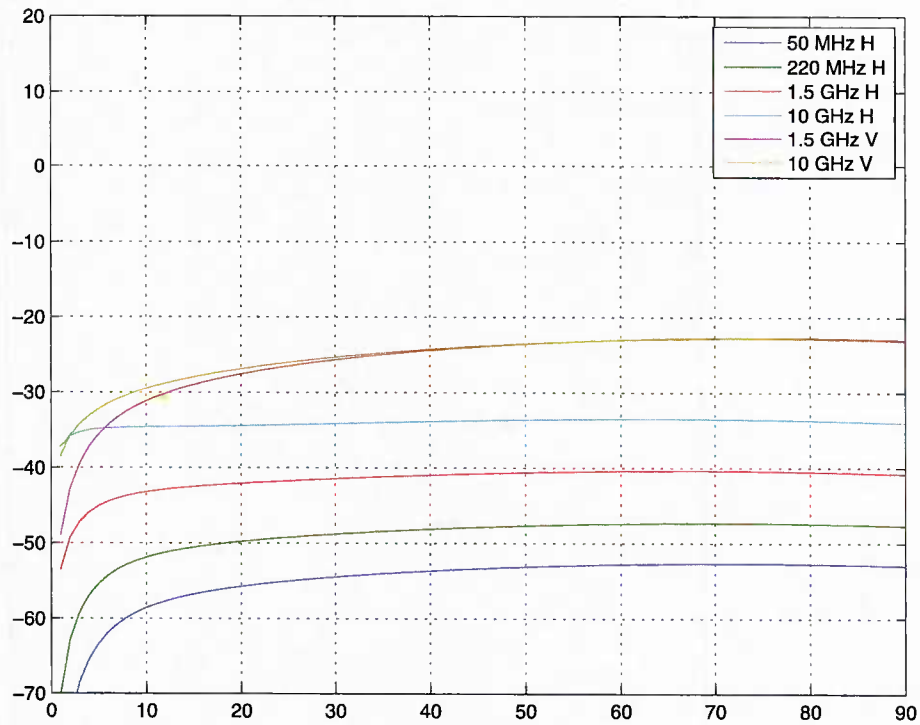
General trends reported in Skolnik also suggest that for a calm sea, the radar echo is small (except near normal incidence). But as the winds increase above 5 to 10 knots, the sea echo increases [21]. These trends are also evidenced by the above reflectivity equation. Plots for SS= 0 are shown below, and may be compared with the Figure above for SS=4 at the low grazing angles. A significant reduction in reflectivity for a calm sea state is indicated.
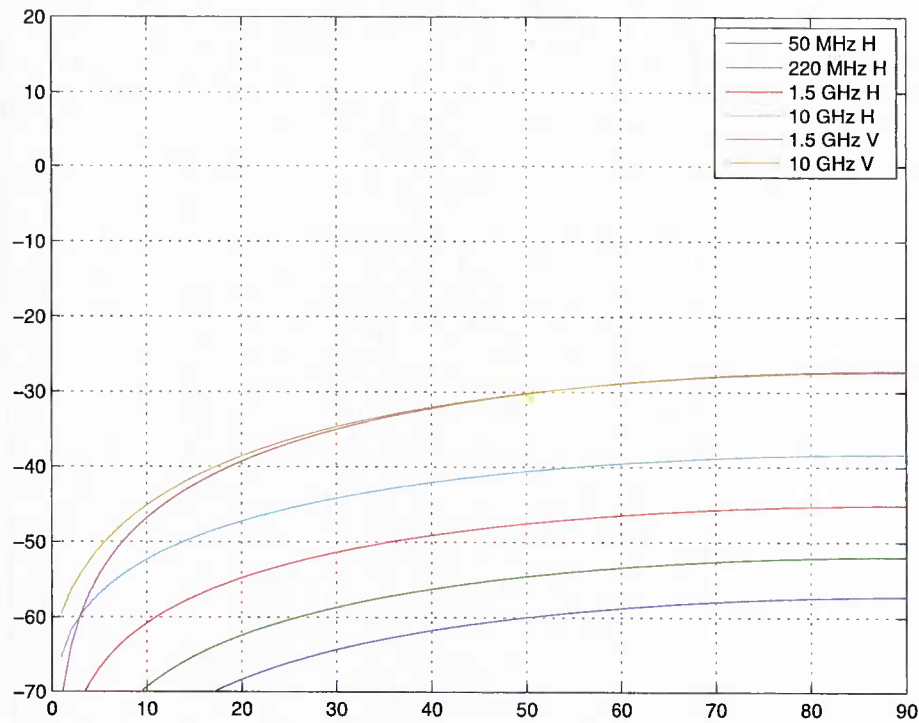
Radar resolution also impacts the observed statistics. For low resolution radar, clutter tends to be distributed in range with little variation about the mean values. Over time scales on the order of 0.1s, the return intensity is distributed according to an exponential distribution (Rayleigh amplitude). Clutter has a fairly short temporal decorrelation period - approximately 10 ms. For a radar employing frequency agility with deviations exceeding the transmitted pulse bandwidth, the pulses are decorrelated from pulse to pulse [56].

The trends are different for high resolution radar. As the cell size is reduced, sea spikes become prevalent that vary in time and stand out from the background response. These spikes occur for both polarizations, but is more evident for H at small grazing angles. They usually extend one pulse length in range and one beamwidth in azimuth and can remain for around 10s. They are usually fixed in position, except for a drift in the direction of the swell and sea waves [4][75].

Intensity statistics have a dependence on the sea state and the swell direction. Sea swells modulate the intensity in a manner that is correlated in space and time. The intensity is sometimes modeled as a Gamma distribution [56]. The response from capillary waves is modeled as Rayleigh with short correlation times/lengths.
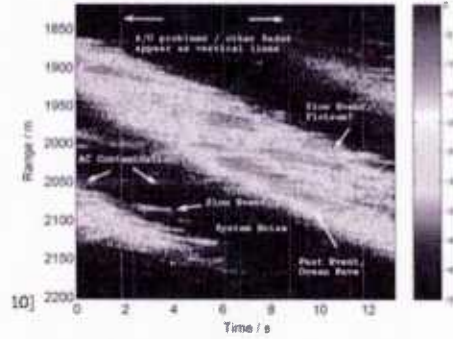
Figure 30. Measured intensity (from [56])

2. Clutter Spectrum

When averaged over long time scales, the Doppler spectrum is of a consistent shape. However, when averaged over medium time scales (~1s), the spectrum has significant structure changes with time [56].   A simple empirical expression for the average spectrum that is commonly cited is:

$$S(f) = Af^{-5}e^{-B(g/2\pi Uf)^4} \tag{94}$$

where g is the acceleration due to gravity, U is the wind speed, and A and B are empirical constants. A polarization dependence in the spectrum does exist. The HH component tends to be associated with higher-velocity responses, and so corresponding Doppler shifts and Doppler spreads are approximately twice that of the VV component.

3. Other Polarization-Based Clutter Response Characterizations

A wealth of experimental investigations have been performed to characterize sea clutter, including polarization-dependent effects. Various trends have been reported, including:

- The average clutter strength increases with grazing angle and with wind speed (as has already been discussed) and is generally larger for VV than for HH. This difference can be extreme in calm seas (e.g., as much as 20-30 dB), but decreases as the sea becomes more rough. The differences diminish as the grazing angle approaches normal. Usually the clutter strength is strongest in the upwind/downwind directions. At low grazing angles,

64

spikiness tends to occur and is more prevalent in the HH component. The cross-polarized response is usually much less than the co-polarized response. In one experiment the differences between the co- and cross-polarized response ranged between 3dB and 24 dB.

- Lower resolution modes with V-pol leads to Rayleigh statistics, whereas at higher resolutions, the statistics are non-Rayleigh. At high resolution with H-pol the statistical models are lognormal.

- At grazing angles above 60 degrees, very little difference is noted in the sea clutter response for different polarizations. At low grazing angles, there can be significant differences [21].

- The critical angle is polarization-dependent (page 26).

- The CPR (Polarization Ratio) is less at X band than at L band. Note that VH and HV are usually not characterized, although these could be important in PMD representations.

- CPR increases with decreasing sea roughness. The maximum ratio can occur at angles as large as 30 degrees. The angle of maximum ratio decreases with decreasing sea state [22].

As evidenced by some of the items above, polarization dependencies in literature are largely reported in a transmit-diversity sense, where intrapulse polarization-frequency behavior of the received echoes is not characterized. By employing coherent measurements between dual-polarized channels, characterizations of these intrapulse polarization-frequency behaviors of sea clutter are possible that may lead to new target detection and identification capabilities. In other words, because the echoes will have delay spread (e.g. from distributed clutter and/or target scattering centers) and polarization-diverse multipath components, the returns will exhibit polarization mode dispersion, or a spread in polarization versus frequency, which has potential to be exploited.

It is clearly important to accurately characterize PMD responses of both sea clutter and of targets for the analysis, features that heretofore have not been measured. Our analysis approach is based on the use of numerical electromagnetic scattering characterizations from a dynamic sea surface model, where statistical models are applied to reflect major trends that have been observed and reported in literature. Additionally, for future model development we anticipate updating the model as appropriate to reflect experimental results that are measured in our research efforts. The current approach has limitations, but it appears to be a good starting point in our study to capture the space-frequency-time-polarization correlations needed in our modeling. The approach enables characterizations of HH, VV, HV, and VH responses as well as the corresponding PMD responses.

D.   Selected Kirchhoff model results

Figure 31 shows the model results (scattering coefficient magnitude) as a function of time for a monostatic radar under various conditions. For the top row of plots, the incident angle is 89 degrees (near grazing), while for the bottom row, the incident angle is 10 degrees (near normal). The 3 columns show results for 3 wind speeds (0, 2, and 10 m/s). Each plot includes four traces identified as VV, HH, VH, and HV where the first letter denotes the receive polarization and the second letter denotes the transmit polarization.
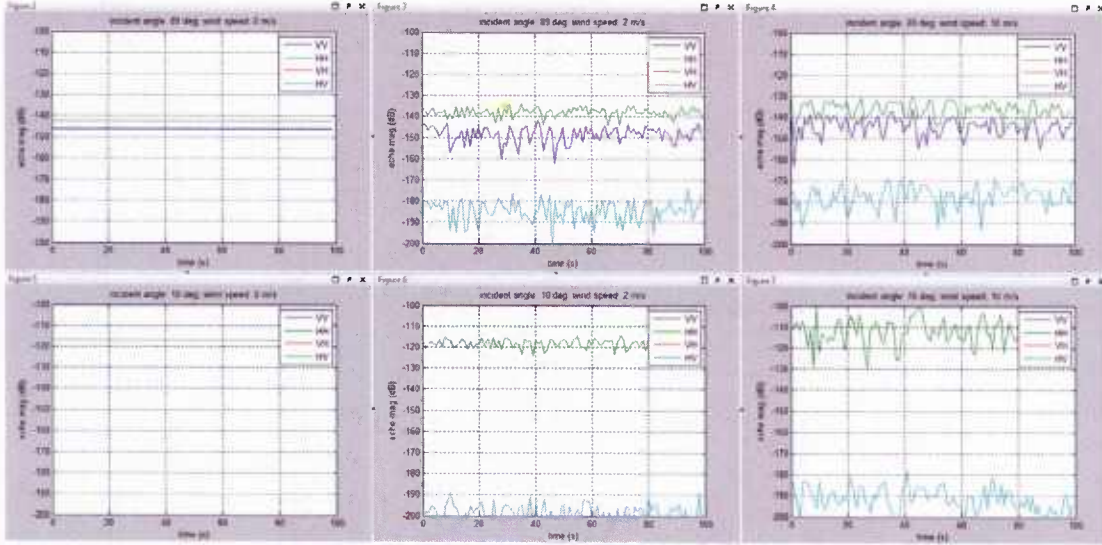
Figure 31. Sample results (monostatic)

For the case of no wind (left-most column of plots), the magnitude is constant versus time as expected. For this special case, the sea is completely flat such that the local incident angle for each facet matches the global incident angle. Therefore, the scattering from each facet is the same such that the overall response matches the reflection coefficients R_H and R_V. Figure 32 shows the reflection coefficient magnitude as a function of local incident angle for a relative permittivity value of 72.4-j216.7. Note that at 89 degrees, the R_V magnitude is approximately -3.7 dB. This matches the difference in HH & VV magnitude shown in the top left plot of Figure 31.
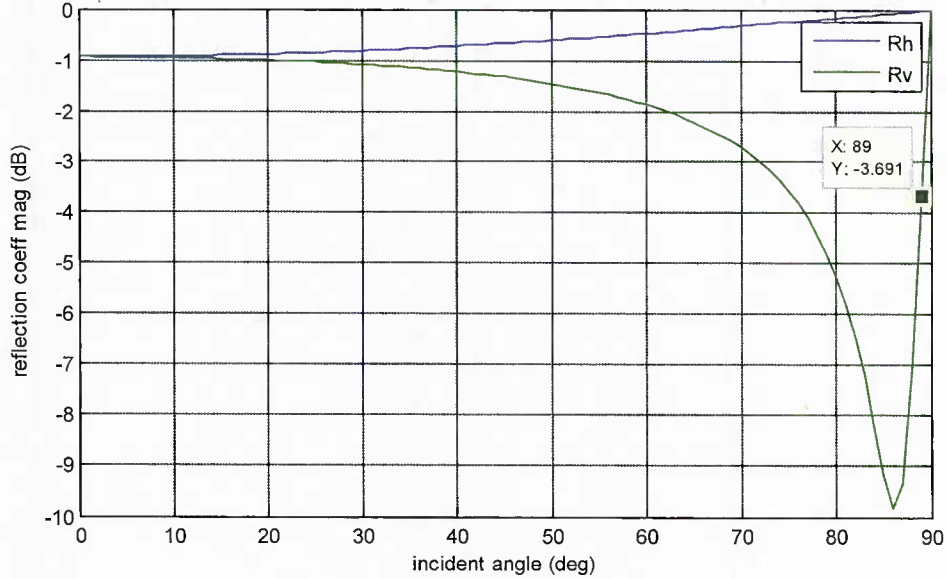
Figure 32. Reflection coefficients versus incident angle

Referring back to Figure 31, there are several observations:

- For the top row of plots (incident angle of 89 deg), note that for all wind conditions, the HH magnitude always exceeds the VV magnitude. This differs from observations and measurements reported in literature in which the VV magnitude often exceeds the HH magnitude at low-to-medium grazing angles in calm to moderate seas.

- VH and HV are identical in all plots. This shows that for the monostatic case, the model reproduces reciprocal results as expected.

- For the cases of wind at 2 and 10 m/s, there is a strong correlation between HH and VV.

- At incident angle of 10 deg, HH and VV are approximately equal in magnitude as expected, but there is an unexpected near-perfect correlation between HH and VV

Figure 33 shows the received power as a function of incident angle for a monostatic system and wind speed of 10 m/s. This is analogous to a "relative" RCS measurement (it is relative since the received power has not been normalized for path losses and illumination area). Note the negative slope for HH and VV such that maximum power occurs at vertical incidence (0 deg) and minimum power occurs at grazing incidence (90 deg). However, note that HH power exceeds VV power for all angles, contrary to published measurements.
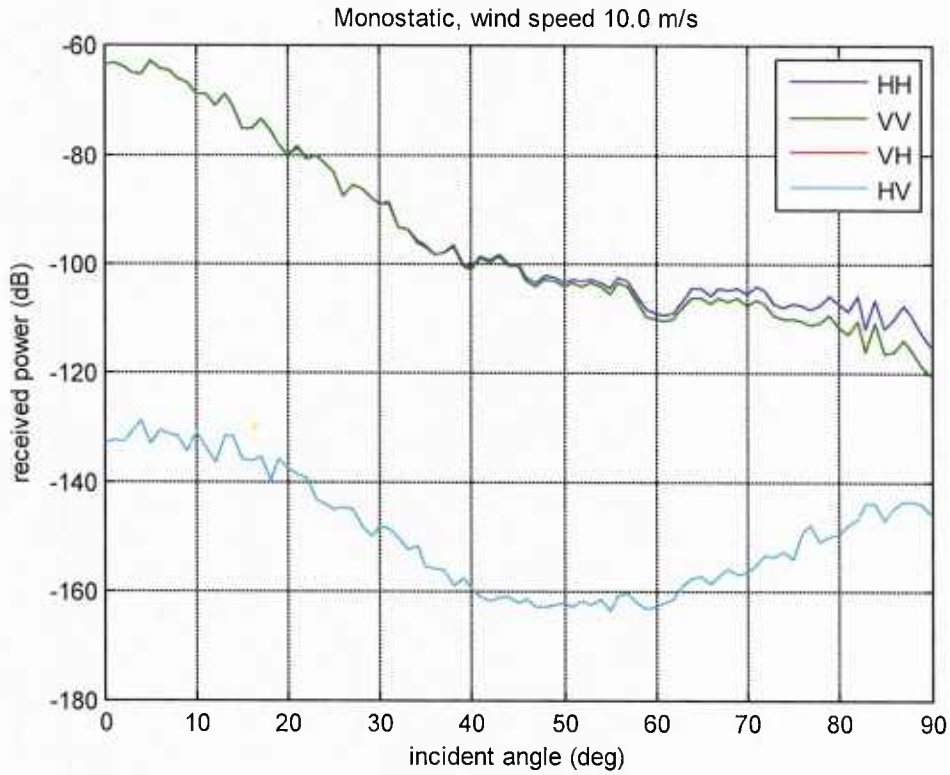
67

Figure 33. Relative RCS versus incident angle

Compare these results (Figure 33) to trends shown in Figure 29. Although the 'x' axes are complements of each other, it is clear that the power decreases in a similar fashion when going from the normal incidence to about 45 degrees incidence representing the normal and plateau regions. However, Figure 33 shows no sharp drop in power at very low grazing angles as in Figure 29.

In order to address the issues mentioned above, the model was extended to incorporate statistical models borrowed from polarization-MIMO communications work.

E.   Model extension

The EM scattering model described in the previous section has some characteristics that require further investigation. First, the magnitude of the HH response generally is equal to or greater than the magnitude of the VV response. This differs from observations and measurements reported in literature [41] in which the VV magnitude generally exceeds the HH magnitude at low grazing angles in calm to moderate seas. Second, there is generally a strong correlation between HH and VV magnitudes. Finally, using current numerical models, for a given sea surface realization, the EM response is deterministic (i.e., there are no statistical variations). A statistical response, however, is desirable, where the statistics should correlate

with those observed in practice. Previous statistical channel modeling work in the area of polarization-MIMO communications [76] utilized models exhibiting frequency-selective full-polarization responses with impulse response delay components exhibiting both fixed component and fluctuating component characteristics. The form of these propagation models have been adopted in our research. The resulting channel matrices defining the polarimetric responses are asymmetrical with regards to HH and VV average power responses, and also the HH/HV and the VV/VH average power responses. Moreover, the various polarization responses may or may not be correlated, and the degree of polarization can be accommodated by the modeling approach.

As a result, we extended the EM scattering model presented above to include a 'fluctuating component' on each channel (HH, VV, HV, and VH), where the relative contribution of the deterministic and fluctuating components can be controlled. Therefore, the model can produce results with the expected behavior of VV magnitude exceeding HH magnitude and with varying degrees of correlation between HH and VV responses.

The model extensions incorporate statistical models borrowed from polarization-MIMO communications work. Specifically, the model was updated to include a 'fluctuating component' on each channel (HH, VV, HV, and VH). The updated model includes weighting factors, K, to adjust the relative contribution of the non-fluctuating component (Kirchhoff) and the fluctuating extension. A large K factor (relative to unity) emphasizes the original Kirchhoff component while a small K factor emphasizes the fluctuating extension.

As part of future research efforts, several experiments will be conducted to better understand scattering characteristics such as HH / VV correlation (especially at near normal incidence) and HV / VH reciprocity which degrades as a function of the bistatic angle between transmitter and receiver. These experimental results will be used to support improvements / extensions to the sea reflectivity model.

Figure 34 includes 6 plots showing the model results as a function of K. The upper left plot shows the original Ogilvy implementation (effectively, $K=\infty$). The remaining plots going across the top row and then continuing across the bottom row show results for decreasing values of K (Parameters: Incident angle: 89 deg; Wind speed: 2 m/s)
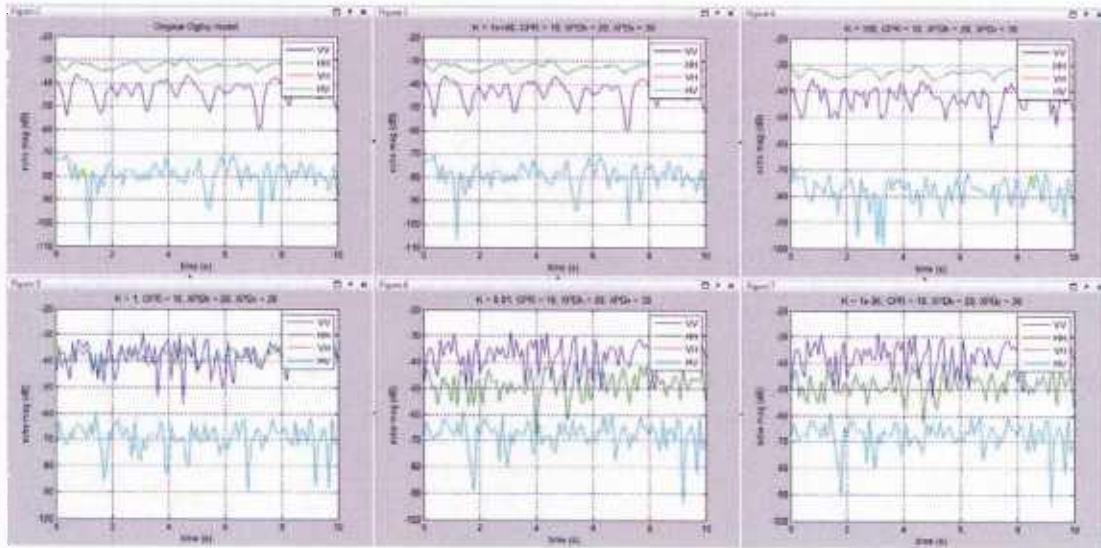

Figure 34. Sample results with extended model

With K=1e6, the plot (upper middle) is almost identical to the original Kirchhoff model results (as expected). With K=100 (upper right), the co-pol traces are largely unchanged, but the cross-pol results are already impacted by the fluctuating component. With K=1 (lower left), the co-pol magnitudes are nearly equal. Thus, the CPR of 10 dB (VV/HH) has nearly exactly "compensated" for the fact that Kirchhoff model results show HH/VV at about 10 dB. With K=0.01 (lower middle) or K=1e-6 (lower right), it appears that the fluctuating component is dominant in all plots. Also, the relative powers among VV/HH/VH/HV all match the input parameters shown in the plot title.

V.   SYSTEM MODELING

Section IV described the electromagnetic scattering model used to model scattering from the sea surface.   In this section, we describe the overall radar model, including parametric control, as well as a simple target model. Combined, these models provide the means to simulate and analyze various target detection and identification algorithms.

A.   Radar Model

The radar model consists of a transmitter and receiver to simulate both monostatic and bistatic systems. Specifically, we are interested in the cases of monostatic systems at both low grazing angles as well as near-normal incidence and bistatic systems at low grazing angles. All of the scattering models are implemented as bistatic models - monostatic is simply a specific case of the bistatic model.

The radar processing is segmented into distinct radar cells. The number of radar cells is selectable in both the down range and cross range dimensions. In our simulation results, the number of cells in each dimension is typically three indicating a three by three grid of radar cells. The target is always placed in the center cell. Most of the results show comparisons between the response of the center radar cell (including the target) to the surrounding radar cells (clutter only).

The size of each radar cell is determined by both the antenna beam width and the range cell size (set equal to the pulse width). The down range cell size is dependent upon both the beam width and the range cell size whereas the cross range cell size is only dependent upon the beam width.

The radar waveform is modeled as a summation of equally spaced tones where the tone spacing is set by the pulse repetition frequency and the bandwidth is proportional to the inverse of the pulse width. Because the scattering model is a linear system, each of the tones can be processed individually such that the composite output signal is the summation of the individually processed tones.

Both transmit and receive antennas are modeled as dual-polarization (H/V) antennas, providing a full polarization characterization that is preserved throughout the various scattering models (sea clutter and target models). The antenna pattern is modeled as a main-beam only sinc pattern. This pattern is used as a "weighting" to the signal incident on the facets of the sea clutter model. Additionally, the beam width is used to determine the radar cell size as mentioned above.

PMD signal processing consists of calculating the Stokes parameters at each PRF line, providing the PMD representation. Additional processing consists of calculation of transfer gains for each PRF line, leading to Jones matrix and Mueller matrix characterizations. As part of the PMD response analysis, statistics are

computed versus time, space, frequency, and polarization. Additionally frequency domain analysis is employed to estimate attitude rates.

B. Target Model

The target is modeled as N dipoles with random position (within a volume), orientation, and reflection coefficient.

Figure 35 depicts a sample target model consisting of 10 dipoles and a target size of 200 by 20 by 10 feet (the axes units are meters). In this figure, each dipole is represented by two end points and a line connecting them. The position of a dipole is the midpoint of the line. The orientation of a dipole is indicated by the orientation of the line. The reflection magnitude of the dipole is indicated by the length of the line.
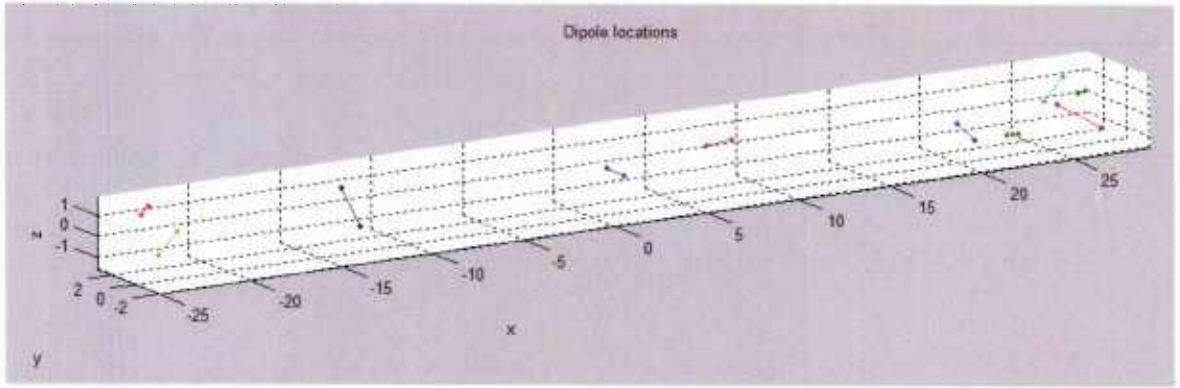
Figure 35. Illustration of multiple dipole target model

The overall target model can be set to arbitrary roll, pitch, & yaw such that the N dipoles' position and orientation is accordingly updated.

The overall scattering matrix for the N dipole model is computed as the sum of the individual scattering matrices for each of the individual dipoles.

1. Scattering matrix for an individual dipole

The dipole gain, G_D, is a function of the signal direction $\widehat{k}$ and the electric field vector $\widehat{e}$ [77].

$$G_D(\widehat{k}, \widehat{e}) = \sqrt{1.641}(\widehat{e} \cdot \widehat{d}) \frac{\cos\frac{\pi}{2}\xi}{1 - \xi^2}$$

$$\xi = \widehat{d} \cdot \widehat{k}$$

where

$\widehat{d}$ is the dipole orientation vector

$\widehat{k}$ is the signal propagation vector (incident or scattered)

$\hat{e}$ is the electric field vector (incident or scattered, H or V)

Figure 36 shows the antenna patterns, G_D, for a dipole oriented along the 'x' axis. Note that the H pattern has zero gain along the 'x' axis (y=0) when viewed from above. Note that the V pattern has zero gain for any direction in the x-y plane when z=0.
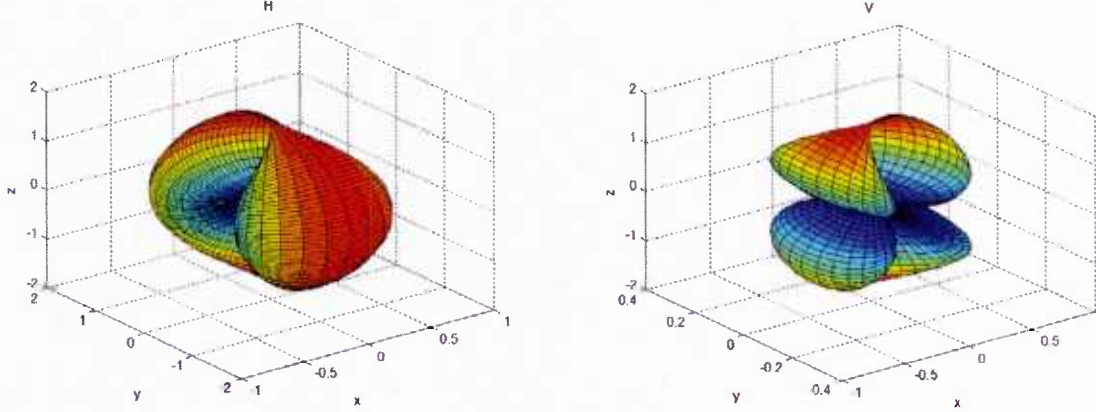

Figure 36. Individual dipole antenna pattern (dipole oriented along 'x' axis)

The dipole phase, ϕ_D, is computed based on path length for each dipole location r.

$$\phi_D = e^{j(k_i - k_s) \cdot r}$$

In calculating the overall signal reflection magnitude for a given dipole, the antenna pattern of the dipole is applied twice, once in the TX antenna direction and once in the RX antenna direction (these will be the same for the monostatic case). Additionally, each dipole is assigned a random complex reflection coefficient, Γ, which has normal distribution (zero mean, unity standard deviation) for both the real and imaginary components.

By calculating G_D for all 4 combinations of incident and scattered H and V, we can determine the dipole 2 by 2 scattering matrix, $\boldsymbol{G_i}$

$$\boldsymbol{G_i} = \begin{bmatrix} G_D(\hat{k}_s, \hat{e}_{hs})G_D(-\hat{k}_i, -\hat{e}_{hi}) & G_D(\hat{k}_s, \hat{e}_{hs})G_D(-\hat{k}_i, \hat{e}_{vi}) \\ G_D(\hat{k}_s, \hat{e}_{vs})G_D(-\hat{k}_i, -\hat{e}_{hi}) & G_D(\hat{k}_s, \hat{e}_{vs})G_D(-\hat{k}_i, \hat{e}_{vi}) \end{bmatrix} \Gamma e^{j(k_i - k_s) \cdot r}$$

where

$\hat{k}_i$ and $\hat{k}_s$ are the incident and scattered wave vectors

$\hat{e}_{hi}, \hat{e}_{vi}, \hat{e}_{hs},$ and $\hat{e}_{vs}$ are the incident and scattered electric field vectors

r is the dipole location vector

Γ is the dipole reflection coefficient

2. *Scattering matrix for N dipole model*

The overall (composite) scattering matrix, G_c, is the sum of the N individual scattering matrices.

$$G_c = \sum_{i=1}^{N} G_i$$

Figure 37 shows the composite pattern (for this 10 dipole example) for wave vectors in the x-y plane. Note the significant variability as a function of wave vector angle.
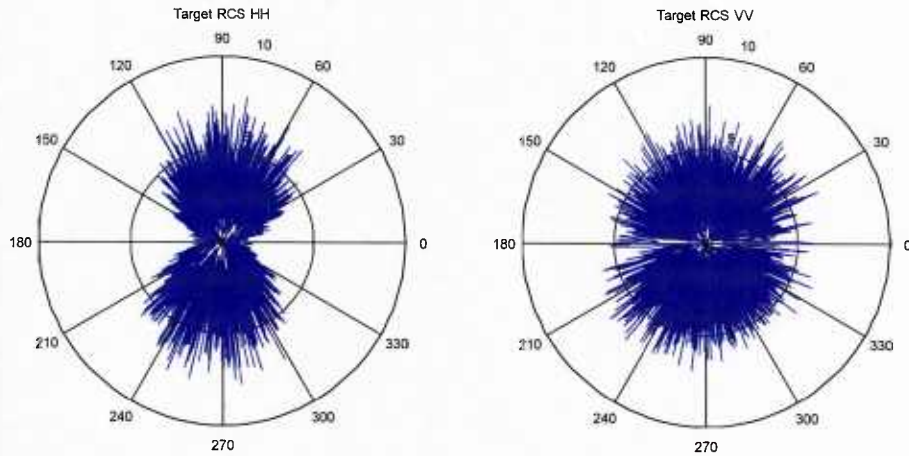

Figure 37. Composite pattern in x-y plane

VI.   POLARIZATION-BASED METHODS

In this section we designate the polarization responses using a two-letter moniker, where, as before, the first letter represents the transmit antenna's matched polarization and the second letter represents the receive antenna's matched polarization. For convenience, we restrict the matched polarizations of the transmit and receive antennas to vertical (V) and horizontal (H) polarizations, recognizing that responses for other polarization states will be linear combinations of these components.

Polarization-based radar detection is discussed in a large body of literature, for example, in remote sensing applications [90][91].   Typically, the techniques employ VV, HH, and sometimes VH and HV intensity characterizations. Researchers have employed more sophisticated techniques, exploiting the coherence between full-polarization target responses. For example, in [92], Mueller matrix component statistics from radar returns are considered for a narrowband formulation. In [72], Hsu exploits the coherence between full-polarization responses in backscatter applications.   Other work, such as that discussed by Boerner for SAR imaging, leverages the coherence between full-polarization responses to characterize responses in terms of descriptors such as the Huynen polarization fork, co/cross polarization power density plots (van Zyl plots), co/cross polarization phase correlation plots (Agrawal plots), and lexicographic and Pauli-based covariance matrices.

While recognition of frequency dependence on a macro scale is well-known (see references [14, 15, 19] in [6]), the frequency dependence of the polarization state over the bandwidth of the received signal does not appear to be recognized in radar literature, and this is the principle phenomenon that our work leverages. Prior methods, which are based on monochromatic models, are often applied to wideband channels, and do not consider polarization dispersion. The neglect of PMD by prior methods limits potential opportunities for new and perhaps improved characterizations enabled by PMD-based processing. By dividing the received signal into subbands, a polarization mode dispersion characterization is possible, and the prior techniques can be applied in each subband, potentially leading to improvements in characterizations available to those approaches. While we recognize that gains are possible by integrating PMD-based processing with other techniques, we focus on approaches that specifically leverage PMD.

A.   Prior Art

In our discussion of prior polarization-based sensing approaches, we shall begin with a brief presentation of the methods discussed in Hsu [72], since these most closely resemble the technology that we consider. As with traditional polarimetric

characterizations, Hsu employs a full polarization Sinclair matrix to represent the polarization behavior associated with target reflections,

$$\mathbf{S} = \begin{bmatrix} S_{hh} & S_{hv} \\ S_{vh} & S_{vv} \end{bmatrix} \tag{95}$$

The monostatic case is considered along with a reciprocal target, and so the scattering coefficients s_{vh} and s_{hv} are equal. For targets that are not reciprocal in this manner, for example targets with ferrites, this relationship does not hold true. Assuming symmetric VV and HH responses, the clutter plus noise covariance matrix takes on the following symmetric form:

$$\mathbf{R} = E[x_s(k)x_s^h(k)] = \sigma_c^2 \begin{bmatrix} 1 & \sqrt{r\delta} \\ \sqrt{r\delta} & 1 \end{bmatrix} + \sigma_n^2 I \tag{96}$$

The signal covariance may be then computed for each of the distinct signal components

$$R_{hv} = \sum_{\substack{i,j=-k \\ i,j\neq0}}^{k} [x_{hh_i} \quad x_{hv_i} \quad x_{vv_i}]^H [x_{hh_j} \quad x_{hv_j} \quad x_{vv_j}]^T \tag{97}$$

and a detection metric can be formed from the covariance matrix.

$$\eta_{hv} = [x_{hh} \quad x_{hv} \quad x_{vv}]R_{hv}^{-1}[x_{hh} \quad x_{hv} \quad x_{vv}]^T \tag{98}$$

We note here that the indicated processing leverages the coherence between the VV, HV, and HH components to arrive at a detection metric. The approach is shown to achieve improved detection over common diversity approaches, and the results from the paper are shown below in Figure 38:
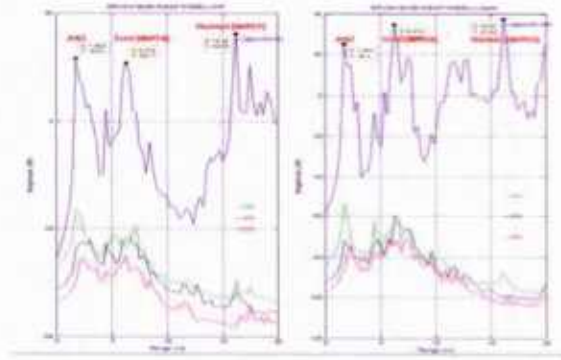
Figure 38. Improved detection results leveraging coherence between VV, HV, and HH (from[72])

Our approach leverages coherence between all of the components, including for asymmetric co-polarized power responses and for non-reciprocal targets, but in a different manner. In particular, we characterize the responses as a function of the subbands of the signal, which are distinct due to polarization mode dispersion induced by the propagation channel. Prior works have apparently not considered this phenomenon. A useful feature is that PMD characterizations can be made for arbitrary transmit polarizations but require the use of orthogonally polarized signal components at the receiver to measure the resultant PMD. Hence characterizations are applicable to systems using a single transmit polarization or to systems using multiple polarizations, such as for full-polarization characterizations. In the radar problem, we use PMD characterization to compute measures based on coherent ratios between multiple pairs of transmit/receiver polarization components. Assuming V and H transmissions and a V and H polarization basis at the receiver, we utilize PMD derived from VV and VH measurements as well as from HV and HH measurements. Note that due to radar coherency, measures based on the coherency between HH and VV are possible in the backscatter (monostatic) formulation. Using appropriate transmission waveforms, coherency between the VV and HH responses is also possible in the bistatic case, and such methods will be explored in our future analysis. This pair may be of particular interest because the difference in power between these modes is expected to be small, which may not be true for other pairs of signals. In section X, we discuss a potential approach to efficiently acquire a full-polarization PMD matrix estimate for bistatic characterizations.

Finally, the VH and HV pair is considered. An interesting feature in the monostatic case is that for reciprocal targets, HV and VH are the same, suggesting that if the target is not reciprocal, the response may provide an indication of the presence of a target with nonreciprocal features. This pair is expected to gauge channel reciprocity in the monostatic case and may provide detectable features when echoes from a nonreciprocal target exist. However this pair is expected to suffer from the lowest SNR of all of the pairings considered.

A key difference between the Hsu processing and our processing is the narrowband representation applied by Hsu. Because he employs a narrowband scattering representation, his approach, when applied to a wideband channel, leads to a loss in the degree of polarization of the signal at the receiver. In contrast, we assume a wideband target representation and employ PMD techniques to characterize the target response in a manner that is largely void of loss of degree of polarization.

Poelman

Another paper from the survey dealing with polarization-based suppression motivates the use of two technologies that are enabled by PMD-based processing. In [73], polarization processing is described to increase the SINR through two mechanisms: adaptive transmission and polarization-based suppression at the receiver. The concept, which is illustrated in Figure 39 (taken from [73]), shows that the transmit signal polarization is set to minimize the unpolarized component, while the receive polarization is set orthogonal to the polarization of the completely polarized component.
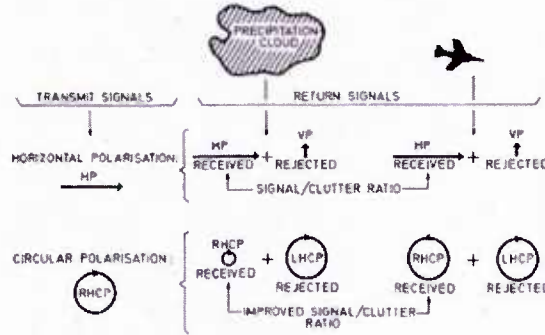

Figure 39. Adaptive transmission and polarization-based suppression at the receiver

As with Hsu, the approach is based on a narrowband representation of the target using a Sinclair matrix.

$$\mathbf{T} = \begin{bmatrix} H-H & H-V \\ V-H & V-V \end{bmatrix} = \begin{bmatrix} a_{yy}\exp(j\alpha_{yy}) & a_{yx}\exp(j\alpha_{yx}) \\ a_{yx}\exp(j\alpha_{yx}) & a_{xx}\exp(j\alpha_{xx}) \end{bmatrix} \qquad (99)$$

More effective control of the transmit polarization would be possible by adjusting the polarization as a function of the frequency component of the transmitted signal [11]. Also, the methods described in [9][10] could also more effectively suppress

the interference using polarization-based processing that is subband dependent [48], instead of the single-band approach that is used by Poelman.

Margarit

A final work identified in the survey that has significant relevance discusses polarimetric SAR-based characterizations of ships [54]. The detection technique considered in the work is based on the supposition that with sufficient spatial resolution, ships may be characterized by a particular spatial arrangement and polarization state distribution of dominant scattering centers, where the polarization-sensitive response is determined in terms of so-called permanent polarimetric scatterers (PePs). The author states that robust classification is possible using quad-pol imagery, and demonstrates results using a scene of 60 x 60 m^2 based on quarter wavelength facets and different Pauli mechanisms (trihedral, dihedral, and antisymmetric) as targets. The approach requires high resolution to resolve PePs for classification and uses comparisons of Sinclair representations.

In contrast to this approach, which characterizes individual scatterers, our approach relies on a time-dispersed target model, capturing coherent returns from a collection of target scatterers within a range cell. PMD-based detection algorithms are then applicable for both detection and identification purposes.

In summary, existing polarization-based models/measurements that we found in literature do not attempt to characterize or leverage the primary phenomenon that we intend to exploit, polarization dispersion. While prior methods do employ coherent processing of the signals associated with a full-polarization representation, narrowband representations are apparently exclusively applied. Wideband representations based on PMD characterization are not used to support either detection or identification. In contrast, our approach is based on a wideband representations using PMD. The consideration of PMD characterizations appears to be new in radar applications.

Recent PMD-based technology developments to date in space-polarization MIMO communications and remote sensing applications can potentially be leveraged for radar applications. For example, forward scattering models developed for remote sensing may be of use in electromagnetic propagation modeling. Also, techniques applied in remote sensing may provide an ability to detect attitude rates of a target, assuming the rates are sufficiently different. Other unique detection techniques are anticipated as the research continues. In the next section, before describing these techniques, we describe the PMD technology.

B.   PMD CHARACTERIZATION

1.   Polarization Representation on the Poincare Sphere

We employ the Poincare sphere to represent the polarization state of the received signal.   Every point on the sphere corresponds to a unique polarization state, and all polarization states can be uniquely represented. The poles represent the circular polarizations, the equator represents the linear polarizations, and the states in-between represent elliptical polarizations.   Although a number of schemes to represent polarization on the sphere are discussed in literature, we utilize Stokes parameters, denoted as S_0, S_1, S_2, and S_3. The S_0 term is used to represent the power of the signal, whereas S_1, S_2, and S_3 provide Cartesian components relative to the origin of the sphere, where S_1, S_2, and S_3 are components aligned with H, S45, and LHC, respectively. As noted in the Figure 40, V is represented by S_1=-1, $S_2 = S_3 = 0$. Representations for other polarization states are also shown.
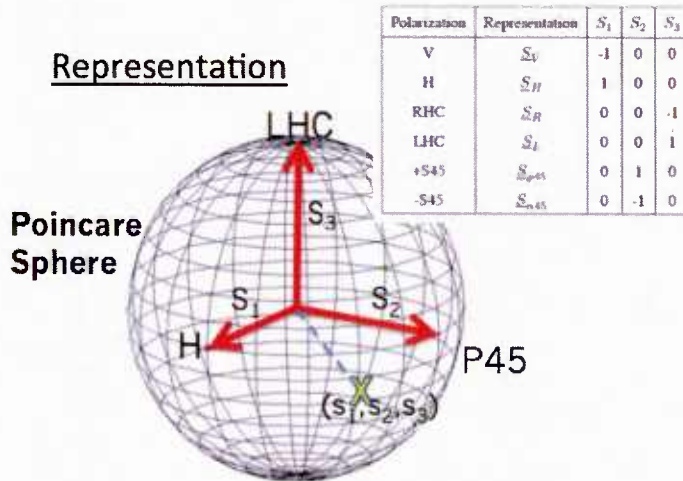

Polarization	Representation	S_1	S_2	S_3
V	S_V	-1	0	0
H	S_H	1	0	0
RHC	S_R	0	0	-1
LHC	S_L	0	0	1
+S45	S_{p45}	0	1	0
-S45	S_{n45}	0	-1	0

Figure 40. Poincare sphere polarization representation

2.   Introduction to Polarization Mode Dispersion Phenomenon

Polarization mode dispersion is a phenomenon that results in a spreading of the polarization state at the receiver as a function of the frequency components of the received signal. PMD results in part from a group delay difference between the polarization components of the received signal and also depends on the signal bandwidth and the transmit polarization. On the sphere, PMD appears as a continuous curve on the sphere. PMD is well known in the optical fiber community, where input to output models have been proposed to help characterize polarization effects in optical fiber. The representations were based on a principle state of polarization, and a rotation about this principal state, as shown in Figure 41 [24].
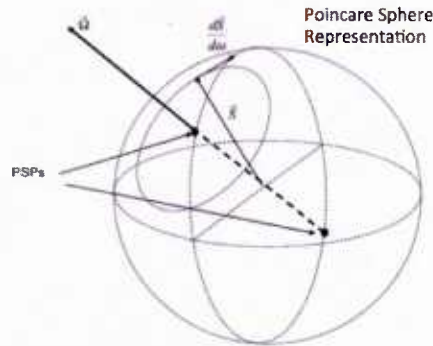
Figure 41. Principal state of polarization used in optical fiber communications

In optical fiber communications, the group delay differences between polarization components occur due to birefringences in the fiber, resulting in asymmetric propagation properties of the orthogonally-polarized signal components. More recently, PMD has been recognized to occur in RF channels [25]. Namely, since about 2006, RF propagation channels (which would include forward scatter and backscatter channels) were observed to exhibit PMD and PDL, albeit through different propagation phenomena than in optical fiber channels, and that these behaviors can be represented using a similar input/output perspective [25][26].

Group delay asymmetries exist in RF channels, leading to PMD. It has been shown that PMD will exist in wireless channels if the channel is temporally dispersive and if the channel exhibits depolarization. An example of PMD from wireless measurements is shown in Figure 42. The experiment employed a 10 MHz transmit signal in an indoor propagation channel.

Figure 42. Polarization mode dispersion from indoor measurements using a 10 MHz transmit signal bandwidth

The PMD response is color coded according to contiguous 1 MHz subbands. We note that the particular response can be characterized as a rotation about a

principal state of polarization, similar to those described in optical fiber communications literature. This response is indicative of a two path response, in this case a LOS component and a single major multipath component. More complicated multipath structures leads to more complicated PMD responses, as evidenced in Figure 43.
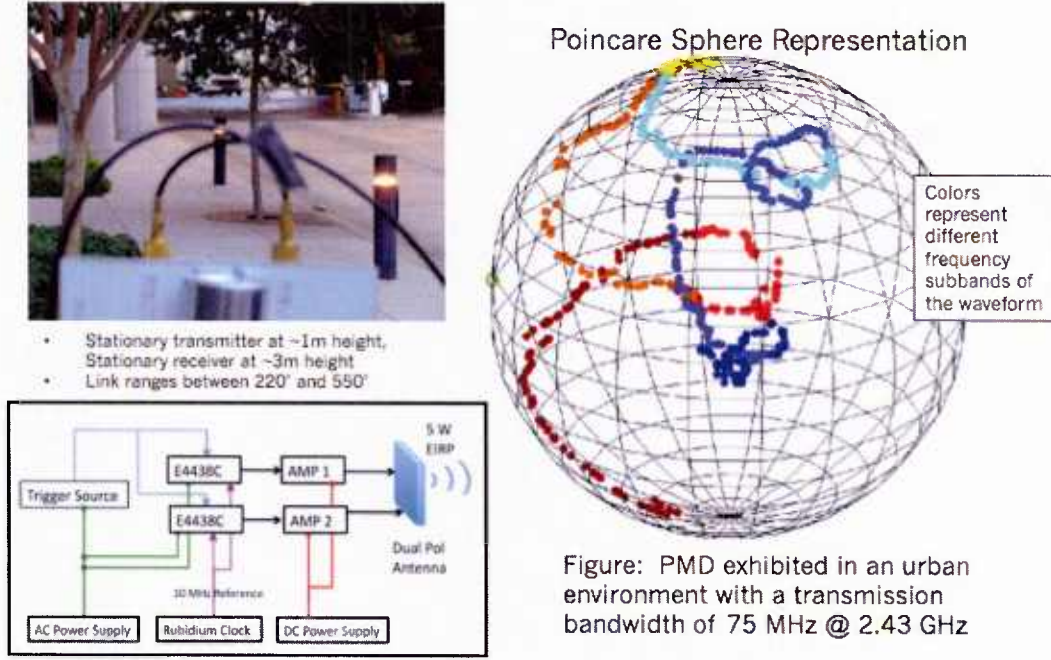
Figure 43. PMD response from a 75 MHz transmit signal bandwidth in an outdoor channel

A second channel impairment that is incurred in multipath channels is polarization dependent loss (PDL), which defines the polarization-sensitive power coupling behavior of the channel. PDL for the kth subcarrier is defined as

$$PDL_k = 10 \log_{10} \frac{\lambda_{k,max}}{\lambda_{k,min}}$$ (100)

where $\lambda_{k,max}$ and $\lambda_{k,min}$ are the maximum and minimum eigenvalues associated with the matrix $\mathbf{H}_k \mathbf{H}_k^H$ for subcarrier k [36], respectively. The magnitude of the PDL associated with each subcarrier is dictated by eigenvalues of the subcarrier channel matrix and the polarization state of the transmitted signal relative to the associated polarization eigenmodes. For each subcarrier, there exists a specific polarization

state that optimizes power transfer through the given multipath channel, a behavior that may be predicted through PDL characterizations. An example of the power coupling dependency on transmit polarization for a particular subcarrier is illustrated in Figure 44, where the dark spot on the Poincare sphere corresponds to the transmit polarization yielding maximum power transfer through the channel. In general, the transmit polarization state optimizing power transfer will be a function of frequency. It follows that gains will accrue through use of adaptive polarization, since the transmit polarization can be adjusted to achieve the state leading to the maximum power transfer. We also note that they can also be adjusted adaptively for other reasons, e.g., to enhance clutter mitigation.
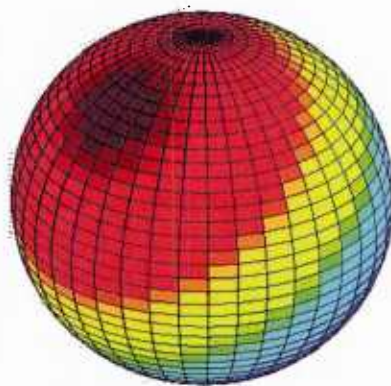
Figure 44. Polarization dependent loss

This figure shows that for a given subcarrier, the power transferred to the receiver is dependent upon the polarization of the transmitted signal. By selecting the polarization state that maximizes the power transfer for each subcarrier, the signal power transferred through the channel may be optimized.

3.   *Input-to-Output Polarization Response Model*

The polarimetric modeling that we employed involves the characterization of the input-to-output polarization response of the seaborne clutter as a function of the frequency subbands of the transmit signal, which may be accomplished through PMD and PDL characterizations. The response depends on the transmit polarization as illustrated in Figure 45, which shows measured PMD characterizations derived from measurements between stationary vehicles conducted in an urban setting. Each Poincare sphere in the figure is associated with a different transmit polarization: right hand circular (RHC), left hand circular (LHC) and vertical polarizations. The polarization states of the corresponding received signal are plotted on the Poincare sphere as a function of frequency. Due to the wide variation in the polarization state as a function of frequency evidenced in these plots, single-polarized receive antennas will experience substantial power coupling loss as a function of frequency. This can be averted through the use of adaptive polarization

transmission techniques to optimize power coupling from transmit to receiver, and through the use of dual-polarized antennas at the receiver to capture energy using two orthogonally-polarized modes. However, receivers that only process the full-band signal without subbanding can experience significant loss of degree of polarization relative to subbanded systems, so that the measured polarization state is not well-defined. Therefore use of subbanded architectures is preferred to accommodate PMD behavior and achieve enhanced system performance.

RHC   LHC   Vertical
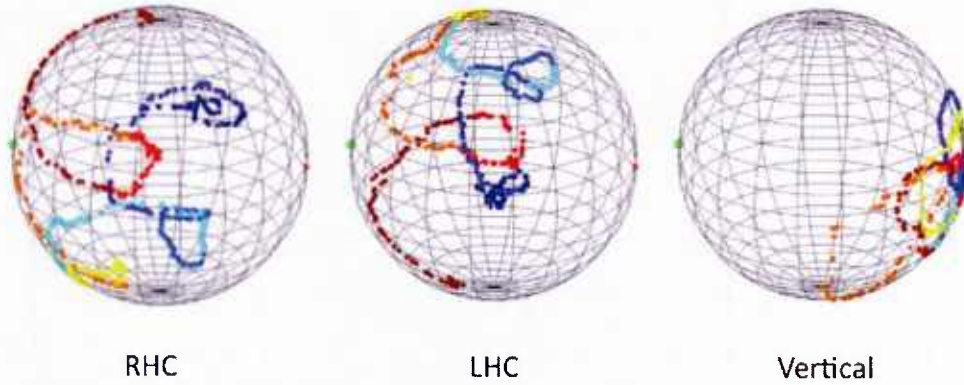
Figure 45. Examples of measured PMD trajectories for different transmission polarizations using a 70 MHz bandwidth signal

4. Time-Dispersive Response Model
a) Modified Sinclair Matrix

To represent clutter and target responses in a manner that enables PMD characterizations, we turn to the Sinclair matrix [6], which is often employed to represent polarimetric backscatter in remote sensing applications. However, we propose a modified representation to accommodate PMD-based modeling. Conventional Sinclair models generally treat the target response within a resolution cell as a flat-faded response (e.g., zero delay between reflected components). A backscatter formulation using a Sinclair matrix, **S**, is of the form:

$$q = \begin{bmatrix} q^v \\ q^w \end{bmatrix} = \frac{1}{4\pi r} \begin{bmatrix} s^{vx} & s^{vy} \\ s^{wx} & s^{wy} \end{bmatrix} \begin{bmatrix} u^x \\ u^y \end{bmatrix} e^{-jkr} = \frac{1}{4\pi r} \mathbf{S} \mathbf{u} \, e^{-jkr} \tag{101}$$

Many examples of the use of the Sinclair matrix are presented in literature. Conventional formulations do not attempt to explicitly reflect frequency dependencies in the channel backscatter. We propose to modify the conventional representation by integrating a distributed clutter/target representation comprised

of multiple time-dispersed reflections. The revised scattering matrix formulation is given by:

$$
\begin{bmatrix} q^v \\ q^w \end{bmatrix} = \frac{1}{4\pi r} \begin{bmatrix} \sum_{n=1}^{N} s_n^{vx} \delta(t - \tau_n^x) e^{j\omega\tau_n^x} & \sum_{m=1}^{M} s_m^{vy} \delta(t - \tau_m^y) e^{j\omega\tau_m^y} \\ \sum_{n=1}^{N} s_n^{wx} \delta(t - \tau_n^x) e^{j\omega\tau_n^x} & \sum_{m=1}^{M} s_m^{wy} \delta(t - \tau_m^y) e^{j\omega\tau_m^y} \end{bmatrix} \begin{bmatrix} u^x \\ u^y \end{bmatrix}
$$

$$
= \frac{1}{4\pi r} \begin{bmatrix} \sum_{n=1}^{N} s_n^{vx} u^x (t - \tau_n^x) e^{j\omega\tau_n^x} + \sum_{m=1}^{M} s_m^{vy} u^y (t - \tau_m^y) e^{j\omega\tau_m^y} \\ \sum_{n=1}^{N} s_n^{wx} u^x (t - \tau_n^x) e^{j\omega\tau_n^x} + \sum_{m=1}^{M} s_m^{wy} u^y (t - \tau_m^y) e^{j\omega\tau_m^y} \end{bmatrix} \quad \textbf{(102)}
$$

The resulting delay spread yields a frequency-selective target response that more adequately reflects scattering phenomenology associated with distributed sea clutter and a distributed target. It has been shown [11] that PMD occurs only if the reflections are time-dispersive and polarization diverse. To see this, the polarization basis can be selected to enable the following representation:

$$
\begin{bmatrix} v^{x'}(t, \omega) \\ v^{y'}(t, \omega) \end{bmatrix} = \begin{bmatrix} h_1^{x'} \sum_{g=1}^{N+M} \alpha_g u^{x'}(t - \tau_g) e^{j\omega\tau_g} \\ h_1^{y'} \sum_{g=1}^{N+M} (\alpha_g + \Delta_g) u^{x'}(t - \tau_g) e^{j\omega\tau_g} \end{bmatrix} \quad \textbf{(103)}
$$

Without delay spread (where $\tau_g = \tau$ for all g), one obtains

$$
\begin{bmatrix} v^{x'}(t, \omega) \\ v^{y'}(t, \omega) \end{bmatrix} = \begin{bmatrix} h_1^{x'} u^{x'}(t - \tau) e^{j\omega\tau} \sum_{g=1}^{N+M} \alpha_g \\ h_1^{y'} u^{x'}(t - \tau) e^{j\omega\tau} \sum_{g=1}^{N+M} (\alpha_g + \Delta_g) \end{bmatrix} \quad \textbf{(104)}
$$

and the output polarization is seen to be independent of frequency. It is also observed that without polarization-diverse multipath ($\Delta_g = 0$), the output polarization is independent of frequency:

$$\begin{bmatrix} v^{x'}(t,\omega) \\ v^{y'}(t,\omega) \end{bmatrix} = \begin{bmatrix} h_1^{x'} \sum_{g=1}^{N+M} \alpha_g u^{x'}(t - \tau_g) e^{j\omega\tau_g} \\ h_1^{y'} \sum_{g=1}^{N+M} \alpha_g u^{x'}(t - \tau_g) e^{j\omega\tau_g} \end{bmatrix} \tag{105}$$

In fact, PMD occurs only if the delay spread is nonzero and if the multipath is polarization-diverse.

b)   *PMD Modeling Theory*

Key attributes of polarimetric propagation channels that can be leveraged by a polarimetric receiver system include the polarization dispersion behavior of the channel, the polarization dependent loss, and the polarization mode fading statistics. In this subsection, we briefly describe the polarimetric framework relevant to the study. The model described below, which was developed for communications applications, has been modified for both forward scatter and backscatter radar formulations to accommodate Doppler spread in the channel matrix components that are introduced through path-dependent Doppler shifts. We assume the clutter response and the target response can be modeled as a frequency-selective L-tap multipath fading channel with contiguous subchannels in frequency that are time-invariant over the coherence time interval [35]. The pseudo-stationary response may be defined by the channel matrix [11]

$$\mathbf{h}(t,\omega)$$
$$= \begin{bmatrix} \sum_{n=1}^{N} h_n^{xv} \delta(t - \tau_n^x) e^{j\omega\tau_n^x} e^{j2\pi f_n^d t} & \sum_{n=1}^{N} h_n^{yv} \delta(t - \tau_n^y) e^{j\omega\tau_n^y} e^{j2\pi f_n^d t} \\ \sum_{n=1}^{N} h_n^{xw} \delta(t - \tau_n^x) e^{j\omega\tau_n^x} e^{j2\pi f_n^d t} & \sum_{n=1}^{N} h_n^{yw} \delta(t - \tau_n^y) e^{j\omega\tau_n^y} e^{j2\pi f_n^d t} \end{bmatrix} \tag{106}$$

where N is the number of multipaths, $\tau_r^p < T_s L$ is the propagation delay associated with the rth propagation path for the p-polarized components, T_s is the tap delay, and h_r^{ij} is a complex channel gain between the input signal vector component i and the output signal vector component j for the rth propagation path. Assuming the transmission of a signal vector, $\boldsymbol{u}(t)$, where the vector elements correspond to orthogonal polarization components, the time-domain signal at the output of the channel is given by

$$\begin{bmatrix} v^v(t,\omega) \\ v^w(t,\omega) \end{bmatrix} = \int_{-\infty}^{\infty} \mathbf{h}(\tau,\omega)\boldsymbol{u}\,(t-\tau,\omega)d\tau$$

$$= \begin{bmatrix} \sum_{n=1}^{N} h_n^{xv} u^x(t-\tau_n^x)e^{j\omega\tau_n^x}e^{j2\pi f_n^d t} + \sum_{m=1}^{M} h_m^{yv} u^y\left(t-\tau_m^y\right)e^{j\omega\tau_m^y}e^{j2\pi f_n^d t} \\ \sum_{n=1}^{N} h_n^{xw} u^x(t-\tau_n^x)e^{j\omega\tau_n^x}e^{j2\pi f_n^d t} + \sum_{m=1}^{M} h_m^{yw} u^y\left(t-\tau_m^y\right)e^{j\omega\tau_m^y}e^{j2\pi f_n^d t} \end{bmatrix} \quad (107)$$

which has the form of the modified Sinclair model that was introduced earlier. We reiterate that PMD exists only if polarization-distinct multipath components exhibit differential delay. Under these conditions, which are usually present in multipath channels, the channel is said to exhibit polarization mode dispersion. Because the received signal will have frequency-dependent polarization, the power that couples into any one receive antenna will generally be frequency dependent.

Over the coherence time interval, which will be related to the Doppler spread, the channel transfer function associated with subcarrier k may be represented by the pseudo-stationary matrix $\mathbf{H}_k$, where

$$\mathbf{H}_k(t) = \mathcal{F}\big(\mathbf{h}(t,\omega)\big)\big|_k = \begin{bmatrix} H_k^{xv}(t) & H_k^{yv}(t) \\ H_k^{xw}(t) & H_k^{yw}(t) \end{bmatrix}, k = 0,1,\dots,K \quad (108)$$

and $\mathcal{F}(\mathbf{h}(t,\omega))|_k$ indicates the kth subcarrier of the K-point FFT of each element of $\mathbf{h}(t,\omega)$. The superscript pairs in the matrix entries correspond to the transmit and receive polarization basis components, respectively. We assume that K is selected so that the channel exhibits flat fading in each sub-carrier of bandwidth $(KT)^{-1}$ Hz. Using a frequency-domain representation, the polarization state of subcarrier k of the received signal may be represented by the vector

$$V_k(\text{t}) = \begin{bmatrix} V_k^v(t) \\ V_k^w(t) \end{bmatrix} = \alpha_k \mathbf{H}_k(t) \mathbf{U}_k(\text{t}) = \alpha_k \mathbf{H}_k(t) \begin{bmatrix} U_k^x(t) \\ U_k^y(t) \end{bmatrix} \tag{109}$$

where α_k is a normalization constant to synthesize a unit magnitude Jones vector, $\mathbf{U}_k(\text{t}) = \mathcal{F}(\mathbf{u}(t))|_k$, $U_k^x(\text{t}) = \mathcal{F}(u^x(t))|_k$ and $U_k^y(\text{t}) = \mathcal{F}(u^y(t))|_k$. The corresponding Stokes vector, $\mathbf{S}_v(t,k)$ may be obtained from $V_k(\text{t})$ using

$$\mathbf{S}_v(t,k) = \begin{bmatrix} J_{11}(t,k) + J_{22}(t,k) \\ J_{11}(t,k) - J_{22}(t,k) \\ J_{12}(t,k)J_{21}^*(t,k) + J_{21}(t,k)J_{12}^*(t,k) \\ j\big(J_{12}(t,k)J_{21}^*(t,k) - J_{21}(t,k)J_{12}^*(t,k)\big) \end{bmatrix} \tag{110}$$

where

$$\mathbf{J}(t,k) = \begin{bmatrix} J_{11}(t,k) & J_{12}(t,k) \\ J_{21}(t,k) & J_{22}(t,k) \end{bmatrix} = \mathrm{E}\left[V_k(t)V_k^H(t)\right] \tag{111}$$

The set consisting of the $\mathbf{S}_v(t,k)$ for $k = 0,1, ..., K\text{-}1$ is the PMD response that forms the basis of the PMD modeling approach.

To develop a PMD-centric formulation, we treat the sea as a collection of facets, each characterized by a complex reflection coefficient. The relative magnitude and phase of the coefficient depend on several factors: the surface normal, the dielectric properties, the propagation distance, the scattering geometry parameters, the illumination pattern, and associated statistical behaviors and correlations. The coefficient for each multipath is weighted according to the effective area of the facet, the antenna pattern gains, and impacts of the waveform to arrive at the responses for the HH, HV, VH and VV components. The PMD is then characterized for each signal subband of the transmit signal.

5.   Clutter PMD Response Model

These relationships are applied in an example, with a purpose to illustrate the use of the reflection coefficients to generate an estimate of the polarization mode

dispersion response. The fundamental theory associated with PMD is described in [53] [11] and references therein. We utilize this theory to characterize the polarization-frequency response of the channel.

The path delays associated with each path from the transmitter to the receiver are computed and the relative amplitudes of the signals are estimated. For this latter computation, omnidirectional antenna patterns at the receiver and the transmitter are assumed. Also, relative path losses are neglected since the losses will all be comparable when the ranges are similar. Finally, effective areas associated with each scatterer are assigned, where the areas would normally be tied to the ground surface features, but in our case we simply assign random relative areas (i.e., relative reflection powers) to each of the scatterers.

Using the aforementioned models, we derive the transfer functions from a vertically-polarized transmitter to the receiver, including the VV and the VH components. These impulse responses have the form:

$$h_{VV}(t) = \sum_{n=1}^{N} \Gamma_{VV}^{n} \delta(t - \tau_n) e^{j2\pi f_n t} \tag{112}$$

and

$$h_{HV}(t) = \sum_{n=1}^{N} \Gamma_{HV}^{n} \delta(t - \tau_n) e^{j2\pi f_n t} \tag{113}$$

and the corresponding transfer functions are given by:

$$H_{VV}(w) = \sum_{n=1}^{N} \Gamma_{VV}^{n} e^{-i2\pi(f+f_n)\tau_n} \tag{114}$$

and

$$H_{HV}(\text{w}) = \sum_{n=1}^{N} \Gamma_{HV}^{n} e^{-i2\pi(f+f_n)\tau_n} \tag{115}$$

where the carrier and absolute phase have been ignored. The transfer functions are then used to estimate the polarization response as a function of frequency. The ratio

$$H(\text{w}) = \frac{H_{VV}(\text{w})}{H_{HV}(\text{w})} = \frac{\sum_{n=1}^{N} \Gamma_{VV}^{n} e^{-i2\pi(f+f_n)\tau_n}}{\sum_{n=1}^{N} \Gamma_{HV}^{n} e^{-i2\pi(f+f_n)\tau_n}} \tag{116}$$

provides the relative amplitudes and phases as a function of frequency, and these are in turn used to find the PMD response. Similarly for Horizontal polarization, the channel impulse responses, the transfer functions, and the polarization response are given by:

$$h_{HH}(\text{t}) = \sum_{n=1}^{N} \Gamma_{HH}^{n} \delta(t - \tau_n) e^{j2\pi f_n t} \tag{117}$$

$$h_{VH}(\text{t}) = \sum_{n=1}^{N} \Gamma_{VH}^{n} \delta(t - \tau_n) e^{j2\pi f_n t} \tag{118}$$

$$H_{HH}(\text{w}) = \sum_{n=1}^{N} \Gamma_{HH}^{n} e^{-i2\pi(f+f_n)\tau_n} \tag{119}$$

90

$$H_{VH}(\text{w}) = \sum_{n=1}^{N} \Gamma_{VH}^n e^{-i2\pi(f+f_n)\tau_n} \qquad \qquad (120)$$

and

$$H(\text{w}) = \frac{H_{HH}(\text{w})}{H_{VH}(\text{w})} = \frac{\sum_{n=1}^{N} \Gamma_{HH}^n e^{-i2\pi(f+f_n)\tau_n}}{\sum_{n=1}^{N} \Gamma_{VH}^n e^{-i2\pi(f+f_n)\tau_n}} \qquad \qquad (121)$$

Resultant PMD responses are plotted on Poincare spheres in Figure 46 for different transmit polarizations.
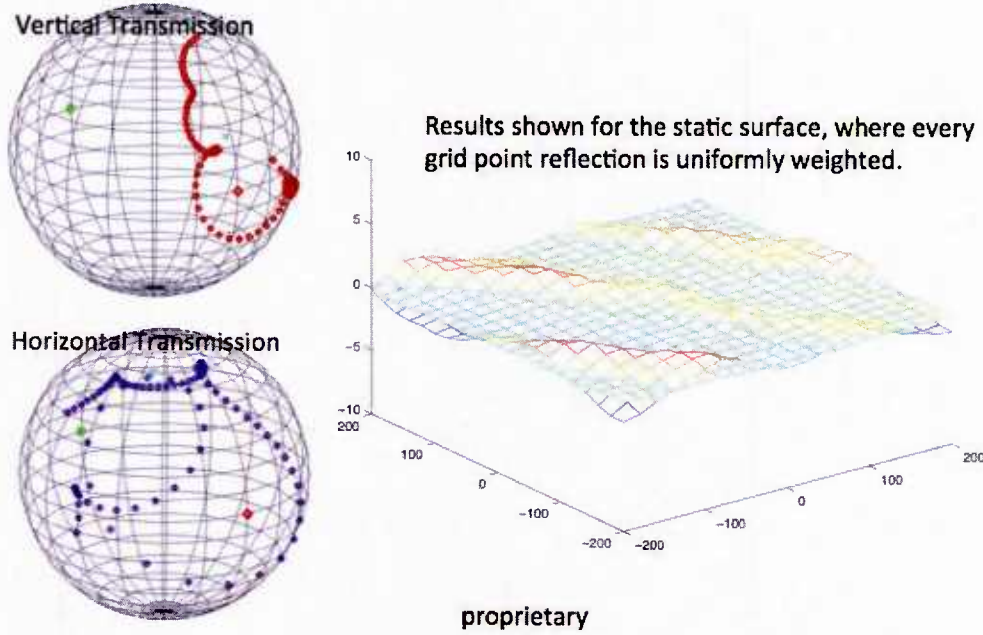
Figure 46. PMD Responses for V and H Transmissions for a given Sea State

6.   Target/Clutter Response Model

A primary goal in this research is to investigate the hypothesis that PMD characterization can be exploited for improved target detection and identification.

The approach assumes that the target response can be projected onto a signal dimension space that is roughly orthogonal from the response of the sea clutter. The results will depend on the statistics of the scatterers and also on the fact that the target scatterers remain approximately fixed relative to each other.

Figure 47 illustrates an example of a target that induces a substantive PMD-response. The target consists of a flat plate conductor and a corner reflector that are spatially separated by a distance d. The incident RF signal is right-hand circularly polarized. The return from the reflected plate will yield a left-hand circularly polarized response whereas the corner reflector will yield a right-hand circularly polarized response. Since the aggregate signal return consists of time-dispersive and polarization-diverse responses, the received composite echo will exhibit PMD.
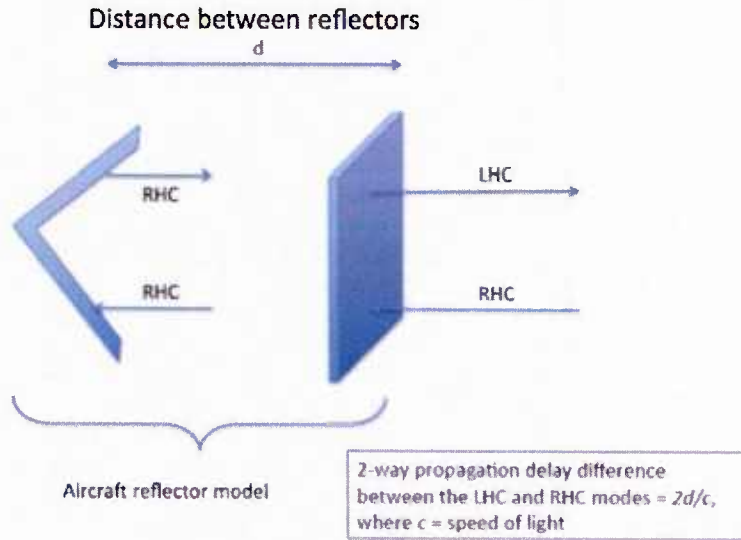
Figure 47. Illustration of an extended target leading to a target echo exhibiting polarization mode dispersion

The target detection problem may be recast by separating the response from the target and the response from the clutter. Assuming a transmit signal s(t) having the form

$$s(t) = A(t)e^{j2\pi ft} \qquad (122)$$

the orthogonally polarized components of the return may then be expressed as:

92

$$
\begin{array}{cc}
\textit{Target} & \textit{Clutter}
\end{array}
$$

$$
\boldsymbol{r}(t)
$$

$$
= \begin{bmatrix} \displaystyle\sum_{n=1}^{N} \alpha_n^v s(t - \tau_n) e^{j2\pi f_d t} + \displaystyle\sum_{m=N+1}^{N+M} \alpha_m^v s\big(t - \tau_m(t)\big) e^{j2\pi(\Delta f_m + f_d)t} \\[2em] \displaystyle\sum_{n=1}^{N} \alpha_n^h s(t - \tau_n) e^{j2\pi f_d t} + \displaystyle\sum_{m=N+1}^{N+M} \alpha_m^h s\big(t - \tau_m(t)\big) e^{j2\pi(\Delta f_m + f_d)t} \end{bmatrix} \quad \textbf{(123)}
$$

Here, the first term represents the target scatterers, which remain fixed relative to each other over the dwell. The second term represents returns from the sea clutter scattering centers, which shift in time relative to the target scatterers. We have assumed a clutter-limited representation and therefore neglect receiver noise.

VII. EXPERIMENTAL AND SIMULATED CLUTTER CHARACTERIZATIONS

In order to better understand the polarimetric characteristics of the reflectivity from sea clutter, a series of measurements were undertaken at two campus locations. The wave tunnel measurements included multiple antenna orientations, multiple wave types, and both fresh water and salt water. The St Joseph Lake measurements included both monostatic and bistatic antenna orientations, multiple frequencies, and multiple waveforms.

The following sections present selected results from these measurements.

A. *Wave tunnel measurements*

The wave tunnel measurements were undertaken on two occasions: first with the tank filled with fresh water and later with the tank filled with salt water. The measurement equipment also differed on the two occasions both in the signal generation and the signal capture.

Three antenna configurations were used in the wave tunnel measurements. Figure 48 shows a picture of the antenna mounting relative to the wave tunnel for all three configurations. For the case "monostatic from above (ma)", both transmit and receive antennas were mounted directly above the wave tunnel with a near-normal incident angle. For the case "monostatic grazing (mg)", the both antennas were mounted above the wave tunnel at one end and oriented with a near-grazing incident angle. For the case "bistatic grazing (bg)", the transmit and receive antennas were mounted at opposite ends of the wave tunnel (facing each other) and oriented with a near-grazing incident angle.
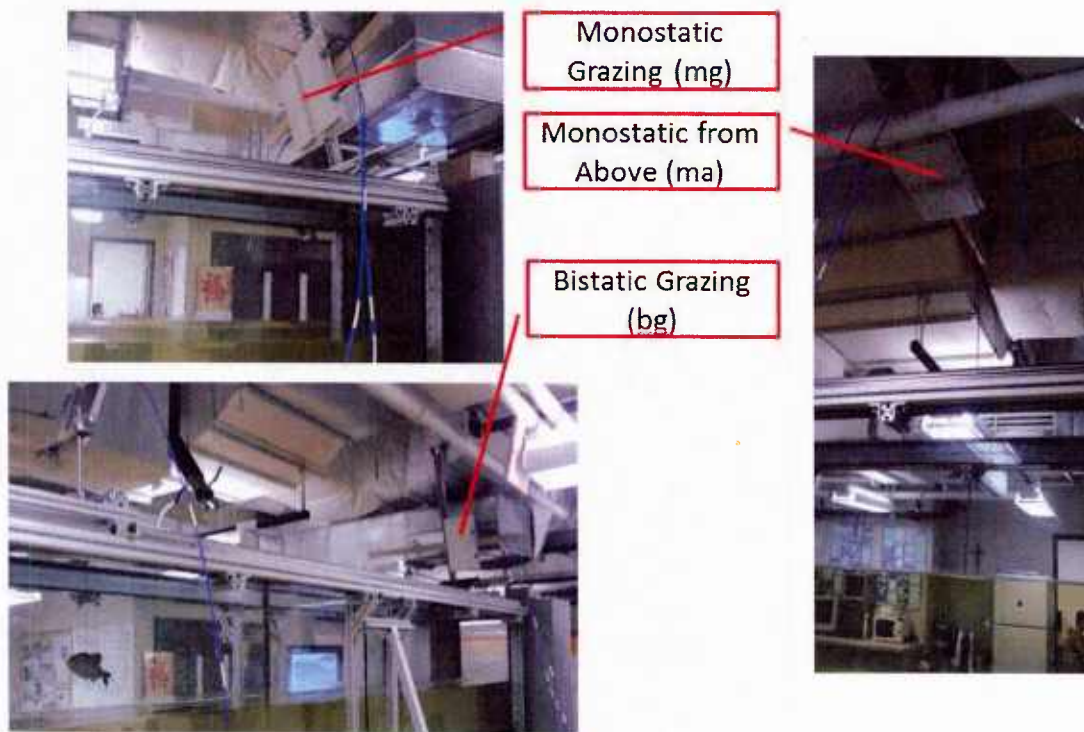
Figure 48. Wave tunnel antenna configurations

Measurements were performed for several wave types. Figure 49 and Figure 50 show pictures of a standing wave (SW) and two waves produced by introducing an obstruction into the water flow: obstruction large wave (OL) and obstruction small wave (OS). Finally, a moving wave (MW) (not shown) was created by shutting off the water pump to create a backward traveling wave.
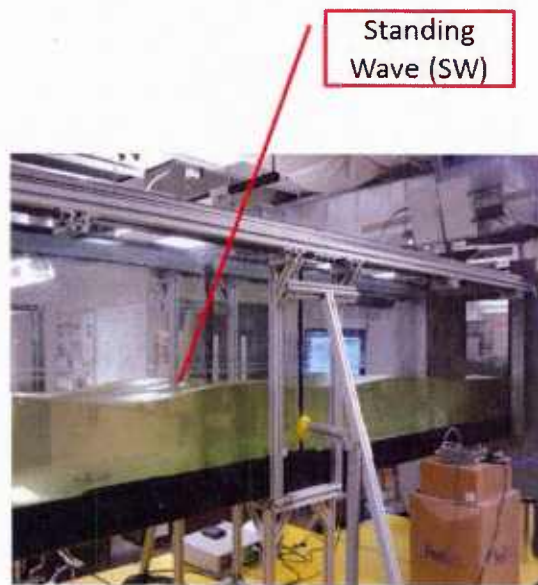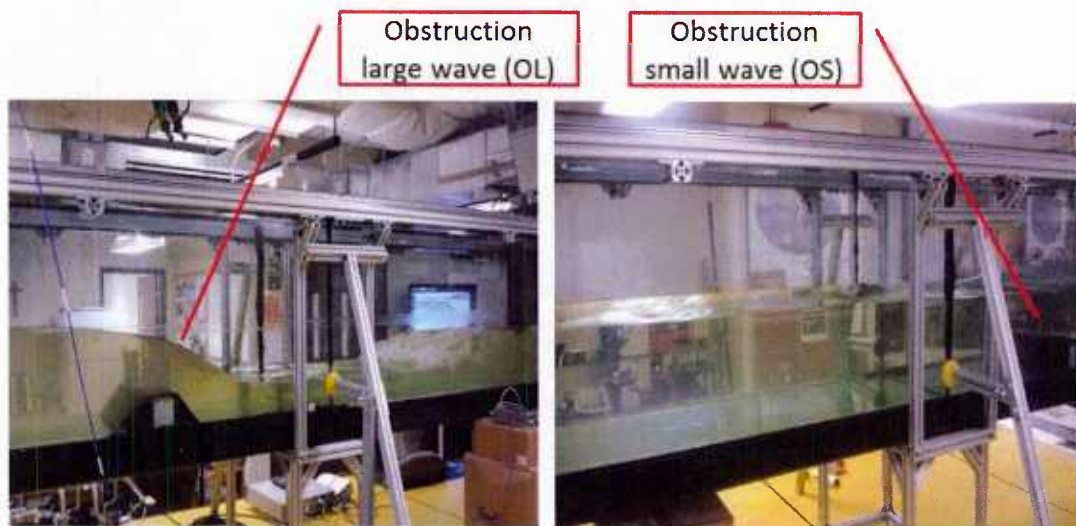
Figure 49. Standing wave

Figure 50. Obstruction waves

Table 5 shows a summary of the measurement conditions for the wave tunnel measurements.

Table 5. Wave tunnel measurement details

Fresh water measurements	Salt water measurements

• 2013-06-10
• Fresh water
• Signal generator
  – Cisco AP
  – WiFi channel 1 (2412 MHz, ±10MHz)
• Digitizer
  – GaGe 144002U
  – Captures: 2 ms, 10 ms, 80 ms
  – Sample rate: 200 MSa/s
• Transmit Polarizations
  – H, V
	• 2013-06-12
	• Salt water (~2.5% salinity)
	• Signal generator
	  – Agilent E4438C (ESG)
	  – 20 MHz Pi/4 DQPSK at 2412 MHz
	  – 20 dBm
	• Digitizer
	  – Agilent digitizing oscilloscope
	  – Captures: 2.5 sec
	  – Sample rate: 200 Msa/s
	  – Rx amplifiers added for some antenna configurations
	• Transmit Polarizations
	  – V (Slant 45 for Monostatic Above)

Figure 51 shows four plots of PMD curves for all wave types for the case of Monostatic Above. The sampling rate of these curves (100 ms) is coarse so the transition from one curve to the next is not clear. However, these plots provide a representative sample of the curves throughout the 2.5 sec data capture. Greater variability is seen in both the Moving Wave and Obstruction Large Waves where turbulent flow is visibly evident.
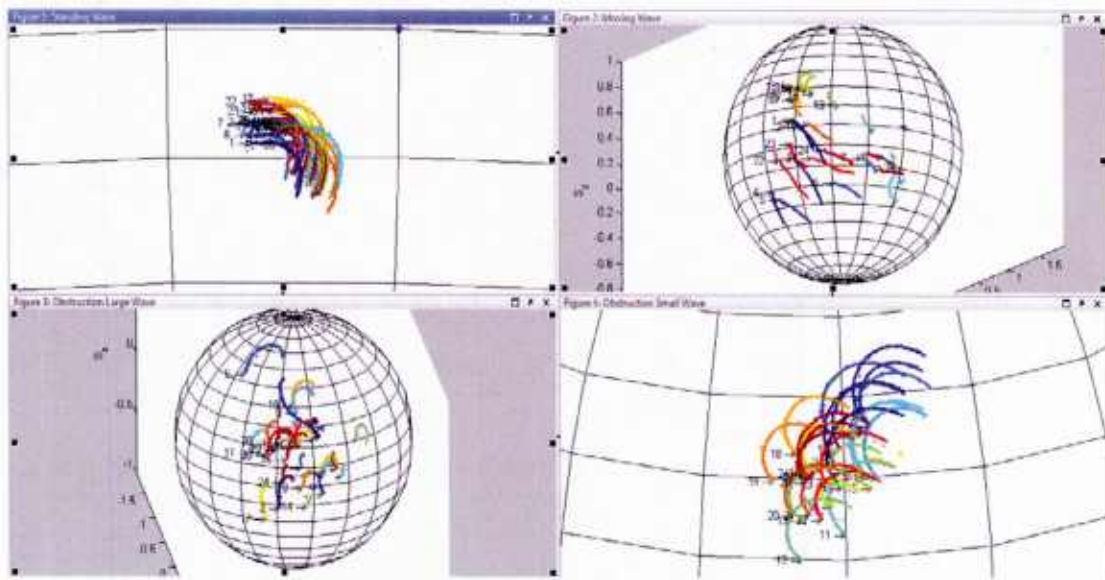
Figure 51. Sample PMD curves for monostatic above (all wave types)

Figure 52 shows PMD curves for just one wave type (Moving Wave) over four time segments. This is the same data as shown in the previous figure (upper right plot), but with a much smaller time interval between curves (8 ns versus 100 ns in the previous figure). The smaller time interval allows us to follow the changes in the PMD curves over time. The upper left plot shows the first 25 PMD curves (starting with dark blue and finishing with dark red). The upper right plot shows the next 25 PMD curves (again starting with dark blue such that this first dark blue curve follows the dark red curve from the upper left plot). This progression continues with the lower left and right plots such that the full figure shows a continuum of PMD curves representing a duration of 800 ms.
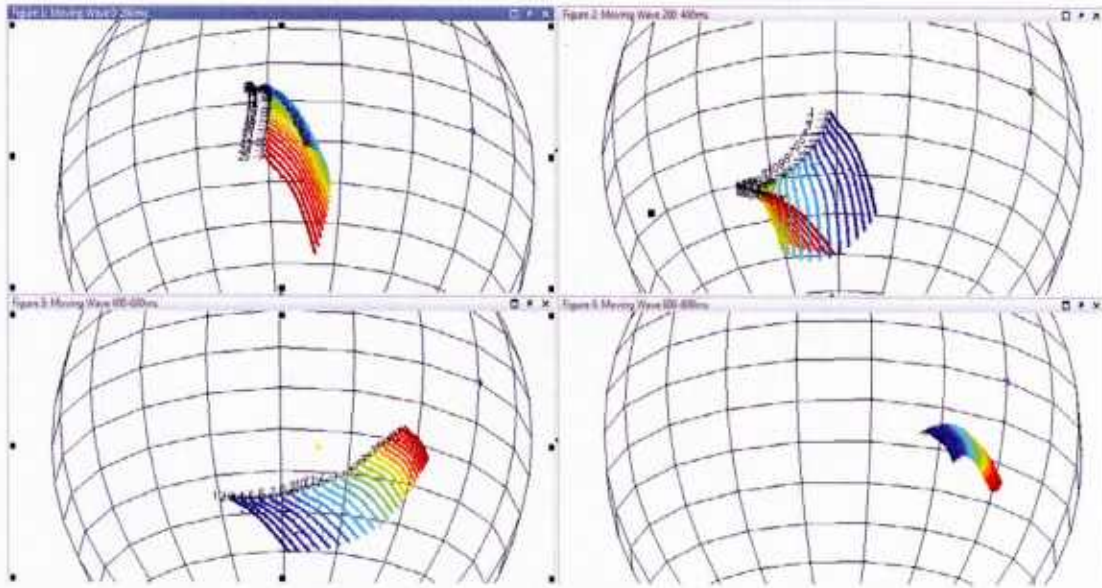
Figure 52. PMD curves, monostatic above, moving wave

Figure 52 shows the PMD centroid (mean value across bandwidth) for all wave types. Each dot represents the average of a single PMD curve at a given time step. In these curves the time span is the full duration of the 2.5 second measurement. Note that for the Obstruction Large Wave case (where turbulent flow is visibly evident in the previous wave tunnel photographs), the curve appears largely random. The greatest movement of PMD centroid is seen in the Moving Wave case.
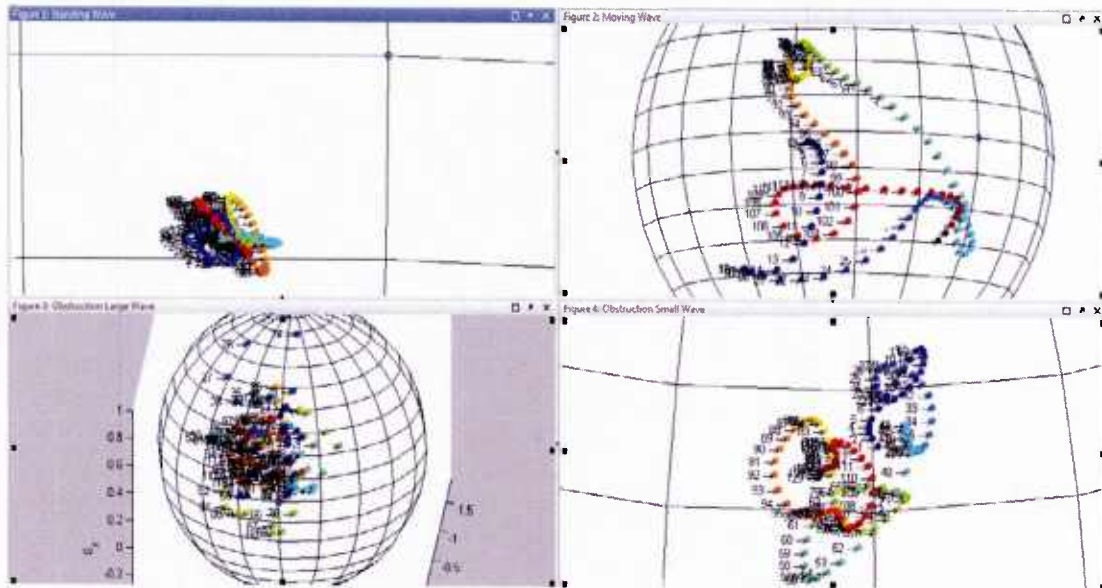
Figure 53. PMD centroid, monostatic above, all wave types

Figure 54 through Figure 56 show similar results to those presented above, but for the case of 'monostatic grazing' antenna configuration.
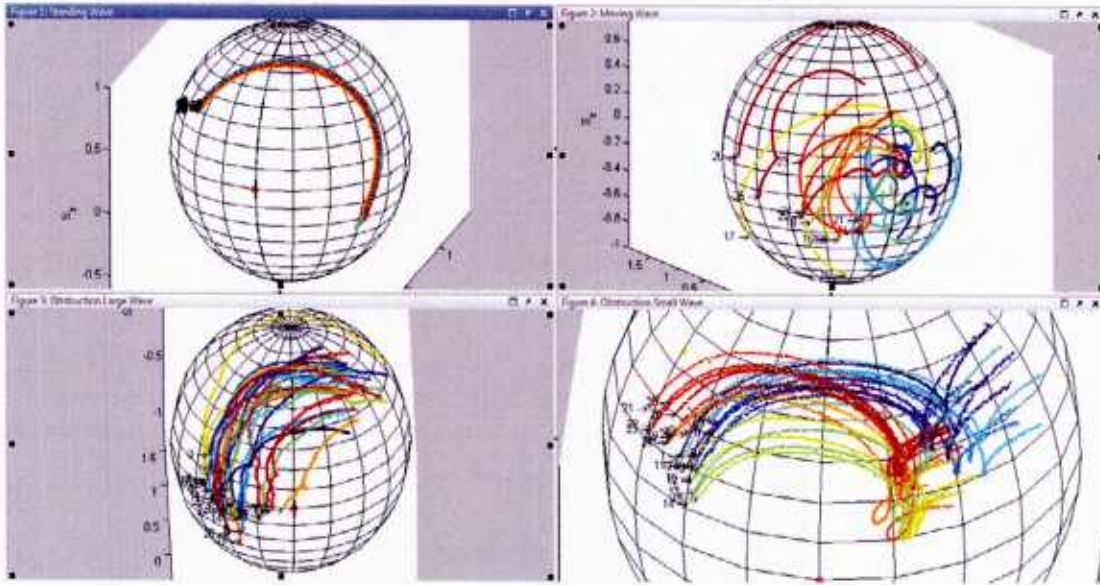
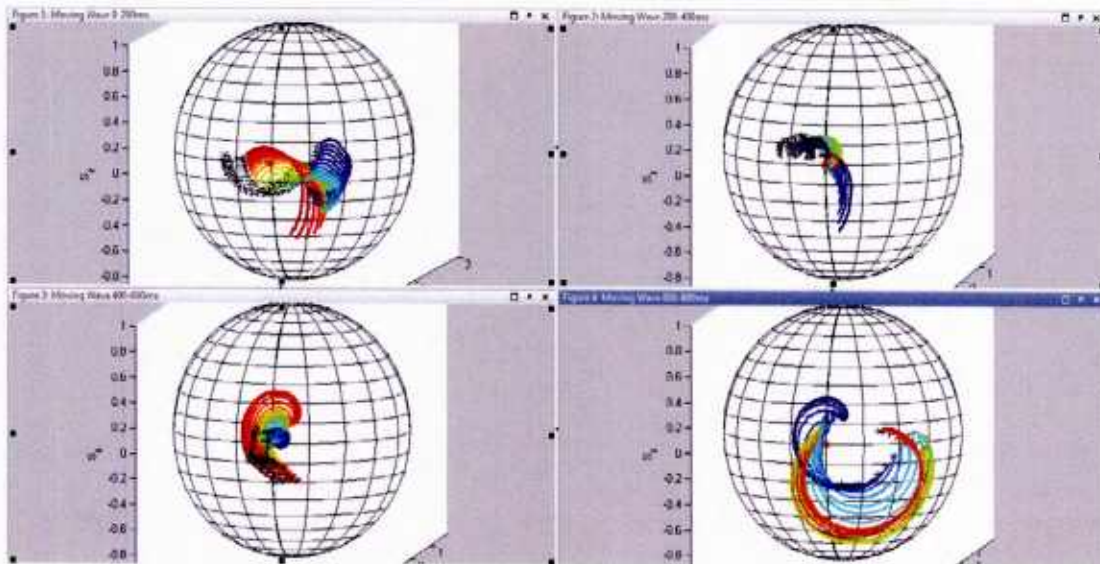*Figure 54. PMD curves for monostatic grazing (all wave types)*

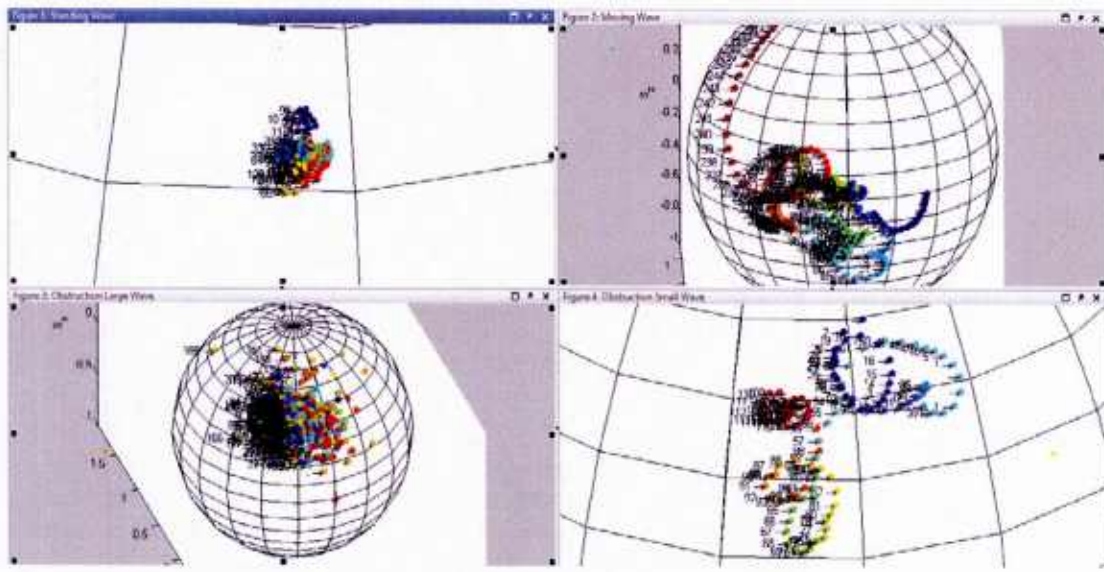*Figure 55. PMD curves, monostatic grazing, moving wave*

Figure 56. PMD centroid, monostatic grazing, all wave types

Figure 57 through Figure 59 show similar results to those presented above, but for the case of 'bistatic grazing' antenna configuration.
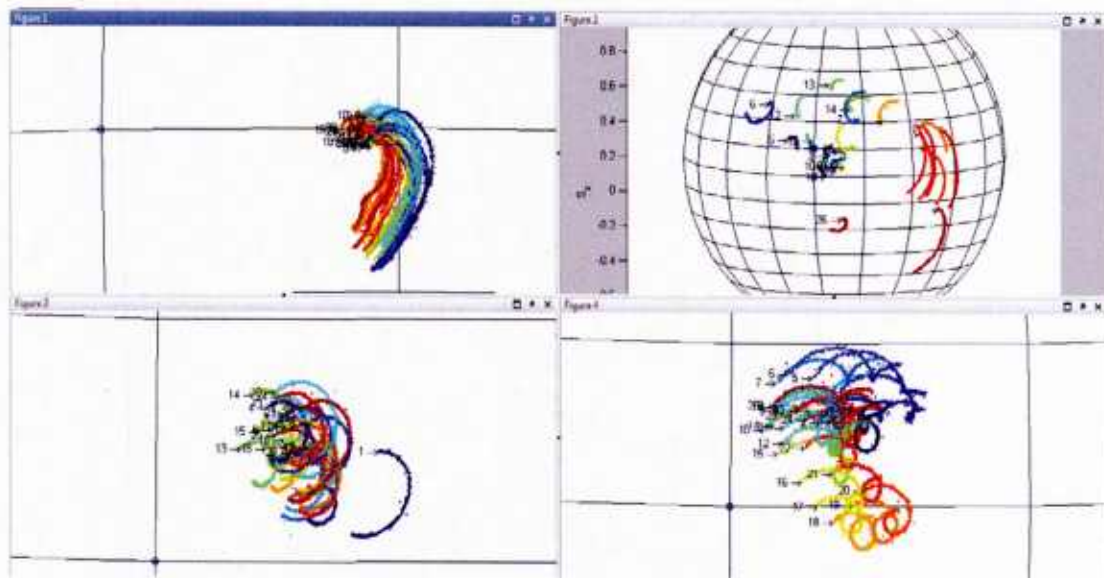

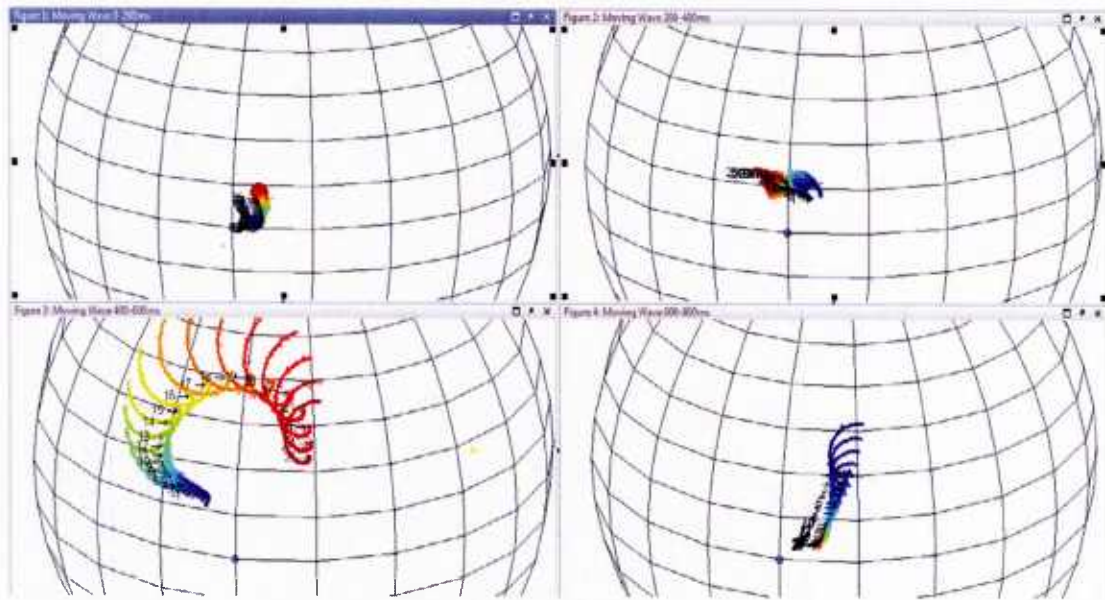*Figure 57. PMD curves for bistatic grazing (all wave types)*

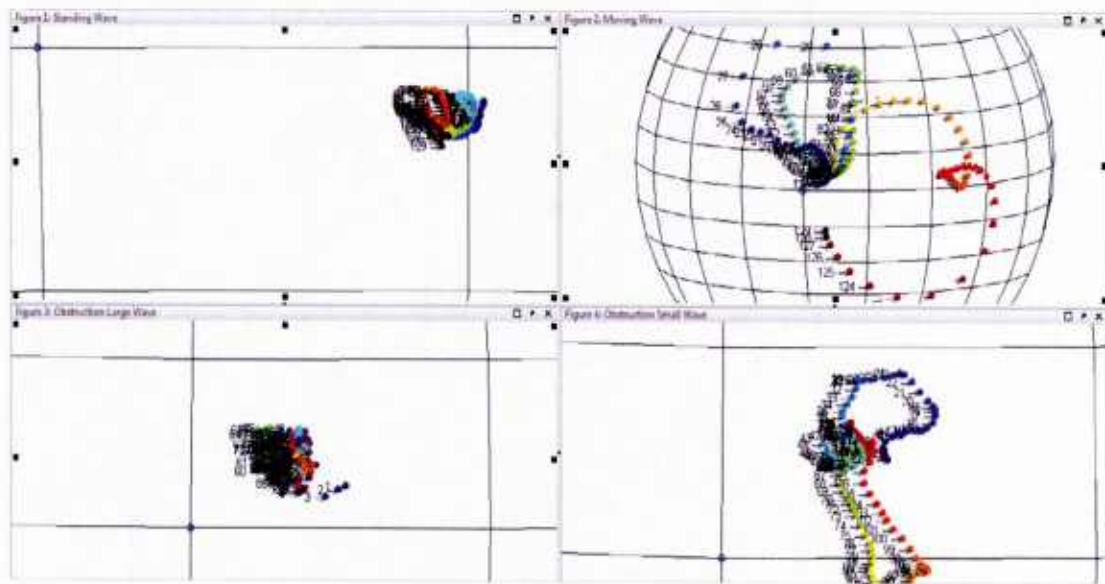*Figure 58. PMD curves, bistatic grazing, moving wave*

Figure 59. PMD centroid, bistatic grazing, all wave types

In the results presented above, greater variability in the PMD curves were observed for wave types Moving Wave and Obstruction Large Wave for which the flow was visibly turbulent. Although not shown in this report, the results for salt water and fresh water did not differ in any obvious way. However, direct comparisons were impeded by different measurement setups between the two cases.

B.   Lake measurements

Polarization measurements were conducted at St Joseph Lake on Notre Dame's campus using dual polarized antennas for both transmit and receive.

Measurements were taken using three antenna configurations (see Figure 60, Figure 61, and Figure 62): monostatic pointed at the center of the lake, monostatic pointed at some turbulence caused by power plant discharge, and bistatic pointing across the lake from the dock to a clear region approximately 250 meters away. For each configuration, measurements were taken for three carrier frequencies: 2412 MHz, 915 MHz, and 470 MHz.

Figure 60. Map of St Joseph Lake

- Below: Monostatic toward center of lake
- Top right: Monostatic toward power plant discharge
- Bottom right: close-up of turbulence at power plant discharge

Figure 61. Monostatic antenna setup

- Top left: Looking from TX (at dock) to RX
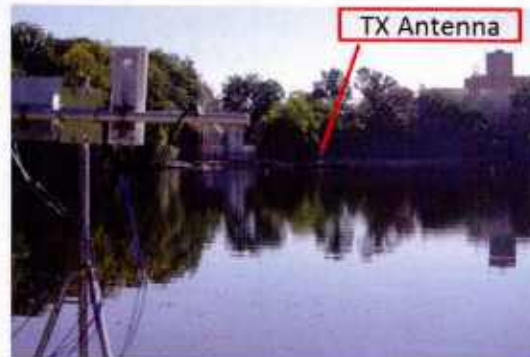- Bottom right: looking from RX to TX (at dock)

Figure 62. Bistatic antenna setup

104

Two different transmit waveforms were tested. The first was a multitone waveform consisting of 128 equally spaced sinusoids over a 20 MHz bandwidth producing a tone spacing of 156 kHz (see Figure 63). The second was a pulsed CW waveform (pulse width 0.1 μs, pulse repetition interval 2 μs). This pulsed waveform produces a tone spacing of 500 kHz.
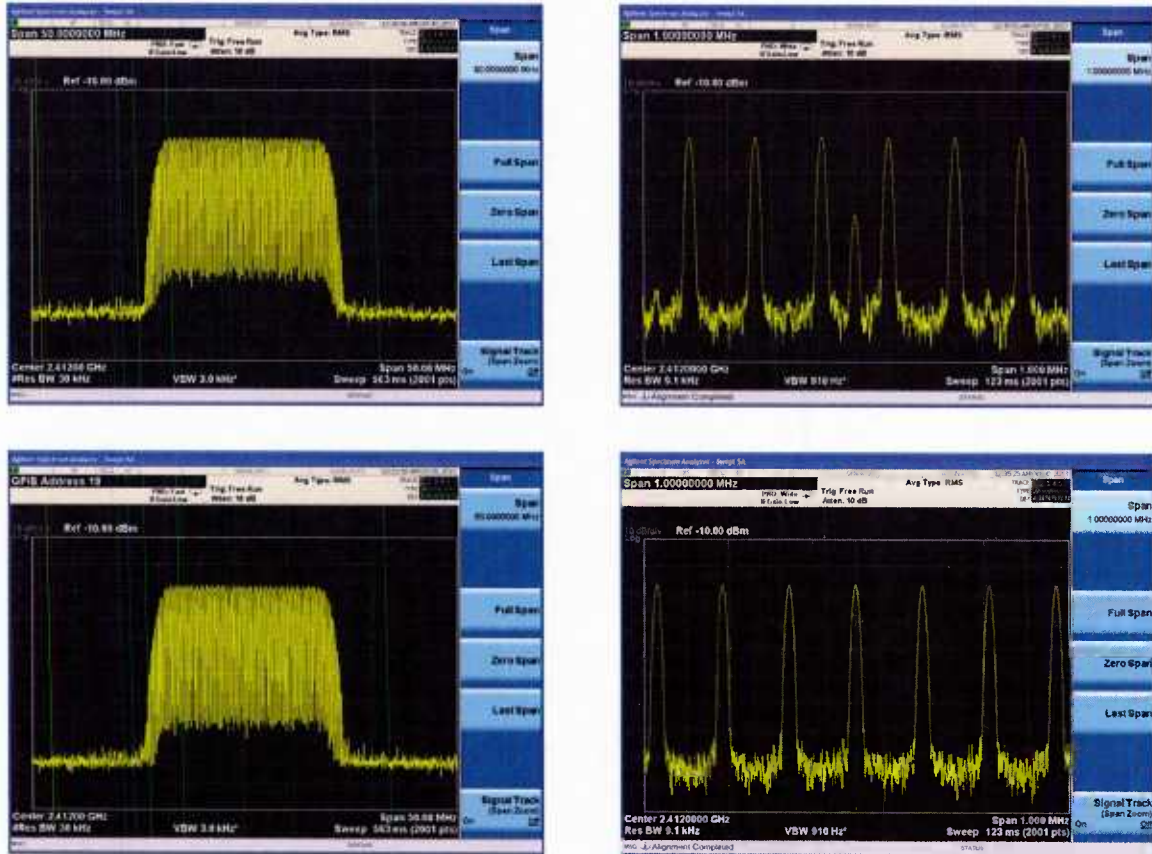

Figure 63. Multitone waveform

Separate transmit signal sources were used for the two ports of the dual-pol transmit antenna. The RF frequency of the two signal generators (feeding the TX-H and TX-V antennas) was offset by half the tone spacing in order to interleave the tones. Thus, the effects of each TX polarization could be recovered in the RX data by selecting the corresponding frequencies of interest.

The following paragraphs show results from the monostatic measurements pointing at the center of the lake at 915 MHz. Three measurements were conducted with each measurement consisting of a continuous data collection over 10 seconds. Figure 64 shows the lake conditions for the three measurements. Note the changes in the lake conditions among these measurements where the surface ripples are most evident in the first measurement.
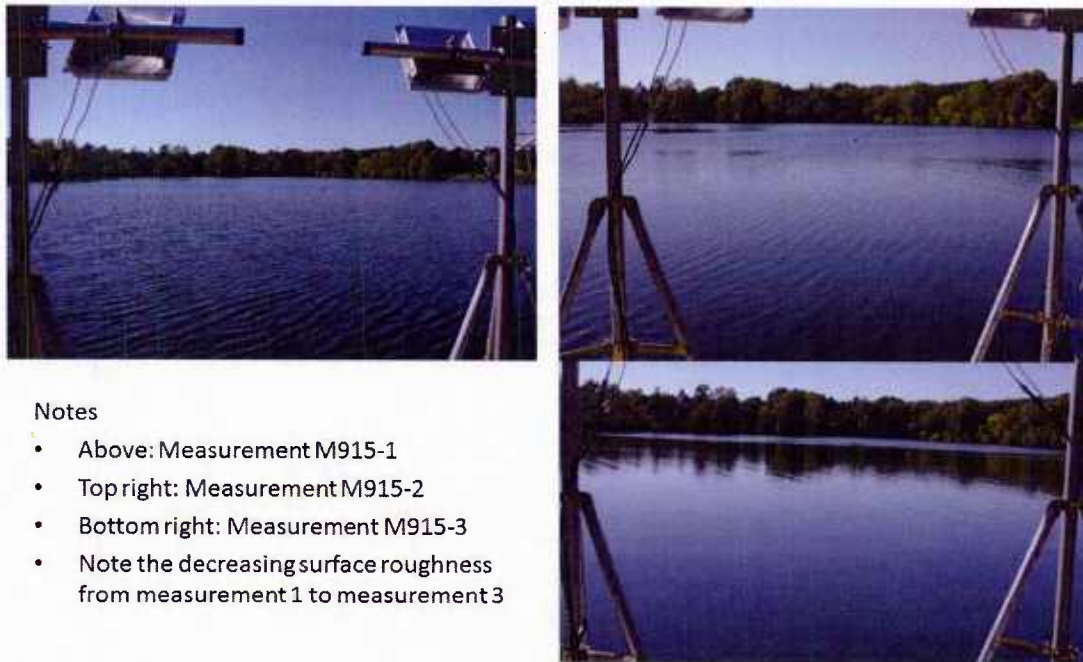
Notes
- Above: Measurement M915-1
- Top right: Measurement M915-2
- Bottom right: Measurement M915-3
- Note the decreasing surface roughness from measurement 1 to measurement 3

Figure 64. Lake conditions for monosatic (pointed at center of lake)

Figure 65 shows the PMD curves for the monostatic measurements at 915 MHz. Each of the three panes in this figure shows two spheres with PMD curves. The top sphere represents the response for horizontal transmission while the bottom sphere represents the response for vertical transmission. The three distinct panes represent the three measurements conducted. The colors among the curves represent a progression in time. It is clear from these plots that the PMD curves in the first pane have the largest variance while those in the third pane have the smallest variance. This matches the visual observations of surface roughness evident in Figure 64.
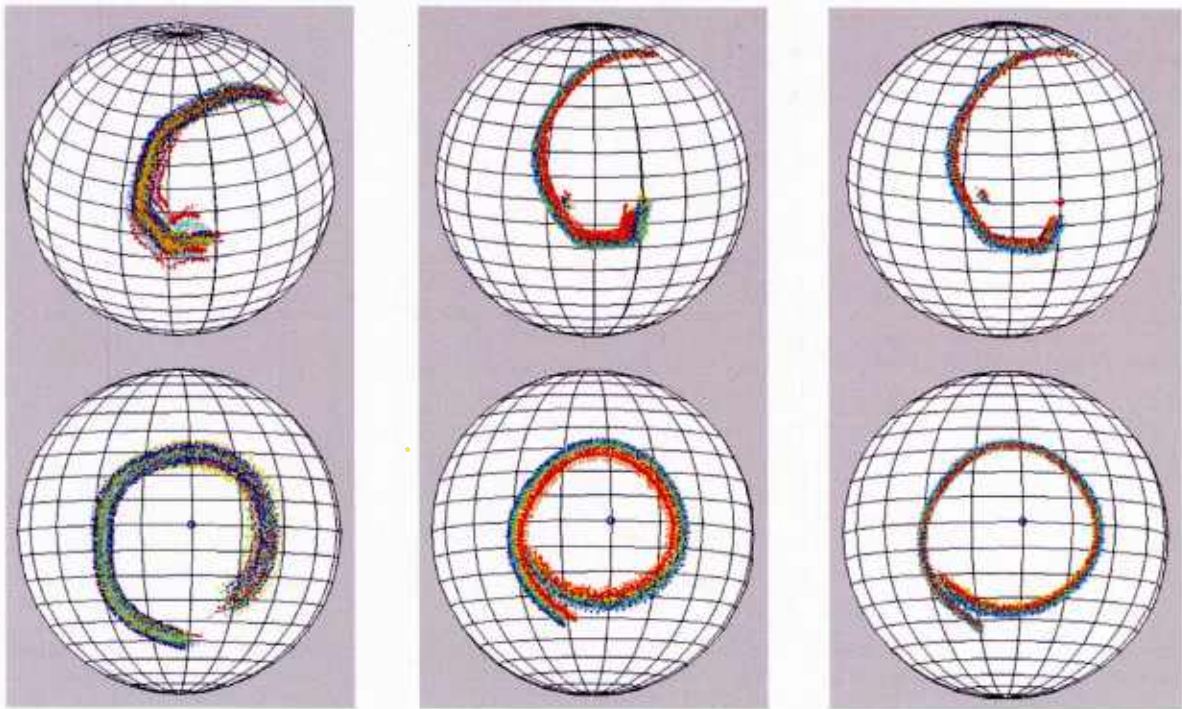
Figure 65. PMD curves for monostatic case, 915 MHz

The PMD curves from Figure 65 were processed to compute the PMD centroid which collapses a given PMD curve to a single point on the sphere. Since the sphere has unity magnitude, each point can be represented by two angles, θ and ϕ. Figure 66 shows plots of these angles as a function of time for each of the three measurements and for each transmit polarization.
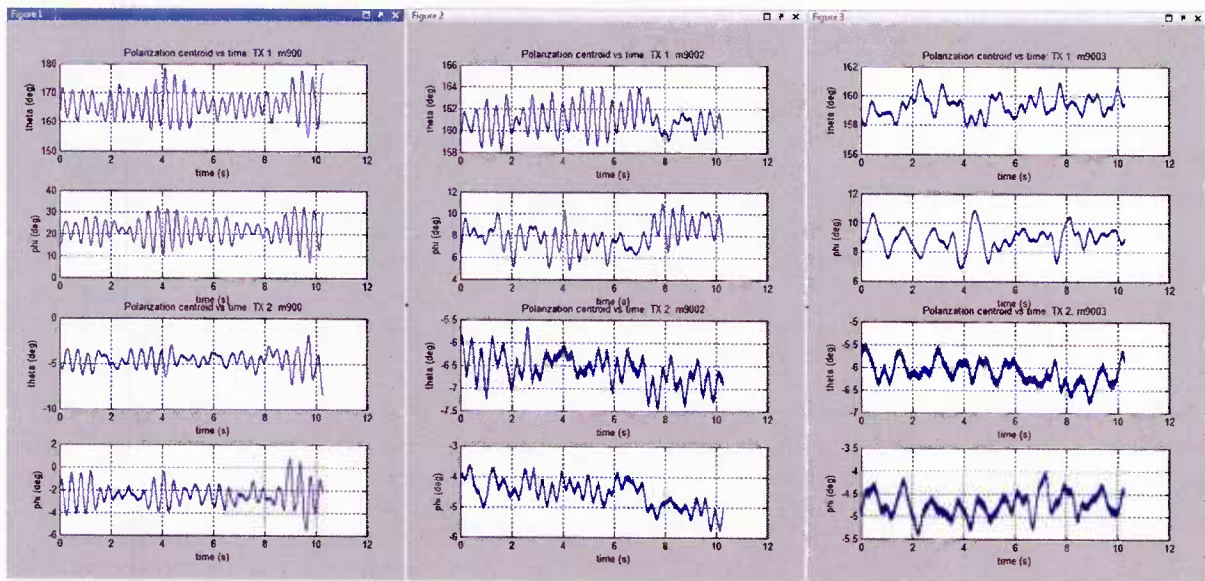

Figure 66. PMD centroid versus time, 915 MHz

Note the periodic nature of the PMD centroid as a function of time. Also, note that the magnitude variations are largest for the first measurement and smallest for the third. Again, this matches the visual observations of surface conditions.

By computing an FFT of the time domain signals θ and ϕ, we can determine the frequency content of the PMD centroid. Figure 67 shows the resulting power spectra for the three measurements for each transmit polarization. Note the strongest content at approximately 2-3 Hz which is most evident in the first measurement.
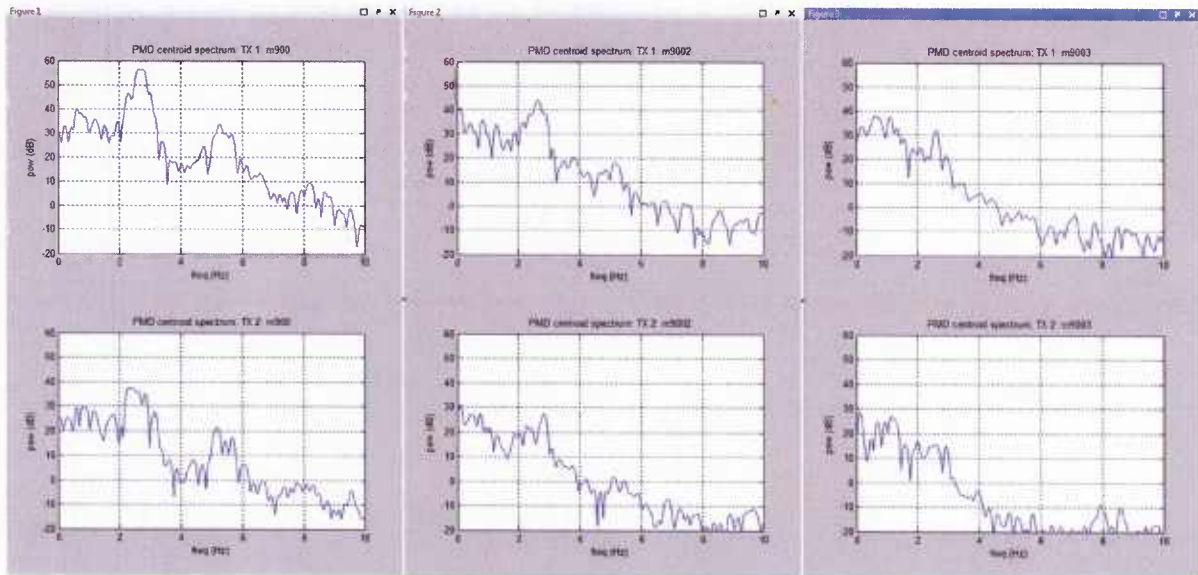

Figure 67. PMD centroid frequency spectrum, 915 MHz

Remarks regarding PMD curves

- Long PMD curves indicate a large polarization spread over the signal bandwidth which would be seen as depolarization in a single-pol system

- Circular shape of curves indicates the presence of two scatterers (one dominant) with different delays

Remarks regarding PMD centroid processing

- Plots indicate oscillations at approximately 2-3 Hz

- Assuming these oscillations are caused by the cyclic motion of gravity waves, this implies a wavelength of 0.25 meters

Although not presented here, results for 470 MHz and 2412 MHz are similar to the results for 915 MHz.

Bistatic measurements

Additional measurements were conducted for the bistatic case. These measurements were collected on Nov 8, 2013 for two waveforms: interleaved multitone (128 tones) and pulsed CW. Measurements were made at 470, 915, and 2412 MHz, but only the data from 915 MHz is presented below.

Figure 68 shows a picture of the transmit antenna pointing across the lake toward the receive antenna on the far bank. This picture also gives an indication of the surface roughness at the time of the measurement.

Figure 68. Bistatic measurement at 915 MHz

Figure 69 shows the power as a function of frequency (left plots) and time (right plots) for the multitone waveform. For the frequency plots, the top plot shows the full captured bandwidth where the signal is centered at an intermediate frequency of 15 MHz with a bandwidth of approximately 20 MHz. The bottom plot is the same as the top but it is "zoomed in" to show only 1 MHz around the signal center frequency. It is easy to see the interleaved tones which represent the received signal from horizontal (blue) and vertical (green) transmissions. The right plots show the results after filtering to separate the horizontal and vertical transmissions. The upper plot shows the receive power for horizontal transmission, while the lower plot shows the receive power for vertical transmission. For both plots, the blue trace represents horizontal receive while the green trace represents vertical receive. In these results, the power from all relevant frequency bins has been combined (summed) to produce the aggregate power shown over time.
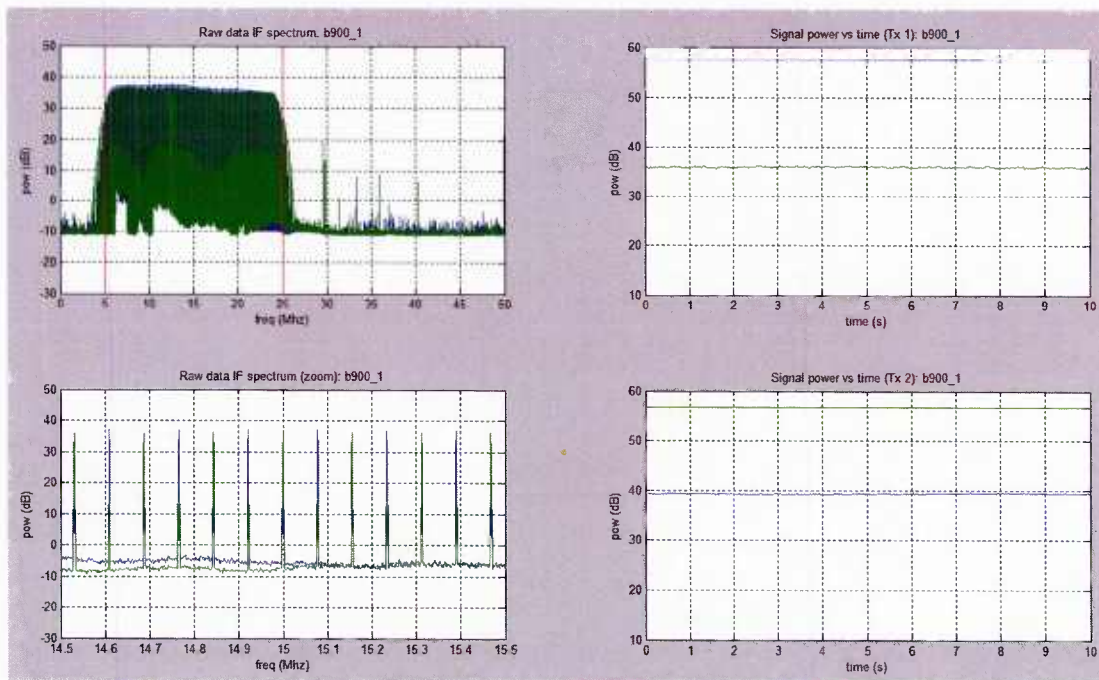
Figure 69. Bistatic receive power versus frequency (left) and time (right) for multitone waveform

Figure 70 shows the PMD curves for both waveforms, where the multitoned waveform is shown in the top two subplots and the pulsed CW waveform is shown in the bottom two subplots. In each case, the left plot represents horizontal transmission while the right plot represents vertical transmission.
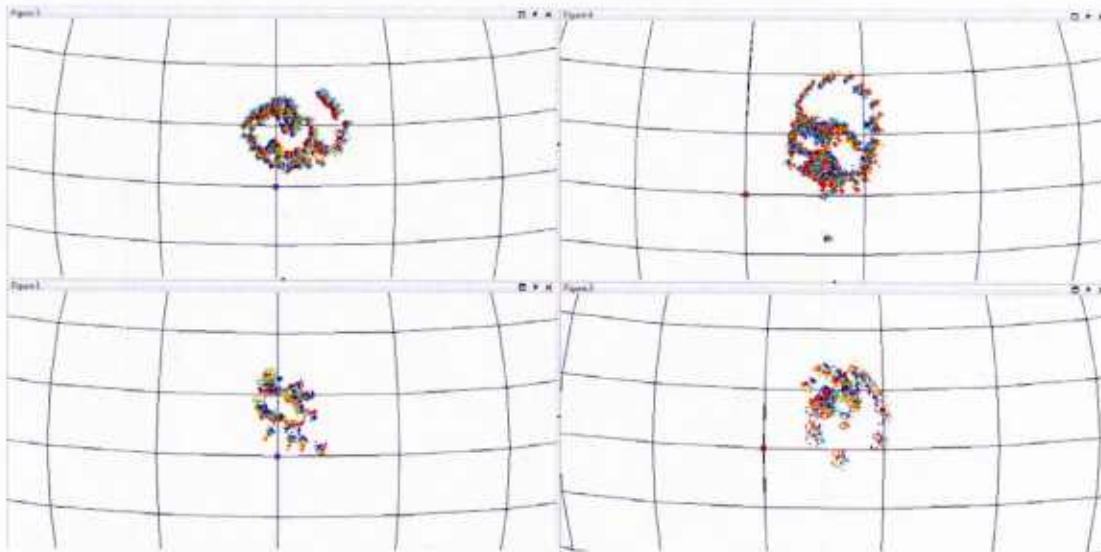

Figure 70. Bistatic PMD curves for multitone waveform (top) and pulsed CW (bottom)

In Figure 70, note the similarity of the PMD curves for the case of each waveform. The primary distinction in the curves is that the curves for pulsed CW contain less

110

frequency "samples" because the PRF lines are spaced further apart than the tone spacing from the multitone waveform.

The PMD centroid is defined as the mean value (averaged over frequency) of PMD Stokes vectors. Thus, at any given time, it can be displayed as a single point on the Poincare sphere. By computing this quantity as a function of time, it is possible to detect oscillation rates of the PMD centroid which correspond to oscillation of some scatterer or collection of scatterers (such as an ocean wave or a target oscillation). Figure 71 shows the frequency spectrum of the PMD centroid for the multitone waveform. Note the clear spectral content at 1.5-2 Hz for both horizontal (top) and vertical (bottom) transmission.
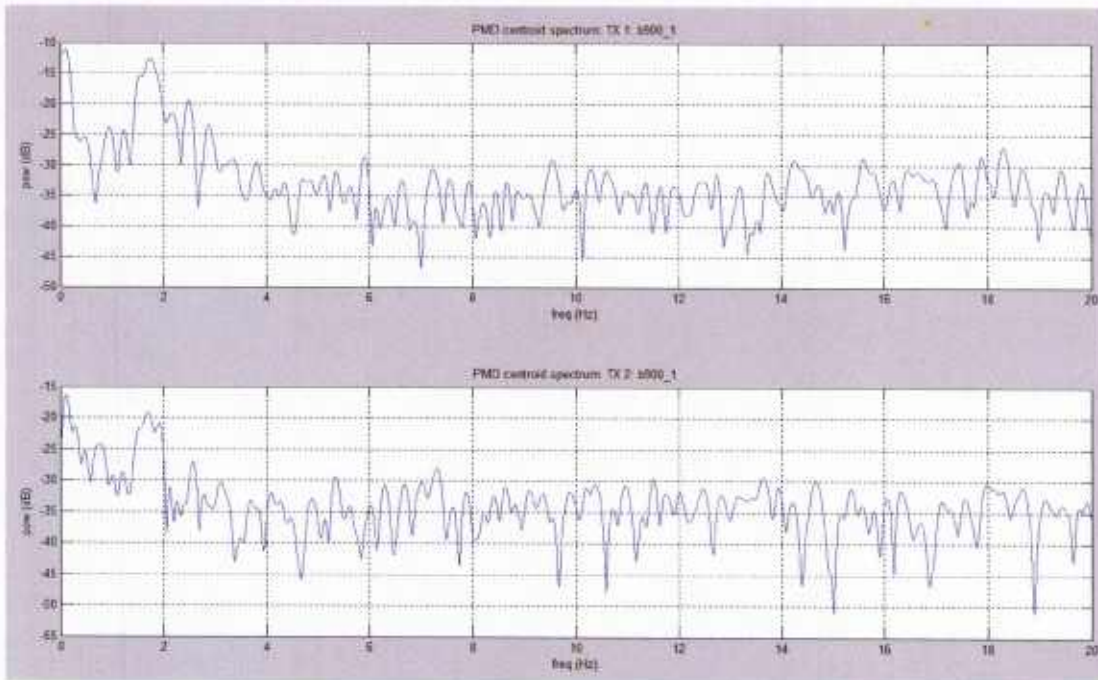

Figure 71. Bistatic PMD centroid power spectrum

C.   *Simulated Clutter Response*

The background clutter response plays a significant role in target detection / identification. Earlier in the report, the ergodicity of the clutter response was demonstrated through simulated responses that compared temporal statistics at a single spatial point with spatial statistics at a single time. The concept of ergodicity also can be extended to resolution cells, i.e., the time-domain statistics from a particular radar range cell are similar to the space-domain statistics taken at a time instant. In this section, we evaluate the "likeness" of clutter responses from adjacent cells with the purpose of assessing the variability in the response as a function of sample support. As the sample support increases, the clutter statistics are

anticipated to be increasingly similar, enhancing the possibility of discriminating a cell containing a target.

Results are presented below for the case of a monostatic radar with incident angle of 88 degrees (grazing angle of 2 degrees) with respect to the mean clutter plane. For this case, the sea surface was generated for a wind speed of 5 m/s. There were nine radar resolution cells in a three by three grid with respect to azimuth and range. Each resolution cell was approximately 87m (cross range) by 30m (down range) with a grid spacing of 0.1 m in both directions. Sea surfaces were generated at a sample interval of 5 ms over a duration of 20 s. Frequency samples were computed every 100 kHz over a bandwidth of 7.5 MHz.

Under these assumptions, the model was executed to produce the scattering response for each polarimetric channel. The resulting data was further processed to produce the Stokes parameters (S0, S1, S2, and S3) as a function of both time and frequency subband. This process was repeated for both horizontal and vertical transmit sources.

The following four figures (Figure 72 through Figure 75) present the results for various dwell times from 0.2 s to 10.0 s. In each figure, there are eight subplots arranged in two columns. Each column has 4 subplots showing the CDF estimates for the four Stokes parameters. The left column shows the results for horizontal transmission and the right column shows the results for vertical transmission. The nine colored traces in each subplot represent the various resolution cells.
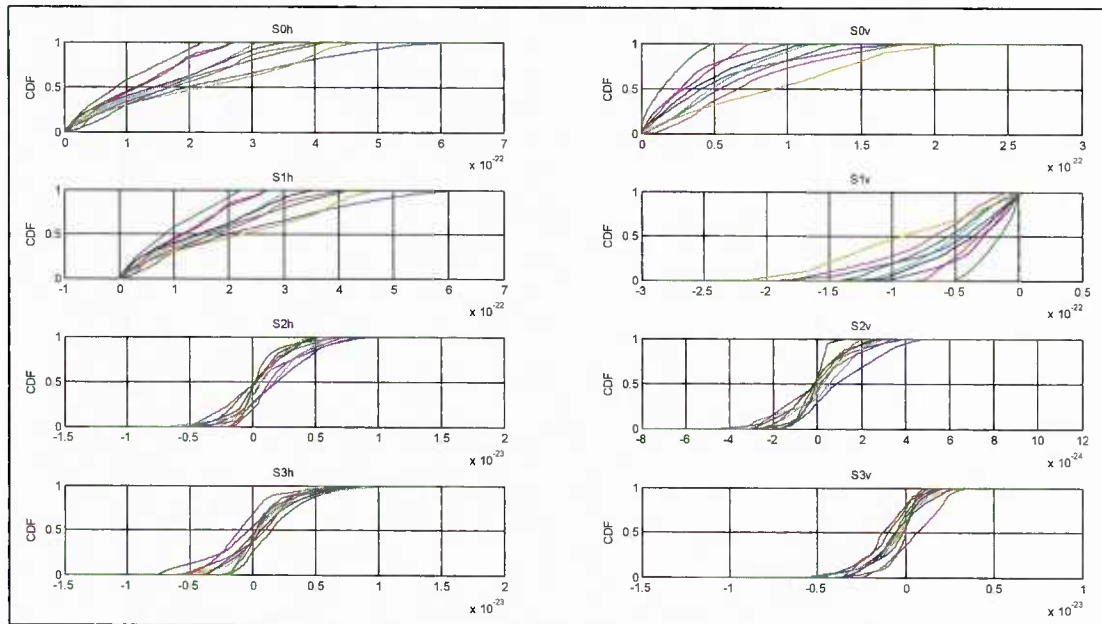

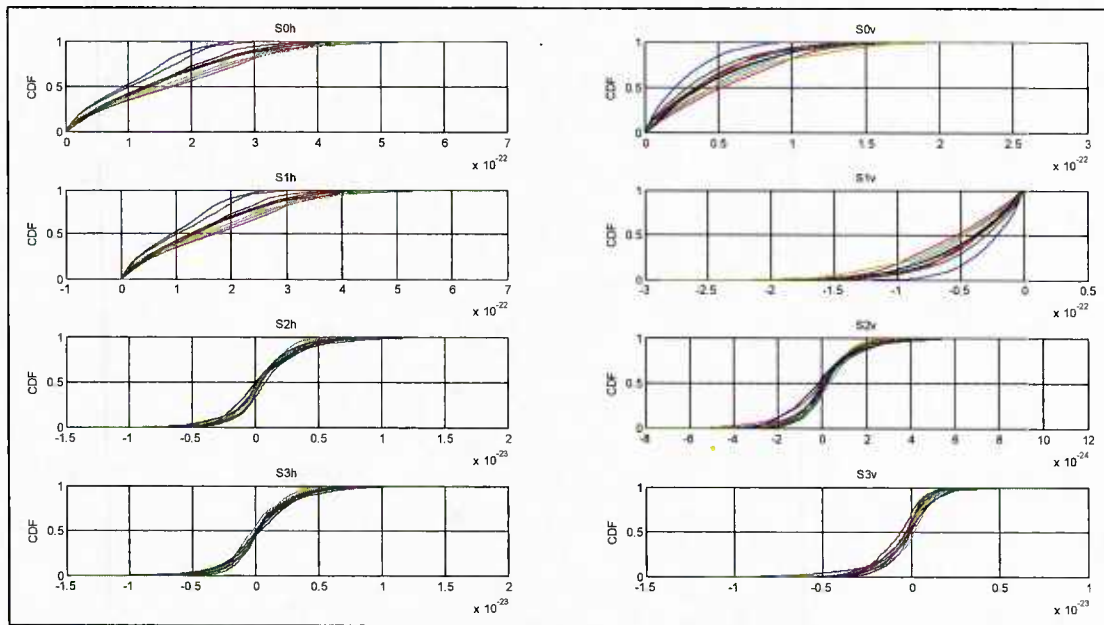*Figure 72. Clutter statistics for dwell time of 0.2 s*
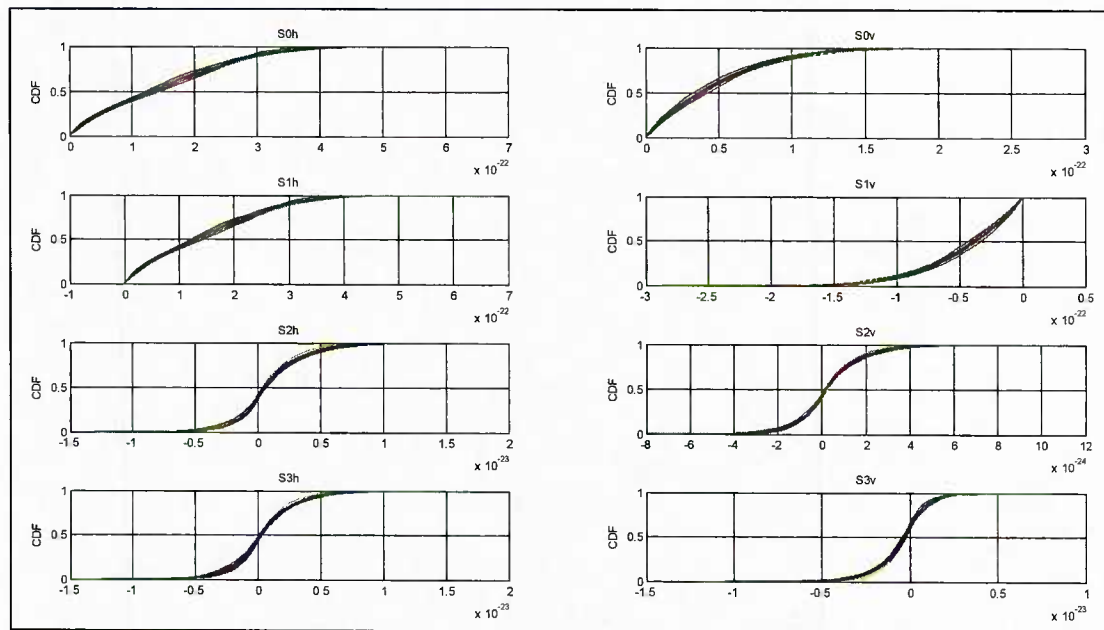
Figure 73. Clutter statistics for dwell time of 1.0 s

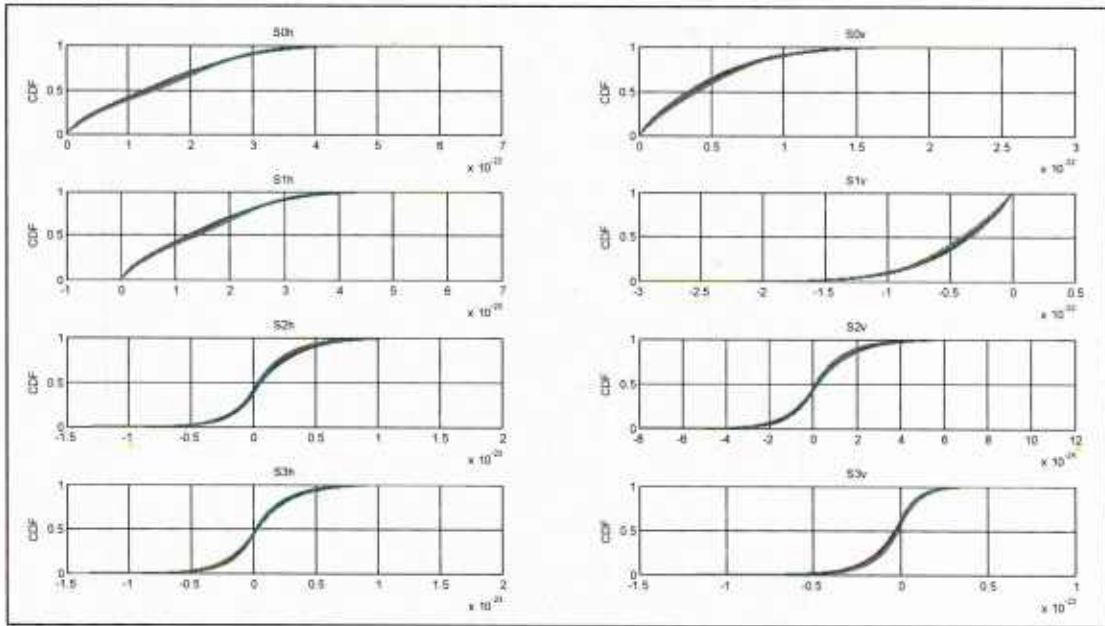*Figure 74. Clutter statistics for dwell time of 5.0 s*

113

Figure 75. Clutter statistics for dwell time of 10.0 s

For Figure 72 with a dwell time of 0.2 s, it is clear that there is variation in the statistics among the nine radar cells. For this case, the number of time / frequency "samples" used to generate the CDF estimates is relatively small at approximately 3000. For Figure 73 with a dwell time of 1.0 s, the number of samples increases (~15000) and the CDF estimates for the various radar cells start to converge. For Figure 74 with a dwell time of 5.0 s (~75000 samples) and for Figure 75 with a dwell time of 10.0 s (~150000 samples), the convergence among the radar cells is quite good.

These results match the expectation that as the dwell time increases, the statistical responses from multiple radar resolution cells would converge. For a resolution cell that contains both clutter and a target, the statistical response is likely to be different and will thereby provide a means for discrimination. The degree to which the statistical response is different will depend on the signal-to-clutter ratio and/or the degree to which the target shadows the clutter response in that resolution cell. In Section IX, additional results are presented where a target has been added to the center resolution cell.

VIII. METHODS FOR TARGET DETECTION AND IDENTIFICATION

Time varying clutter responses and pseudo-stationary target responses are received and processed to yield PMD-based responses. Our intention is to exploit the PMD response in a number of ways for target detection and identification. The responses will depend on the composition of the scatterers in the resolution cell size and so depends on waveform parameters (e.g., bandwidth, pulse width, and carrier frequency) and antenna parameters (beamwidth). A number of methods were hypothesized for detection and identification, and these are briefly described here.

One approach follows the methods of [37], which involves an analysis of the statistics of the polarimetric response. These methods were used to detect weak targets in a background of noise without need for measuring noise power levels to establish a suitable threshold. In the absence of a target response, receiver noise exhibits a polarimetric response (in terms of the Stokes parameter) that yields a linear CDF, while in the presence of a target, the CDF of the response deviates from a linear CDF. Several ratio detectors have been proposed in [37] that include the following forms:

$$r_1(n) = \frac{Y_1(n) - Y_2(n)}{Y_1(n) + Y_2(n)}$$

$$r_2(n) = \frac{2\Re(y_1 y_2^*)}{Y_1(n) + Y_2(n)} \tag{124}$$

$$r_3(n) = \frac{2\Im(y_1 y_2^*)}{Y_1(n) + Y_2(n)}$$

where $Y_i = |y_i|^2$ and where, in the absence of a target, y_i is a bivariate Gaussian sequence. These ratios were used to detect deviations in joint statistics due exclusively to noise. Similar statistical approaches using Stokes parameters may be possible in a clutter-limited environment.

Another related approach is a method based largely on polarization decorrelation sensing that is described in [10]. That approach was used to determine when a very weak signal was simultaneously present with a much stronger signal.

A third approach involves examination of the structure of the PMD signature. The PMD response will usually exhibit loops resulting from destructive interference between multipath components. Such features may be able to be interpreted to identify differential delays that remain constant over a dwell, indicating the likelihood of the presence of a target.

Other methods include:

- CFAR-like processing wherein the PMD responses of nearby resolution cells is compared with the target cell to identify detectable differences.

- Comparison of responses in HV and VH to assess whether or not a nonreciprocal reflector is contained in the resolution cell

A. Bistatic Correlation Analysis: Forward and Backscatter

From Boerner's notes from a course on POL-SAR [6], the scattering matrix for forward scatter and backscatter exhibit distinct forms. In the monostatic (backscatter) case, the scattering matrix is symmetric (assuming the medium between the radar and target is reciprocal and also that the radar is reciprocal between transmit and receive operation), but in the forward scatter case, the scattering matrix is not symmetric in general.

> "In both equations the incident fields are those at the target, the received fields are measured at the receiver, and r_2 is the distance from target to receiver. The *'Sinclair matrix* $[S]$' is mostly used for **back-scattering**, but is readily extended to the **bistatic scattering** case. If the name **scattering matrix** is used without qualification, it normally refers to the Sinclair matrix $[S]$. In the general bistatic scattering case, the elements of the Sinclair matrix are not related to each other, except through the physics of the scatterer. However, if the receiver and transmitter are co-located, as in the **mono-static** of back-scattering situation, and if the medium between target and transmitter is reciprocal, mainly the Sinclair matrix $[S(AB)]$ is symmetric, i.e. $S_{AB} = S_{BA}$. The Jones matrix is used for the forward transmission case; and if the medium between target and transmitter, without Faraday rotation, the Jones matrix is usually normal. However, it should be noted that the Jones matrix is not in general normal, i.e., in general the Jones matrix does not have orthogonal eigenvectors. Even the case of only one eigenvector (and a generalized eigenvector) has been considered in optics (homogeneous and inhomogeneous Jones matrices). If the coordinate systems being used are kept in mind, the numerical subscripts can be dropped."

Using our existing clutter model, we investigate the bistatic angles near 0 over which the HV and VH responses are symmetric. The driving question that we attempted to answer was, "Over what deviation can the Sinclair matrix be considered to be symmetric for bistatic topologies, assuming a reciprocal target?"

To investigate this problem, we considered a field of scatterers as shown in Figure 76. The goal was to quantify the maximum bistatic angle for which HV remains approximately equal to VH. A numerical analysis was conducted to aid in identification of the driving factors. Based on numerical analyses, the symmetry of the Sinclair matrix off-diagonals was found to depend upon a few key parameters

- The number and relative range and response of dominant scatterers in the resolution cell
- The signal bandwidth
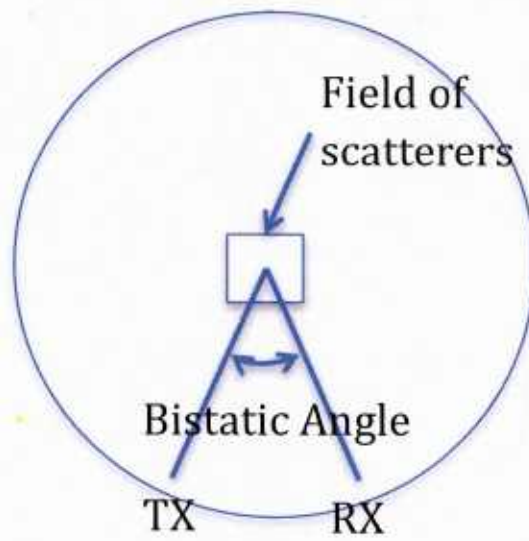- The carrier frequency
- The bistatic angle

Figure 76. Bistatic scattering geometry

To help illustrate some of these dependencies, results are shown in Figure 77 through Figure 79. Figure 77 shows the correlation between HV and VH resulting from a single scatterer that is offset from the origin of the arc traversed to change the bistatic geometry. The results illustrate the anticipated result that higher bandwidth will induce decorrelation over shorter traversed paths. Figure 78 illustrates the response when the grid size of scatterers is increased to a 2x2 grid. In this case the signal bandwidth was 20 MHz, and matrix symmetry is retained for bistatic angle out to about 2 degrees. Figure 79 incorporates a 5x5 grid of scatters over roughly an 80m by 80 m resolution cell. In this case, the bandwidth is reduced to tens of kilohertz, leading to a symmetric response out to about 6 degrees in arc length. Since the technology that we invoke involves subbanding and processing using narrow bandwidths for each subband, we anticipate that HV-VH symmetry may occur over several degrees in a bistatic configuration in reciprocal channels.

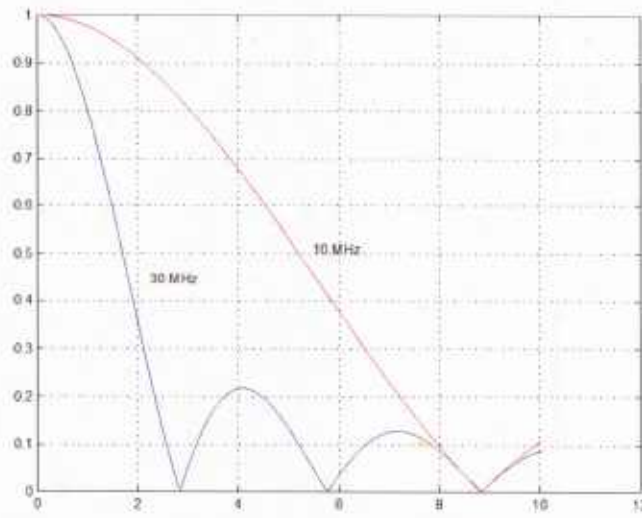*Figure 77. Correlation between HV and VH as a function of arc length (in degrees) for two signal bandwidths*
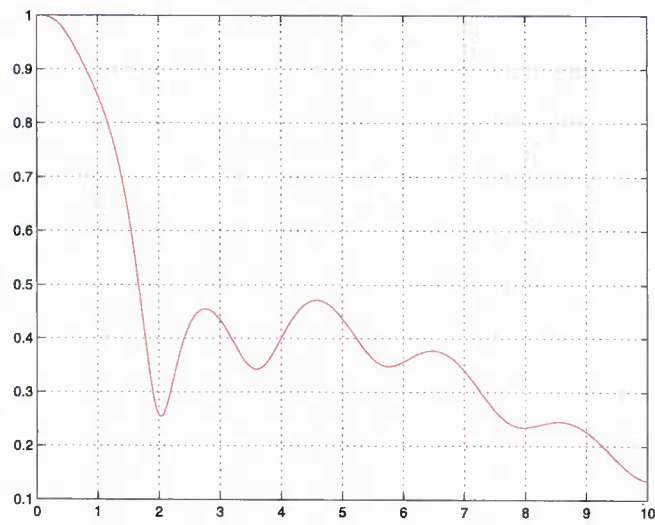

Figure 78. Correlation between HV and VH as a function of arc length (in degrees) for 2x2 grid of scatterers and tens of MHz bandwidth
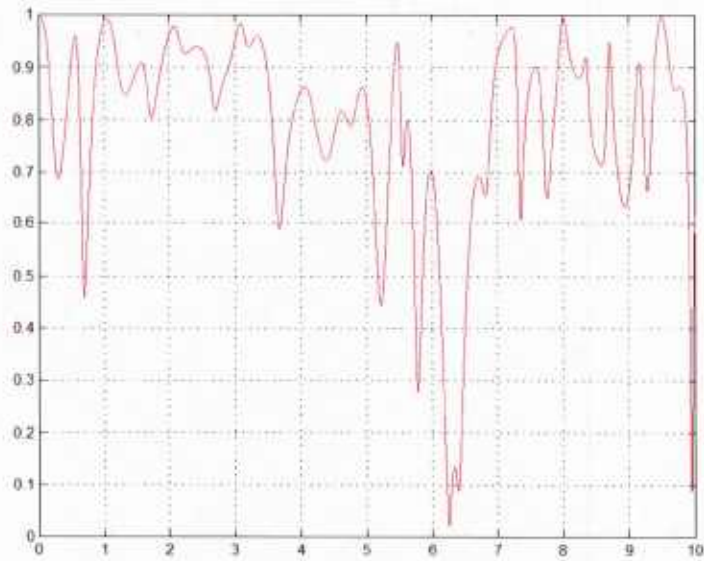
Figure 79. Correlation between HV and VH as a function of arc length (in degrees) for 5x5 grid of scatterers and tens of kHz bandwidth

This suggests a potential method for nonreciprocal target detection in marginally bistatic configurations through comparison of the VH and the HV responses.

B.   Periodic Response Detection

For identification purposes, the time domain variations of the PMD response are known to provide indications of rotational rates[52]. The idea is illustrated in Figure 80 for a single axis. In the figure, a target is yawing with an arbitrary yaw rate. As a result of the scattering surfaces and the relative geometry between the radar and the target, the relative path lengths and reflection coefficients of the dominant scatterers will change with the target motion, and the motion will be approximately periodic. Hence the time variations of the target will lead to PMD responses that repeat, and these can be processed to identify the attitude rate. A contrived example of PMD variations is shown in Figure 81.

Polarization properties of reflectors will change with aspect

yaw motion

d_1 d_2 d_3 d_4

$d_1+\alpha_1$ $d_2+\alpha_2$ $d_3+\alpha_3$ $d_4+\alpha_4$
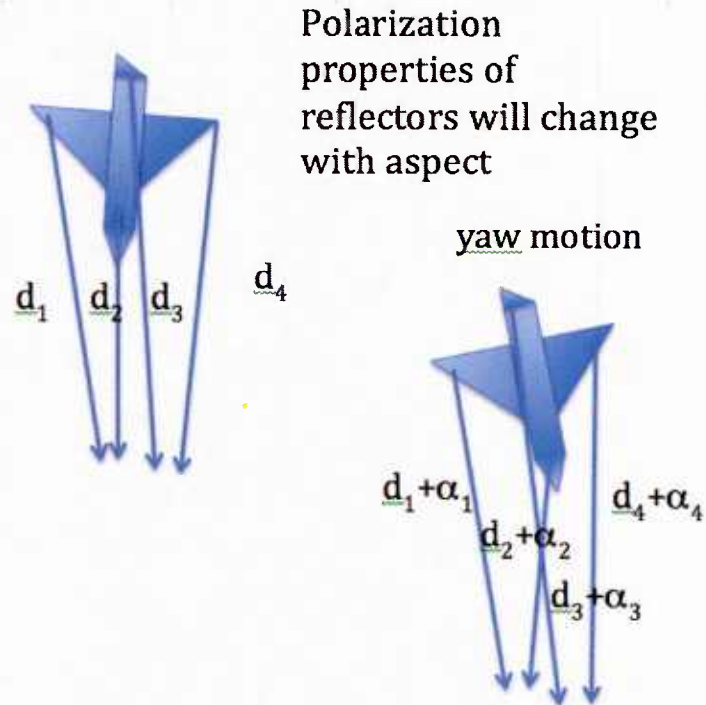
Figure 80. Detection of attitude rate of a target

- Contrived illustration of PMD variations derived from Rayleigh fading model

- Time-domain variations can be used for target feature detection

d_1 d_2 d_3 d_4

$d_1+\alpha_1$ $d_2+\alpha_2$ $d_3+\alpha_3$ $d_4+\alpha_4$

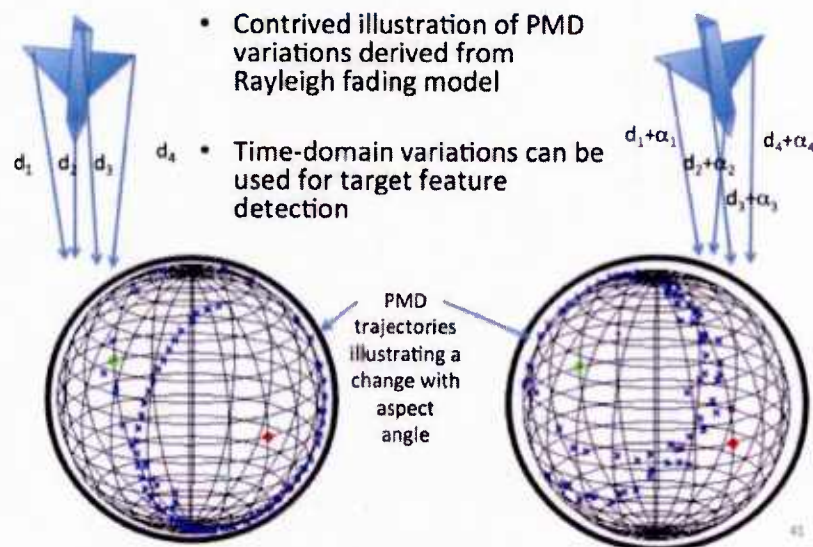PMD trajectories illustrating a change with aspect angle

Figure 81. Contrived PMD curves due to target attitude change

We anticipate that these methods can be directly applied to simultaneously estimate pitch, yaw, and roll rates of a target (e.g., for long range target identification).

Referring to Figure 82, RF signal multipaths are modulated by the attitude rates, leading to time-varying polarimetric changes. The resulting time-varying PMD curves can then be used to isolate the attitude rates, provided that the attitude rates are resolvable in the frequency domain. That this is feasible has been demonstrated for both two-dimensional and three-dimensional motion in a laboratory setting. We anticipate that similar approaches can be used to simultaneously determine target pitch, yaw, and roll rates. Such rates would be expected to be a function of the target size, weight, etc. and potentially can contribute to aid in target identification and target association in MIMO radar applications.

The algorithms rely upon distributed target models rather than point target models, i.e., the target is comprised of multiple spatially separated complex scatterers with polarization–diverse scattering. This model, incidentally, is consistent with the physics of the problem and exploits the distributed polarimetric response from target scatterers. The target extent and the uncompressed radar signal bandwidth are key parameters that drive the PMD response. A rule of thumb is that substantive signatures occur when the product of the time delay and the signal bandwidth exceeds about 0.1.
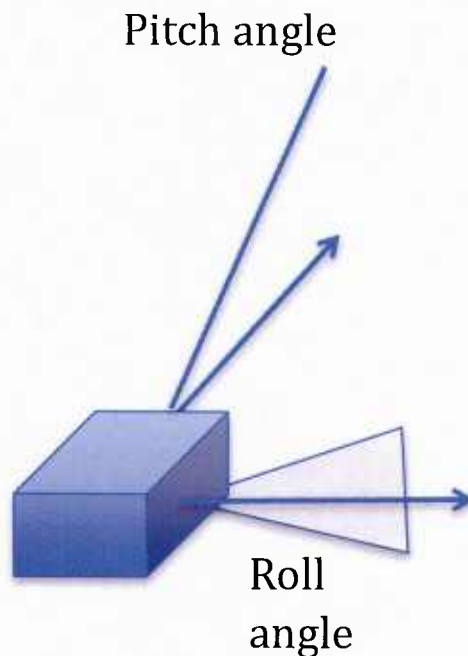

Figure 82. Identification of simultaneous attitude rates

C.   Estimating vibration rates using DFT of PMD centroid

One approach to identifying a target is to estimate the roll, pitch, and yaw oscillation rates which are generally unique to a target. A method to estimate these attitude rates is to compute the spectrum for the PMD centroid and to identify the frequencies with the highest energy content.

This method was evaluated for two scenarios. The first scenario involves a laboratory setup of three tuning forks vibrating along the three principal axes. The second scenario involves using the previously discussed models (Target Model, Radar / Processing Models) and processing the received radar signal to identify the vibration rates. These are discussed below.

1.   Tuning Fork Experiment

Three tuning forks were oriented orthogonally to each other in order to create 3-axis vibrations as shown in Figure 83. The resonant frequencies of the forks were 100, 256, and 320 Hz. After striking each fork, dual-polarized measurements were collected and processed to estimate the vibration frequencies.
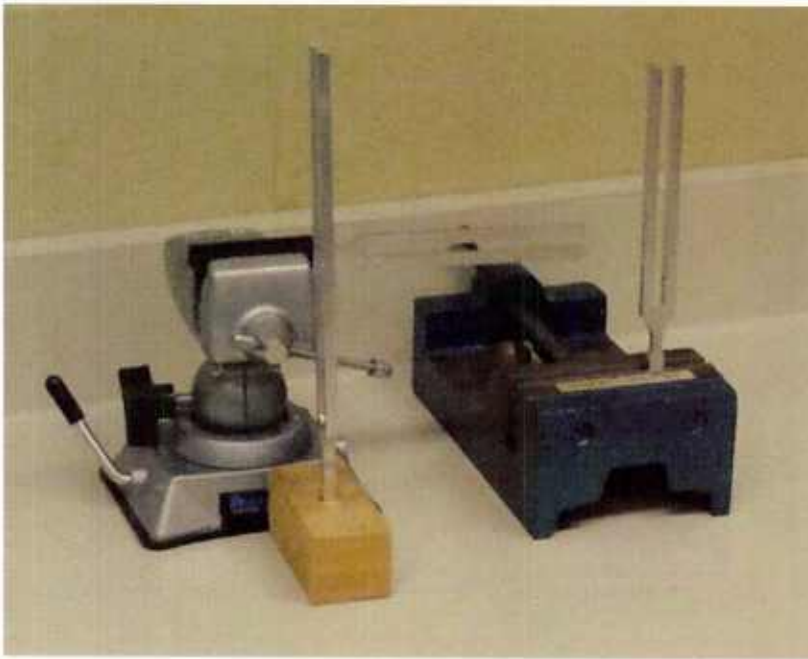
Figure 83. Tuning fork experiment with forks oriented along the three principal axes

The setup consisted of a transmit signal with a center frequency of 2412 MHz, bandwidth of 20 MHz, and slant 45 polarization. The scattered response was received on both channels of a dual-polarized receiver, downconverted to an IF of 35 MHz, digitized, and processed to produce the PMD response. Finally, the PMD centroid was computed over time and the frequency spectrum of this centroid was evaluated using the DFT.

Figure 84 shows the resulting plots for 2 successive trials of this experiment. In both plots, the resonant frequencies of all three tuning forks are apparent (tuning forks resonant frequencies: 100, 256, & 320 Hz).
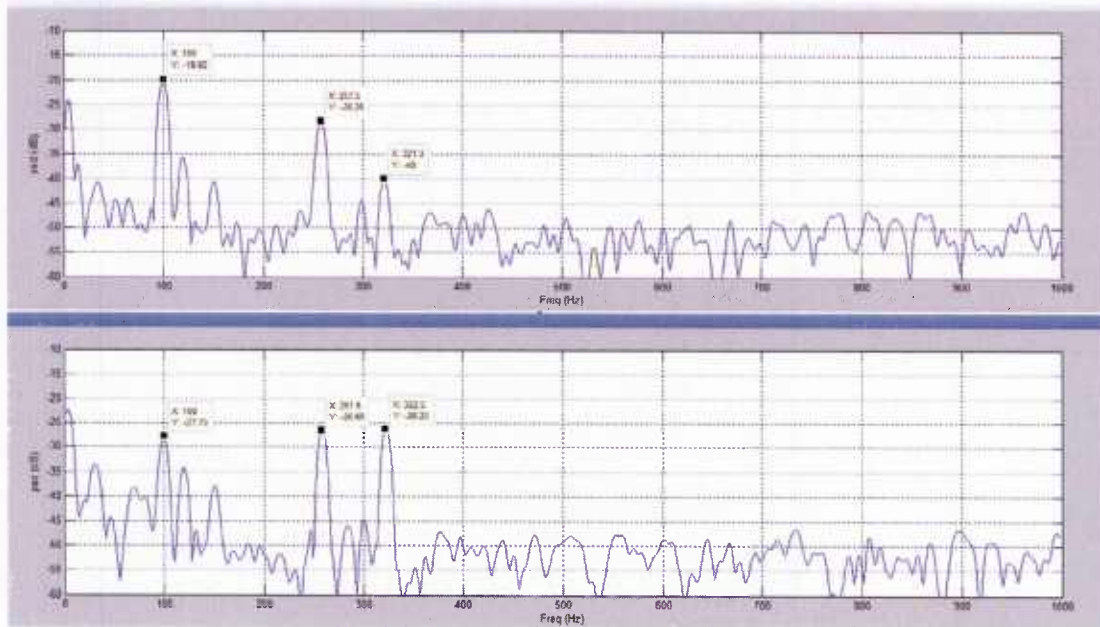
Figure 84. Spectrum for tuning fork experiments

2. Simulation

The Target Model was exercised for three simulation cases in order to investigate the utility of PMD processing in determining the target roll, pitch, and yaw rates in the absence of sea clutter. For the first two cases, the amplitude of the sinusoidal variations was set intentionally large (20 deg). For the third case, the amplitude was reduced to 1 deg for each axis.

The following list indicates the parameters for each case:

- Case #1: Near vertical incidence (incident angle 10 deg) with 20 deg roll, pitch, & yaw amplitudes

- Case #2: Small grazing angle (incident angle 89 deg) with 20 deg roll, pitch, & yaw amplitudes

- Case #3: Small grazing angle (incident angle 89 deg) with 1 deg roll, pitch, & yaw amplitudes

For all cases, the roll rate was 0.2 Hz, the yaw rate was 0.33 Hz, and the pitch rate was 0.14 Hz. The target was oriented broadside to a monostatic radar.

Figure 85, Figure 86, and Figure 87 show the results for each of these cases where the plot shows the spectrum of the PMD centroid. For case 1(Figure 85), note that

the roll and pitch rates (0.2 and 0.14 Hz) are evident, but yaw rate (0.33 Hz) is diminished. For case 2 (Figure 86), note that the highest power peaks identify the desired roll, pitch, and yaw rates. For case 3 (Figure 87), note that it is not easy to pick out the desired roll, pitch, and yaw rates. Multiples of the pitch rate (0.143 Hz) appear in many places making it difficult to find the other rates of interest (0.200 and 0.333 Hz).
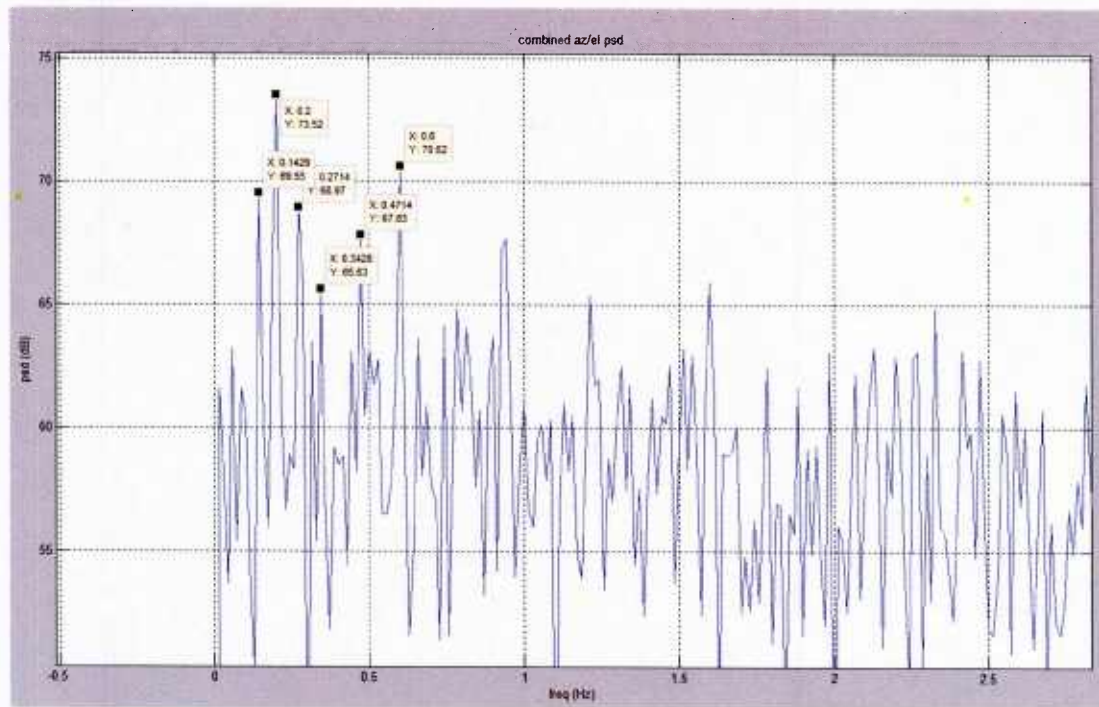

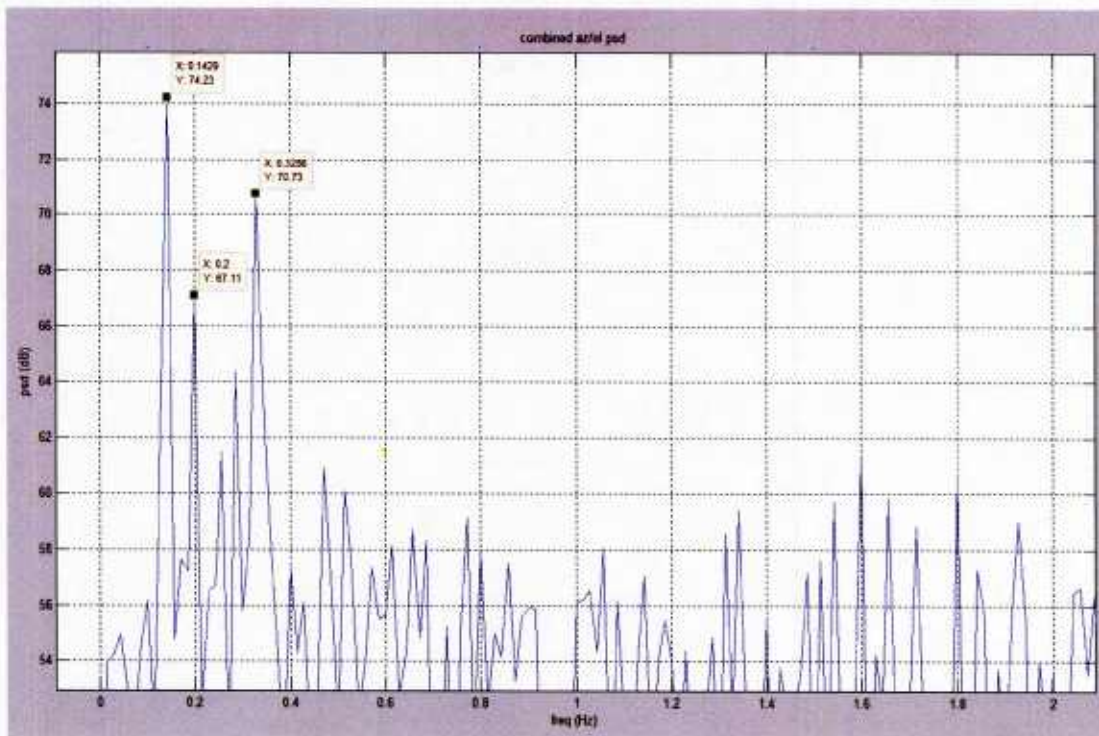*Figure 85. Simulation case 1, near vertical incidence with large target oscillations*

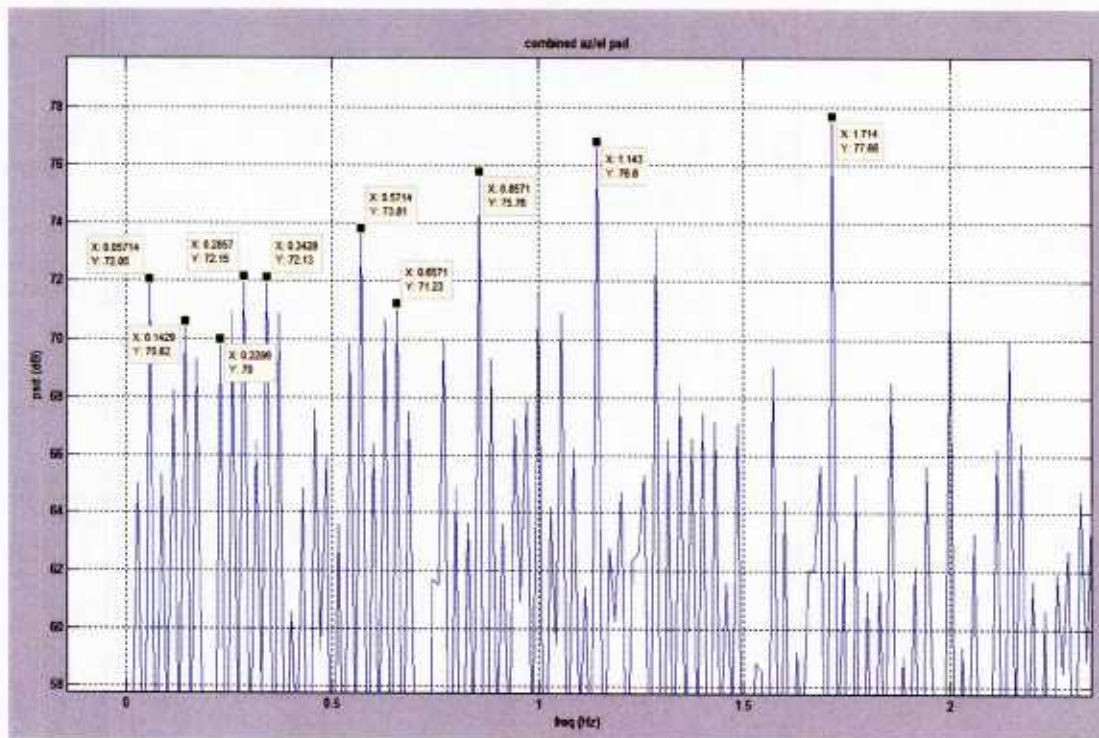*Figure 86. Simulation case 2, small grazing angle with large target oscillations*

Figure 87. Simulation case 3, small grazing angle with small target oscillations

The preceding analysis has shown that spectral estimation of the PMD centroid can be used to identify the attitude rates of a target. When the amplitude of the target oscillations is very large (case 1 and 2 above), these rates are evident in the resulting spectrum. However, with smaller oscillation amplitudes (such as in case 3 above), there is spectral energy at multiple frequencies, including several harmonics of the vibration rates. More advanced processing may be needed to identify the fundamental rates.

D.   Advanced methods for target attitude rates detection

In the tuning fork experiments, lab-based target attitude rates sensing results were obtained by directly identifying vibration frequencies from Discrete Fourier Transforms of the polarimetric data, i.e., the centroid of the Stokes parameters. This approach is relatively straight-forward, but yields suboptimal detection of sinusoids. More sophisticated detection algorithms, including joint maximum likelihood (ML) techniques, can potentially be applied to the PMD data in order to improve detection and estimation of the vibration modes embedded in the received signals. Examples of techniques for complex-valued sinusoidal detection include Akaike Information Criterion (AIC) and Minimum Description Length (MDL). For real-valued time series, Extreme Value Theory (EVT) has been used. Both AIC and MDL methods are well-known, but exhibit relatively large overestimation probabilities when low sample support exists. EVT methods can provide improved overestimation probabilities when low sample support exists, but EVT methods were previously limited to single sensor, real-valued applications.

Recently, the EVT method has been extended to the consideration of complex signals and a multiplicity of sensors [78]. The method was developed to characterize specular signal components in a background of temporally-white but spatially correlated noise among the sensors, enabling estimation of the number and features of complex sinusoids. The particular application that was addressed involved the measurement, characterization, and modeling of communications propagation channels so that correlation properties between sensors could more accurately be modeled by removing the impact of specular components. The presence of these specular components in the received signals biases the correlation estimates of the underlying fluctuating components, and it is useful to subtract the specular components from the received signals to improve the accuracy of the channel characterizations.

The extended EVT theory, which is capable of leveraging the outputs from multiple sensors, has likely application to the detection of target attitudes in a background of clutter. In particular the theory can potentially be applied to the correlated outputs in the polarization-frequency domain, where each of the outputs is treated as a virtual sensor. By utilizing a dual polarized antenna, the number of virtual sensors

can be extended further (by a factor or two). We anticipate that this strategy will aid in the detection and characterization of the number of sinusoids as well as their frequencies and amplitudes. We believe that additional efforts are warranted to pursue the use of this theory in concert with PMD characterizations to evaluate these methods for attitude identification of targets at long ranges.

The theory associated with the extended EVT method is contained in [87] and is briefly summarized here. The approach assumes the following model for noisy observations $x(t)$ from an unstructured array of p sensors, where K complex sinusoids are embedded in the received signals:

$$x(t) = \sum_{j=1}^{K} \mu_j e^{i\omega_j t} + \xi(t) \quad , \quad t = 1, \ldots, n$$

The signal amplitude and frequency associated with sinusoid j are μ_j and ω_j, respectively, and ξ is temporally white and spatially correlated noise with a zero-mean complex normal distribution and complex correlation matrix Q. The goal of the detector is to estimate the parameter vector

$$\theta_{(k)} = \begin{cases} [\omega_{(k)}^T, \beta_{(k)}^T, \sigma^T(Q_k)]^T & \text{for } k > 0 \\ \sigma(Q_k) & \text{for } k = 0 \end{cases}$$

where

$$\beta_{(k)} = [\text{Re}\{\mu_1^T\}, \text{Im}\{\mu_1^T\}, \ldots, \text{Re}\{\mu_k^T\}, \text{Im}\{\mu_k^T\}]^T$$

which estimates parameters associated with the complex sinusoids and also provides an estimate of the covariance matrix of the fluctuating component of the received signals. For accurate parameter estimation, it is necessary to estimate the number of sinusoids present in the received signals, i.e., the model order. This is accomplished by employing a generalized likelihood ratio test (GLRT) that is used in a sequential fashion to estimate the number of sinusoids:

$$G_k = \frac{1}{n} \ln \left(\frac{\mathcal{L}(\hat{\theta}_{(k+1)}; X)}{\mathcal{L}(\hat{\theta}_{(k)}; X)} \right) \overset{\mathcal{H}_{k+1}}{\underset{\mathcal{H}_k}{\gtrless}} C(n, p) \quad , \quad k = 0, 1, \ldots$$

where n is the number of samples, $C(n,p)$ is a penalty term, and $\mathcal{L}$ is the likelihood operator. The model order estimate is incremented until the GLRT is no longer satisfied. At each candidate number of sinusoids, joint ML estimates of the parameter vector are formed, and the estimated sinusoids are subtracted from the original signal so that the GLRT can be applied to the residue to determine if another sinusoid is present.

The mechanism for estimating the model order is dependent upon the penalty term $C(n,p)$. Penalty terms have been determined in prior literature for MDL, AIC, and simple EVT tests. In the most recent work, a penalty term for EVT associated with the case of multiple sensors and correlated noise is derived. The penalty term can be arbitrarily set to yield a constant probability of model overestimation.

For a given estimate of the model order, the frequency parameters are estimated through application of maximum likelihood estimation:

$$\ln \mathcal{L}(\hat{\theta}_{(k)}; \mathbf{X}) = \max_{\omega_{(k)}} \max_{\mathbf{M}_{(k)}, \mathbf{Q}_{(k)}} \ln \mathcal{L}(\theta_{(k)}; \mathbf{X})$$

$$= \max_{\omega_{(k)}} \mathcal{L}_\omega(\omega_{(k)}; \mathbf{X})$$

$$\overset{(a)}{=} \max_{\omega_{(k)}} \left(-np \ln \pi - n \ln \det(\frac{1}{n} \mathbf{X} \mathbf{P}^{\perp}_{\mathbf{A}_{\omega_{(k)}}} \mathbf{X}^\dagger) - np \right)$$

The remaining signal and noise parameters can then be estimated via:

$$\hat{\mathbf{Q}}_k = \frac{1}{n} \mathbf{X} \mathbf{P}^{\perp}_{\mathbf{A}_{\omega_{(k)}}} \mathbf{X}^\dagger$$

$$\hat{\mathbf{M}}_{(k)} = \mathbf{X} \mathbf{A}_{\hat{\omega}_{(k)}} (\mathbf{A}^\dagger_{\hat{\omega}_{(k)}} \mathbf{A}_{\hat{\omega}_{(k)}})^{-1}$$

where

$$\hat{\mathbf{Q}}_k = \frac{1}{n} \sum_{t=1}^{n} \left(x(t) - \sum_{j=1}^{k} \hat{\mu}_j e^{i\hat{\omega}_j t} \right) \left(x(t) - \sum_{j=1}^{k} \hat{\mu}_j e^{i\hat{\omega}_j t} \right)^\dagger$$

When the algorithms converge to the final estimate of the model order, estimates for the sinusoid parameters are also obtained. An illustration of the model order probability of correct estimation is shown in Figure 88 below for AIC, MDL, and EVT methods in the case when 16 sensors exist. In our application, we anticipate a large set of sensors (in space and frequency), which might impact the relative performance between the techniques.
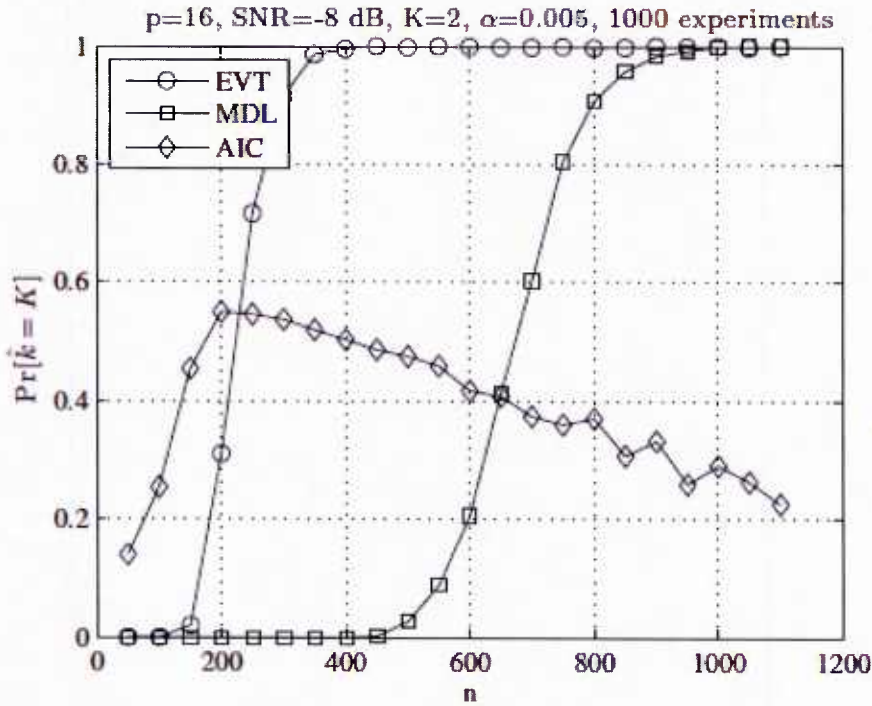
Figure 88. Probability of correct estimation as a function of model order

E.   Additional approaches

Other potential identification methods that may be pursued in future research include the following:

- The structure of the PMD response can also potentially be interpreted to identify the size of the target. This approach in an inversion problem. In other words, given a PMD signature, the goal is to ascertain the multipath structure leading to the observed PMD structure. By monitoring the response over several dwells, it may be possible to ascertain the scattering delays that remain fixed due to the rigid nature of a target body, giving an indication of the target extent.

- Target features may also be discernable through other means that exploit all of the PMD response variants (VV/VH, HH/HV, VV/HH, HV/VH). The dimension can be increased further by integrating space-polarization architectures to take advantage of correlations introduced through the addition of the space dimension. Target features will potentially be more discernible by exploiting joint space-polarization dimensions associated with an array of dual-polarized elements.

- A test measurement system being developed at Notre Dame will enable capability to measure and evaluate responses associated with space-polarization architectures in future research.

IX.   MODELING RESULTS

A.   *Effects versus Grid Resolution*

This section shows illustrative modeling results as a function of the chosen grid resolution (or facet size). The model includes only sea clutter scattering (without a target or noise). Additionally, the sea clutter scattering weighting is configured to emphasize the deterministic component and de-emphasize the fluctuating component. The goal is to show that as the grid resolution decreases below some threshold, the response will converge to the "true" response.   This threshold will be used as a guide in setting grid spacing in subsequent numerical analyses.

In the following, we present modeling results for the case of a sea surface generated under conditions with wind speed at 10 m/s. The overall grid extent was initially assumed to be 75 by 87 meters, the frequency was selected to be 400 MHz, and the sampling interval was chosen to be 0.1 seconds. The radar model was configured as a monostatic system and the incidence angle was selected to be 85 degrees.

Figure 89 includes four plots, each showing channel power versus time for a given grid spacing. The grid spacing for the four plots are identified below:

- Top left: 1m by 1m
- Top right: 0.25m by 0.25m
- Bottom left: 0.1m by 0.1m
- Bottom right: 0.05m by 0.05m

As the grid spacing decreases, the results are anticipated to look more and more alike, thus indicating that the selected grid spacing is not affecting the results.   The same underlying curve is evident, although the interplay between the grid spacing and the pseudo-periodic waves induces a periodic structure due to constructive and destructive interference of the scatterer collections.   The plots generally suggest that a finer resolution is required.
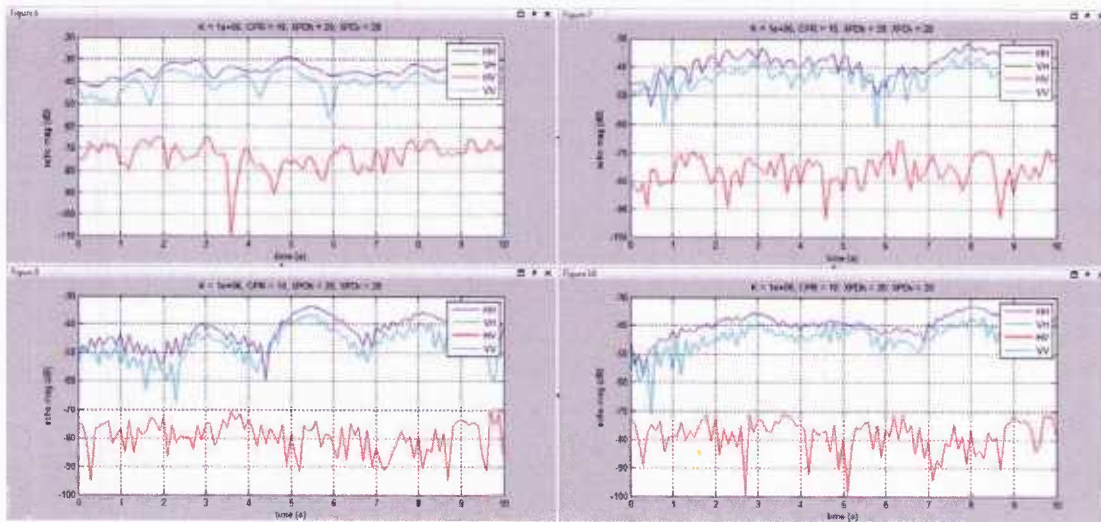
Figure 89. Channel magnitude versus time for four grid spacings (1.0, 0.25, 0.1, 0.05) for wind=10 m/s

Figure 90 shows the sea wave amplitudes as a function of the spectrum of wavelengths for the modeled sea surface at the wind speed of 10 m/s. This figure was provided as a reference in order to compare the grid spacing to the wave energy as a function of wavelength. From a spatial sampling perspective, the grid spacing should be less than half of the smallest wavelength in order to avoid aliasing. For the particular sea surface considered, the lowest wavelength is identified to be approximately 1.3 m.
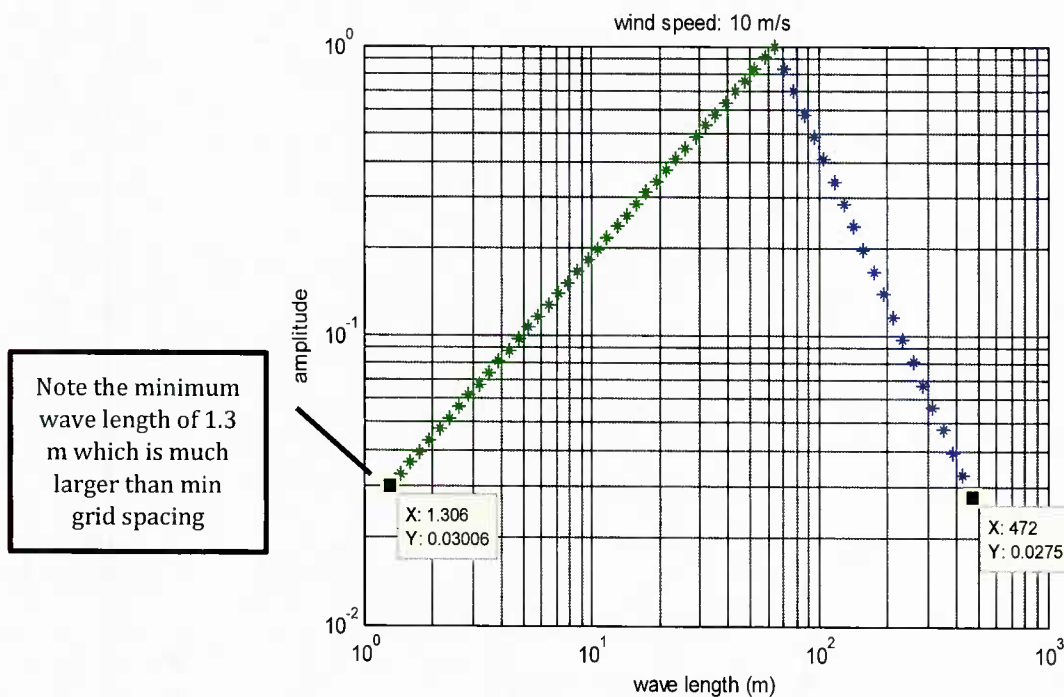
Figure 90. Wave amplitude versus wavelength (wind=10 m/s)

Previously (Figure 89), we have shown receive power as a function of time for selected grid spacing. Our objective now is to reduce the grid spacing further to determine the upper bound on the grid spacing at which the electromagnetic response converges. However, in order to make the analysis more tractable (i.e., to reduce computational burden) for finer grid spacings , the following results are generated for a single instant in time. The overall grid extent was reduced in these plots to 10 by 10 meters (rather than 75 by 87 meters previously) because at very small grid spacings, the computation time rises dramatically with the sea dimension.

Figure 91 includes 2 plots. Both plots show channel power versus grid spacing, but at different instants in time and hence in wave structures (left plot at time t=0 secs, right plot at t=2 secs). The wave synthesis parameters are identical to the previous case with the wind speed = 10 m/s.
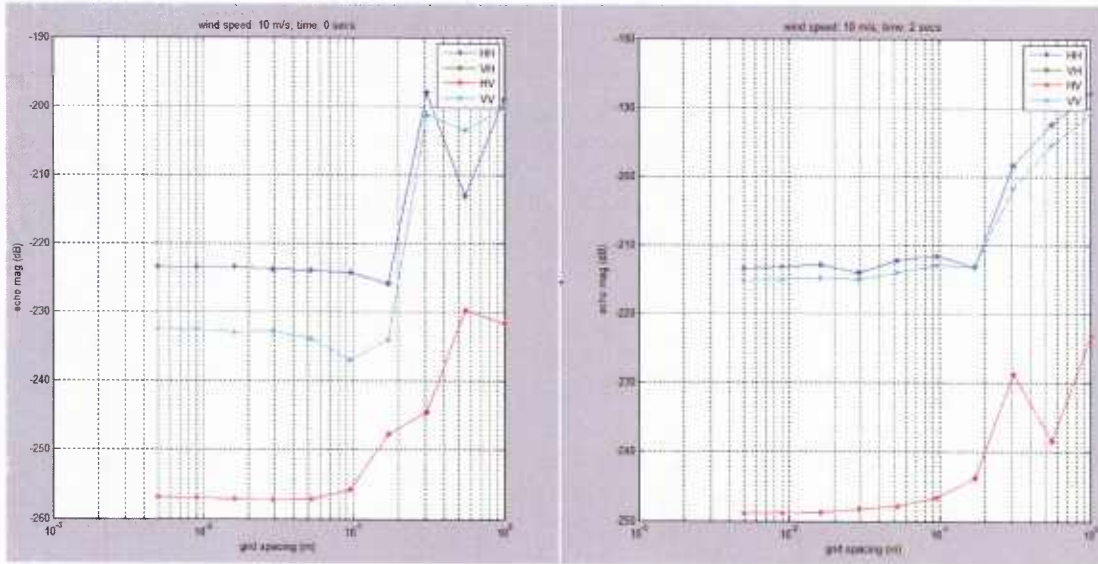
Figure 91. Results versus grid spacing (10 by 10 m grid)

Note that results show convergence below approximately 0.1 meter spacing for a 10m by 10m grid.

Figure 92 presents similar results to Figure 91 except for the larger grid size (75 by 87 m as compared to 10 by 10 m above). Note that convergence is not evidenced even at very low grid spacings. For example, HH response is about 5 dB different for a 0.04 m grid spacing as compared to 0.05 m. Also, VV response is about 6 dB different for a 0.02 m grid spacing as compared to 0.03 m.
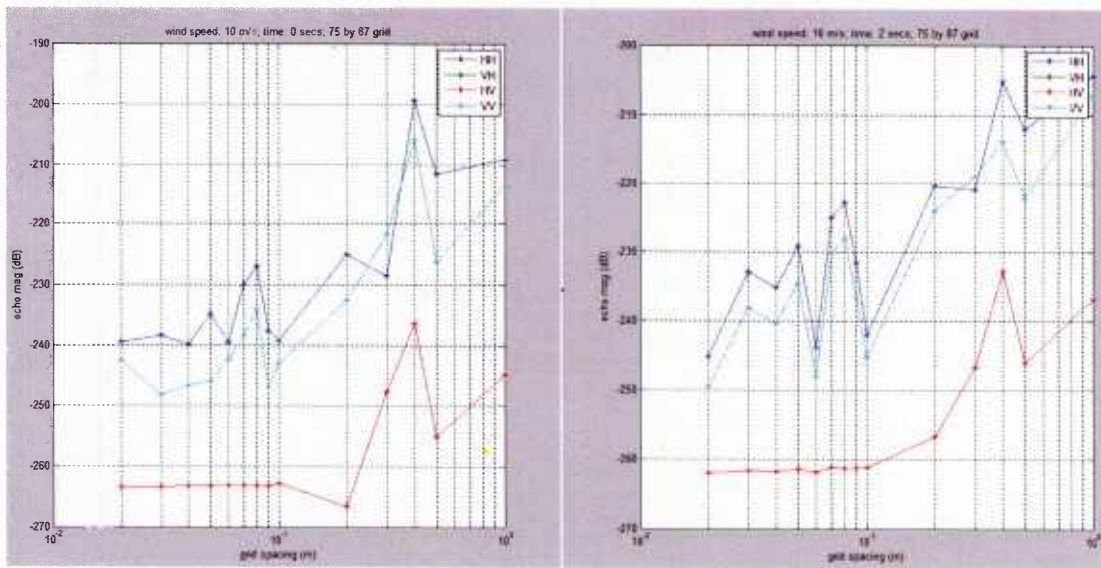
Figure 92. Results versus grid spacing (75 by 87 m grid)

The previous plots have all shown plots of absolute channel magnitude. However, it is possible to also show relative comparisons by plotting the PMD curves (which incorporate relative amplitude and relative phase responses between receive channels).

Figure 93 shows the PMD curves for four grid spacings (0.05, 0.1, 0.25, and 1 meters). These plots were generated using the same model parameters as above with wind at 10 m/s, time t=0 secs, and grid extend of 75 by 87 meters. The left plot corresponds to H transmission while the right plot corresponds to V transmission. For a given transmission, note that the PMD curves are converging at the smallest spacings of 0.1 and 0.05.
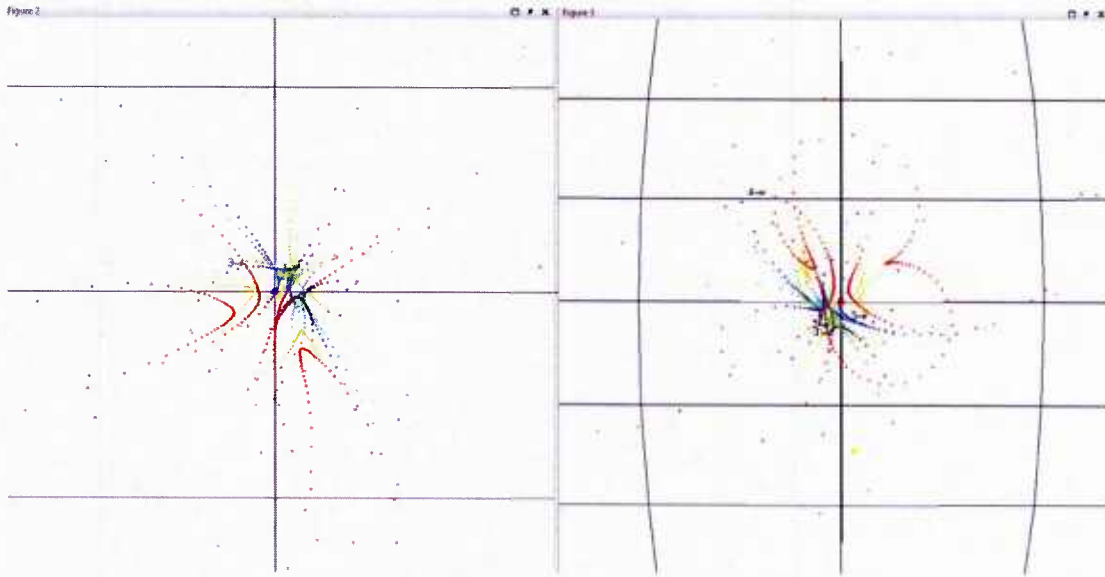
Figure 93. PMD curves for four grid spacings (0.05=Dk Blue, 0.1=Lt Blue, 0.25=Yellow, 1=Red)

Figure 94 shows an additional four curves at even smaller grid spacings. These curves confirm that as the grid spacing continues to decrease, the PMD curves become very similar.
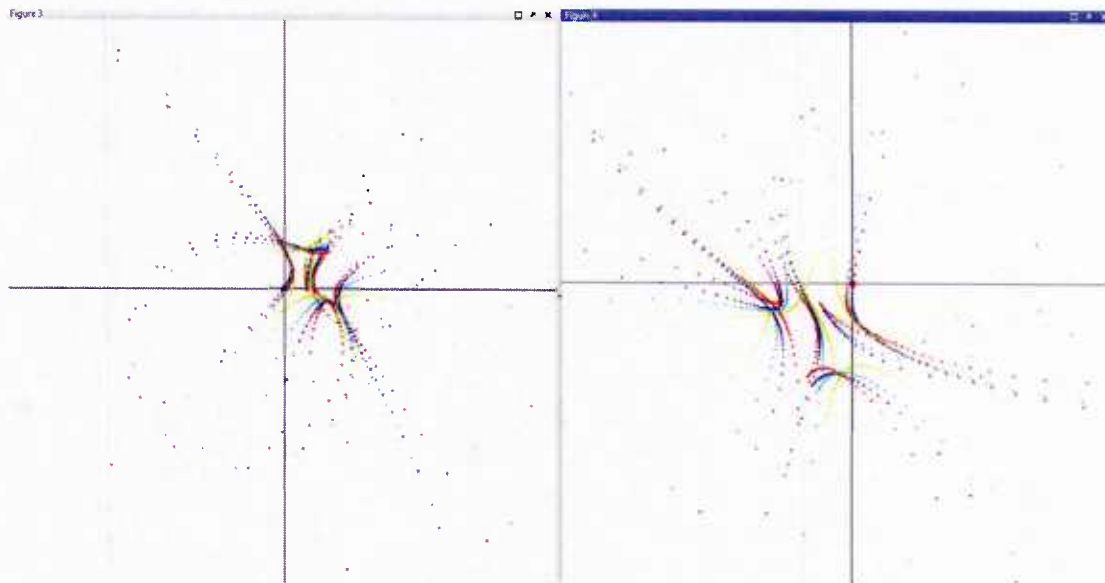
Figure 94. PMD curves for four more grid spacings(0.03=Dk blue, 0.05=Lt blue, 0.07=Yellow, 0.09 = Red)

The plots above (Figure 93 and Figure 94) indicate that for grid spacings of approximately 0.1 meters and below, the resulting PMD curves show convergence. For the magnitude only plots (Figure 91 and Figure 92), the convergence depends

on grid extent with the smaller grid size showing convergence with grid spacings of approximately 0.1 meters and below.

Figure 90 shows the spectrum of wave amplitude as a function of wavelength for the case of wind=10 m/s. The minimum wavelength for the collection of individual waves making up the composite sea surface is approximately 1.3 meters. From a spatial sampling perspective, the grid spacing should be at most half this amount or 0.6 meters.

Based on these considerations listed above, a grid spacing of 0.1 meters by 0.1 meters was selected for subsequent modeling runs.

B. Radar and Target Model Parameters

There are a large number of parameters that control the various clutter, target, and radar models. Many of these parameters were kept fixed for all modeling runs. In this section, we describe both the fixed and varied parameters and provide the range of values used for these parameters.

Radar Topology

The location of both the radar transmitter and receiver are arbitrary in the model. Thus, it is possible to simulate any monostatic or bistatic topology. In the subsequent model runs, the topology is chosen from one of three options:

1. Monostatic mode where the incident angle to the target is at 88 degrees

2. Monostatic mode where the incident angle to the target is at 5 degrees

3. Bistatic mode where the incident angle to the target is at 88 degrees

In all cases, the distance to the target from both the transmitter and receiver was set to 5 km. This distance, when combined with the incident angle and the radar beamwidth, determines the beam footprint on the surface and thus the surface extent modeled.

Target Model

The target model consists of a number of dipoles with random locations within the target extent, random orientations, and random reflection coefficients. In the modeling runs, ten dipoles were used to represent the target and the locations, orientations, and reflection coefficients were randomized but held constant throughout all runs. Table 6 shows the actual values used. The overall target-to-clutter ratio was adjusted over the range of -10 to +10 dB.

Table 6. Individual dipole specifics for 10-dipole model

Orientation (unit vector)	Location (x,y,z) in meters	Reflection Coefficient

-0.1341	0.9129	0.3854	-25.3982	0.9565	-0.0314	0.3362 - 1.0360i	
0.9185	-0.3522	0.1798	-22.3676	0.7803	-0.4893	-0.9047 + 1.8779i	
-0.8830	0.1898	-0.4294	-19.9153	-1.2684	1.3769	-0.2883 + 0.9407i	
0.2638	0.4536	-0.8513	-6.6501	-0.4168	1.2815	0.3501 + 0.7873i	
0.9084	0.1552	-0.3883	20.2061	-2.9543	-1.3638	-1.8359 - 0.8759i	
0.0933	-0.9911	-0.0950	18.4978	2.9516	0.7252	1.0360 + 0.3199i	
0.4960	-0.2634	-0.8274	-26.8005	-2.0295	-0.7039	2.4245 - 0.5583i	
0.8157	-0.3152	0.4850	-6.1428	-2.4011	-0.2353	0.9594 - 0.3114i	
-0.4204	0.7930	-0.4409	1.6388	-0.7780	0.1459	-0.3158 - 0.5700i	
-0.9016	-0.4299	-0.0471	-5.0732	-1.8407	1.3498	0.4286 - 1.0257i	

Sea State Model

The sea height model has a number of parameter settings as described in Section III.C. Table 7 shows the settings used in the modeling runs. The only variable parameter used in the modeling runs was the wind speed, which is set to either 5 or 10 m/s.

Table 7. Summary of sea height model parameter settings

Param	Description	Value
b	Wavenumber spacing factor $(K > K_o)$	1.105
a	Wavenumber spacing factor $(K < K_o)$	$1/b$
d	Fractal dimension $(K < K_o)$	2.1
ξ	Adjusts fractal dimension $(K < K_o)$	3.9
N	Number of waves $(K > K_o)$	40
M	Number of waves $(K < K_o)$	20
α	Phase	Random (uniform)
β	Wave direction	Random (von Mises) $\mu = 0; \kappa = 4$
U	Wind speed (m/s)	5 or 10 m/s
τ	Sea surface tension (N/m)	0.074
ρ	Sea water density (kg/m^2)	1025

Table 8 lists the actual random numbers used for the waveform directions, β_1 and β_2, and phases, ϕ_1 and ϕ_2. The number of values listed for β_1 and ϕ_1 is M (20), while the number for β_2 and ϕ_2 is N (40).

Table 8. Random wave directions and phases

β_1(rad)	β_2(rad)		ϕ_1(rad)	ϕ_2(rad)	
0.1130	0.2900	0.3233	-0.8329	1.2488	0.0030
0.0280	-0.2639	-0.4699	3.0661	-1.8987	-0.1817
0.8486	0.6657	0.2591	-2.9045	-2.9497	-2.7670
-0.3497	0.0661	0.3344	2.4201	1.5336	1.1434
-0.9296	0.1216	0.3042	2.5968	0.0001	-2.8750
0.0363	-0.0666	0.5687	1.8610	-0.1262	-2.6927

0.8951	-0.1463	-0.1685	-2.5214	2.5429	0.1360
-0.0270	0.5682	-0.1884	-1.4962	0.6903	-2.5338
0.4741	0.7083	-0.1844	-1.0345	0.7393	1.9990
-0.8513	-0.3608	0.4017	1.1293	2.2584	1.9952
0.0943	-0.0978	0.3949	-2.2836	1.9194	1.3976
-0.2934	0.3791	0.2133	1.3900	0.4821	-2.2000
1.0893	-0.2907	0.2172	-2.4708	-1.9923	1.0028
-0.5637	-0.0880	-0.1807	0.9661	-1.6341	0.1168
-0.2128	-0.1985	0.2714	-0.0366	2.4285	2.9718
-0.3034	-0.6135	0.0674	1.7533	-2.9614	0.9361
-0.6952	-0.3068	-0.4725	1.3511	-0.0635	1.8870
1.0991	0.0338	0.4315	2.5367	-2.0865	-0.2903
0.0597	0.5634	-0.5212	2.4562	3.0076	-0.4248
-0.6017	-0.1523	-0.7127	-1.0420	1.3364	2.0440

Sea Reflectivity Model

The sea reflectivity model consists of a deterministic component and a fluctuating component. For the deterministic component, the parameters are the following:

- Surface extent: this is controlled by the pulse width and beam widths as discussed under Radar Model

- Surface facet size: 0.1 meter by 0.1 meter (see Section IX.A)

- Transmitter / Target / Receiver topology: this was discussed above under Radar Topology

For the fluctuating component, the correlation between the responses at the receive antennas are modeled as:

$$C_{rx} = C_{tx} = \begin{bmatrix} 1 & 0.1 \\ 0.1 & 1 \end{bmatrix}$$

The relative power between the deterministic and fluctuating components, which is controlled by the K matrix is modeled as:

$$K = k \begin{bmatrix} 1 & 1 \\ 1 & 1 \end{bmatrix},$$

where k is a scalar (normally 1).

The power ratios between the various channel responses are characterized by the copolar ratio, CPR, which is set to 10 dB, and the cross-polarization discrimination power ratios, which are set to $XPD_h = 15dB, XPD_v = 15dB$. *We note that more accurate parameter characterizations can be ascertained from experimental measurements. In the absence of such data, we use the values identified above.*

Radar Model

The radar model includes settings for frequency, pulse width, antenna beam width, pulse repetition interval, and integration time. The following values were used in the modeling runs:

- Frequency: 400 MHz

- Pulse width: 0.5 μs

- Pulse repetition interval: 10 μs

- Antenna beam width: 1 degree

- Integration time: varies per run (up to 10 secs)

C.   Modeling Runs

1.   Polarization Statistics

In each of the simulation runs, nine radar resolution cells (a 3 by 3 grid in range/az space) are considered. Each cell is approximately 87 by 75 meters. The cells are numbered 1 through 9 with the target always in the center cell, number 5. In some figures, the cells are identified using this index (1-9) while in other figures the cells are identified using the coordinate pair indicating the location within the 3 by 3 grid. In such cases, the target cell is identified by the coordinate pair, (2,2).

Figure 95 shows the results for one simulation run (monostatic, 2 deg grazing angle) where the plotted point represents the mean polarization of the received signal for a given radar cell. The mean polarization is averaged across both frequency and time over a period of 2 seconds. The left plot shows results for target-to-clutter ratio of 10 dB while the right plot shows results for target-to-clutter ratio of 0 dB. Note that the target cell (identified by the number 5 in both figures) is distinct from the other cells providing a possible means of detection.
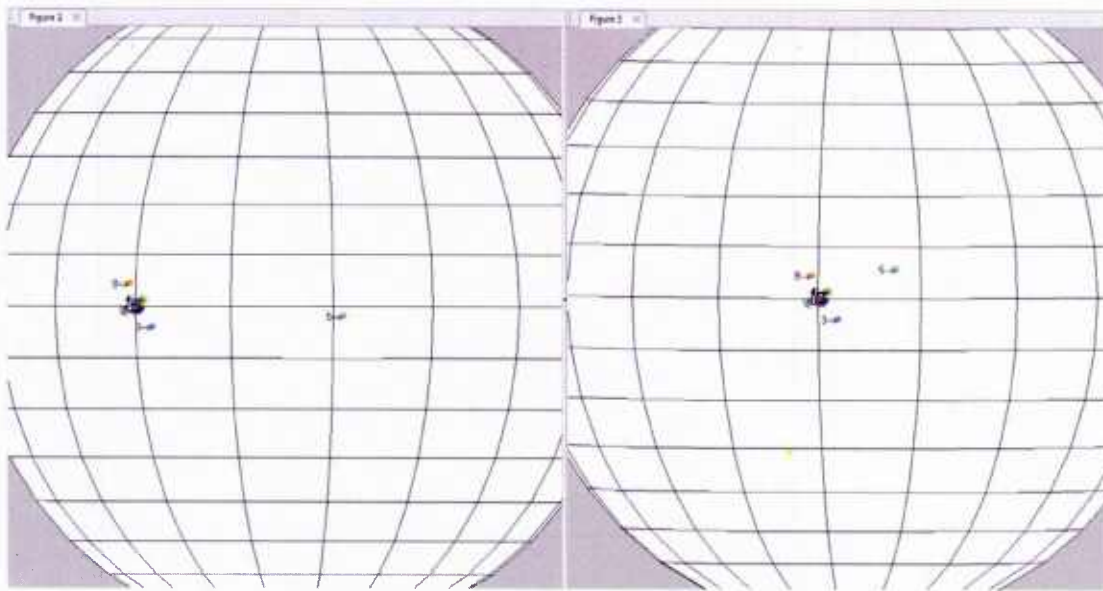
Figure 95. Mean polarization (left T/C=10 dB, right T/C=0 dB)

Figure 96 shows the same results, but instead of calculating the mean polarization of all the polarization points (versus time and frequency), the cumulative distribution function for all points are shown. Again, the left plot shows results for a target-to-clutter ratio of 10 dB, while the right plot shows results for a target-to-clutter ratio of 0 dB. Note that in both plots, the cell with the target (magenta trace) is distinct from the other cells. This is particularly evident for the left plot.

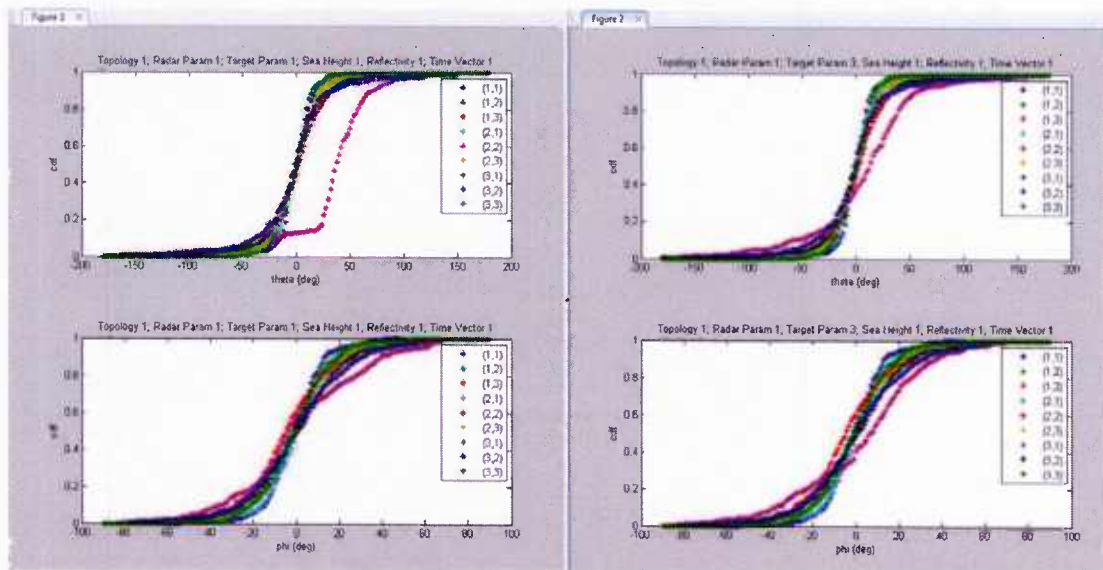*Figure 96. CDF of polarization (left T/C=10 dB, right T/C=0 dB)*

Figure 97 shows the received signal power for each of the radar cells where the colored traces represent the various polarization channels. These plots provide data typical for conventional (non-polarimetric) processing where the receive

139

power in a given cell is compared to the power in the surrounding cells. Note that in the right plot (T/C = 0 dB), the power in the target cell (2,2) is not easily distinguishable from that of the clutter cells, especially for the VV case. In these results, clutter-limited detection is assumed, and hence the noise component is not considered.
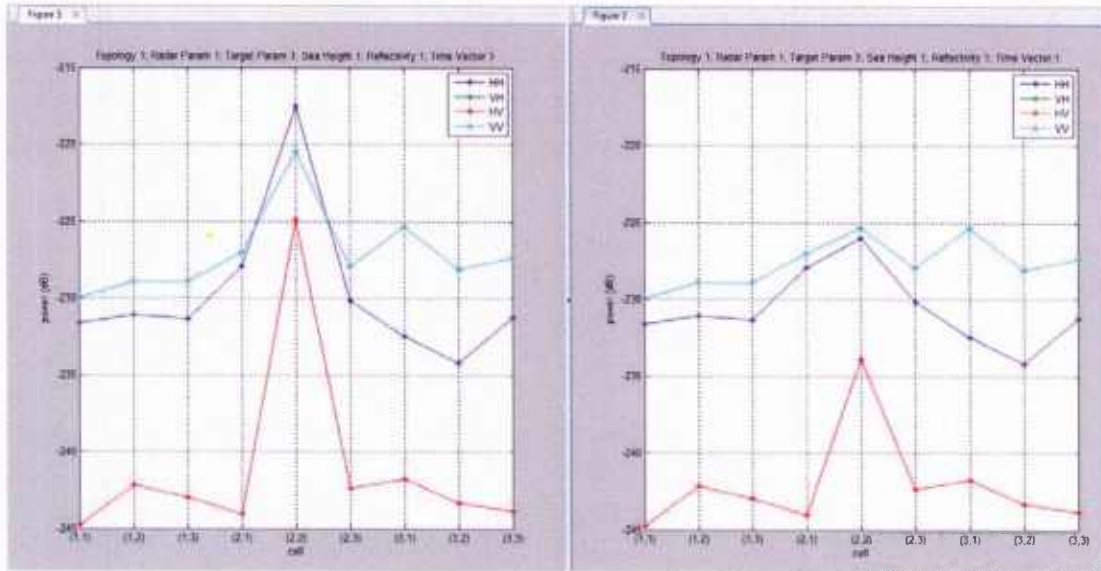
Figure 97. Received signal power as a function of radar cell (left T/C=10 dB, right T/C=0 dB)

Figure 98 (T/C = 10 dB) and Figure 99 (T/C = 0 dB) show results for another modeling run with a monostatic system at near-normal incidence (a 5 degree incidence angle). These plots are similar to those described above, but the plots are combined differently. The mean polarization is shown in the left plot while the CDF is shown on the right. This format emphasizes the relationship between the mean value and the full statistical distribution (shown in the CDF). The full distribution represented in the CDF provides more information than the mean alone. For example, it is possible for the mean value of the target cell to be indistinguishable from the surrounding clutter only cells, but for the CDF of the target cell to differ from the surrounding cells. However, in these plots, both mean and CDF are distinguishable from the surrounding cells.

140
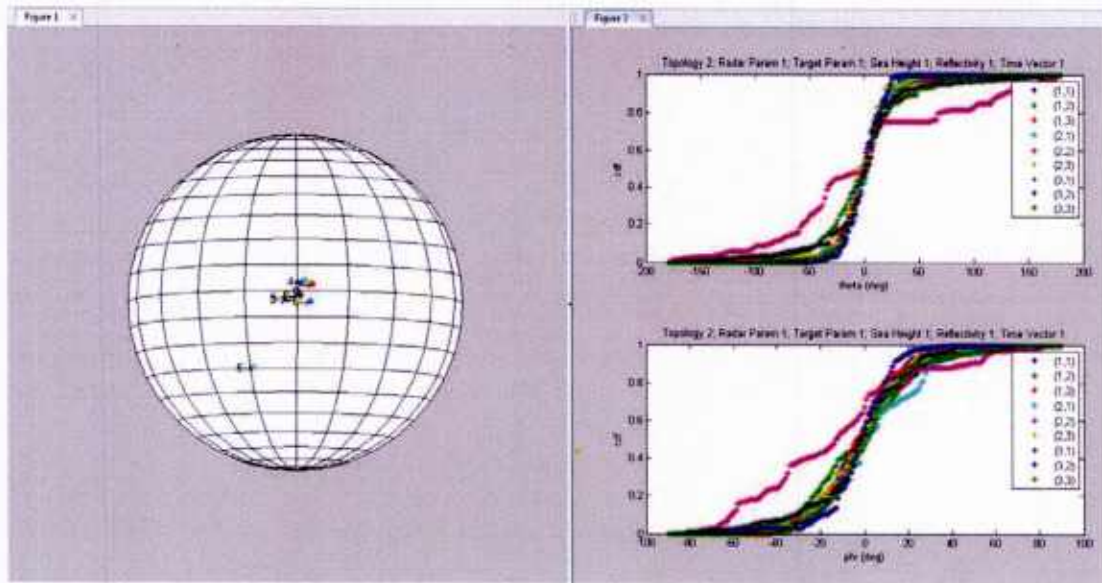
Figure 98. Mean polarization and CDF for monostatic near normal incidence (T/C = 10 dB)

Figure 99. Mean polarization and CDF for monostatic near normal incidence (T/C = 0 dB)

Figure 100 shows the results when processing each cell for power only. Note that in the right plot where T/C ratio is 0 dB, the target cell is indistinguishable from the surrounding cells. Also, even in the left plot with T/C ratio of 10 dB, the VV power is indistinguishable from the clutter only cells.
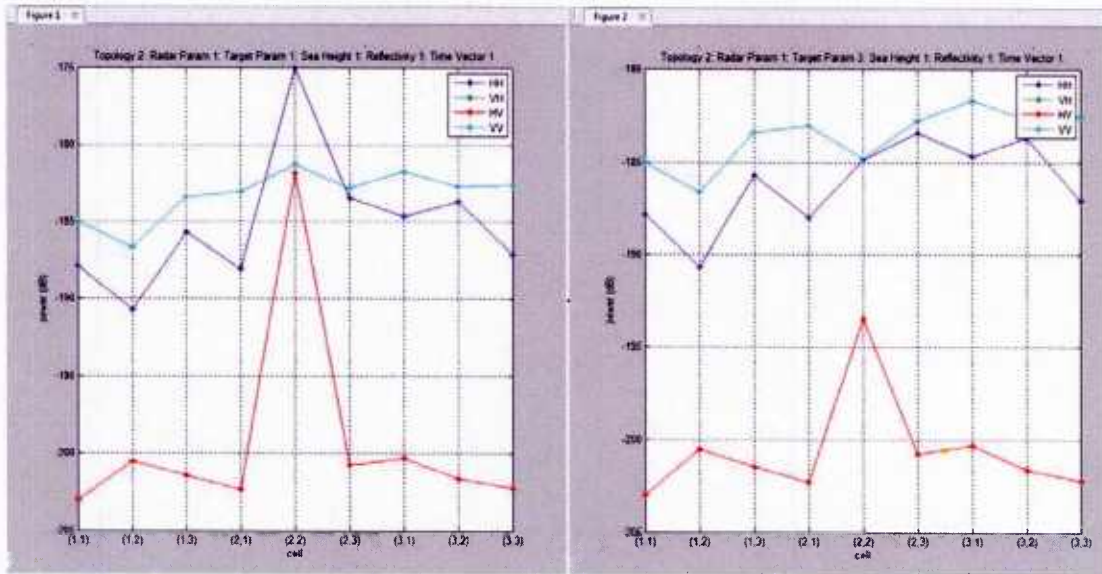
Figure 100. Received signal power versus radar cell, monostatic, near normal (left T/C=10 dB, right T/C=0 dB)

Figure 101(T/C = 10 dB) and Figure 102 (T/C = 0 dB) show results for another modeling run with a bistatic system and grazing incident angle (88 degree incidence angle). In Figure 101, the mean polarization for the target cell is nearly on the opposite side of the Poincare sphere relative to the clutter only cells.

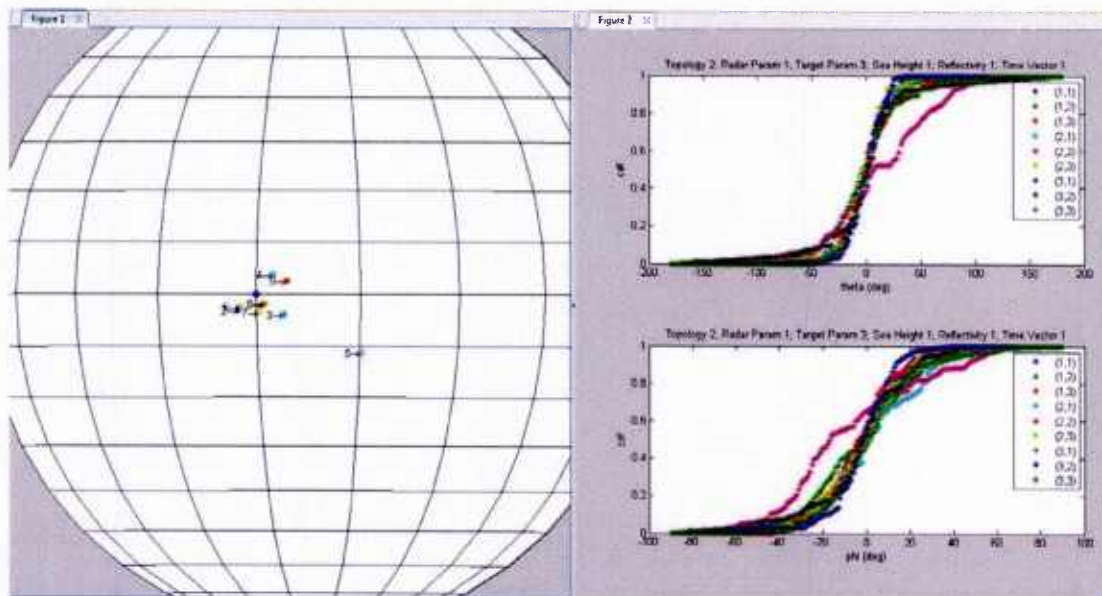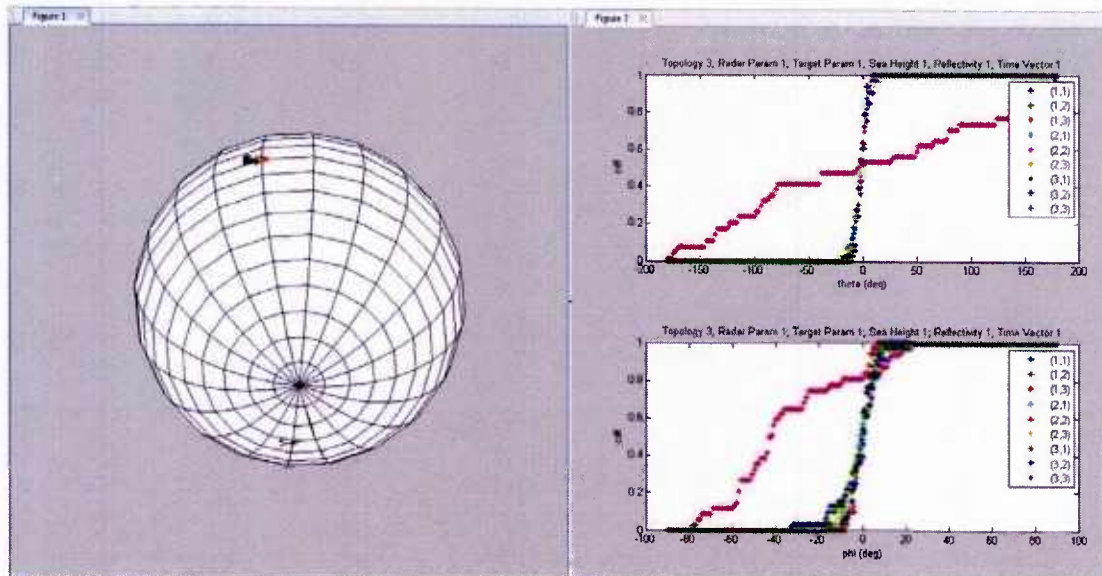*Figure 101. Mean polarization and CDF for bistatic grazing incidence (T/C = 10 dB)*
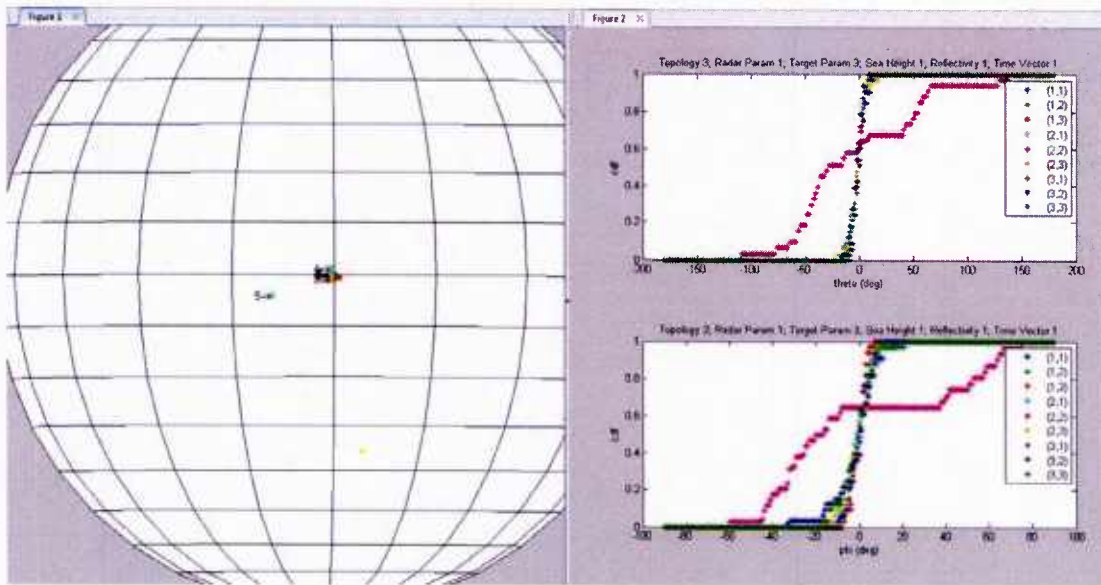
Figure 102. Mean polarization and CDF for bistatic grazing incidence (T/C = 0 dB)

Figure 103 shows the results when processing each cell for power only. This plot is similar to previous such plots in which the target cell is distinguishable in some cases (e.g., left plot VV trace) and not in others (e.g., left plot HH trace).
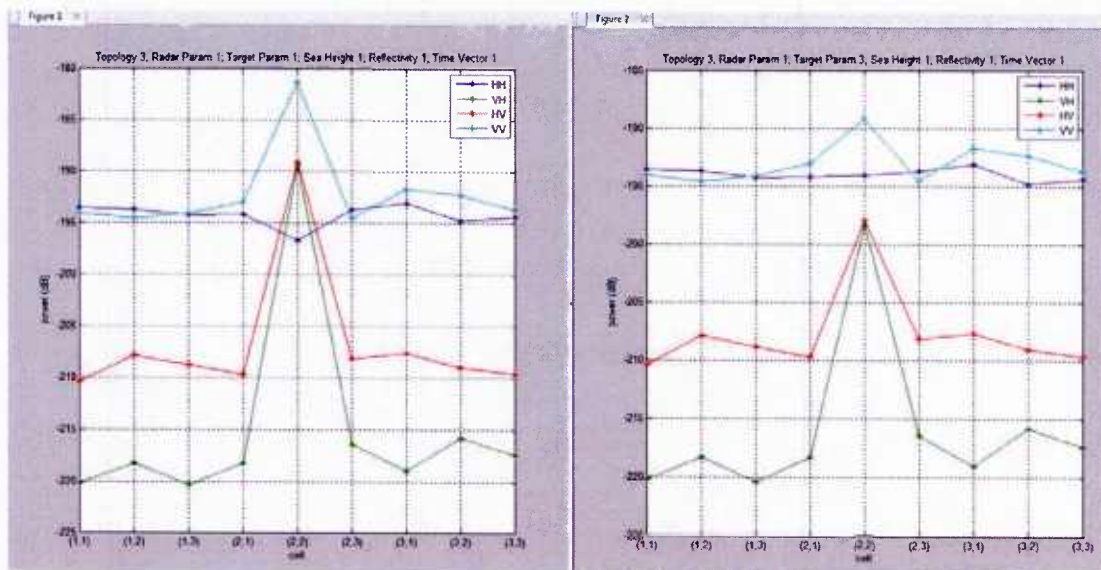
Figure 103. Received signal power versus radar cell, bistatic, grazing incidence (left T/C=10 dB, right T/C=0 dB)

In all of the previous plots, the polarization statistics (including mean value) from clutter-only radar cells is very similar. With the addition of a target to a given radar

143

cell, even small changes to the polarization mean value are distinguishable from the clutter-only radar cells.

2. ROC curves

In the previous section, results were presented showing the statistical characteristics of both clutter-only and clutter-plus-target cells. These results qualitatively show the potential for using polarimetric techniques for detecting the presence of a target in a given radar cell. However, in order to evaluate quantitatively the performance of such techniques, it is necessary to introduce one or more target detectors.

The first detector is a traditional power detector. This detector computes the power in either the HH or VV response and sums the power across frequency. The results for this detector are used as the baseline for evaluating other detectors.

The second detector is identified as the "S0" detector. This detector is based on the Stokes S_0 parameter and is similar to a traditional power detector except that it combines both co-polarized and cross-polarized signal components. The Stokes parameters are calculated for each subband within the full signal bandwidth and then summed to obtain the detector value. Because of the similarity of this detector to a traditional power detector, the results are expected to be similar to (but in some cases superior to) those of the traditional power detector.

The third detector is identified as the "PMD-pc" detector (the "pc" designation indicates *power coupling*). This detector computes a PMD curve (polarization versus frequency response) for each of the nine radar cells. A "reference" curve is computed based on the average of the nine cells and then each individual PMD curve is compared to the reference curve by computing a "distance" between the individual curve and the reference curve. The distance is a sum of the subband distances between corresponding subbands in the individual and reference curves.

In future research additional detectors will be considered to detect and identify targets and features in clutter.

In the current simulation runs, a reference curve is generated at each time step from the 9 range/az cells for that time step. The model runs used for this presentation contain "uncorrelated" time steps such that the sea surface was randomized at each time step. This was necessary to facilitate the collection of statistics needed to generate the various ROC curves.

The following figures show the results for two wind speeds (10 m/s and 5 m/s) and two target-to-clutter (T/C) ratios (0 dB and -10 dB). All cases involve a monostatic radar with a target at low grazing angle. For each figure, the top subplot shows results for Tx-H and the bottom subplot shows results for Tx-V.

Figure 104 shows the ROC curves for the case of wind speed = 10 m/s and a T/C = -10 dB. For this case, the performance of all detectors is roughly equal with none of the detectors able to distinguish the target from clutter.
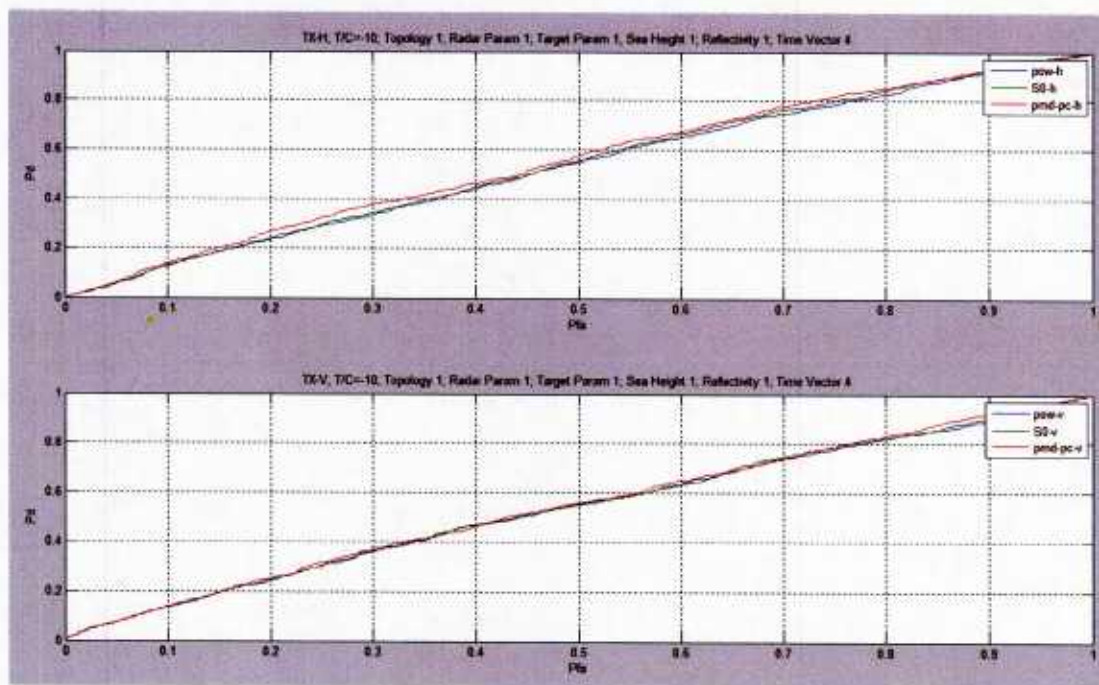
Figure 104. ROC curve, wind speed = 10 m/s, T/C = -10 dB

Figure 105 shows the results for the case of T/C = 0 dB. For this case, the results are dependent upon the transmit polarization. In the bottom plot with Tx-V polarization, the performance of all detectors is roughly equal. In the top plot with Tx-H polarization, the "PMD-pc" detector shows significant improvement over the other two detectors.

Figure 105. ROC curve, wind speed = 10 m/s, T/C = 0 dB

Figure 106 shows results for the case of wind speed = 5 m/s and T/C = -10 dB. The results are similar to the results for the case of wind speed = 10 m/s with none of the detectors able to distinguish the target from clutter.
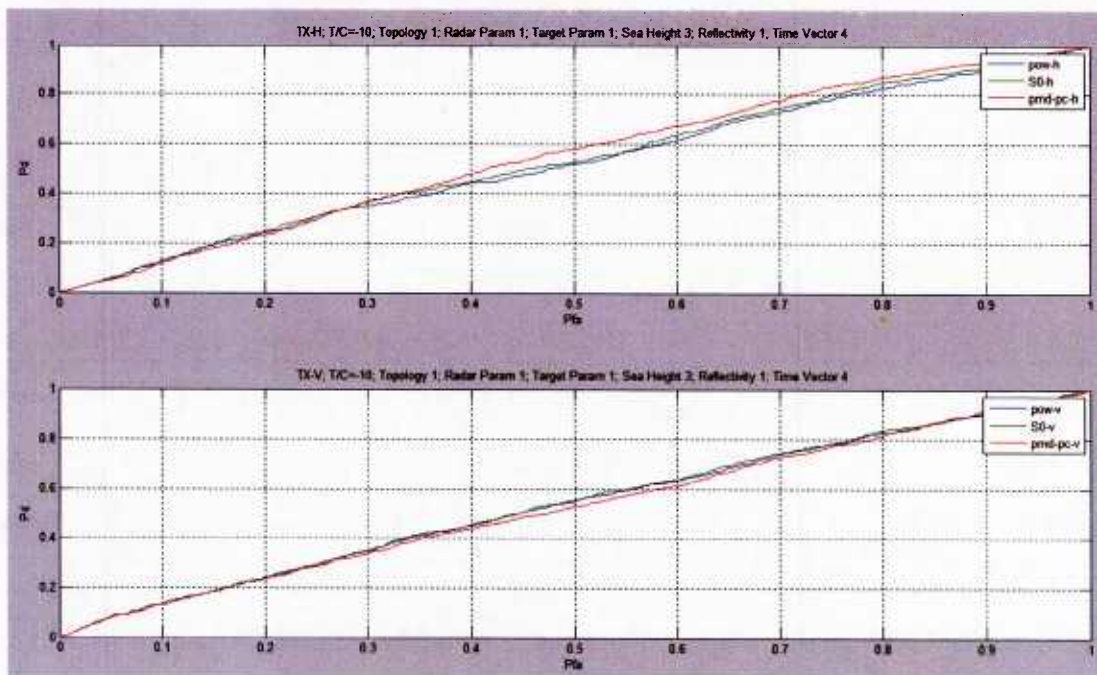
Figure 106. ROC curve, wind speed = 5 m/s, T/C = -10 dB

Figure 107 shows the results for T/C = 0 dB. As was the case for wind speed = 10 m/s, the results are dependent upon transmit polarization. For the bottom plot with TX-V polarization, the performance of all detectors is roughly equal. For the top plot with TX-H polarization, the "PMD-pc" detector is superior for high false alarm rates, but in the critical area of low false alarm rates (Pfa<0.1), the "S0" detector is superior with the other two detectors approximately the same.
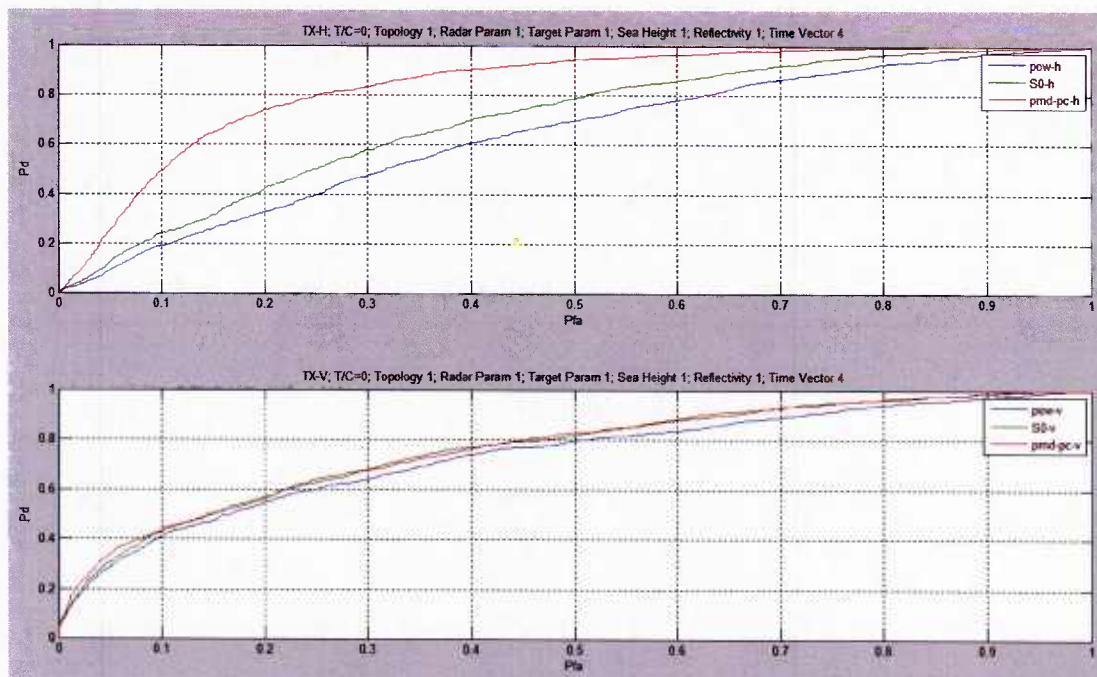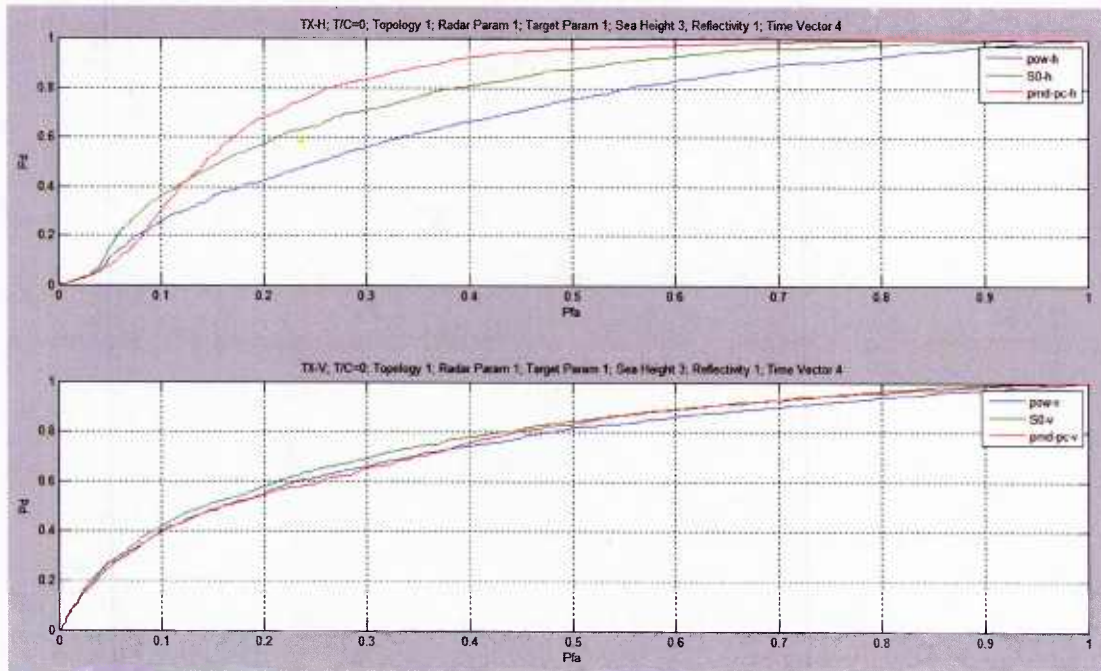

Figure 107. ROC curve, wind speed = 5 m/s, T/C=0 dB

Figure 108 shows results for the case of wind speed = 10 m/s and T/C = -10 dB. These are the same conditions as previously shown in Figure 104. The only difference in this case is the random starting phase for the target roll, pitch, and yaw attitudes. In this run, the target is indistinguishable from clutter for the case of TX-V polarization (which was also true in Figure 104). But, for the case of TX-H polarization, there is a noticeable advantage for the "PMD-pc" detector.
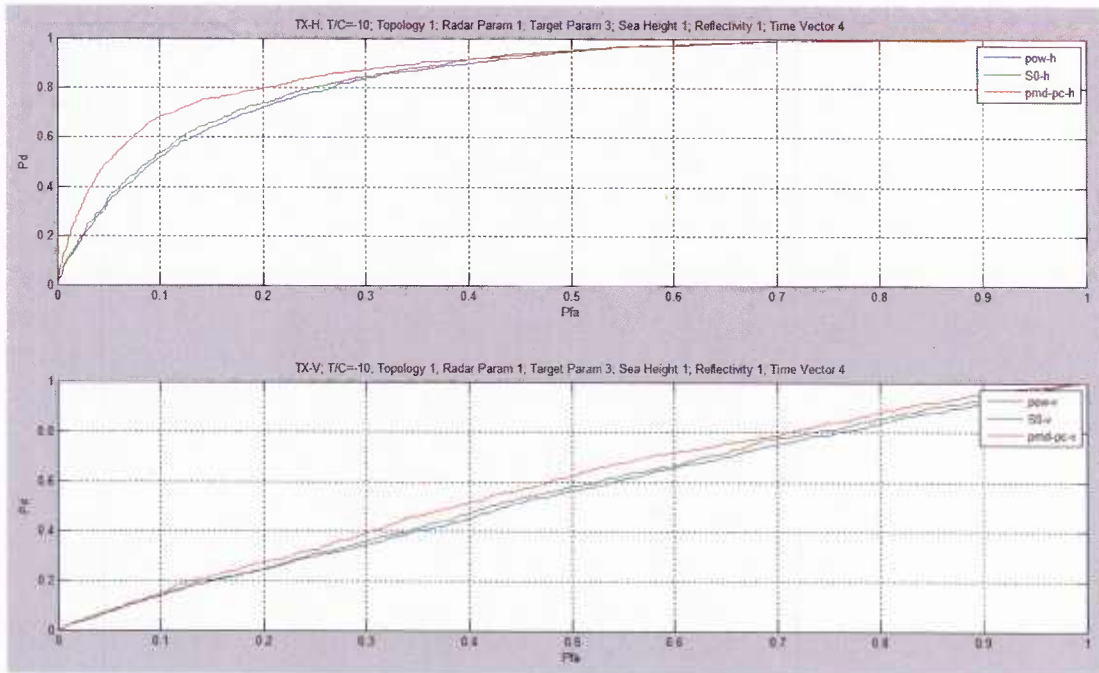
Figure 108. ROC curve, wind speed = 10 m/s, T/C = -10 dB

The difference in results shown in Figure 104 and Figure 108 is surprising given that the only difference is the starting orientation of the target. This implies that the ability to distinguish target from clutter is quite sensitive to the target orientation. At certain orientations, the polarization of the target return does not differ enough from the clutter polarization to enable detection.

One item of note in the preceding figures is that the "S0" detector shows at least equal and in some cases superior performance to the "pow" detector. This is not surprising given that the "S0" detector includes the power contributions from both H and V receive signals. In this sense, it is akin to a diversity detector where it achieves performance levels similar to the receive port (H or V) with the highest power.

Another item of note in the preceding figures is that the "PMD-pc" detector sometimes outperforms the other two detectors (or at least performs equally well). This indicates potential detection advantages with such a detector. However, as shown in Figure 107, there are cases where this detector does not perform particularly well at low probabilities of false alarms, which is where systems

typically operate. This characteristic of this detector is not yet understood at this time and warrants further investigation.

3. *Statistical processing over time / frequency*

A final topic to consider regarding the ROC curves presented above is that the detectors are formed from the results obtained from a single time sample. The reference curve for the "PMD-pc" detector is calculated based on the surrounding eight clutter-only cells. With only eight such cells and a single time sample, the statistics for the reference curve are not likely representative of the larger sea surface. By collecting statistics for a longer time (as the sea surface changes) or over a much larger sea surface area, the reference curve will be a better representation of the larger sea surface and enable better detection of the target cell.

One approach for processing results from multiple time samples involves computing statistics for the collection of time/frequency samples over a specified dwell time. In this approach, the statistics are used to estimate the Cumulative Distribution Function (CDF) over the dwell. Detection for a given cell is based on the estimation of the CDF curve for the given cell as compared to the collective CDF curve of all cells.

There are two processing algorithms considered:

- Stokes processing: computing Stokes parameters as a function of frequency subband and estimating CDF curves for each parameter individually
- Conventional processing: creating CDF curves using the magnitude response for either HH or VV

In both cases, the measure of the similarity of a given cell's CDF to the reference CDF is based on the RMS "distance" between the two CDFs. This distance is normalized by the RMS distance of all of the curves from the various range/az cells at each point of the CDF. The following paragraphs and figures illustrated the processing approach.

Figure 109 shows an example of Stokes processing where the 8 subplots show the CDF curves for the 4 Stokes parameters for both H and V transmit (the four plots on the left represent H transmit and the four on the right represent V transmit). On each subplot, the traces represent the 9 radar cells as well as the "reference" curve (black) representing the average or collective CDF. The magenta trace represents the center radar cell which includes the target.
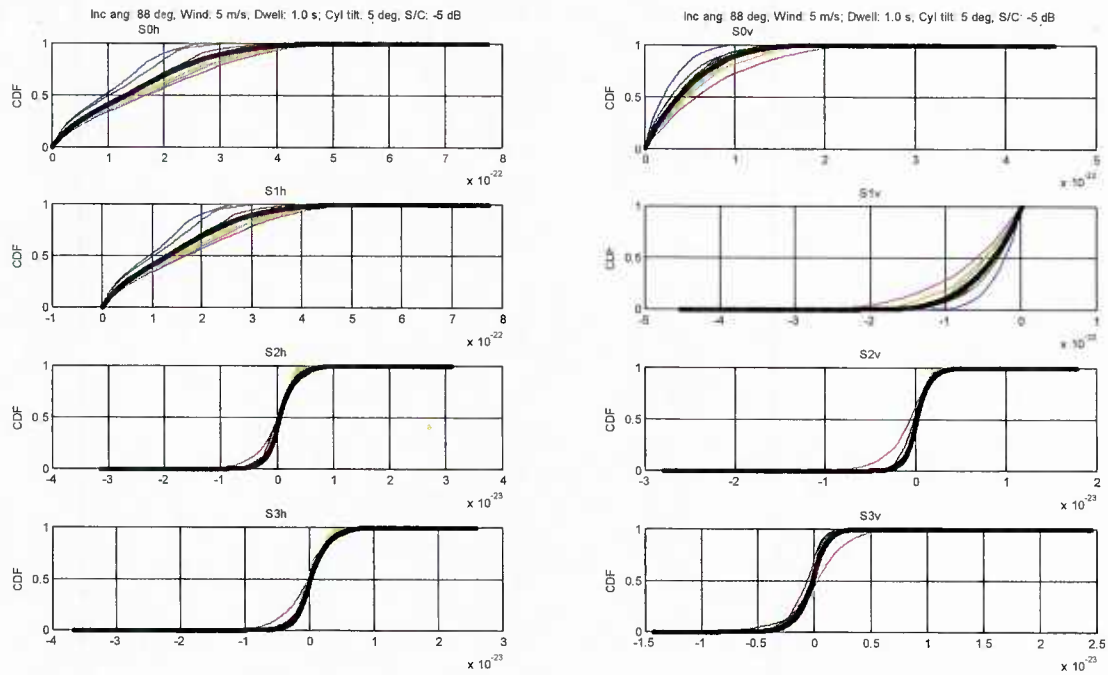
Figure 109. CDF estimate for Stokes paramters over 1 sec dwell

Figure 110 shows the calculation of the RMS "distance" between the CDF for a given cell versus the reference CDF for each of the individual Stokes parameters (S1 to S3). The 3 by 3 grid of radar cells are indexed 1 to 9 (x-axis) with index 5 as the center cell (target cell). Note that the target cell, cell 5, typically shows a peak indicating that the CDF for cell 5 is relatively "far" from the collective CDF. However, also note that for some of the Stokes parameters there are other cells that have high detection values (for example, cells 8 and 9 from the top left subplot).
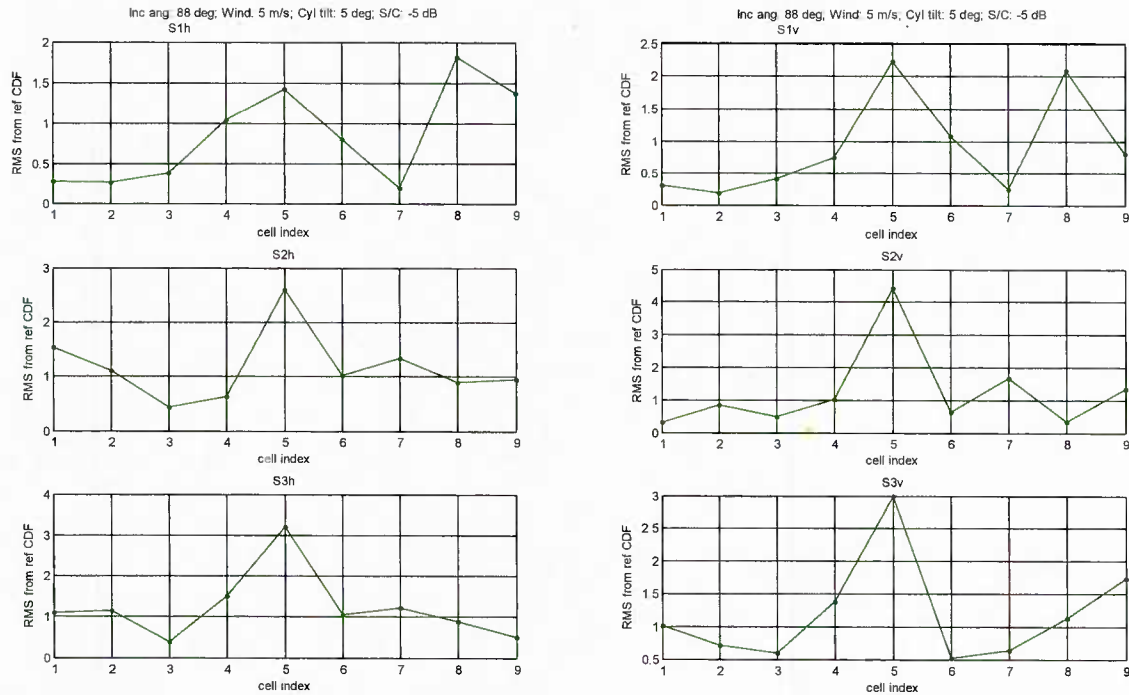
Figure 110. Detection for individual Stokes parameters

Figure 111 shows the results of combining the RMS distances of the individual Stokes parameters (S1 to S3) to form a single metric (TX-H on left, TX-V on right). Note again that the target cell, cell 5, shows the highest detection value for both H and V transmisions.
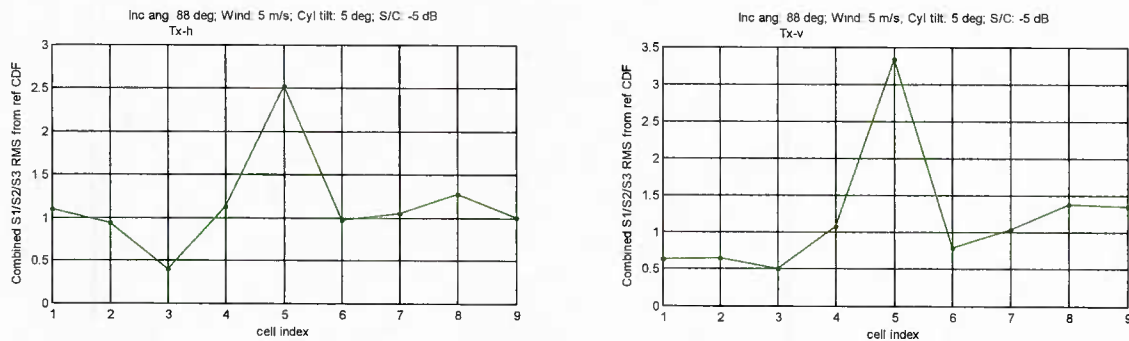
Figure 111. Detection for combined Stokes parameters

Figure 112 shows the results for several dwell times (indicated in the figure legend). The results for a dwell time of 1 sec are the same ones previously presented in Figure 111. Note that for longer dwell times, the detection values become better for the target in cell 5, as expected.
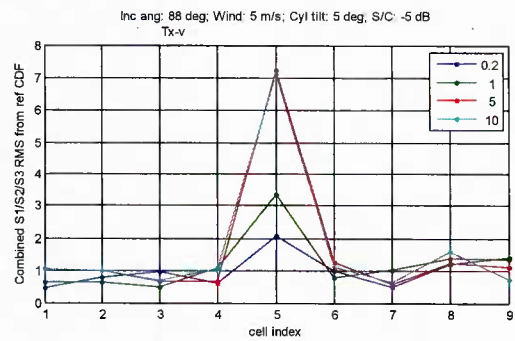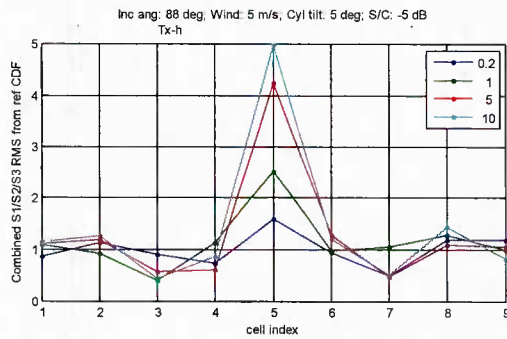
Figure 112. Detection as a function of dwell time

The preceding paragraphs and figures describing the processing approach using CDF estimates from all time / frequency samples within a user-defined dwell are not presented in order to show specific results for a given target and set of conditions. Rather they are presented in order to show a promising processing approach that deserves additional investigate in future research efforts. This processing approach may be exercised over a wide range of target, radar, and sea surface parameter combinations in order to evaluate the potential of this approach.

X. ADDITIONAL TOPICS

A. *Polarization-Based Interference Suppression*

Electromagnetic energy falling within appropriately designed receiver suppression filters can be used to suppress interference, for example to suppress the clutter response for radar detection of a target. When Doppler discrimination between the clutter and the target is not feasible and when the clutter and target are co-directional, suppression filtering based on space and frequency cannot readily be applied. However, discrimination based on polarization responses may be feasible. The particular technology being considered in this section involves the exploitation of polarization-frequency characterizations, where polarization dispersion effects versus the signal frequency components are considered. With this technology polarization-frequency domain filtering may provide a viable means to help separate a target from clutter returns. The purpose of this section is to provide qualitative assessments of different polarization-based suppression methods, including polarization and polarization-frequency techniques, to support the radar detection problem. Polarization-based techniques to be considered include those of Compton [57], Pratt and Walkenhorst [9][10][15][48], and Sparrow [79].

Compton

Compton proposes the use of polarization filters to suppress narrowband signals. Polarization suppression techniques offer unique capabilities that are distinct from those of adaptive arrays. Arrays, for example, form directional nulls using digital signal processing where minimum mean square error (MMSE) solutions are formed to maximize the resulting signal to noise ratio. However, if the desired signal is in the direction of the interference, both the desired signal and the interference are subject to filter suppression effects, limiting achievable Signal-to-Interference (SIR) ratios. In more advanced space-time adaptive processing (STAP) systems, where delay taps are combined with array element, an additional dimension is applied that enables joint space-frequency suppression. These techniques enable the processor to suppress interference exhibiting delay spreads due to temporal dispersion induced by the channel. However such processing still has limited application for interference that is co-directional with the desired signal, especially for signals with comparable Doppler frequencies. In contrast, polarization-based techniques provide a degree of freedom that enables suppression of interference that is co-directional with the desired signal. The optimal polarization filter maximizing the SIR is related to the null polarization of the interference, the polarization of the desired signal and the signal-to-interference power ratio (SIR) level, as presented in [80].

The polarization suppression technique described above is ultimately a narrowband suppression technique that is suitable when the interference signal exhibits flat

fading across the signal bandwidth and hence can largely be mitigated by the same polarization filter. In frequency-selective multipath channels, such as exhibited by a target in a background of sea clutter when linear frequency-modulated (LFM) radar waveforms are used, a single filter would not be adequate to suppress the interference across the entire signal bandwidth. The Compton technique must therefore be extended to provide suppression capabilities as a function of the interference frequency components, as described next.

Pratt and Walkenhorst

In multipath channels with temporal dispersion (delay spread) and polarization coupling (depolarization), the polarization state of a signal is known to be dispersive in polarization. In other words, the signal polarization state at the receiver will vary with the signal's frequency components, a phenomenon referred to a polarization mode dispersion (PMD). Because of PMD, a single polarization filter will not be sufficient to suppress interference in a frequency-selective multipath channel. Rather, it is necessary to employ distinct polarization filters as a function of the subband of the received signal. Methods for such PMD-based suppression have been described in [9][10][15][48]. The basic idea is to divide the received signal into frequency subbands, apply polarization filtering within each subband, and then combine the residues. Equalization of the residue signal can then be applied (for example in a communications system) to compensate for the polarization filtering effects to enable decoding. The actual processing can be applied either in the time domain or the frequency domain, and different suppression algorithms can be applied as well, such as zero-forcing or MMSE suppression. The suppression filtering is typically applied in digital signal processing, i.e., after the analog-to-digital converter. This approach has been demonstrated using a wideband communications testbed at the University of Notre Dame and would likely have direct application to radar detection of a target in sea clutter.

A challenge, however, is to elicit a PMD response using suitable waveforms and receiver signal processing. Measurement of the PMD response, or a comparable characterization, is needed for each radar resolution cell so that frequency-dependent polarization filters can be applied. For example, conventional processing of LFM waveforms, such a "stretch processing", would not lead to PMD characterizations, and alternative receiver processing is needed to identify and apply suitable frequency-dependent polarization filters. Therefore, some thought must be given to the design of the radar waveform and the receiver processing algorithm that operates on the radar echoes.

Appropriate designs will facilitate frequency-dependent polarization-based filtering. Assuming polarization filtering can readily be applied, an important question is how the polarization filters should be set to suppress clutter. Although this is an open problem, one candidate approach is to identify the average polarization response as

a function of radar waveform frequency in the cells around the target cell and use this estimate to design the polarization suppression filter for the target cell. In so doing, the clutter response in the target cell is expected to be largely suppressed, leading to higher visibility of the target response.

Sparrow

Another approach to be briefly described is a suppression approach described in [79], where interference suppression filtering is applied in the analog RF domain prior to analog-to-digital conversion. The approach is based on the use of a nulling network, such as the one shown in Figure 113, providing a form of zero-forcing. The nulling network is a two-port in two-port out device consisting of a phase shifter segment, a hybrid, another phase shifter section, followed by another hybrid. The two outputs correspond to the matched polarization response and to the null response. To achieve the null, the phase shifters are set based on measured polarization parameters of the received signal. The approach described in Sparrow addresses only narrowband suppression, where the polarization filter is applied across the entire signal bandwidth, which clearly would not be suitable in a frequency-selective environment. In such a case, the Sparrow approach would have to be applied across all of the frequency content of the signal.
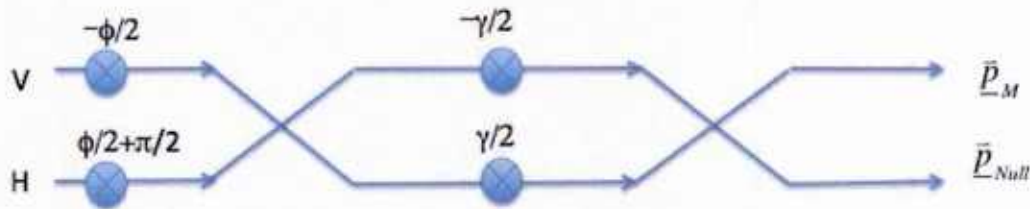
Figure 113. Nulling network from [Sparrow]

Pratt

An extension of this approach has been described in [48] and [80], involving an analog version of the PMD-suppression techniques. The method relies on a bank of analog filters, each similar to the Sparrow network, or other suitable filter, to enable frequency-dependent polarization suppression in the analog domain. This front-end applique is anticipated to help provide improved dynamic range in environments with strong interference (typical of radar and other cosite arrangements) that cannot be achieved after analog-to-digital conversion in digital signal processing.

B.   *Adaptive Polarization Transmission Techniques*

Adaptive transmission has been widely considered in radio frequency systems as a strategy for enhancing system performance. The premise of these approaches is to obtain channel state information at the transmitter and then to use this information to adapt transmissions to improve the system performance according to some metric (e.g., capacity). An obstacle to implementing adaptive techniques is the need to obtain channel state information and to obtain it in a timely manner. In communications systems, the most practical approaches that have been considered include measuring the channel directly from a transmission from the intended receiver, for example in a time-division duplex (TDD) communications system. A second approach is to have the intended receiver measure the channel and provide feedback to the transmitter through a separate control channel. In the case of monostatic radar systems, the channel state information can be measured directly on a pulse-to-pulse basis, suggesting that adaptive techniques can readily be applied in radar systems.

Several adaptive schemes have been discussed in literature, including for communications systems that take advantage of channel state information at the transmitter (CSIT).   In these systems, CSIT is normally leveraged so that data can be transmitted over the eigenmodes of the channel, usually with the purpose of maximizing system capacity. These systems often use waterfilling methods to distribute power among the eigenmodes. We anticipate that radar systems can similarly leverage CSIT to benefit radar system performance through adaptive transmission schemes.

In the specific case of RF systems with transmit *polarization* agility, polarization modulation schemes can be applied either in a blind fashion without channel state feedback, or in an adaptive fashion when CSIT is available.   One example of a blind implementation involves switching between two orthogonally-polarized states [Sibecus] to help reduce the impact of polarization-related degradation. Similar methods have been proposed in optical fiber communications systems [81].   Others have used polarization switching to help reduce peak-to-average-power ratios and to improve intercarrier interference tolerance by doubling the co-polarized subcarrier spacing in an OFDM system [82][83]. A wide variety of blind polarization modulation techniques are considered by [84], where equalization at the receiver is used with pilots to aid in the recovery of the polarization state.

Channel state information for systems with dual-polarized antennas facilitates the possibility of adaptive polarization transmission schemes. Apparently, very few examples of adaptive polarization transmission are available in open literature. In a patent by [79] dealing with electronic warfare system technology, adaptive polarization transmission systems are described that are designed to degrade adversarial RF systems. In these EW systems, the polarization state of the signal

from the adversarial system is measured, and a polarization network or a digital RF memory is used to respond with a transmission that controls the polarization to achieve effective electronic attack. Others have considered adaptive polarization control, primarily for adaptive power control among the dual-polarized antenna elements [85][13]. The above systems address narrowband adaptation, where the polarization response is applied across the entire bandwidth of the transmitted signals. Polarization control, however, can also be adapted on a wideband basis, and adaptive polarization transmission methods have been proposed to exploit the system eigenmodes for wideband communications [49].

In [11], wideband adaptive polarization transmission techniques were analyzed to achieve a number of interesting effects at the receiver. Primary contributions of this work included the strategy of adapting the polarization state as a function of the frequency subband due to PMD effects, and also recognizing various ways that such control could be used to achieve different signaling effects at the receiver. Adaptive transmission strategies that were identified and considered included: 1) maximizing the SNR, which is akin to eigenmode analysis; 2) interference avoidance (e.g., achieving a null at a specified receiver antenna); 3) facilitating simple MIMO processing at the receiver by achieving orthogonal signals at a receiver with a dual polarized antenna; 4) achieving zero polarization dispersion across the signal bandwidth, and other strategies.

Several of these adaptive schemes may have relevance to monostatic radar processing, where CSIT can readily be measured at the radar after each pulse (or as needed) in order to adapt subsequent transmit polarizations to enhance system performance. We now qualitatively consider the application of some of these strategies to the radar detection problem.

Maximizing the SNR

RF multipath channels typically exhibit both polarization mode dispersion and polarization dependent loss. Due to the impact of polarization dependent loss, power transfer between the transmitter and receiver will depend upon the transmit polarization state. The transmit polarization state that optimizes power transfer through the channel will depend upon the particular frequency component of the signal. Therefore, we fully anticipate that by adapting the transmit polarization state versus frequency, maximum power transfer can be achieved as a function of frequency through a multipath channel for a particular radar resolution cell. In the acquisition phase, the transmitted waveform is typically used to interrogate a large number of different resolution cells. Since each resolution cell will exhibit different multipath structure, the method would not yield an optimal response for each resolution cell, but rather for a single cell. For these reasons, we would not expect this method to be particularly relevant to the acquisition phase.

The methods could apply to the track mode. When a track is established, the transmit waveform can be designed specifically to optimize the power transfer associated with the target cell. It is important to note that SNR maximization techniques will not necessarily improve target detection performance in clutter-limited environments. However, transmit polarization control may facilitate maximization of target returns relative to the clutter, for example by measuring the statistics of the clutter in adjacent resolution cells and setting the transmit polarization accordingly. Additionally, receiver processing, such as polarization-based nulling could also be applied to enhance discrimination.

It should be noted that any polarization changes imparting amplitude and phase modulations on the radar waveform will modify the transmitted spectrum and would require equalization at the receiver to limit their effects on pulse compression gains. Such effects can be minimized or eliminated through the use of diversity transmission, where orthogonal transmit polarizations are transmitted in a manner that they can be separated at the receiver. Virtual transmit control can be achieved at the receiver by using weighted combinations of the separable signals.

A summary of the key points that have been discussed includes the following:

- Direct transmit polarization control would be valid only for a single resolution cell since each cell has a different multipath structure, and therefore may be best suited for the target tracking mode.

- A more flexible solution is to provide coherent H/V transmit schemes that are separable at the receiver so that any arbitrary transmit polarization can be reconstructed at the receiver. This provides maximum flexibility and also provides a form of diversity.

- Polarization control for SNR enhancement would not be useful in clutter-limited environments. Polarization control for target/clutter discrimination would likely be more useful. Schemes to determine appropriate polarization values would have to be tested. For example, polarization values could be keyed to the noise resolution cells about the target resolution cell.

Interference Avoidance

Interference avoidance involves controlling the transmit polarization to elicit a null response in one of the antenna ports at the receiver. The method requires "channel" knowledge in order to adaptively set the transmit polarization state. To obtain this channel state information in the case of radar, the response associated with each resolution cell would need to be measured from the returns, and in general, the channel response from these resolution cells would be different. As with SNR maximization, when direct polarization modulation of the transmit waveform is

applied, nulls for each resolution cell cannot be simultaneously programmed onto the waveform, i.e., a null can only be established in a single resolutions cell. We conclude that the approach using a directly modulated transmission is not useful in acquisition modes, but perhaps could be used in tracking modes to help elicit target features from a known target cell.

A more flexible approach to achieving an interference avoidance capability for all resolution modes is to design the transmit signal with phase-coherent H and V transmission that are separable at the receiver (e.g., separable in time or frequency subcarrier). The receiver can then employ digital signal processing such as weighted combining to achieve interference avoidance on all of its received ports and for all resolution cells, a capability that generally could not be achieved through direct modulation of the transmit waveform.

Achieving Zero Polarization Dispersion

Another possible strategy in adaptive transmission systems is to control the transmit polarization state to achieve a signal at the receiver exhibiting zero polarization dispersion. In other words, the received signal would have an identical polarization state across the entire signal bandwidth. For a given polarization-compensated transmitted signal, this could be achieved only for a single resolution cell, and so would appear to be mostly useful in target tracking modes. By employing a transmission employing separable phase-coherent V and H modes, processing at the receiver could be employed to achieve zero dispersion for all resolution modes.

Conclusions

Consideration of adaptive transmission techniques and the unique capability of radar operation to interrogate multiple resolution signals using a single waveform leads to an important conclusion that adaptive transmission, when directly applied at the transmitter, is useful particularly in the tracking mode. However a more flexible option is to employ phase-coherent simultaneous orthogonally polarized transmit signals that are separable in time or frequency subbands (or other convenient space) so that the receiver can reconstruct arbitrary transmit polarization conditions through a weighted combinations of the separable signals. This leads to the possibility of employing these techniques in the acquisition mode, where each radar resolution cell could potentially benefit from adaptive polarization transmission techniques.

XI. RECOMMENDED WORK

A. Modeling Work

As part of the current research effort, first-order models were developed to simulate the radar detection process for a target in a background of sea clutter. This work included theoretical / numerical modeling and analysis as well as some field experimentation to support polarization-based PMD characterizations for one or more sea states. These characterizations aided development of both forward- and backscatter clutter response models of PMD necessary to evaluate PMD-based target detection and target feature characterization at different signal-to-clutter power ratio regimes.

At least two modeling issues were identified based on these efforts. First, it was suggested that a nuance of PMD representations be utilized. Instead of using HH/HV or VV/VH pairs of signals, it was proposed that VV and HH signals collected in a phase coherent fashion should be employed. This approach has a key advantage that the power of HH and VV responses are usually much higher than the VH or HV components and would enable the application of these detection techniques at longer ranges. A potential issue that needs to be resolved (e.g., in future experiments), is whether or not the HH and VV components are correlated in their responses. Current deterministic electromagnetic response models developed to date yield highly correlated returns (for example at near normal incidence), which would negatively impact detection approaches based on HH/VV processing. It is more likely that these responses are partially or highly uncorrelated, and this uncertainty needs to be resolved, especially through experimentation to guide the representation of these characterizations.

A second issue requiring further investigation that could also lead to novel detection approaches involves the assumption of reciprocity in the HV and VH returns for monostatic and pseudomonostatic topologies. Channel reciprocity is almost always assumed in literature for the monostatic case, although reciprocity would not hold true in the case of a non-reciprocal (e.g., ferrite) reflectors. Since sea clutter is presumably reciprocal, any resolution cells exhibiting nonreciprocity would suggest the presence of a target. A question in the application of this strategy is whether or not such changes are truly detectable and how far separated the transmitter and receiver can be before the reciprocal channel assumption breaks down. Investigation of this question, especially through future experimentation, will lead to the development of suitable modeling approaches and detection algorithms.

Additional modeling development is needed to extend the existing sea reflectivity model, target model, and radar model to incorporate additional features. For the sea reflectivity model, this involves adding simulation of the impact of wave spray and capillary waves on the space and time correlations and associated polarization

statistics. A proposed technique is to incorporate higher densities of uncorrelated scatterers to represent these additional characteristics. To support model development, experimentation will be conducted to help guide the development of the models.

Other model extensions should include augmentation of the radar model with Linear FM based waveforms and extensions of the target model to include various containers and other specific target models. The outcome of this work would yield improved models that can be leveraged in theoretical and/or numerical analyses.

Following model development, the models should be exercised over a variety of waveforms, topologies, and sea states to produce time-varying full-polarization transfer functions for sea clutter and targets. These results can be evaluated and compared with experimental measurements, where feasible, to better understand the effects.

B.   Experimental Work

Experimentation will be needed to acquire measured responses to aid in the development of suitable statistical characterizations. Newly acquired field research vehicles as well as improved transceiver measurement subsystems will significantly improve such experimental capability.

Experimentation is needed to support extensions to the sea reflectivity model. The following are some of the experimentation objectives:

- To estimate the degree of correlation between HH and VV responses especially at near-normal incidence). This can be readily accomplished through the use of simultaneous separable orthogonal transmissions.

- To investigate the loss of reciprocity as the bistatic angle transitions from a monostatic orientation (reciprocal) through a transition region to a bistatic orientation (non-reciprocal)

- To characterize the statistical features of wave conditions such as sea spray and capillary waves.

Experimentation should also be conducted with various waveforms under bistatic, monostatic, and pseudomonostatic conditions to assess associated impacts on performance. The waveforms that should be considered include chirped waveforms with selectable levels of compression in receiver processing; pulsed Doppler waveforms; wideband structured noise waveforms, and simultaneous separable orthogonal transmissions. Further study is needed to better exploit these transmission strategies and associated signal processing algorithms.

Notre Dame has recently acquired two custom field research vehicles as well as wideband universal software radio peripherals (USPRs) that when combined will greatly improve capability to conduct polarimetric measurements and provide flexibility to operate in bistatic or monostatic modes over extended periods of time, with control of system antenna architectures. The following subsections describe the anticipated resources at Notre Dame for conducting future experiments.

1. Field Research Vehicles

The University of Notre Dame recently acquired (Jan 2015) two field research vehicles funded through a 2013 DURIP grant from the Navy. A photo of one of the two identical vehicles with mast extended is shown in Figure 116.

Each vehicle is equipped with interior dedicated desk space and wide-screen computers at four stations; space for radio frequency equipment racks; a 42' telescoping mast; a shared data network among the computers, the instrumentation in the vehicle and the instrumentation on the mast; a 50" monitor; optical fiber between the vehicle and masthead; rooftop antenna mounting locations; a 12 KW gas generator; stabilizer jacks; and other features to enable long term field experimentation. Embedded solar panels and a wind generator on the vehicles provide green power sources, enabling long-term collection without need for the gas-powered generators or off-board power sources. Several photos showing the field research vehicles and some of their key features are shown in Figure 115.

Figure 114.Recently acquired field research vehicle with 42' telescoping mast, 1 kW solar, and 400W wind power
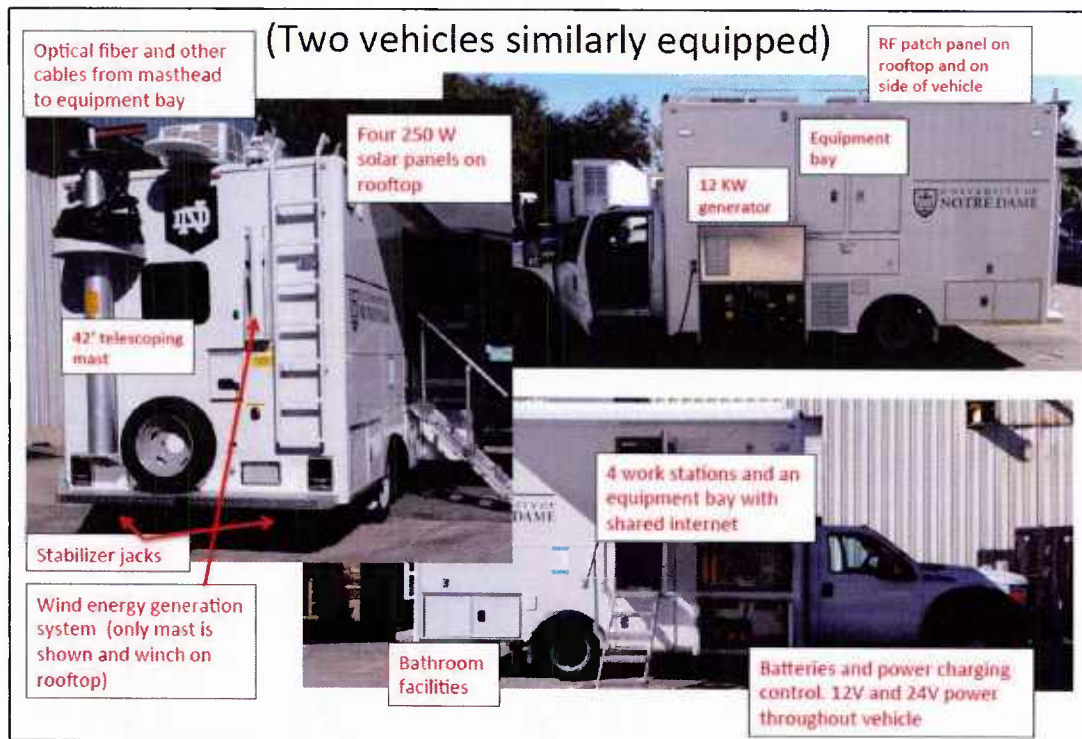

Figure 115. Features of Notre Dame's field research vehicles

The vehicles include a Nycoil conduit with various electrical and fiber optics cables used to provide the interface between the equipment in the main body of the vehicle and the equipment at the top of the mast. The cables include 24 multi-mode fibers (MMF), 12 single mode fibers (SMF), a CAT6A network cable, two LMR-240 coax cables, control cables for pan/tilt control of the masthead, and various discrete wires for general purpose use such as DC power.

The fiber bundles in particular provide a unique capability for very high bandwidth data transport between the vehicle and the masthead. These fibers support high bandwidth applications including 10Gb Ethernet, RF over fiber, and PCI Express extensions over fiber. This capability is essential for the intended operation with USRPs located at the top of the mast streaming high bandwidth digital data to computers in the vehicle.

2. *Universal Software Radio Peripherals (USRPs)*

Notre Dame has recently acquired several low cost USRPs (from both Ettus Research and National Instruments) that provide coherent multichannel transmit and receive capability over a broad spectrum. Each device has two transmit and two receive channels and operates at frequencies up to 6 GHz. Multiple devices can be combined and synchronized to provide coherent operation for any number of transmit or receive channels. However, integration efforts are required in order to achieve and validate coherent operation.

The USRP receiver performs signal filtering, downconversion, and sampling such that its outputs are the digital baseband I/Q samples representing the receive signal. For the transmitter, the process is reversed such that the host computer provides the digital baseband I/Q samples to the USRP, which then performs D/A conversion, upconversion, and filtering.

An important consideration regarding USRP operation is the very high data rate streaming needed for both transmit and receive operation. This streaming necessitates use of a high-speed interface such as 10Gb Ethernet or PCI-e in order to support multi-channel signal bandwidths on the order of 20 MHz or more. It also mandates the use of a high performance computer that can process and/or store the large volume of receive data.

When integrated in the field research vehicles, we intend to deploy three USRPs (2 x 2) at the top of the mast, each connected to a dual-polarized antenna. Locating the USRPs atop the mast in close proximity to the antennas minimizes cable losses and channel-to-channel mismatches inherent in systems with long RF cable runs. With this design, signal impairments are minimized because all analog components are located atop the mast with relatively short cable lengths.

We anticipate using one of the USRPs for transmit and two for receive, but it is possible to dedicate all for either transmit or receive or even for simultaneous

transmit and receive. Although a single USRP can simultaneously transmit and receive, we prefer to locate the transmit and receive functionality in separate boxes in order to maximize transmit / receive isolation. Synchronization among the USRPs will be achieved using a common 10MHz clock source and a common pulse-per-second (PPS) source.

The USRPs are to be connected to computers in the main part of the vehicle via the Nycoil fibers described above. The computers in the vehicles are used to control the measurement acquisition as well as process / display or store the incoming receiver data. These computers have a high performance CPU (quad core i7), a large amount of RAM (32 GB), and solid state drive (SSD). They also contain an I/O card for handling the high data rate streaming for transmit and receive. In the future, we plan to add RAID storage capability to achieve long duration real-time streaming of receiver data to storage.

The integration of this USRP-based transceiver system into the field research vehicles provides a unique measurement capability that we plan to utilize in augmenting polarimetric characterizations of sea clutter and evaluating target detection and identification algorithms.

3.   *Polarimetric Radar Testbed Instrumentation*

The polarimetric radar testbed includes the following instrumentation:

- Agilent E82667D Signal Generator: This system has capability to generate pulsed radar signals with pulse widths as narrow as 10 ns.

- DSO91304A Real-Time Sampling Scope: The vector signal analyzer serves as a wideband multi-channel coherent receiver to enable signal capture. It can also serve as a spectrum analyzer to monitor signals being generated by the channel emulator/signal generator combination to evaluate signal quality and channel emulation operation.

- Agilent N5106A: This 2X2 MIMO signal generator/channel emulation system can be configured with arbitrary waveform generation capability and has capability to support polarimetric channel emulation at baseband.

- Agilent N9010A EXA signal analyzer (26GHz)

C.   *Algorithm Development*

Future work should involve additional development and investigation of algorithms for target detection and identification. The merits of the polarization ratio HH/VV as compared to traditional approaches involving HH/HV or VV/VH is an example. As part of the present effort, polarization-based interference suppression and adaptive polarization transmission were assessed from a *qualitative* standpoint with

references to potential methods, architectures, and/or algorithms. Further investigation is required to produce a *quantitative* evaluation of polarization-frequency interference suppression methods and adaptive transmission techniques and/or the use of simultaneous separable orthogonal transmissions to aid detection and enhance system performance.

Variable linear FM compression algorithms should also be analyzed using experimental data to understand the utility of different time bandwidth products and the PMD representations with different frequency resolution and tradeoffs in system performance.

Future work in target detection could involve quantitative evaluation of target detection performance for customized targets including both a cylindrical target and a non-reciprocal target such as might be expected from magnetic material. Additionally, the ability to discriminate containers made of different materials should be analyzed, where evaluations based on both numerical and experimental data would be appropriate.

Future work in target identification is recommended for the development of improved attitude rate estimation algorithms. These attitude rate estimates can potentially provide important target associations for rigid bodies exhibiting distinct vibration rates. Evaluations for a variety of aspect angles and transmit waveforms should be considered.

Finally, a detection approach based on full-polarization channel matrix correlation behaviors can potentially be considered, where the presence of a target will skew the correlation properties in comparison to surrounding cells. This approach is motivated by the work in [86].

XII. SUMMARY

This research has taken a first look at electromagnetic modeling and analysis of PMD-based radar and associated concepts, particularly for target detection and for long range target identification in sea clutter. An important component of the research has been the development of modeling techniques to represent behaviors of targets and sea clutter that, as yet, have not been reported in radar literature and that are based on polarization dispersion responses. These models were developed from communications-inspired channel models coupled with available trends reported in radar literature for individual polarization component responses of sea clutter, along with supporting experimental measurements conducted at Notre Dame. The models were incorporated into simulation models used to evaluate methods for radar detection and characterization of targets on the surface of the sea.

The modeling incorporated a first-order Weierstrass-Mandelbrot function to represent the sea surface. The sea "manifold" was divided into facets using a uniform grid in the mean plane and then a time-varying augmentation of the Weierstrass-Mandelbrot function was used to model the wave height at each grid location and time. Adequate gridding and time resolutions depend upon the sea structure and the radar wavelength, and we employ values corresponding to conditions leading to a converging PMD response. The sea surface model also included the use of random variables for the component wave directions and their associated phasing. We chose a von Mises distribution for the wave directions because of its flexibility to control the concentration and the mean of the wave directions.

For the polarization-sensitive electromagnetic response model, we first implemented a model based on specular reflection using Snell's law and Fresnel equations that was a function of the plane of incidence and the wave height. Later, the model was extended using vector Kirchhoff theory in conjunction with far-field assumptions yielding the Stratton-Chu equation defining the far-field response from a surface integral, which we numerically compute as a summation over all surface facets. An extension of this model, based on previous statistical channel modeling from polarization-MIMO communications, was introduced to add a statistical fluctuating component to the scattering response. This statistical approach, in combination with the use of variable gridding, we believe can be used for stochastic representations of sea clutter and target polarimetric responses associated with various sea states.

From the electromagnetic responses, first order PMD responses for radar range resolution cells were computed in the model. For the PMD response computation, we proposed a modified Sinclair matrix to extend the monochromatic equations to account for multiple time-dispersed reflections. Next, we formulated the composite

transfer function and obtained frequency domain representation as a function of the subcarriers using a K-point FFT. Finally, we obtained the Stokes parameters as a function of the subcarriers, which forms the basis of the PMD modeling approach.

Using the sea-surface model, the EM scattering response model, and the PMD response estimates, we analyzed the reciprocity between HV and VH for bistatic configurations as a function of the angular separation between the transmitter and the receiver. The goal was to evaluate the bistatic angle over which reciprocity can be expected to hold. This analysis showed that if narrowband processing is employed, HV and VH may be highly correlated at angular separations up to several degrees, provided the reflectors in the radar field of view are reciprocal.

In order to better understand the polarimetric characteristics of the reflectivity from sea clutter, a series of measurements were undertaken at two campus locations. Wave tunnel measurements were conducted in a laboratory setting using multiple antenna orientations and multiple wave types. Measurements were also conducted at St Joseph Lake on the campus of Notre Dame. The lake measurements included both monostatic and bistatic antenna orientations at multiple frequencies. Both experiments first and foremost demonstrated the existence of polarization mode dispersion features, confirming the primary premise of the work. The measurement results showed significant variations in polarization as a function of frequency subcarrier and time. Long PMD curves indicate a large polarization spread over the signal bandwidth (20 MHz for the test waveform), which would be seen as depolarization in a conventional single-polarization system. The tests also showed dependence on the sea state, where the PMD responses were more "chaotic" for rougher states, exhibiting shorter polarization-frequency correlation and increased time variability. Pseudo- periodicities in the PMD responses induced by the periodicities in the wave structure were also evident, supporting the notion that statistics in clutter cells should be similar when the dwell times are sufficiently long. We computed the spectral content of the PMD centroid and identified energy peaks at approximately 2-3 Hz, matching the expected rate for cyclic motion from small waves such as were visibly present throughout the measurements. Similar trends were observed at all frequencies tested, although the responses varied somewhat in structure. For example, higher-frequency operation led to higher-bandwidth variations in the transfer functions defining the PMD response.

Using "clutter-only" simulations, we evaluated the statistical "likeness" of clutter responses from adjacent cells with the purpose of assessing the variability in the response as a function of sample support. The simulation results matched the expectation that as radar dwell times increase, the statistical responses from multiple radar resolution cells tend to converge (due to space/time ergodicity). For a resolution cell that contains both clutter and a target, the statistical response will

generally deviate from these statistics and will thereby provide a means for discrimination.

Both radar and target models were developed and integrated into the simulation model. The radar model accommodates typical radar signal parameters such as frequency, bandwidth, resolution cell size, and antenna pattern. The target model consists of N dipoles with random position, orientation, and reflection coefficient. The resulting models were then used to investigate preliminary target identification and target detection techniques.

The target identification technique involved consideration of the detection of the attitude rates of the target in a background of sea clutter. We presented a method for target identification based on the periodic vibration rates and conducted a laboratory experiment involving 3-axis vibrations using tuning forks. This experiment demonstrated the ability to simultaneously identify all three vibration frequencies with a single-aspect measurement. In simulations, the distributed 10 dipole target model was employed and treated as a rigid body that experienced pitch, yaw, and roll. The simulations showed capability for detecting oscillation rates when the target oscillation amplitude was quite large. However, with smaller oscillation amplitudes, spectral energy was observed at multiple frequencies, including several harmonics of the vibration rates such that more advanced processing may be needed to identify the fundamental rates. We presented an extension of Extreme Value Theory (EVT) as a potential advanced processing method to be used for detection of complex sinusoids.

Using the various models described in the report (sea surface height model, sea reflectivity model, target model, and radar model), we also conducted a number of simulation runs to evaluate target detection performance. In each of these runs, nine radar resolution cells were considered with the eight perimeter cells containing clutter only and the center cell containing both clutter and target. Several processing approaches were considered. In the first approach, multiple samples accumulated over both time and frequency subband were combined to estimate the cumulative distribution function (CDF) of the polarization angles (angular coordinates of Stokes vector) for a given cell. The results illustrate that it is often possible to distinguish the distribution of the target cell from the distributions of the remaining clutter-only cells. However, this was primarily a qualitative evaluation in the sense that although the target cell was visibly distinct from the clutter-only cells, the degree of improvement relative to conventional power detectors was not quantified.

In the next approach, a "power coupling" polarimetric detector, PMD-pc, was defined as the RMS distance between the PMD curve for a given cell and a reference PMD curve created by averaging the curves from all cells. The results of this polarimetric detector were compared to a traditional detector in the form of

receiver operating characteristic (ROC) curves. The ROC curves demonstrated that the PMD-pc detector "usually" outperformed the conventional power detector, but there were instances where the PMD-pc detector did not perform particularly well at low probabilities of false alarms, which is where systems typically operate. Another detector, S0, was defined as the sum of the Stokes S0 parameter over the signal bandwidth. The performance results of this detector were always equal to or superior to results of the conventional power detector. This is not surprising given that the "S0" detector includes the power contributions from both H and V receive signals. In this sense, it is akin to a diversity detector where it achieves performance levels similar to the receive port (H or V) with the highest power.

In the final approach, a promising detector is presented that computes the distance between the CDF estimate of a given cell and the "reference" CDF estimated from the average of all cells. This is similar to the power coupling detector in that it computes the distance between the curve for a given radar cell and the reference curve created from the responses in all cells. However, for the power coupling detector, the "curve" is the PMD curve, while for this detector, the "curve" is the CDF estimate. The results for this detector, especially at longer dwell times for which the clutter statistics for clutter-only cells become more alike, show a promising processing approach that deserves additional investigate in future research efforts. This processing approach may be exercised over a wide range of target, radar, and sea surface parameter combinations in order to evaluate its potential.

Finally, we provided qualitative assessments of two special techniques: polarization-based interference suppression at the receiver and adaptive polarization transmission techniques. We proposed general techniques that would appear to give substantial benefit to polarization-based radar systems. Use of tunable polarization filters, which are likely most easily implemented in the digital domain, provide a mechanism to selectively suppress particular polarization contributions as a function of the frequency subband of the radar signal return. This can be applied on a range-cell basis, leading to the conclusion that such techniques could be valuable in a radar processor.

Consideration of adaptive transmission techniques was also considered. While radar has a unique capability to obtain channel estimates needed for adaptive polarization transmission, the inability of a single waveform to apply to multiple resolution signals leads to an important conclusion that adaptive transmission, when directly applied at the transmitter, is useful particularly in the tracking mode.

However a more flexible option that was conceptualized is to employ phase-coherent simultaneous orthogonally polarized transmit signals that are separable in time or frequency subbands (or other convenient space) so that the receiver can reconstruct arbitrary transmit polarization conditions through a weighted combinations of the separable signals. This leads to the possibility of employing

these techniques in the acquisition mode, where each radar resolution cell could potentially benefit from this form of polarization transmission.

REFERENCES

[1] H. Chan, "Radar sea-clutter at low grazing angles," *Radar and Signal Processing, IEE Proceedings F* , Vol. 137, No.2, pp. 102-112, Apr 1990

[2] N. Guinard, J. Daley, "An experimental study of a sea clutter model," *Proceedings of the IEEE* , Vol. 58, No. 4, pp. 543-550, April 1970

[3] G. Trunk, "Radar Properties of Non-Rayleigh Sea Clutter," *Aerospace and Electronic Systems, IEEE Transactions on* , Vol. AES-8, No.2, pp. 196-204, March 1972

[4] M. Long, "On the polarization and the wavelength dependence of sea echo," *Antennas and Propagation, IEEE Transactions on* , Vol. 13, No. 5, pp. 749-754, Sep 1965

[5] J. Wright, "A new model for sea clutter," *Antennas and Propagation, IEEE Transactions on*, Vol. 16, No. 2, pp. 217-223, Mar 1968

[6] W.M. Boerner, "Introduction to Synthetic Aperture Radar (SAR) Polarimetry," Wexford College Press, 2007.

[7] E. Pottier, J. S. Lee, and L. Ferro-Famil, "Advanced Concepts," PolSARPro V3.0 Lecture Notes

[8] J. Shang, H. McNairn, C. Champagne, and X. Jiao, "Application of Multi-Frequency Synthetic Aperture Radar (SAR) in Crop Classification,"
http://www.intechopen.com/source/pdfs/9536/InTech-
Application_of_multi_frequency_synthetic_aperture_radar_sar_in_crop_classification.pdf

[9] T. Pratt, H Tapse, B. Fette, R. Baxley, B. Walkenhorst and G. Acousta-Marum," Polarization Based Zero Forcing with Multiple Degrees of Freedom", MILCOM 2011, Baltimore MD, 2011

[10] T. Pratt, H Tapse, R. Baxley, B. Walkenhorst and G. Acousta-Marum, "Polarization Based Zero Forcing with Channel Estimation", MILCOM 2011, Baltimore MD, 2011

[11] T. Pratt, B. Walkenhorst, and S. Nguyen, "Adaptive Polarization Transmission of OFDM Signals in a Channel with Polarization Mode Dispersion and Polarization Dependent Loss," IEEE Transactions on Wireless Communications, Vol. 8, No. 7, July 2009, pp. 3354-3359

[12] H. Seunghyeon, T. Sarkar, Signal enhancement through polarization adaptivity on transmit in a near- field MIMO environment, IEEE Antennas and Propagation Society International Symposium, Volume 2A, 3-8 July 2005, pp. 301 304.

[13] T. Ohno, Adaptive Transmit Power Control for MIMO Diversity Employing Polarized Diversity in OFDM Radio Access, Masters Thesis, Keio University, Yokohama Japan, March 2005.

[14] D. Tse and P. Viswanath, Fundamentals of Wireless Communication, Cambridge University Press, 2005.

[15] B. Walkenhorst and T. Pratt, "Polarization-Based Interference Mitigation for OFDM Signals in channels with Polarization Mode Dispersion," MILCOM'08, MCS-12.2, San Diego, CA, November 17, 2008.

[16] A. Zajic, G. Stuber, T. Pratt, and S. Nguyen, Statistical Modeling and Experimental Verification for Wideband MIMO Mobile-to-mobile Channels in Urban Environments; 15th Annual Conference on Telecommunications, ICT2008.

[17] Y. Deng, A. Burr, and G. White, "Performance of MIMO systems with Combined

Polarization Multiplexing and Transmit Diversity," *IEEE 61st Vehicular Technology Conference*, Vol. 2, 30 May-1 June, 2005, p. 869-873.

[18] Universal Mobile Telecommunications System (UMTS); Spatial channel model for Multiple Input Multiple Output (MIMO) simulations (3GPP TR 25.996 version 6.1.0 Release 6); ETSI TR 125 996 V6.1.0 (2003-09).

[19] A. Paulraj, R. Nabar, and D. Gore, Introduction to Space-Time Wireless Communications, Cambridge University Press, 2003.

[20] A. Forenza, F. Sun, and R. Heath, Jr., "Pattern diversity with multi-mode circular patch antennas in clustered MIMO channels," *IEEE Symposium on Antennas and Propagation*, Vol. 3B 3-8 July 2005, p. 438-441.

[21] M. Skolnik, "A Review of Radar Sea Echo," NRL Memorandum Report 2025, July 1969.

[22] F. Macdonald, "Radar Sea Return and Ocean Wave Spectra," *Proceedings of the Conference on Ocean Wave Spectra*, Prentice Hall, pp. 323-329, 1963.

[23] S. C. Rashleigh and R. Ulrich, Polarization mode dispersion in single-mode fibers, *Optics Letters*, Vol. 3, Issue 2, pp. 60-62

[24] C.D. Poole, N.S. Bergano, R.E. Wagner, and H.J. Schulte, Polarization dispersion and principal states in a 147-km undersea lightwave cable, *Journal of Lightwave Technology*, vol. LT-6, pp. 1185-1190, July 1988.

[25] T. Pratt, H. Tapse, B. Walkenhorst, and G. Acosta, "A Modified XPC Characterization for Polarimetric Channels," *IEEE Transactions on Vehicular Technology*, Vol. 60, No. 7, pp. 2004-2013, Sep 2011

[26] T. Pratt, R. Srinivasan, and S. Nguyen, "Input-to-Output Cross Polarization Discrimination (IOXPD) Dispersion Model for Mobile-to-Mobile LOS Wireless Communications MIMO Channels," *Wireless Telecommunications Symposium*, pp. 341-347, 2008

[27] J. Chen and T. Pratt, "Three-Dimensional Geometry-Based Statistical Modeling of 2x2 Dual-Polarized Wideband MIMO Mobile-to-Mobile Channels," paper accepted, *Special Issue on Modeling and Simulation of Mobile Radio Channels*, Hindawi Publishing Corporation, 2012.

[28] J. Chen and T. Pratt, "Space-Polarization MIMO Testbed," ISRCS 2013, San Francisco, August 2013.

[29] F. Talebi and T. Pratt, "Approximating the Outage Capacity of Asymmetric 2x2 Dual-Polarized MIMO at High SNR," ICNC'12, San Diego, CA, Jan. 2103.

[30] F. Talebi and T. Pratt, "Codeset Overlay for Complementary Code Keying Direct Sequence Spread Spectrum," UBICOMM 2012, Barcelona, Spain, September 2012.

[31] F. Talebi and T. Pratt, "Bounding the Ergodic Capacity of Asymmetric 2X2 Dual-Polarized Channels," paper accepted, MILCOM 2012, Orlando, FL, November 2012.

[32] G. Zhang, Y. Liu, "Separation method of polarization states", *IEE Proceedings Radar, Sonar, and Navigation*, Vol. 147, pp 75-79, Apr 2000.

[33] D. Stapor, "Optimal receive antenna polarization in the presence of interference and noise", *IEEE Transactions on Antennas and Propagation*, Vol. 43, No. 5, May 1995.

[34] M. Takahashi, M., H. Takahashi, T. Tanaka, "Cross polarization interference canceler for microcellular mobile communication systems", *IEEE International Conference on Communication*, Vol. 2, pp 910-914, Jun 1995.

[35] G. Stuber, Principles of Mobile Communication, Second Edition, Kluwer Academic Publishers, 2001.

[36] E. Collett, Polarized Light in Fiber Optics, The PolaWave Group, 2003.

[37] T. Pratt and H. Tapse, "Joint Detection of Bivariate Gaussian Noise Sequences," *IEEE Transactions on Aerospace and Electronic Systems*, 2011.

[38] J. A. Ogilvy, "Theory of Wave Scattering from Random Rough Surfaces," Adam Hilger, IOP Publishing, Bristol, England 1991.

[39] J. A. Kong, "Electromagnetic Wave Theory, second edition," John Wiley & Sons, New York, 1990.

[40] D. K. Cheng, "Field and Wave Electromagnetics, second edition," Addison-Wesley Publishing Company, Reading, Massachusetts, 1992.

[41] M. Skolnik, "Radar Handbook, Third Edition," McGraw Hill, New York, 2008.

[42] J. R. Schott, "Fundamentals of Polarimetric Remote Sensing", SPIE Press, Bellingham, WA, 2009.

[43] B. Paul and S. Nasar, "Introduction to Electromagnetic Fields," McGraw Hill, New York, 1982.

[44] T. Pratt, J. Chen, and F. Talebi, "Adaptive Space Polarization MIMO Communications" Final Report, Contract N00014-11-1-0607, April 30, 2013.

[45] D. Barton, Radar Systems Analysis and Modeling, Artech House, 2004

[46] D. Barton, Modern Radar Systems Analysis, Artech House, 1988.

[47] M. Long, Radar Reflectivity of Land and Sea, 2001.

[48] T. Pratt and B. Walkenhorst, "Methods for Polarization-Based Interference Mitigation," USPTO Patent No. 20100098044, April 22, 2010

[49] T. Pratt and B. Walkenhorst, "Systems and Methods for Adaptive Polarization Transmission," USPTO Patent Application, US 20140169428 A1, December 10, 2013

[50] T. Pratt, "Methods and Apparatus for Radio Frequency Polarimetry Sensing," non-provisional application, Feb. 2012

[51] J. Mueller and T. Pratt, J. Mueller and T. Pratt, " A Non-contact, Remote-sensing Vibration Transducer using Radio Frequency Polarimetry," submitted to *IEEE Transactions on Instrumentation and Measurement*, 2012

[52] J. Mueller and T. Pratt, "A Radio Frequency Polarimetric Sensor for Rotating Machine Analysis," *Sensors Journal, IEEE* , Vol. 13, No. 12, pp. 4866-4873, Dec. 2013.

[53] T. Pratt, M. van Iersel, M. Higginson, and Q. Xue, "Remote Sensing of Soil Moisture with RF Polarimetry," Annual International Meeting, American Society of Agricultural and Biological Engineers, Louisville, KY, August 7-10, 2011.

[54] G. Margarit, J. Mallorqui, J. Fortuny-Guasch, C. Lopez-Martinez, "Exploitation of Ship Scattering in Polarimetric SAR for an Improved Classification Under High Clutter Conditions," *IEEE Transactions on Geoscience and Remote Sensing*, Vol. 47, No. 4, pp. 1224-1235, 2009

[55] Wang Yun-Hua, Guo Li-Xin,Wu Zhen-Sen. "The application of an improved 2D fractal model for electromagnetic scattering from the sea surface," *Acta Phys. Sin.*, 55(10): pp. 5191-5199, 2006

[56] G. Davidson, "Simulation of coherent sea clutter," *IET Radar, Sonar and Navigation, Special Issue on Radar Clutter*, Vol. 4, Iss. 2, pp. 168-177, 2010

[57] R. Compton, "On the performance of a polarization sensitive adaptive array", *IEEE Transactions on Antennas and Propagation*, Vol. AP-29, No. 5, Sept 1981.

[58] R. Fante, "Principles of adaptive space-time-polarization cancellation of broadband interference", published by The Mitre Corporation, http://www.mitre.org/work/tech_papers/tech_papers_04/fante_adaptive/fante_adaptive.pdf

[59] R. O. Harger, "A sea surface height estimator using synthetic aper- ture radar complex imagery," *IEEE J. Ocean. Eng.*, Vol. OE-8, No. 2, pp. 71–78, Apr. 1983.

[60] N. Xie, H. Leung, and H. Chan, "A multiple-model prediction approach for sea clutter modeling," *IEEE Trans. Geosci. Remote Sens.*, Vol. 41, No. 6, pp. 1491–1502, Jun. 2003.

[61] W. J. Plant, W. C. Keller, and K. Hayes, "Measurement of river surface currents with coherent microwave systems," *IEEE Trans. Geosci. Remote Sens.*, Vol. 43, No. 6, pp. 1242–1257, Jun. 2005.

[62] F. Berizzi, E. Dalle Mese, G. Pinelli, "A two-dimensional fractal model of the sea surface and sea spectrum evaluation," *Radar 97 (Conf. Publ. No. 449)* , pp.189-193, Oct 1997

[63] Liu Wei, Guo Li-Xin, and Wu Zhen-Sen, "Polarimetric Scattering from a two-dimensional improved sea fractal surface," *Chin. Phys. B*, Vol. 19, No. 7, 2010.

[64] Guo L. X. and Wang Y H, 2005 Progress in Electromagnetics Research Symposium, Hangzhou China, 22-26 August, 2005, p23.

[65] T. Pratt, Z. Lin, S. Silliman, and P. Yang, "Polarization Characterization of Microwave Reflections for Sensing of Soil Moiture," pending submission to *Journal of Microwave Power and Electromagnetic Energy"*

[66] M. Sadiku, Elements of Electromagnetics, 3rd ed. New York: Oxford University Press, 2010.

[67] S. Evett and G. Parkin, "Advances in Soil Water Content Sensing: The Continuing Maturation of Technology and Theory," *Vadose Zone Journal*, 4: 986-991, 2005.

[68] J. Huisman, S. Hubbard, J. Redan, and A. Annan, "Measuring Soil Water Content with Ground Penetrating Radar: A Review," *Vadose Zone Journal* 2:476-491, 2003.

[69] J. Stratton, *Electromagnetic Theory.* Wiley-IEEE Press, 2007.

[70] S. Kwon and G. Stuber, "Geometrical Theory of Channel Depolarization," *IEEE Transactions on Vehicular Technology*, Vol. 60, No. 8, pp. 3542-3556, Oct. 2011

[71] Schrader, D. and D. McNelis, "Microwave Irradiation of Plant Roots in Soil," *Journal of Microwave Power*, 1975.

[72] C. Hsu, H. Mendelson, A. Burgstahler, D. Hibbard, and J. Faist, " Polarimetric Detection for Slowly Moving/Stationary Targets in Inhomogeneous Environments," *Proc. Of SPIE*, Vol. 8058, pp. 80581G-1 through 80581G-11, 2011

[73] A. J. Poelman, "Virtual polarization adaptation: A method of increasing the detection capability of a radar system polarization-vector processing," *Proc. IEE Part F,* 128, 261-270, 1981.

[74] V. Gregers-Hansen and R. Mital, "An Empirical Sea Clutter Model for Low Grazing Angles," *IEEE Radar Conference*, Pasadena CA, pp. 1-5, May 2009

[75] D. Shnidman, "Comparison of Low Angle Radar Clutter Models," *IEEE Transactions on*

Aerospace and Electronic Systems, Vol. 41, No. 2, pp. 736-746, Apr. 2005

[76] F. Talebi and T. Pratt, "Time-Domain Correlation-based Multipath Modeling of Wideband Space-Polarization MIMO Channels", MILCOM 2013, San Diego, CA, November 2013

[77] T. Taga, "Analysis for mean effective gain of mobile antennas in land mobile radio environments," *Vehicular Technology, IEEE Transactions on* , Vol. 39, No. 2, pp.117-131, May 1990

[78] F. Talebi and T. Pratt, "Model Order Selection for Complex Sinusoids in the Presence of Unknown Correlated Gaussian Noise," *IEEE Transactions on Signal Processing*

[79] M. Sparrow et al., "Digital Polarimetric System for Generating Polarization Agile Signals," USPTO Patent No. US 6,608,587 B1, Aug 2003.

[80] B. Hochwald, N. Laneman, and T. Pratt, Proposal to DARPA, 2013

[81] Mandai, K. and Kikuchi, N. and Sasaki, S., "Polarization multiplexing transmitter and transmission system," US Patent 8,417,126 B2, Apr 9 2013

[82] S. Emami, C. Corral, G. Rasor, S. Sibecas, and G. Stratis, "Enhanced OFDM by use of alternating polarization states," USPTO Patent Application, US20040125880 A1, Jul 1 2004

[83] S. Emami, C. Corral, and G. Rasor, "Improved Performance OFDM Exploiting Polarization," *Signals, Systems and Computers, 2005. Conference Record of the Thirty-Ninth Asilomar Conference on*, pp.965-968, October 28 - November 1, 2005

[84] S. Sibecus, "Polarization State Techniques for Wireless Communications," USPTO, Patent No. US 7,310,379 B2, Dec. 18, 2007

[85] H. Seunghyeon, T. Sarkar, "Signal enhancement through polarization adaptivity on transmit in a near-field MIMO environment," *Antennas and Propagation Society International Symposium, 2005 IEEE* , Volume 2A, pp.301-304, 3-8 July 2005

[86] F. Talebi and T. Pratt, "Channel Sounding and Parameter Estimation for a Wideband Correlation-Based MIMO Model," *IEEE TVT*, paper accepted

[87] F. Talebi and T. Pratt, "Model Order Selection in the Presence of Unknown Colored Noise," paper accepted, MILCOM2014, Baltimore, 5 pages, Nov. 2014

[88] F. Talebi and T. Pratt, "Time-Domain Correlation-based Multipath Modeling of Wideband Space-Polarization MIMO Channels," MILCOM 2013, San Diego, CA, pp. 1227-1232, Nov. 2013

[89] F. Talebi and T. Pratt, "Correlation-based Multipath Modeling of Indoor Wideband Space-Polarization MIMO Channels in Presence of Specular Reflections," submitted to *IEEE Transactions on Wireless Communications*

[90] P. Dubois, J. Van Zyl, T. Engman, "Measuring soil moisture with imaging radars," *Geoscience and Remote Sensing, IEEE Transactions on* , Vol. 33, No.4, pp. 915-926, Jul 1995

[91] Y. Oh, K. Sarabandi, F. Ulaby, "An empirical model and an inversion technique for radar scattering from bare soil surfaces," *Geoscience and Remote Sensing, IEEE Transactions on* , Vol. 30, No. 2, pp. 370-381, Mar 1992

[92] F. Ulaby, K. Sarabandi, A. Nashashibi, "Statistical properties of the Mueller matrix of distributed targets," *Radar and Signal Processing, IEE Proceedings F* , Vol. 139, No. 2, pp. 136-146, Apr 1992